

***INVESTIGATIONS ON
NANOMETALLOPOLYMERS AND QUANTUM
DOTS WITH THEIR HUMIDITY AND GAS
SENSING APPLICATIONS***

Thesis

**Submitted for the Award of the Degree
of**

Doctor of Philosophy

**in
Applied Physics**

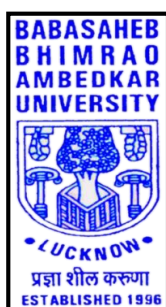
Submitted By

Priyanka Chaudhary

Enrollment No. 683/12

Under the supervision of

Prof. Bal Chandra Yadav



**Department of Applied Physics
School for Physical Sciences
Babasaheb Bhimrao Ambedkar University
(A Central University)
Lucknow -226025, U.P. (India)**

2021

DECLARATION

I declare that the thesis entitled "*Investigations on Nanometallopolymer and Quantum Dots with their Humidity and Gas sensing Applications*" has been prepared by me under the supervision of Prof. Bal Chandra Yadav, Department of Applied Physics, School for Physical Sciences, Babasaheb Bhimrao Ambedkar University, Lucknow. No part of this thesis has formed the basis for the award of any degree and diploma previously. Further, I declare that the material presented in the current work is based on original research work and the appreciation to others has been accordingly acknowledged at applicable places. This is also declare that the thesis is essentially free from all kinds of plagiarism.

Priyanka Chaudhary
(Priyanka Chaudhary)

Department of Applied Physics,
School for Physical Sciences,
Babasaheb Bhimrao Ambedkar University,
Vidya Vihar, Raebareilly Road, Lucknow-226025, U.P., India.

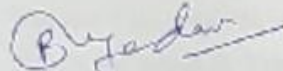
6/9/21 Date:

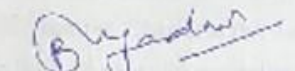
Place: Lucknow

CERTIFICATE

This is to certify that the thesis titled "Investigations on Nanometallopolymer and Quantum dots with their Humidity and Gas Sensing Applications" submitted by Ms. Priyanka Chaudhary is an original research work and has not been previously submitted in part or full for the award of any other degree or diploma to this or any other university.

The thesis submitted to the Babasaheb Bhimrao Ambedkar University, Lucknow satisfies all the requirements as stipulated in the *Doctor of Philosophy (Ph.D.) regulations -1999 as amended in 2008/2010/2013* and it is fit for submission and evaluation for the award of the degree of Doctor of Philosophy of the University.


Prof. B. C. Yadav
(Supervisor)


Prof. B. C. Yadav
(Head of the Department)

Date: 06/09/2021

Place: Lucknow

ACKNOWLEDGEMENT

It is my firm belief that any major research work to result in a positive outcome including a worthy thesis requires the culmination of several factors such as a meaningful subject which can motivate a determined researcher to take up the challenge, a learned and sincere guide in the form of friend, relative and colleague who selflessly encourage and help the researcher throughout the research. I had the honor and privilege to have **Prof. Bal Chandra Yadav** as an excellent guide. I take this opportunity to place on record my heartfelt and sincere gratitude and deep indebtedness to him, without whose guidance this work could not have been meaningfully concluded.

I also owe my sincere thanks and sense of deep gratitude to **Prof. Devesh Kumar**, School of Physical and Decision Science, Babasaheb Bhimrao Ambedkar University, for providing theoretical facilities in the department in a very kind behavior. I am extremely thankful to my teachers **Dr. Ramesh Chandra, Dr. Anil K. Yadav, Dr. Khem B. Thapa, Dr. Devendra Singh** for their valuable suggestions and encouragements which have been a great asset to me during the entire course of study. I owe my deep gratitude towards them for their constant motivation and moral support. I feel myself blessed to have such teachers.

Also, I am thankful to staff members at Babasaheb Bhimrao Ambedkar University especially **Dr. Mukesh Kumar** (USIC), **Mr. Amit Kumar** (DAP), **Mr. Om Awasthi** (DAP) **Mr. Mukesh Tyagi** (DAP) and **Mr. Shatrughan Lal**.

I express my gratitude towards **Dr. Samiksha Sikarwar**, Resource Person, Integrated B.Sc. - M.Sc. (Basic Science), BBAU and **Dr. Sarita Yadav**, Inspire Faculty, University of Allahabad for their constant support in academic upliftment. Also, I am thankful to **Dr. Ravi Kant Tripathi**, DSK Fellow, DAP, BBAU for his valuable suggestions and encouragements. Also, I express my gratitude towards. Further, I'm grateful to **Dr. Rakesh K. Sonker**, Assistant Professor, DoP, Acharya Narendra Dev College, University of Delhi for his support and providing help at the hour of need.

I would like to acknowledge the contribution of my friends and colleagues, **Dr. Pawan Singh, Mr. Krishan Pal, Mr. Ajeet Kumar** and **Mr. Arpit Verma**. Without

their support, the thesis cannot be in its present form. Also, I want to acknowledge **Dr. Utkarsh Kumar, Mr. Shakti Singh, Mrs. Monu Gupta, Ms. Abhisikta Bhaduri, Ms. Shalu Rawat (DES), Dr. Rashmi Kumari** and **Ms. Lata Verma (DES)** for a joyful and healthy environment around me to work.

Finally, I would like to pay my highest regard to my parents **Shri Avadesh Kumar Chaudhary** and **Smt. Shanti Devi** for their love, support and sacrifice from the very first day of my journey of life. Also, I express my sincere thanks to my Uncle **Shri Jitendra Kumar Chaudhary** and aunt **Smt. Maya Devi** for providing me with every kind of support. Also, I am highly thankful to my pride, my siblings **Mrs. Rubi Chaudhary, Ms. Mamta Chaudhary** and **Mr. Sandeep Chaudhary** for their unconditional love and support. I would like to acknowledge the sweet smile of my cousins **Suraj, Sunakshi Chaudhary** and **Omkar** who imparted happiness in my life. Also, I'm thankful to my brother in law **Mr. Pramod Kumar Chaudhary**, Principal, SDCPPIC, Patni who inspired and gave me strength to overcome the failures and to start over again.

Last but not the least, my final words of thanks will be for Almighty God, for His countless blessings, mercy and companionship through all turmoil of my life.

Priyanka Chaudhary
(Ph.D. Scholar)

LIST OF PUBLICATIONS

Published work included in the thesis in the refereed journals:

1. **Priyanka Chaudhary**, Dheeraj Kumar Maurya, Samiksha Sikarwar, B.C. Yadav, G. I. Dzhardimalieva, Rajiv Prakash, Development of nanostructured nickel reinforced polyacrylamide via frontal polymerization for a reliable room temperature humidity sensor European Polymer Journal. 112 (2019) 161–169.
2. **Priyanka Chaudhary**, Dheeraj Kumar Maurya , Ravi Kant Tripathi , B.C. Yadav, Nina D. Golubeva , Evgeniya I. Knerelman , Igor E. Uflyand, Gulzhian I. Dzhardimalieva Synthesis of $\text{Cu}_{0.8}\text{Zn}_{0.2}\text{Sb}_2$ -polyacrylamide nanocomposite by frontal polymerization; highly sensitive for moisture and photo detector performance, Materials Advances 1 (2020) 2804-2817.
3. **Priyanka Chaudhary**, Dheeraj Kumar Maurya, Anwesh Pandey, Arpit Verma, Ravi Kant Tripathi, Sudhir Kumar, B. C. Yadav, Design and development of flexible humidity sensor for baby diaper alarm: Experimental and theoretical study, Sensors & Actuators: B. Chemical (Minor revision).
4. **Priyanka Chaudhary**, Dheeraj Kumar Maurya, Sarita Yadav, Anwesh Pandey, Ravi Kant Tripathi and B.C. Yadav Ultrafast response humidity sensor based on roasted gram derived carbon quantum dots: Experimental and theoretical study, Sensors & Actuators: B. Chemical 329(2020) 1–14.
5. **Priyanka Chaudhary**, Dheeraj Kumar Maurya, Ajeet Singh, and B.C. Yadav, One-pot synthesis of phosphine free indium selenide (InSe) QDs and their structural characterization for LPG and humidity sensing, Surface and interfaces (Under review).

Work not included in Thesis

1. **Priyanka Chaudhary**, Samiksha Sikarwar, B.C. Yadav, G.I. Dzhardimalieva, Nina D. Golubeva, Igor E. Uflyan, Synthesis and characterization of copper (II) nitrate polyacrylamide & its application as opto-electronic humidity sensor, Sensors and Actuators A 263 (2017) 415–422.
2. Surbhi Mishra, Pooja Lohia, **Priyanka Chaudhary**, Bal Chandra Yadav, D K. Dwivedi, Development of an Impedance-Based Electrical Humidity Sensor

- Using Sb-Doped Ge-Se-Te Chalcogenide Glasses, *J. Electron. Mater.* 49(2020) 6492–6500.
3. Arpit Verma, **Priyanka Chaudhary**, Ravi Kant Tripathi, Bal Chandra Yadav
The functionalization of polyacrylamide with MoS₂ nanoflakes for use in transient photodetectors, *Sustain. Energy Fuels* 5 (2021) 1394-1405.
 4. Arpit Verma, **Priyanka Chaudhary**, Ravi Kant Tripathi, Bal Chandra Yadav,
Sensors and Actuators A : Physical Transient photodetection studies on 2D ZnO nanostructures prepared by simple organic-solvent assisted route, *Sensors Actuators A. Phys.* 321(2021) 112600-112606.
 5. Navneet. Yadav, **Priyanka Chaudhary**, Kajal.Kumar Dey, Sarita Yadav, Bal Chandra Yadav and Raja Ram Yadav, Non-functionalized Au nanoparticles can act as high- performing humidity sensor, *JMSE.* 7 (2020) 17843–17854.
 6. Vikas Kumar, Vishnu Chauhan , Jagjeevan Ram , Rashi Gupta , Shalendra Kumar , **Priyanka Chaudhary**, B.C. Yadav, Sunil Ojha , Indra Sulania , Rajesh Kumar, Study of humidity sensing properties and ion beam induced modifications in SnO₂ -TiO₂ nanocomposite thin films, *Surf. Coat. Technol.* 392 (2020) 125768.
 7. Bal Chandra Yadav, Samiksha Sikarwar Rolly Yadav, **Priyanka Chaudhary** G. I. Dzhardimalieva N. D. Golubeva, Preparation of zinc (II) nitrate poly acryl amide (PAAm) and its optoelectronic application for humidity sensing. *Journal of Materials Science: Materials in Electronics.* 29 (2018) 7770–7777.
 8. Dheeraj Kumar Maurya, Samiksha Sikarwar, **Priyanka Chaudhary**, Subramania Angaiah and Bal Chandra Yadav, Synthesis and characterization of nanostructured Copper Zinc Tin Sulphide (CZTS) for humidity sensing applications, *IEEE Sens. Jour.* 19(2019) 2837-2845.
 9. Sarita Yadav , **Priyanka Chaudhary**, K. N. Uttam, Ashish Varma, Manu Vashistha, and B C Yadav, Facile synthesis of molybdenum disulfide (MoS₂) quantum dots and its application in humidity sensing, *Nanotech.*, 30 (2019) 295501.
 10. Ravi Kant Tripathi, O. S. Panwar, Ishpal Rawal, C. K. Dixit, Arpit Verma, **Priyanka Chaudhary**, A. K. Srivastava, B. C. Yadav, Study of Variable Range Hopping Conduction Mechanism in Nanocrystalline carbon thin films deposited

- by modified anodic jet carbon arc technique: Application to light-dependent resistors, *Journal of Materials Science: Materials in Electronics*, 2 (2021) 1-8
11. R. Sanmugapriya, **Priyanka Chaudhary**, E Ranjith Kumar, A Balamurugan, Ch Srinivas, G Prasad, B.C Yadav, DL Sastry, Evaluation of structural, dielectric and electrical humidity sensor behavior of $MgFe_2O_4$ ferrite nanoparticles, *Ceramics International*, 47(2021) 15995-16008.
 12. Krishan Pal, **Priyanka Chaudhary**, B.C.Yadav, K.B.Thapa, Co-precipitation synthesis with a variation of the sulphur composition of Kesterite phase Cu_2ZnSnS_4 (CZSS) without annealing process, *Journal of Physical Science*, 32(2) 2021.
 13. Sunanda Singh, **Priyanka Chaudhary**, Richa Srivastava, Ravi Kant Tripathi, Rajeev Kumar and B. C. Yadav, Improved growth of nano tin ferrites with their decoration on carbon foam for wastewater treatment, *Environmental Nanotechnology, Monitoring & Management* 16 (2021) 100546.
 14. Surabhi Mishra, **Priyanka Chaudhary**, B. C. Yadav, Ahmad Umar, Pooja Lohia and D. K. Dwivedi, Fabrication and Characterization of an Ultrasensitive Humidity Sensor Based on Chalcogenide Glassy Alloy Thin Films, *Eng. Sci.*, 15 (2021)138–147.

Papers presented in International Conferences/Proceedings

1. Training School on Instrumentation and Characterization (TraSIC) May 24-25, 2018, BBAU Lucknow, U.P. India
2. National Seminar on Nano Science and Nano Biotechnology, 25th – 26th February, 2017, DAVC, Kanpur.
3. 4th Lucknow Science Congress (LUSCON-2017), 3rd – 4th March, BBAU, Lucknow.
4. International Conference on Renewable Energy for Sustainable Environment: Challenges and Remedies, 20th – 21st March, 2017, SMVDU, Jammu.
5. International Conference on Nanoscience and Nanotechnology (ICNN-2013), 24th – 26th September, 2017, BBAU, Lucknow.

Achievements

- ❖ **“Best Poster Presentation Award”** in National Seminar on Nano science and Nano Biotechnology, Feb. 25-26, 2017, D.A.V College, Kanpur.
- ❖ **“Best Poster Presentation Award”** in 4th Lucknow Science Congress (LUSCON-2017), March 3-4, 2017, **BBAU, Lucknow.**
- ❖ **“Best Poster Presentation Award”** in International Conference on Renewable Energy for Sustainable Environment: Challenges and Remedies, March 20-21, 2017, SMVDU, Jammu.

ABSTRACT

Human health drew immense attention and pledged to secure health through proper control on pollution, sanitation, hygienic food, drug, disease observation, urban development, and professional health. It is an essential need to assess the safe environment for healthy living. In recent years, a variety of toxic gases such as hydrogen sulfide (H_2S), carbon monoxide (CO), oxygen depletion (O_2), carbon dioxide (CO_2), ammonia (NH_3), benzene (C_6H_6) have been released from industries and manufacturing activities from raw materials. Hence it becomes very important to control and monitor these toxic gases present in the atmosphere raising a serious concern to human life. In this direction, humidity is much important for human comfort and the environment. Water must be the most crucial element on the earth playing a vital role in the existence of human life. It exists at varying rates in the gas phase (as water vapour) in our air. The importance of the water is that without water vapour in the air, the temperature of the earth's surface would be much cooler (water molecules are the most important for greenhouse gas). However, a high amount of humidity is also leading to discomfort due to imbalance. Water is a very necessary compound for humans as well as the environment. The water molecule exists in gaseous forms in the form of humidity and obeys gas laws. Water is a high dipolar molecule, which condenses and evaporates with the temperature of the atmosphere. These water molecules change in the atmosphere according to the temperature of the atmosphere and warm air has a better capacity to clamp water than does the cold air. The warm air stores a more amount of energy in the environment. Various humidity sensors have been reported based on metal oxides and based nanocomposites. Polymers are one of them attractive materials in the field of sensors. The organic polymers display unique properties due to their high length. They are very useful for our living life, and applicable in many things, named as plastic age. Nowadays macromolecules have great interest in the field of education and research. Scientifically, the chemistry of macromolecules overlaps the disciplines of engineering science and material physics. Moreover, except carbon, the main elements in chain developing organic macromolecules are oxygen, sulfur and nitrogen. The silicon, phosphorus-containing macromolecules are also very important. Organic macromolecules are limited and

have some drawbacks such as low thermal stability, binding interaction, electron transfer process and healing effect. Hence it is very important to remove these drawbacks by developing a new class of material.

According to the periodic table, the only hydrogen is a univalent element and can play the role to replace any groups and is incapable of generating stable macromolecules in solution. To improve the structural, electrical, photoelectrical, conductivity, stability, magnetic and thermal properties of macromolecules new class of materials able to be developed. Also, there performance to be extremely interdisciplinary potentials for application in maximum fields and fundamental research.

Because of these, the combination of metal ions and macromolecules are given both properties active and selective with high stability performance. The first step regarding these materials is the successful synthesis of macromolecules containing metals or nanocrystals. The essential second step is a comprehensive study by characterization tools and the third is application. There are various combinations of metal macromolecules, organic metals, inorganic metals and semi-organic macromolecules. So the interaction of metal ions and macromolecules have numerous possibilities. Semiconductor nanocrystalline and nanometallopolymer materials have great interest in the field of nanoscience and nanotechnology. Quantum dots (QDs) are compounds with specific characteristics like the bandgap of QDs increases when the size of the particle decreases. Also, the colour that QDs emits is directly proportional to its size (smaller dots appear blue). Few limitations of organic metallopolymer (sensitivity, stability etc.) have motivated us towards QDs to make their nanohybrids in the future for humidity/gas sensing applications, as the humidity/gas sensors play a vital role in various fields like medical, agriculture, industries etc.

Chapter 1 deals with the fundamental concept of sensors and their comparison with the existing sensing devices. Briefly introducing the classification of humidity, gas and photosensors, the underlying mechanism and their performance index. A detailed overview of current sensor materials (metal oxide polymer composite, metallopolymer and quantum dots), strategies of enhancing the performance with their characteristics of sensing materials. The sensing mechanism and responsible parameters of sensing material are also discussed in detail. The chapter concludes with

the concept of metallopolymers and quantum dots materials for humidity, gas and photosensors and the plausible solutions to overcome the present challenges. The wide literature review of the past decade has been also tabulated. The multipurpose applications of impedance and capacitance-based humidity sensors have also been explained in this chapter. The orientation of work, aims and objectives of the present research work are well described at the end of the Chapter. The inclusive study of the recent accomplishments in the field of sensors. Presently, the enthusiastic technological advancement of modern appliances raises a serious concern of environmental deterioration and release of toxic gases bad for human health. There is a deep urge to develop highly sensitive gas and humidity sensors for the precise monitoring of toxic gases and humidity present in the atmosphere. Recently a variety of such sensors are available for the industry as well as domestic applications.

Chapter 2 presents the nanostructured $\text{Ni}(\text{NO}_3)_2(\text{AAm})_4 \cdot 2\text{H}_2\text{O}$ thin film as an electrical humidity sensor. For this purpose, films were prepared by spin-coating method to investigate the adsorption/desorption of humidity at room ambient. The sensing element was investigated through X-ray diffraction (XRD), Scanning Electron Microscope (SEM), Transmission Electron Microscope (TEM) and UV–Vis absorption techniques. XRD exhibited the crystalline nature of the nanomaterial thin film and evaluated the average crystallite size was 30 nm. SEM showed highly porous nanostructures of different sizes distributed throughout the film. The energy bandgap of the film was estimated as 4.034 eV. TEM image revealed the nanostructures with an average grain size of 4-21 nm and SAED confirmed the crystalline nature of the material. The film was further employed for humidity sensing which gave a maximum average sensitivity of 37.79 $\text{M}\Omega/\% \text{RH}$ at room temperature.

Chapter 3 includes the solvent-free synthesis of nanocomposite for humidity sensors which are gaining immense interest to fulfil the criteria for its practical application. Further, it describes the development of CdS/ polyacrylamide nanocomposite as a flexible humidity sensor, which has been fabricated by the facile spin-coating technique on PET (polyethylene terephthalate) substrate. The morphological, optical and crystalline nature of CdS/polyacrylamide nanocomposite were investigated using SEM, TEM, XRD, DSC, FTIR, UV-Visible, and Particle size analysis. Characteristic surface area and pore volume were estimated using BET

analysis whereas the hydrophilicity of the sample was investigated using contact angle measurement. As fabricated sensor showed an outstanding humidity sensing response with good linearity in the humidity ranging from 11% to 95% RH. The average sensitivity of nanocomposite was calculated as 125.57 nF/%RH and may be utilized for moisture detection of the commonly used baby diaper with alarm. The simulated & optimized computer model of the synthesized composite (CdS & Polyacrylamide) using density functional theory and performed several analyses. HOMO-LUMO and correspondingly obtained other electronic parameters were studied, which revealed that the bandgap of the synthesized composite material tends to decrease upon increasing the level of water molecules owing to be better humidity sensing mechanism, and therefore it is applicable for humidity sensors.

Chapter 4 describes the synthesis of $\text{Cu}_{0.8}\text{Zn}_{0.2}\text{Sb}_2\text{AAM}$ -polymer nanocomposite via frontal polymerization technique with its humidity sensing and photoconductive behaviour. The surface texture was examined using scanning electron microscopy (SEM) analysis. X-ray diffraction and transmission electron microscopy (TEM) studies confirm the crystallinity of as-fabricated nanocomposite thin film-based sensing element. The surface area, particle size, optical absorbance and thermal stability of as-fabricated thin film were successively investigated using Brunauer–Emmett–Teller (BET), Particle size analysis, Ultra-Violet absorption, Fourier Transform Infrared (FTIR) spectroscopy, Thermogravimetric analysis, X-ray photoelectron spectroscopy (XPS) and Differential Scanning Calorimetric (DSC) analysis respectively. Humidity sensing characteristics were also investigated via the capacitive performance of $\text{Cu}_{0.8}\text{Zn}_{0.2}\text{Sb}_2\text{AAM}$ film with the exposure of moisture. The average sensitivity (S) of as-fabricated sensor was found to be ~ 168.477 pF/%RH at an optimum frequency of 20 Hz. The sensor exhibited a rapid response and recovery time of 4.6 sec and 5.6 sec with persistent stability of 96 % after 60 days. Thus, $\text{Cu}_{0.8}\text{Zn}_{0.2}\text{Sb}_2\text{AAM}$ polymer-based capacitive humidity sensor ensures its potential towards reliable and safer use in the detection of humidity levels as well as a photoconduction. In this chapter, the capacitance-based humidity sensor shows very few response recovery times as compared to $\text{Ni}(\text{NO}_3)_2(\text{AAM})_4 \cdot 2\text{H}_2\text{O}$

Chapter 5 reports the sustainable, cost-effective and rapid synthesis of gram derived carbon quantum dots (GCQD) employed as capacitive humidity sensor.

Synthesis of GCQDs C-1 & C-2 at different carbonization temperatures has been performed by the pyrolysis method. The crystallinity of as prepared GCQDs were confirmed by XRD and TEM analysis revealing the average particle size 5.5 and 2 nm for C-1 & C-2 respectively. The optical properties of samples were further analysed by UV-visible and photoluminescence meter which gave the bandgap as 3.82 and 4.20 eV. Compositional analysis of GCQDs was confirmed by using XPS analysis. GCQDs were subjected to a sensing test at frequency 20 – 2 MHz. The C-2 gave an enhanced sensing performance with an average sensitivity of 254.861 pF/%RH. Also, the sensor showed rapid response and recovery times of 7.3 & 4.7 sec respectively. Theoretical modelling has been performed to further look into the insight of interaction between functional group of GCQDs and water vapour molecules. Transient parameters such as charge density, HOMO-LUMO gap, electron clouds and H-bonds were calculated using B3LYP hybrid functional at 6-31g diffused and polarised basis set. This study provides insight chemistry of GCQDs with water toward an efficient humidity sensor development. In this chapter, the experimental results correlate with the theoretical results, which proven that the sensing behaviour of the materials also depends on the functional group of the material

Chapter 6 reports the novel material synthesis of Indium selenide (InSe) quantum dots, via a one-pot route without any phosphene solvent. TEM analysis reveals that the particles were spherical and most of them were within the size range of 4-6 nm. The particle size distribution curve shows that the average particle size of InSe QDs is ~13 nm. Optical characterization displays that InSe also had the luminescence property. The excitation wavelength at 370 nm, shows a strong broad emission peak ranging from 400 to 700 nm, with two max positions at ~ 405 and 432 nm. The UV-Visible spectra confirmed the absorption spectra of the quantum dots and also increases the optical band gap as compared to the electronic bandgap. The estimated optical energy band gap is 2.2 eV (inset). Here, the bandgap increases with a decrease in the size of quantum dots. The TRPL (Time-resolved photoluminescence) of InSe QDs was also calculated as 6.41 ns. These InSe quantum dots were used as gas and humidity sensors, for this, we have fabricated the sensing element by a spin coating method. Our results show that InSe quantum dots are able to perform as a well-performing humidity sensor. The average

sensitivity of the sensing element was found as $8.89 \text{ M}\Omega/\%RH$. Response and recovery times of the InSe quantum dot were calculated as 5.3 sec & 12.4 sec

PREFACE

The field of nanotechnology is one of the most popular areas for current research and development in basically all technical disciplines. Another field of interest is metal-organic frameworks (MOF) which mainly include metallopolymers. Nanometallopolymers are emerging polymer nanocomposites, which are very cost-effective and can be used as solar cells, chips, and energy storage devices. Polymer gels are significant materials for both fundamental and scientific research. Also, hydrogels are quite interesting owing to their excellent property of absorption/desorption which ensures their applicability in biomedical engineering. Acrylamide-based hydrogels can be best suited for versatile applications.

During the last few years, the optical and electronic properties of semiconductor nanostructures have been of great interest, both theoretically and experimentally. At the nanometer scale, continuous energy levels change into discrete energy levels due to the quantum confinement phenomena. Quantum confinement effects are present in many systems e.g. in quantum well, quantum wire and quantum dots. In quantum dots, due to the 3-D confinement, the density of states shows discrete energy levels. The energy levels can be monitored to different values by controlling the shape, size, dot material and confinement potential. The electronic transitions in the discrete energy levels can be used to tailor the optical properties of quantum dots. Quantum dots are very tiny particles, having a diameter of 2 to 10 nanometers. They have unique optical and electronic properties due to their three-dimensional quantum confinement regime. In a semiconductor bulk material, the conduction and valence band are separated by a bandgap and when light absorption takes place, the electron is excited from the valence band to the conduction band, creating a hole in the valence band. After a certain time (10^{-8} sec), when the electron returns to the valence band, fluorescence is observed. Because of the small-time lag in the process of light absorption, the electron and hole don't move independently due to the Coulomb attraction and form hydrogen-like species. When all the three dimensions of the semiconductor material are reduced to few nanometers and the particle becomes smaller than the Bohr radius, the quantum confinement effect comes into the scene and in this situation, these nanoparticles are defined as quantum dots. Quantum dots (QDs) are compounds with specific characteristics like the bandgap of QDs increases when the size of the particle decreases. Also, the colour that QDs emits is directly proportional to its size (smaller dots appear blue). Few limitations of organic metallopolymers (sensitivity, stability etc.) have

motivated us towards QDs to make their nanohybrids in the future for humidity/gas sensing applications, as the humidity/gas sensors play a vital role in various fields like medical, agriculture, industries etc.

Chapter 1 deals with the fundamental concept of sensors and their comparison with the existing sensing devices. Briefly introducing the classification of humidity, gas and photosensors, the underlying mechanism and their performance index. A detailed overview of current sensor materials (metal oxide polymer composite, metallopolymers and quantum dots), strategies of enhancing the performance with their characteristics of sensing materials. Also, the sensing mechanism and responsible parameters of sensing material have been discussed in detail. The chapter concludes with the concept of metallopolymers and quantum dots materials for humidity, gas and photosensors and the plausible solutions to overcome the present challenges. The wide literature review of the past decade has been tabulated. The multipurpose applications of impedance and capacitance-based humidity sensors have also been explained in this chapter. The orientation of work, aims and objectives of the present research work are well described at the end of the Chapter. **Chapter 2** deals with the synthesis of nanometallopolymers $\text{Ni}(\text{NO}_3)_2(\text{AAm})_4 \cdot 2\text{H}_2\text{O}$ and its fabrication by spin coating. The humidity sensing application at room temperature has also been investigated. In **Chapter 3** deals with to synthesize the CdS/polyacrylamide using the frontal polymerization route. Further, its film was fabricated using the spin coating technique for the detection of humidity at room temperature. A new approach to the application of an as-developed humidity sensor to detect the moisture/ wetness in the Baby diaper with an alarm system was also investigated in this chapter. **Chapter 4** deals with the synthesis of ternary metal-doped polyacrylamide as a humidity sensor. **Chapter 5** describes the synthesis of carbon quantum dots from roasted grams using the pyrolysis method. These quantum dots easily interact with water molecules and were utilized as humidity sensors. Also, the DFT data confirmed the experimental results. **Chapter 6** designates the synthesis, characterization and humidity sensing properties of quantum dots such as carbon quantum dots and InSe quantum dots. In this chapter the gas sensing properties were also investigated. **Chapter 7** deals with a study of synthesis, characterization, humidity and gas sensing properties of nanometallopolymer and quantum dots which are summarized in the present chapter. This chapter also provides the guidelines for further research work in the field of nano dimensional materials as humidity and gas sensors.

LIST OF ABBREVIATIONS

S. No.	Abbreviation	Full Name
1.	FESEM	Field Emission Scanning Electron Microscopy
2.	SEM	Scanning electron microscopy
3.	XRD	X-ray diffraction
4.	TEM	Transmission electron microscopy
5.	TG/DSC	Thermogravimetry/Differential Scanning Calorimetry
6.	XPS	X-ray photoelectron spectroscopy
7.	TRPL	Time-Resolved Photoluminescence
8.	DI	Deionized water
9.	% RH	Relative humidity
10.	LPG	Liquefied Petroleum Gases
11.	InSe	Indium selenide
12.	QDs	Quantum dots
13.	PAAm	Poly acryl amide
14.	AAm	Acryl amide
15.	DFT	Density Functional Theory
16.	TOPO	Tri-n-Octal phosphine

LIST OF TABLES

Table No.	Table Caption	Page. No.
Table 1.1:	Confinement types with their conditions	41
Table 1.2:	The confinement structure with their wave equations.	41
Table 1.3:	The international and national developments in the field of sensors summarized year-wise thorough literature survey.	42
Table 2.1:	Elemental analysis data of Ni(II) nitrate AAm complex.	64
Table 3.1:	Average sensitivities of CdS-Polyacrylamide at different frequencies in three regions.	89
Table 3.2:	Photoconduction parameters at different power.	89
Table 3.3:	Electronic properties of the composite without and with interaction from water molecules.	90
Table 3.4:	Thermochemical properties of the composite without and with interaction from water molecules.	91
Table 3.5:	Interactions distances with water molecules.	90
Table 4.1:	A detailed literature survey of other humidity sensing materials with %RH.	126
Table 4.2:	Comparative study of response and recovery times.	126
Table 4.3:	Sensitivity at different frequencies of Cu _{0.8} Zn _{0.2} Sb ₂ AAm polymer nanocomposite.	127
Table 5.1:	The literature survey related to the capacitive carbon-based humidity sensor.	157
Table 5.2:	Sensitivity at different frequencies of gram carbon quantum dots (C-1).	157
Table 5.3:	Sensitivity at different frequencies of gram carbon quantum dots (C-2).	158
Table 5.4:	h-bond distance.	158
Table 5.5:	The HOMO-LUMO gap of the carbon quantum dots.	159

Table 6.1:	LPG sensing parameters of InSe based sensor	181
Table 7.1:	A chapter-wise outline of the Thesis	195

LIST OF FIGURES

Figure No.	Figure Captions	Page no.
Figure 1.1:	Schematic diagram of the present environmental challenges and needs of the sensor.	43
Figure 1.2:	Representation of importance of sensors in our daily life.	43
Figure 1.3:	Role of humidity sensors in diverse fields	44
Figure 1.4:	Humidity sensors affecting parameters.	44
Figure 1.5:	Classification of humidity sensors.	45
Figure 1.6:	Classification of ceramic humidity sensors.	45
Figure 1.7:	Impedance based humidity sensing mechanism.	46
Figure 1.8:	The schematic presentation of humidity sensing mechanism; three regions as low, middle, and high-level %RH.	46
Figure 1.9:	Classification of metal complex polymers.	47
Figure 1.10:	Color and size-dependent property of quantum dots.	47
Figure 1.11:	Bandgap energy levels from bulk to quantum dots.	48
Figure 1.12:	Display the comparison between energy levels of bulk and nanomaterial with Bohr radius and exciton of an atom.	48
Figure 1.13:	Quantum confinement of the nanomaterial with density functions.	49
Figure 1.14:	Quantum dots based humidity sensing mechanism.	49
Figure 1.15:	Schematic for LPG sensing mechanism.	50
Figure 1.16:	Frontal polymerization (left) and its three dimensional process.	50
Figure 1.17:	Schematic of the nucleation stage of quantum dots in the framework of the LaMer model (left), Representation of the simple synthetic apparatus preparation of quantum dots	51
Figure 2.1:	Schematic for frontal polymerization reaction technique.	65
Figure 2.2:	Block diagram for synthesis of Ni(II) nitrate polyacrylamide (PAAm).	65

Figure 2.3:	Schematic of the experimental set-up for the electrical humidity sensor.	66
Figure 2.4:	SEM image showing surface morphology of nickel nitrate polyacrylamide at (a) 5 μm and (b) 1 μm scales presenting porous nature.	66
Figure 2.5:	TEM image of Ni(II)nitrate PAAm where the inset shows the diffraction pattern of atoms obtained by SAED (b) Powder XRD pattern of Ni(II)nitrate PAAm.	66
Figure 2.6:	(a) Particle size distribution curve obtained from Nano-ZS90 showing the minimum range of particles between 3-23 nm (b) The absorption spectrum along with Tauc plot of the Ni(II)nitrate PAAm film where the estimated optical energy band-gap is 4.034 eV.	67
Figure 2.7:	The graph between temperature ($^{\circ}\text{C}$) and (a) weight% showing the TGA; (b) heat flow (nW) showing the DTA of the material.	67
Figure 2.8:	Variation of impedance in accordance with %RH to show (a) sensing response (sensitivity of 37.79 $\text{M}\Omega/\%\text{RH}$), (b) repeatability test (c) Ageing effect after 3 and 4 weeks, and (d) response time (15.1 s) and recovery time (75.2 s).	68
Figure 2.9:	Schematic of Grotthuss chain reaction showing the interaction of surface morphology with humidity.	68
Figure 3.1:	Flow chart illustration of Chemical reactions involved during the synthesis of CdS/Polyacrylamide.	93
Figure 3.2:	Schematic of humidity sensing set-up.	94
Figure 3.3:	Schematic for the fabrication of sensing element.	94
Figure 3.4:	FESEM images of CdS-Polyacrylamide nanocomposite at different magnifications.	95
Figure 3.5:	DLS spectra of CdS-Polyacrylamide nanocomposite (b) BET analysis nanocomposite (c) FTIR analysis (d & e) TEM analysis at 100 nm scale HRTEM inset inside, the polymer layer shows at 20 nm (f) XRD diffraction pattern.	95

- Figure 3.6:** XPS analysis of the CdS/polyacrylamide nanocomposite: (a) full scan data; (b) Cadmium (3d) element, (c) sulphur (S2p) element, (d) Oxygen (O1s) element, (e) carbon (C 1s) element, (f) nitrogen (N1s) element, (g) atomic weight% ratio of elements, (h) histogram showing the binding energies and (i) Peak area of elements 96
- Figure 3.7:** The sensing response at different %RH (b) Variation of capacitance corresponding to the %RH at different frequencies in increasing mode (c) Variation of capacitance corresponding to various %RHs at different frequencies in decreasing mode (d) Impedance variation with %RH in increasing mode at different frequencies (e) Impedance variation with %RH in decreasing mode at different frequencies (f) Hysteresis curve 97
- Figure 3.8:** The capacitive humidity sensor response at logarithmic scale with respect to relative humidity (b) linearly fitted sensitivity curve in three regimes at 20 Hz (c) sensor response at logarithmic scale concerning time (d) capacitive stability curve at 20 Hz frequency (e) capacitance sensing response and recovery times (f) The sensitivity response histogram in three regimes at different frequencies with %RH and average sensitivity inset in the figure. 97
- Figure 3.9:** (a) I-V characteristics at different relative humidity (b) Humidity performance in a baby diaper (c) hydrophilic nature of the sensing material (d) device structure and during humidity interaction through the electron transfer process. 98
- Figure 3.10:** (a-e) shows the curves between resistance corresponding with time at different mL, (e-j) exhibit the response and recovery time equivalent with ml (k-l) variation in resistance inside the humidity chamber in baby diaper and flexibility of the substrate. 100

Figure 3.11:	(a-d) shows the photoconduction studies of CdS/polyacrylamide at different power, the change in current in dark and light-medium, responsivity at different power.	100
Figure 3.12:	Humidity sensing mechanism at different regions.	100
Figure 3.13:	HOMO-LUMO Orbitals.	101
Figure 3.14:	Electron donor & acceptor regions.	101
Figure 3.15:	Band gap vs number of water molecules (b) HUMO – LUMO of the water molecules.	102
Figure 3.16:	Interactions distances with water molecules.	102
Figure 4.1:	Flow chart for the synthesis of polymer nanocomposite ($\text{Cu}_{0.8}\text{Zn}_{0.2}\text{Sb}_2\text{AAm}$).	128
Figure 4.2:	Schematic diagram of Photoconduction set-up.	128
Figure 4.3:	Schematic presentation of the preparation of $\text{Cu}_{0.8}\text{Zn}_{0.2}\text{Sb}_2\text{AAm}$ film by the spin coating method.	129
Figure 4.4:	SEM images showing the morphology of $\text{Cu}_{0.8}\text{Zn}_{0.2}\text{Sb}_2\text{AAm}$ thin-film possess a highly porous rigid structure with few cracks and pores on the surface with a different scale.	129
Figure 4.5:	Adsorption-desorption isotherms of ($\text{Cu}_{0.8}\text{Zn}_{0.2}\text{Sb}_2\text{AAm}$) (b) Pore radius distribution curves relative to variation in the pore volume.	130
Figure 4.6:	The TEM image of $\text{Cu}_{0.8}\text{Zn}_{0.2}\text{Sb}_2\text{AAm}$ thin film (b) SAED pattern of $\text{Cu}_{0.8}\text{Zn}_{0.2}\text{Sb}_2\text{AAm}$.	130
Figure 4.7:	The particle size distribution curve shows that the peaks are divided into two major intensities. (b) The optical absorbance spectra of the fabricated film in the wavelength range of 190-1100 nm where inset shows the Tauc plot (c) XRD pattern of $\text{Cu}_{0.8}\text{Zn}_{0.2}\text{Sb}_2\text{AAm}$, confirms the crystalline nature and the presence of Cu, Zn and Sb with their characteristic peaks. (d) IR spectra of $\text{Cu}_{0.8}\text{Zn}_{0.2}\text{Sb}_2\text{AAm}$ thin film.	131

Figure 4.8:	(a) TGA (b) DSC curves of $\text{Cu}_{0.8}\text{Zn}_{0.2}\text{Sb}_2$ polyacrylamide in an argon atmosphere with the heating rate of $10\text{ }^\circ\text{C}$ per minute.	131
Figure 4.9:	(a)XPS analysis of $\text{Cu}_{0.8}\text{Zn}_{0.2}\text{Sb}_2$ polyacrylamide nanocomposite (b) Copper (Cu 2p) element (c) zinc (Zn 2p) element (d) Antimony (sb 3d) element (e) Carbon (C 1s) element (f) Oxygen (O 1s) element (g) Nitrogen (N 1s) element (h) Atomic weight % of elements (i) Histogram for binding energy of the nanocomposites.	132
Figure 4.10:	(a-b)Photoconduction behaviour of $\text{Cu}_{0.8}\text{Zn}_{0.2}\text{Sb}_2\text{AAm}$ nanomaterial.	132
Figure 4.11:	Humidity sensor response curves at room temperature (a) Variation of capacitance corresponding to the variation of %RH in increasing mode at different frequencies (20 Hz to 2 MHz)(b) Capacitive humidity sensor curve at different frequencies in decreasing mode (c & d) Normalized response with exponentially fitting data function for increasing mode and decreasing mode.	133
Figure 4.12:	(a) Variations of capacitance curve with frequency at different %RH (10 to 95 %RH) for Cu-Zn-Sb PAam thin-film based humidity sensor at room temperature. (b) The sensitivity response at different test frequencies at $25\text{ }^\circ\text{C}$ with %RH (c) Humidity sensor response at logarithmic scale (d) Linearly fitted curve for the sensitivity calculation.	134
Figure 4.13:	(a) Response curve showing response time 4.6 s and recovery curve showing recovery time (b) Stability curve of sensing element at different %RH.	148
Figure 4.14:	The schematic presentation of humidity sensing mechanism on the surface of film; three regions as low, mid and high level of %RH	148
Figure 5.1:	Schematic representation of the preparation of GCQDs using pyrolysis technique.	160

Figure 5.2:	FTIR spectra of GCQDs (b) XRD pattern (c) Oxidation state and (d) Binding energies curve of C-2.	160
Figure 5.3:	TEM image of C-1 at 100 nm scale (b) HRTEM image of the GCQDs at 1 nm scale (c) Particle size distribution curve of C-1 (d) TEM image of C-2 at 20 nm (e) HRTEM image of GCQDs at 5 nm scale (f) Particle size distribution curve for the sample C-2.	161
Figure 5.4:	UV absorption spectra of GCQDs (a) Absorbance Vs wavelength (nm) plot for the C-1 with an energy band gap of 3.82 eV (b) Absorbance vs. wavelength (nm) for the C-2 with an energy band gap of 4.2 eV. (c) Photoluminescence of C-1 with an emission peak at 454 nm (d) an emission peak of C-2 at 428 nm	162
Figure 5.5:	(a) Raman spectra of C-1 and (b) C-2 samples.	162
Figure 5.6:	Sensing characteristics of GCQDs based sensor at different operating frequencies (20 Hz -2 MHz) (a,b) increasing and decreasing mode curve at different frequencies of C-1 (c,d) increasing and decreasing mode at different frequencies of C-2	163
Figure 5.7:	(a) Adsorption and desorption curve with hysteresis of gram carbon quantum dot (a) C-1 and (b) C-2. Inset shows corresponding normalized sensor response curve.	163
Figure 5.8:	Variation of capacitance with respect to frequencies (a) increasing mode (b) decreasing mode of C-1 (c) increasing mode (d) decreasing mode curve of C-2.	164
Figure 5.9:	Response and recovery times curve of C-1 and C-2	164
Figure 5.10:	Variation of capacitance with time (a) stability curve of C-1 (b) stability curve of C-2	165
Figure 5.11:	Schematic of humidity sensing mechanism of GCQDs	165
Figure 5.12:	Formation of H-bond interaction for (a) one, (b) two and (c) three water molecules with GCQDs	166

Figure 5.13:	H-donor/acceptor clouded regions of (a) one, (b) two and (c) three water molecules with GCQDs	166
Figure 5.14:	The electron cloud densities in the interaction of (a) one, (b) two and (c) three water molecules with GCQD.	167
Figure 5.15:	HOMO-LUMO molecular orbital structure of gram carbon quantum dots	167
Figure 6.1:	Schematic for the synthesis of InSe QDs by kinetic growth method	182
Figure 6.2:	Schematic for the LPG sensing set-up	182
Figure 6.3:	Experimental set-up for humidity sensing	183
Figure 6.4:	Particle size analysis of QDs (b) UV-Visible absorbance spectra with Tauc plot (c) Time-resolved PL spectra of InSe QDs (d) Photoluminescence spectra of QDs.	183
Figure 6.5:	(a) Topological analysis at 20 nm scale (b,d) HRTEM analysis at 5 nm scale and 1 nm scale (c) pure InSe QDs without UV light (e) XRD analysis of quantum dot (f) fluorescence image of QDs in presence of UV light	183
Figure 6.6:	LPG gas sensing response of the InSe QDs at different vol.% (b) response and recovery time curve shows the 7.5 sec and 6.3 sec respectively at 0.5 vol.% (c) repeatability test at 0.5 vol.% (d) sensor response histogram at different vol.% (e) response and recovery time at different vol.% (f) linear sensor response	184
Figure 6.7:	Schematic for LPG sensing mechanism	184
Figure 6.8:	Humidity sensing response of the InSe QDs (b) ageing effect after one, two, three weeks (c) repeatability test (d) response and recovery curve of the InSe QDs (e) response and recovery time (f) linear sensor response	185
Figure 6.9:	Selectivity of InSe QDs with other gases (b) effect of humidity during LPG sensing	186

Appendix: Experimental Methods and Characterization Technique

Figure No.	Figure Captions	Page no.
Figure A.1:	Frontal polymerization (a) and (b) its three dimensional process	A xvii
Figure A.2:	Schematic of the nucleation stage of quantum dots in the framework of the LaMer model (left), Representation of the simple synthetic apparatus preparation of quantum dots	A xvii
Figure A.3:	Photograph of spin coater (Metrex) used in the preparation of thin film	A xvii
Figure A.4:	Photograph of X-ray diffraction setup (X' Pert PRO PANalytical Ltd., Netherlands).	A xviii
Figure A.5:	Schematic diagram showing the phenomena of Bragg's law	A xviii
Figure A.6:	(a) Photograph of Scanning Electron Microscopes (JEOL, JSM-6490LV) and its (b) working mechanism	A xviii
Figure A.7:	Representation of various types of interactions of electron beam with the sample surface	A xix
Figure A.8:	(a) Photograph of High-Resolution Transmission Electron Microscope (Philips T20ST) and its (b) working mechanism	A xix
Figure A.9:	Photograph of UV-Visible spectrophotometer (Evolution 201) and its (b) working mechanism	A xx
Figure A.10:	(a) Photograph of Particle Size Analyzer (Nano-ZS90) (b) Scattering of light beam through a particle	A xx

Figure A.13: Photograph of the Vibration free table (Newport RS2000-48-8)

A xxi

LIST OF APPENDICES

APPENDIX: Experimental Methods and Characterization Techniques

TABLES OF CONTENTS

Chapter 1: Introduction and Aim of Present Work	1-51
1.1 Introduction	2
1.2. Need of sensor-Health, Environmental Monitoring, and Energy	2
1.3 State of the art-Humidity Sensor	3
1.3.1 Affecting Parameters	3
1.3.2 Measurement of humidity sensor and characteristics	4
1.3.3 Types of Humidity sensor	6
1.3.3.1 Ceramic humidity sensors	7
1.3.3.2 Working principle of impedance humidity sensors	7
1.3.3.3 Working principle of capacitive type humidity sensors	8
1.4 Choice of Material	9
1.4.1 Polymers	9
1.4.2 Acrylamide and its polymerization (Polyacrylamide)	11
1.4.3 Nanometallopolymers	11
1.4.4 Quantum dots	12
1.4.5 Characteristics of Quantum dots	13
1.4.5.1 Shape and size-dependent	13
1.4.5.2 Bandgap	14
1.4.5.3 Quantum confinement	14
1.4.5.4 Density of state	15
1.4 Mechanism- quantum dots based humidity sensor	15
1.5 Photodetectors and their principle	16
1.6 Measurement and characteristics	17
1.7.1 Responsivity	17
1.7.2 External Quantum Efficiency (EQE)	
1.7.3 Specific Detectivity	
1.7.4 Dark Current	
1.7.5 Photoconductive Gain	
1.8 Mechanism for photodetection	18
1.9 Need for Gas Sensor	19

1.10	Synthesis of nanometallopolymers	20
1.10.1	Frontal Polymerization	20
1.10.2	Thermal Frontal Polymerization	21
1.10.2.1	Isothermal Frontal Polymerization	
1.10.2.2	UV exposure Frontal Polymerization	
1.11	One-pot Method	21
1.12	Literature survey	22
1.13	Motivation	23
1.14	Objective of present work	
1.15	Outline of the Thesis	24
	References	28
	Tables	41
	Figures	43
Chapter 2: Development of a reliable room temperature humidity sensor		
using nanostructured nickel polyacrylamide		52-68
2.1	Introduction	53
2.2	Experimental Details	54
2.2.1	Synthesis Method	
2.2.2	Fabrication of sensing element	55
2.2.3	Sensing set-up	55
2.2.4	Characterization Techniques	56
2.3	Results and Discussion	56
2.3.1	SEM Analysis	56
2.3.2	TEM Analysis	56
2.3.3	XRD Analysis	57
2.3.4	Particle Size Analysis	57
2.3.5	UV-visible Absorption Analysis	57
2.3.6	TG-DTA Analysis	58
2.3.7	Electrical humidity sensing	58
2.4	Conclusion	60
	References	61
	Tables	64

Figures	65
Chapter 3: Polyacrylamide decorated CdS nanoparticles based flexible humidity sensor for baby diaper alarm: Experimental and theoretical study	69-95
3.1 Introduction	72
3.2 Experimental Details	72
3.2.1 Synthesis method	73
3.2.2 Sensing set-up	73
3.2.3 Fabrication of sensing element	73
3.3 Results and Discussion	73
3.3.1 FESEM Analysis	73
3.3.2 Particle size Analysis	74
3.3.3 BET Analysis	74
3.3.4 FTIR Analysis	74
3.3.5 TEM and HRTEM Analysis	75
3.3.6 XRD Analysis	75
3.3.7 XPS Analysis	75
3.3.8 Electrical Humidity Sensing Performance	75
3.3.9 Baby diaper with an alarm system	78
3.4 Photoconduction properties	79
3.4.1 Sensing mechanism	80
3.5 Theoretical studies	81
3.5.1 DFT studies	
3.6 Conclusion	81
References	84
Table	88
Figures	93

Chapter 4: Fabrication of Cu_{0.8}Zn_{0.2}Sb₂-polyacrylamide nanocomposite via frontal polymerization and its relevance in moisture sensing and photodetection	103-135
4.1 Introduction	104

4.2 Experimental Details	106
4.2.1 Synthesis	106
4.2.2 Polymerization via Frontal	106
4.2.3 Experimental set-up for photoconduction	107
4.2.4 Fabrication of thin film	107
4.3 Results and Discussion	108
4.3.1 SEM Analysis	108
4.3.2 BET Analysis	108
4.3.3 Transmission Electron Microscopy Analysis	108
4.3.4 Particle size Analysis	109
4.3.5 UV-visible absorption Analysis	109
4.3.6 XRD Analysis	109
4.3.7 IR Spectroscopy study	110
4.3.8 Thermo gravimetric analysis	110
4.3.9 DSC analysis	110
4.3.10 XPS analysis	111
4.4 Photoconduction analysis	111
4.5 Humidity Sensing Measurement	113
4.6 Conclusion	118
References	119
Tables	125
Figures	128

Chapter 5: Improved humidity sensing response of roasted gram derived

carbon quantum dots	136-167
5.1 Introduction	137
5.2 Experimental Methods	139
5.2.1 Preparation of GCQDs	139
5.3 Physical Characterization	139
5.3.1 Theoretical Studies	140
5.4 Results and Discussion	
5.4.2 Fourier Transmission Infrared Spectra Analysis (FTIR)	140
5.4.3 X-Ray Diffraction Analysis	140

5.4.4 X-ray Photoelectron Spectroscopy (XPS)	140
5.4.5 HR-TEM Analysis	141
5.4.6 UV- Absorption Spectroscopy	141
5.4.7 Photoluminescence Spectroscopy (PL) Studies	141
5.4.8 Raman Analysis	142
5.5 Experimental Investigation	142
5.5.1 Capacitive Humidity Sensing Characteristics	142
5.5.2 Sensor response and recovery time	144
5.5.3 Stability Analysis	145
5.5.4 Sensing Mechanism	145
5.6 Theoretical studies	
5.6.1 Interaction of GCQD with water molecule (H ₂ O):	146
5.6.2 Hydrogen Bonding Interaction	147
5.6.3 Electrostatic and Hydrogen Bonding Charge densities	147
5.6.4 HOMO-LUMO Gap	148
5.7 Conclusion	148
References	150
Table	157
Figures	160

**Chapter 6: One-pot synthesis of phosphine free indium selenide (InSe) QDs
and their structural characterization for LPG and humidity
sensing** **168-186**

6.1 Introduction	169
6.2 Experimental Methods	170
6.2.1 Resources	
6.2.2 Preparation Method	170
6.2.3 Selenium solution (Step-1)	170
6.2.4. Preparation of Stock solution (Step-2)	171
6.3 Fabrication of Sensing Element	171
6.4 Characterization Technique	171
6.5 Experimental Set-up	172
6.5.1 LPG measurement system	172

6.5.2 Moisture detection set-up	172
6.6 Results and Discussion	
6.6.1 Particle Size Analysis	172
6.6.2 UV-Visible spectroscopy Analysis	173
6.6.3 Photoluminescence (PL) spectroscopy Analysis	173
6.5.4 TEM, HRTEM and XRD analysis	173
6.6.5 LPG Sensor	174
6.6.5.1 LPG Sensing Mechanism	175
6.6.6 Humidity sensing characteristics	175
6.6.6.1 Selectivity and Effect of Humidity on LPG Sensing	176
6.7 Conclusion	177
References	178
Table	181
Figures	182
Chapter 7: Concluding Remarks and Scope of Further Research	187-195
7.1 Conclusion	188
7.2 Development of a reliable room temperature humidity sensor using nanostructured nickel polyacrylamide	190
7.3 Polyacrylamide decorated CdS nanoparticles based flexible humidity sensor for baby diaper alarm: Experimental and theoretical study	190
7.4 Fabrication of Cu _{0.8} Zn _{0.2} Sb ₂ -polyacrylamide nanocomposite via frontal polymerization and its relevance in moisture sensing and photodetection	
7.5 Improved humidity sensing response of roasted gram derived carbon quantum dots	
7.6 One-pot synthesis of phosphine free indium selenide (InSe) QDs and their structural characterization for LPG and humidity sensing	192
The Scope of Further Research Work	193
Table	195

APPENDIX: Experimental Methods and Characterization Techniques	Ai-Axix
A.1 Introduction	A ii
A.2 Methodology of present work	A ii
A.3 Synthesis	A ii
A.3.1 Frontal Polymerization Method	A iii
Synthesis of nanometallopolymers	
A.4 Fabrication techniques for thin film	A v
A.4.1 Spin coating method	A v
A.5 Annealing	A v
A.6 Characterization techniques	A v
A.6.1 Digital Refractometer	A vi
A.6.2 X-ray Diffractometer	A vi
A.6.3 Scanning Electron Microscope	A vii
A.6.4 Transmission Electron Microscope	A ix
A.6.5 UV-vis Spectrophotometer	A xi
A.6.6 Particle Size Analyzer	A xiii-A xiv
References	A xv
Figures	A xvi-xix

CHAPTER 1

Introduction and Aim of Present Work

This chapter deals with the fundamental concept of sensors and their comparison with the existing sensing devices. Also, it briefly introduces the classification of humidity, gas and photosensors, underlying mechanism and their performance index. A detailed overview of current sensor materials (metal oxide polymer composite, metallopolymers and quantum dots), with strategies of enhancing the performance with its characteristics of sensing materials has been deliberated here. The sensing mechanism and responsible parameters of sensing material also discussed in detailed. The chapter concludes with the concept of metallopolymers and quantum dots materials for humidity, gas and photosensors and the plausible solutions to overcome the present challenges.

1.1 Introduction

The current chapter reports the inclusive study of the recent accomplishments in the field of sensors. Presently, the enthusiastic technological advancement of modern appliances raises a serious concern of environmental deterioration and release of toxic gases, harmful for human health. There is a deep urge to develop highly sensitive gas and humidity sensors for the precise monitoring of toxic gases and humidity in the atmosphere. Recently, a variety of such sensors are available for the industry as well as domestic applications.

This chapter presents the fundamentals introduction, hierarchical development, and significance of the sensors which is schematically represented in Fig. 1.1.

1.2 Need of sensor - Health, Environmental Monitoring and Energy

Human health drew immense attention and pledged to secure health through proper control on pollution, sanitation, hygienic food, drug, disease observation, urban development, and professional health [1]. It is a necessary need to assess the safe environment for healthy living. In recent years, a variety of toxic gases such as hydrogen sulfide (H_2S), carbon monoxide (CO), oxygen depletion (O_2), carbon dioxide (CO_2), ammonia (NH_3), benzene (C_6H_6) have been released from industries [2-3] and manufacturing activities from raw materials. Hence it becomes very important to control and monitor these toxic gases present in the atmosphere [4] raising a serious concern to human life [5].

In this direction, humidity is much important for human comfort and the environment. Water must be the most crucial element on the earth playing a vital role in the existence of human life [6]. It exists at varying rates in the gas phase (as water vapour) in air. However, a high amount of humidity is also leading to discomfort due to imbalance [7-9]. Water is a very necessary compound for humans as well as the environment. The water molecule breaks into gaseous forms. The gaseous forms in the form of humidity obey gas laws. Water is a high dipolar molecule, which condenses and evaporates with the temperature of the atmosphere [10]. These water molecules change in the atmosphere according to the temperature of the atmosphere and warm air has a better capacity to clamp water than does the cold air. The warm air stores more amount of energy in the environment [11].

Meanwhile, it is nearly difficult to harvest, transport, or consume energy without any environmental effects. Many researchers have been dedicated to the field of nanotechnology to overcome these problems. Various materials are reported at the nanoscale to improve human life and the environment field [12]. There are several nanodevices available to store energy. Also, there are many ongoing works in this field to improve the fabrication, synthesis method and designing of device for its better properties. Some of them are shown in Fig.1.2 [13]. Nanomaterials play a vital role in diverse applications as these materials exhibit exceptional physical, chemical, and biological properties [14].

1.3 State of the art - Humidity Sensor

Humidity plays an important role for living organisms and in industrial applications as well. It is necessary to measure and control the humidity under dissimilar conditions from low temperature to high temperatures. There are various applications of humidity sensors as atoms/surface transportation, industrial purpose, medical and instrumentation, agriculture, and civil engineering [15-18]. Recently, many technologies have been developed in order to improve the humidity sensor manufacturing devices in respective fields [19-23] which are shown in Fig.1.3. Additionally, it is very important to know the amount of productivity of each sensor related to its standardization conditions and its sensing mechanism [24].

The need for the safety of environmental situations has been important to part in various humidity sensors based on the usage of its physical and chemical routes in presence of organic/inorganic and hybrid materials [25]. Advancement of humidity sensor systems includes enhanced efforts in the improvement of transducer performance such as sensing materials [26–31], design [32-35], sensing mechanism [36-39], and fabrication methods [40–42]. In this framework, the transducers are the key structures, monitored by the accessibility of appropriate developed technologies [43-44].

1.3.1 Affecting Parameters

❖ Temperature and Pressure

The affecting parameters of humidity sensor are temperature and pressure. Meanwhile, water molecules exist in the gaseous state; it performs in accordance to gas

laws and uses partial pressure in a gas mixture just similar to other gases. The ideal gas law [45] is given by Eq. 1.1 as:

$$PV = nRT \quad \text{..... (1.1)}$$

where P is defined as the total pressure, V is the volume, n is the number of moles of gas, T is total temperature and R is gas constant. The most important gas law for the measurement of humidity is Dalton's law. According to this law, Dalton thought that if a, b and c gases are mixed with known volume and known temperature, then according to ideal gas law [46], partial pressure of the individual gas is given by Eq. 1.2 – 1.4:

$$P_a = \frac{n_a RT}{V} \quad \text{..... (1.2)}$$

$$P_b = \frac{n_b RT}{V} \quad \text{..... (1.3)}$$

$$P_c = \frac{n_c RT}{V} \quad \text{..... (1.4)}$$

These equations are commonly referred to as the “partial pressure” of each gas. The overall pressure would be the sum of the partial pressure of individual gas,

$$P_{total} = P_a + P_b + P_c \quad \text{..... (1.5)}$$

Thus, Dalton's law indicates that the total pressure of the mixture of gases is equal to the sum of the partial pressure of the constituent gases, if each were present individually at same volume and temperature [47].

1.3.2 Measurement of humidity sensor and characteristics

The humidity sensing measurement can be done by different modes, but mainly it's measured as Absolute Humidity (AH) and Relative Humidity (RH). There are two modes for the measurement of Absolute humidity [48]; the first mode is Parts per Million and the second is Dew Point. The ratio of the mass of water vapour in the air to volume of air is called Absolute Humidity and its unit is grams per cubic foot i.e. (1 gram = 1/7000 pound lb.) and is calculated using the relation given in Eqn. 1.6:

$$\text{Absolute Humidity (AH)} = \frac{\text{mass of water vapour}}{\text{Volume of air}} \quad \text{..... (1.6)}$$

The second mode for the measurement of humidity is Relative humidity. Relative humidity is defined as the ratio of the amount of water molecules in the air to

the maximum (saturated) water adsorption level that the air can hold at similar temperature and pressure [49]. The unit of RH measurement is percentage (%) and it is obtained by the relation given in Eqn 1.7:

$$\text{Relative Humidity (\%RH)} = \frac{Q_1}{Q_2} \times 100 \% \quad \dots\dots\dots (1.7)$$

where Q_1 & Q_2 are the amount of moisture content present in a certain volume of air at an assumed temperature and the amount of water vapor required to saturate the same volume of air at the same temperature [50]. The difference between absolute humidity and relative humidity is that relative humidity is temperature dependent quantity hence called the relative measurement.

The relative humidity can be expressed as ratio of partial pressure in air (P_a) to the saturated pressure of moisture content in air (P_s) at the similar temperature (both in Bar or KPa) as specified in Eqn 1.8.

$$\text{Relative Humidity (\%RH)} = \frac{P_a}{P_s} \times 100 \% \quad \dots\dots\dots (1.8)$$

Recently, the most commonly used sensors are based on the capacitance and resistance i.e. change in capacitance of a dielectric material [51] or the change in resistance of a conducting material with the exposure of humidity. The extensively used sensing materials for humidity sensing include resistive ceramics materials [52], organic/inorganic polymers [53] and polyelectrolytes [54]. But the polymer sensors [55] based on structure and having low cost, can measure only a limited characteristic of water molecules and show hysteresis with drift at high humidity levels. Also, electrolytic sensors [57] require constant flow rate measurement. Infrared spectroscopy can be used to measure RH in an infrared hygrometer [58]. Various methods for humidity sensing investigations are based on the surface acoustic waves (SAW) [59-60] and microwave offsetting.

There are certain sensor parameters which decide the effectiveness of a specific sensor at a particular place. These humidity sensing parameters depend upon the types of sensing element and properties of sensing material. The humidity sensing parameters are defined as follows and presented in Fig.1.4 [61-64]:

- ❖ **Sensitivity:** The sensitivity of the sensor is defined as the ratio of the change in the output signal to that of the input signal. The mathematical form is shown in Eq. 1.9.

$$\text{Sensitivity} = \Delta I / \Delta \%RH * 100 \quad \dots\dots\dots (1.9)$$

where ΔI is the change in impedance and $\Delta \%RH$ is the change in %RH.

- ❖ **Linearity:** The output of sensor should be linear with its input.
- ❖ **Less noise:** Unwanted signals should be minimized in a good sensor.
- ❖ **Response time:** The response time of the sensor is defined as the time required in reaching the final position (90% of the sensor output) from its initial position (10% of the sensor output).
- ❖ **Recovery time:** Recovery time is the time taken by the sensing element to return to its initial value after ramp-wise desorption.
- ❖ **Drift:** Drift is defined as the change of the sensor output with time at a constant input of the sensor.
- ❖ **Repeatability:** It defines the accuracy of experimental set-up when measurements are taken after a long time interval under similar environmental conditions.
- ❖ **Hysteresis:** It is defined as the difference between the output signal and the input signal of sensor.

1.3.3 Types of Humidity sensor

The humidity sensors are classified into various groups. The first group contains of humidity sensors based on impedance and capacitance. It measures the deviation in resistance and capacitance of conducting material as a function of relative humidity (RH). The second humidity sensors group is mechanical humidity sensors, which is based on strain and mass effects. The third group is optical sensors, which depends on the change of the optical indicators in form of reflection, transmission and quenching of electromagnetic rays. The last humidity sensor group holds various integrated humidity sensors that enclose active-passive and electronic components for linearization, standardization and communication [65]. A flow chart concerning the classification of humidity sensors established on techniques and strategy is shown in Fig.1.5.

1.3.3.1 Ceramic humidity sensors

The principle of humidity sensors is based on the surface phenomena and during adsorption, the water molecules are directly connected with metal ions on the surface. In this ceramics type humidity sensor, two ohmic electrodes are used and the sensor response depends on the electrodes of the material. The electronic or ceramic humidity sensors are further divided into two parts: resistance-based and capacitance-based that is shown in Fig.1.6. In resistive type humidity sensor, the change of impedance is also measured with humidity to obtain fast response and better linearity [66]. Electronic humidity sensors are especially based on electron contribution from the water molecules to semiconducting material [67], the sensing mechanism depends on the contributor surface from the adsorbed water molecules. In resistive type humidity sensors ceramic coated sensors are used to protect the environment when condensation occurs.

1.3.3.2 Working principle of electrical (impedance) humidity sensors

The possible mechanism shown in Fig.1.7 would be due to the co-adsorption of water molecules on the other adsorbate. It seems to be a formation of a water vapor layer on the surface due to higher humidity levels. It explains that at low humidity, adsorption of water molecules on the metal oxide surface obeys chemisorption and at higher humidity levels, all the active sites on the metal oxide surface are occupied by water molecules, and later it can be formed as an additional layer on the surface following the physisorption. The free movement of the proton occurs along with the water layer as per the diagram and during the physisorption process, the resistance of the film is decreased [68]. Further increase in humidity leads to co-adsorption where the water molecules try to dislodge the adsorbents occupying the active sites[69]. During the chemisorption, resistance drastically decreases while it is being slowed down during physisorption at higher humidity levels and the conductivity change almost ceases during co-adsorption.

1.3.3.3 Working principle of capacitive type humidity sensors:

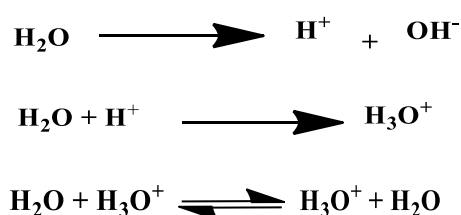
The mechanism devoted to the electrical response of the sensing element upon exposure of humidity is the chemical and physical adsorption of water molecules on the

surface of the sensing element. In capacitive type humidity sensor, the relationship between the capacitance and the %RH can be expressed by the Eq. 1.10:

$$C = (\epsilon_r - i \frac{\gamma}{\omega \epsilon_0}) C_0 \quad \dots\dots\dots (1.10)$$

where C indicates the conductance and ω represents applied frequency. From the above expression, it is clear that the capacitance of the sensing element is proportional to C_0 whereas C is inversely proportional to operating frequency ω [70]. C_0 is related to the physisorption of water molecules on sensing film, therefore, different adsorption processes yield different conduction values. From the formula, it's obvious that the capacitance increases with rising %RH, depending on the frequency.

Initially, at lower %RH, water molecules are chemisorbed onto the available unsaturated nitrogen bonds (hydrophilic group) of the polymer thin film through double hydrogen bonding, considered as the first-layer chemisorption of water. In this regime, it's hard for the water molecules to travel independently because of strong attraction due to double hydrogen bonding. Successively, proton hopping initiates between adjacent hydroxyl groups in the first- chemisorbed layer of water influence more amount of energy thus exhibiting a strong electrical resistance. Later on, a few protons available on the surface of the polymer film are confined by irregular mobile layers. These protons still contribute to the leak conductance C, which ultimately increases the capacitance at a low humidity regime. As the %RH increases, the multilayer physisorbed of water molecules arises [71-72], forming the physisorbed layer, having water molecules attached through single hydrogen bonding on the hydroxyl groups. Consequently, the water molecules become transportable, likely to appear as in the bulk liquid. The formation of subsequent multilayer physical adsorption and the decomposition of physisorbed water causing ionization under an electrostatic field to produce a large number of hydronium ions (H_3O^+) in the form of charge carriers [73]. Thus charge transport on the film took place via the conductivity of the material generated by Grotthuss chain reaction. The charge transport expression is given as below:



Finally, at high %RH, the physisorbed water molecules will penetrate the interlayer of the sensing film [74-75]. A large number of prevailing amide groups in polymer facilitates proton migration as shown in Fig. 1.8. This leads to a sudden increase of capacitance of the material, causing a quite high sensitivity at high %RH which is very fruitful for the dielectric constant of the material.

1.4 Choice of Material

There are various humidity-sensitive materials reported, so it's a very typical task to choose the material for sensor purpose. The different sensing materials such as metal oxides, metal nanocomposites, and quantum dots are capable in terms of their response time, stability and repeatability [72, 73]. Consequently, the present work displays the study of nanometallopolymers and quantum dots based sensors at room temperature. Polymer gels are significant materials of fundamental and scientific concern. Currently, hydrophilic gels are referred to as "hydrogels" and they have drawn exceptional attention as absorbers showing their potential to perform absorption and desorption. Polymer nanocomposites are cost-efficient emerging materials and known for applications as gas/humidity sensors.

Quantum dots are generally synthesized with phosphine solvent, which is very toxic for human beings. To remove this toxicity, we have used phosphine-free solvents for the synthesis of quantum dots. The long-chain capping agents such as oleic acid (OA) or oleylamine (OLA) were used to cap the surface of the quantum dots. These capping agents reduce the size of quantum dots due to its hexagonal chemical structure. Due to the excellent optical and electronic properties, quantum dots have a high surface-to-volume ratio with active sites for the solid-gas interaction and crystalline nature, which is responsible for humidity and gas sensors.

1.4.1 Polymers

Polymer gels are significant materials of fundamental and scientific concern. Currently, hydrophilic gels are referred to as "hydrogels" because they draw exceptional attention as absorbers showing their potential to perform absorption and desorption, thus ensuring their applicability in biomedical engineering [76]. The organic polymers display unique properties due to its long length. They are very useful for our living life, and applicable in many things, named as plastic. Nowadays macromolecules are of great

interest in the field of education and research. Scientifically, the chemistry of macromolecules overlaps the disciplines of engineering, science and material physics [77]. Moreover, carbon is the main element in chain to develop organic macromolecules. The silicon and phosphorus-containing macromolecules are also very important [78]. Organic macromolecules are limited and have some drawbacks such as low thermal stability, binding interaction, electron transfer process, and healing effect. Hence it is very important to remove these drawbacks by developing a new class of material [79].

According to the periodic table, only hydrogen is the univalent element and can play the role to replace any groups and is incapable of generating stable macromolecules in solution [80]. To improve the structural, electrical, photoelectrical, conductivity, stability, magnetic and thermal properties of macromolecules, new class of materials have been developed [81]. The combination of metal ions and macromolecules are giving both properties active and selective with high stability performance. The first step regarding these materials is the successful synthesis of macromolecules containing metals or nanocrystals. The essential second step is a comprehensive study by characterization tools and the third is application. There are various combinations of metal macromolecules, organic metals, inorganic metals, and semi-organic macromolecules. There are several types of macromolecules which are described as follows:

Type I: This type includes linear and cross-linking organic, inorganic, and semi-organic metal macromolecule by interacting with each other via covalent bonds. This organization was firstly given in 1996.

Type II: The second type occurs when the metal ions are directly combined with polymers and removed from the main chain of the polymers.

Type III: As a final point, a new method is recently developed for the polymerization and copolymerization of metallopolymer monomers (metal-containing). Frontal polymerization is one of them, which is a solvent-free and short-time reaction.

1.4.2 Acrylamide and its polymerization (Polyacrylamide)

Acrylamide (AAM) was first synthesized in 1949 and used in the paper industry, glues, and synthesis of dyes and gels in 1950. Acrylamide with molecular formula C_3H_5NO and IUPAC name prop-2-enamide is a white odourless crystalline solid [82].

Acrylamide is formed in roasting, baking, toasting, frying, and grilling. It is soluble in water (2.04 kg/L), ethanol, ether, and chloroform. Acrylamide is unsaturated and highly reactive amide with melting and boiling points as 84.5 °C and 136 °C. Acrylamide decomposes non-thermally to form ammonia and thermally to produce carbon monoxide, and carbon dioxide in nitrogen. Acrylamide-based metabolites are less biologically relevant metal ions due to their biological relevance in peptides and proteins [83]. Polyacrylamide, or PAM, is a form of acrylamide after polymerization. By the polymerization technique, highly structured, branched, and cross-linked variants of the polymers can be obtained with properties of the initially created simple polymers [84]. The frontal polymerization technique is mainly employed for the conversion of monomers to polymer in a confined reaction region under the multi-level system, which proceeds above the whole volume. The interaction of acrylamide (AAm) with metal nitrate complexes during Frontal polymerization are $Mt(NO_3)_x \cdot 4AAm$, where $Mt = Fe(III), Bi(III), Y(III), x = 3; Cu(II), x = 2; Mt(NO_3)_2 \cdot 4AAm \cdot 2H_2O$, where $Mt = Co(II), Ni(II), Zn(II), Cd(II), Mn(II), Ba(II), Pb(II); Pd(NO_3)_2 \cdot 2AAm$. This method is widely used to prepare solvent-free metal-monomer rapidly.

1.4.3 Nanometallopolymers

The polymer matrix may be bulk, microstructure, or nanostructure. The hydrogels are composed of water-soluble hydrophilic polymer chains with 3D network structures linked to each other from side to side with covalent bonds or electrostatic, van der Waal and hydrogen bonding [85]. The hydrogels are hydrophilic due to the presence of functional groups as $-COOH, -SO_3H, -NH_2, -OH$, and $-CONH_2$ which increase the adsorption capacity of the macromolecules and these functional groups are intensely bind with metal ions [86]. Owing to these structures, the hydrogels are made available for a unique property, water adsorbed material from the environment [87]. The metal nanomaterials are responsible for stability and enhance the surface morphology of the macromolecules. Instead of these, hydrogels also have good biocompatibility and environmental friendliness properties; consequently, they showed potential in many applications such as biomedical fields, sensors, photocatalytic activity, and purification processes. Metal complexes of polyacrylamide are implementing in the production of water-soluble polymers that are used in many scientific applications. The types of metal complex-based polymers are shown in Fig.1.9. The solid-state chemistry of acrylamide-

based metabolites with a variety of divalent transition metal ions such as Mn^{2+} , Fe^{2+} , Co^{2+} , Ni^{2+} , Cu^{2+} , Zn^{2+} and Cd^{2+} [85,88] provide a wide range of applications. These metals interact with acrylamide and thus the new materials are formed.

Nanometallopolymers and 3D confine nanomaterials are emerging polymer nanocomposites, which are very cost-effective and advance sensing materials [89-91].

1.4.4 Quantum dots

At the nanometer scale, the energy level changed from continuous to discrete energy level because of confinement phenomena. Quantum confinement effects are present in many quantum structures [92]. In quantum dots, due to the 3-D confinement, the density of states shows discrete energy levels. The energy levels can be observed to different values by controlling the shape, size, dot material, and confinement potential [93]. The electronic transitions in the discrete energy levels can be used to tailor the optical properties of quantum dot nanostructures [94]. Their bandgap energy, luminescence wavelength, transition probability, photo absorption, and emission spectra can be tuned by adjusting the dot size [95].

Quantum dots are very small particles, having a diameter of 2 to 10 nanometers [96]. Due to 3D confinement, they show unique optical and electronic properties. In a semiconductor bulk material, the valence band and conduction band are separated by an energy bandgap and when light is incident on the surface, absorption takes place, the electron is excited from the valence band to the conduction band, producing a hole in the valence band. After a certain time, approximately 10^{-8} sec, when the electron returns to the valence band, fluorescence is observed during this period [97]. Due to the Coulomb attraction, hydrogen-like species are formed in this small time interval; because of this the electron and hole don't move independently [98].

Quantum dots are prominent for their high fluorescent intensity. It is at least comparable to and sometimes better than the intensity observed in conservative fluorescent dyes. In addition, quantum dots have narrow, symmetrical fluorescence curves in the visible light spectrum, while organic dyes have A-symmetrical curves with a tail trailing into the red region [99]. The fluorescent spectrum of quantum dots have a narrower full width half maximum (FWHM, the width of the spectrum at half of the peak intensity) than fluorescent dyes, making dots more precise [100]. The formation of

quantum dots is already reported by chemical route, sol-gel method, exfoliation of nanosheets, hydrothermal and green routes. Our main focus is to synthesize the environment-friendly and highly fluorescent quantum dots. The sol-gel process may be the most widely used and developed one among various synthetic powder preparation methods [101]. It is commonly used to prepare nanocomposite materials because these conversions occur readily with a wide variety of precursors and can be conducted at or near room temperature. In addition, the gel products frequently have properties ideal for desired applications [102]. Pure nano-composite materials in the form of thin films or powders prepared by a sol-gel method or mixed metal oxides lacking nanoparticulate phases [103]. The advantages include excellent compositional control, homogeneity on the molecular level due to the mixing of liquid precursors, and low crystallization temperature.

1.4.5 Characteristics of Quantum dots

1.4.5.1 Shape and size-dependent

The shape and size are very important properties for any material in nanoscience and nanotechnology. Researchers have synthesized a variety of materials according to their properties. In nanoscience and nanotechnology, these materials found the most attention due to their extra-ordinary properties (as optical and electronic properties) [104]. The size-dependent properties of semiconductor or quantum dots rise from the quantum confinement effect and are shown in Fig.1.10. The properties of semiconductors are obvious as the diameter of a nanoparticle approaches the size of Bohr-exciton radius.

The main example for size dependence is CdSe quantum dots which experience the quantum confinement special effects when their diameter is less than $\sim 5-6$ nm. Due to the size effect the surface-to-volume ratio increases [105]. As this ratio of surface to volume increases, the surface properties become dominant over the entire quantum dots.

1.4.5.2 Bandgap

The atom emits a photon of light with the same energy equal to the band-gap that the atom absorbed. The wavelength of the light also depends on the atom; like if we are using iron, the atom emits the green colour. And if we excite an atom by holding that in a hot flame, it emits like white light. That is possible because of the way of their

arrangement of energy levels. It means that different atom gives different wavelength of light. All this is possible because of the quantization that is the energy of an atom is quantized or energy levels in an atom have set values. Quantum dots follow the same phenomena as they have also the quantized energy levels, as shown in Fig.1.11 [106]. Suppose that quantum dots are made from silicon, then it will give out different colours of light depending on the size. The smallest dots will give the smallest wavelength and big dots will give the higher wavelength. Simply we can say that the smallest dots have a bigger band-gap and bigger dots have the smallest band-gap [107].

1.4.5.3 Quantum confinement

The Quantum confinement effect is observed in semiconductor nanocrystals due to their reducing size [27,28]. The physical, chemical, and biological properties of the material changed from bulk phase to nanoscale [29]. Fig.1.12 shows the transition from bulk materials to nanomaterials. Usually, in a semiconductor material, the charge carriers have several energy levels and these energy levels are near to each other, therefore it is termed as energy bands. All charge carriers tend to inhabit the energy levels in the valence band and beyond the energy bandgap, a slight number of charge carriers are present in the conduction band [108]. These charge carriers will then be able to move to the conduction band by obtaining energy provided to the material in a form of heat, electrical field, latent, etc. and they contain holes in the valence band. Such electron hole pair is known as exciton.

The direct energy band-gap semiconductor material, with energy band-gap E_g at $K = 0$ (centered) in the Brillouin zone, when the size of the material develops similar to the exciton Bohr diameter, the electronic properties of the semiconductor materials start changing from comparable to bulk state [30]. The mathematical expression for a set of energy levels of hole-electron (excitons) can be given by the hydrogenic model in Eqn 1.11-1.13 [109]:

$$E_{n,k} = E_g - \frac{\mu e^4}{2n^2 \hbar^2 \epsilon_2^2} + \frac{\hbar^2 k^2}{2(m_e^* + m_h^*)} \quad (C.G.S.) \dots \dots \dots (1.11)$$

$$E_{n,k} = E_g - \frac{\mu e^4}{32n^2 \hbar^2 \epsilon_0^2 \epsilon_2^2} + \frac{\hbar^2 k^2}{2(m_e^* + m_h^*)} \quad (S.I) \dots \dots \dots (1.12)$$

$$K = K_e + K_h, \mu = \text{Reduced exciton mass}$$

$$\frac{1}{\mu} = \frac{1}{m_e^*} + \frac{1}{m_h^*}, \text{Effective masses of the electron and hole} \dots \dots \dots (1.13)$$

Here K is the wave vector of exciton such that $K = k_e + k_h$, E_g is the bulk energy band-gap of the material. The quantum confinement is divided into three parts, according to the connection between microcrystalline radius (R), and the Bohr exciton radius (a_B) of bulk semiconductor where $a_B = a_e + a_h$, if $R \gg a_B$. The condition for every regime is depicted in Table 1.1.

1.4.5.4 Density of states

The density of states is defined as the number of dissimilar states at a specific energy level that electrons are acceptable to inhabit, i.e. the number of electron states per unit volume per unit energy [110]. The properties of bulk material as specific heat, paramagnetic susceptibility, and other electron transport occurrences of conductive solids depend on this function [111]. The density of the states is different for 0D, 1D, 2D, and 3D. The detailed conditions regarding the density of states in terms of wave equations and confinements are depicted in Table 1.2, also presented as Fig.1.13.

1.5 Mechanism-Quantum dots based Humidity Sensor

The humidity sensing mechanism of carbon-based materials (CNTs, Graphene oxide, and Carbon quantum dots) depends on the existence of hydrophilic functional groups present on its surface such as hydroxyl groups and is shown in Fig.1.14. The sensing mechanism of QDs can be related to the capillary condensation of water molecules on the surface of quantum dots, where the conductive water path controls the resistance of the material and the current density variations depending on the adsorption of relative humidity [112-113]. The presence of different functional groups such as epoxide, carboxyl, and hydroxyl in the carbon-based quantum dots structures is essential for the physisorption process of water molecules on the surface of sensing element. The capacitive-based humidity sensor performs according to the change in capacitance

comparative to the change of relative humidity (%RH). For the capacitive humidity sensor, the sensing mechanism depends on the active layer of dielectric constant and also the collection of water molecules on the surface of the sensing material. Since water is a polar molecule, so change in dielectric constant is an essential parameter for the assessment of performance of the sensor.

For the humidity sensor, the hydrophilic nature of the material is essential. Also, the working of a capacitance-based humidity sensor depends on the polarization effect due to the dielectric nature of the material and the distance between the electrode areas.

1.6 Photodetectors and their principle

Photodetectors are also referred to as photosensors, which sense light or other electromagnetic radiations and they are important elements used in optical communications, video imaging, security, biomedical imaging, night-vision, motion detection, and gas sensing [120]. They possess the property to transform light into electrical signals very precisely. Several innovations in optical systems have been initiated with advancements in optical detection. Optical radiation detectors find use in most photonic applications, medical imaging for determining the output of a laser or any other light source [121]. Various optical detectors detect a variety of electromagnetic radiations like ultraviolet, infrared, and visible light. Optical detectors are classified into two categories: photon detectors and thermal detectors. There is a variety of photodetectors that find applications in different fields according to their performance parameters for that particular task.

Photon detectors sense incoming photon energy and result in a voltage or current (due to electron-hole pair) revealing information about the incident light as a function of its intensity. Photodetectors can be photovoltaic or photoconductive (both works with a bias voltage and are semiconductor-based) depending on the type of material used [123]. Thermal detectors work on the principle of converting the energy of photons into heat. There is a bit of delay associated with such detectors as time is required for the temperature to alter. Thus, these are not the best type for many photonic imaging applications.

1.7. Measurement and characteristics

The entire process of photodetection takes place including three major mechanisms: light harvesting, separation of exciton, and transport of charge carriers to their respective electrodes. Various characteristics define the quality and performance of different photodetectors which are given as below:

1.7.1 Responsivity

Responsivity is defined as the ratio of generated photocurrent by a device per unit area to the incident optical power at any given wavelength. Mathematical expression for responsivity is:

$$R = I_{ph} / P_{opt}$$

where P_{opt} is the optical power on the detection area and I_{ph} output current generated by photodetector per unit area. Thus, this factor determines the number of milliamps of photocurrent generated with respect to every milliwatt of input signal optical power [124].

1.7.2 External Quantum Efficiency (EQE)

The number of carriers generated for every incoming photon defines the external quantum efficiency of any photodetector. Mathematical expression is given in Eq. 1.14. This factor depends on the structure of photodiode as well as the semiconductor material used. Thus, this determines the utilization of captured photons.

$$EQE = hv I_{photo} / e P \quad \dots\dots\dots (1.14)$$

where e is the electron charge; I_{photo} is the photocurrent; P is the power of incident light and hv is the energy of each photon.

1.7.3 Specific Detectivity

The ability to differentiate between noise and the smallest light intensity is called as specific detectivity. This is also an important figure of merit for photodetectors and its expression is given in Eq. 1.15 as:

$$D = \sqrt{AB} / NEP \quad \dots\dots\dots (1.15)$$

where B is the bandwidth; A is the effective area; and NEP is the noise-equivalent power.

1.7.4 Dark Current

Dark current is the small amount of current that flows in a photodiode even when no photons are entering to the device. Practically, dark current is caused due to random creation of carriers (electron-hole pairs) inside the depletion region of the photodetector. This is often referred to as *reverse bias leakage current* and this process is observed in all diodes [125-126].

1.7.5 Photoconductive Gain

Photoconductive gain is the ratio of number of free carriers (electrons) collected per unit time to the number of absorbed photons per unit time. The expression for photoconductive gain is given in Eq. 1.16:

$$G = N_{\text{electron}} / N_{\text{photon}} \quad \dots\dots\dots (1.16)$$

1.8 Mechanism for photo detection

When the light beam is incident on the surface of a material, photons of the ray interact with the material causing the generation of the electron-hole pairs. The generated electron-hole pairs at different junctions in the sample can easily be separated by each other. Due to sufficient excitation energy, the electrons transition from the valence band to the conduction band. After the first few cycles of change in resistance, the photoresponse of the nanomaterial gets stabilized. This may also be possible due to the combined effect of slight photodegradation and an increase in the concentration of electron-hole pairs [124-126]. The representative curve exhibits the sawtooth wave characteristic which implies that the response changed subsequently with time and is repeatable. In the light region, material follows a dramatic drop in resistance value. However, when light is turned off, the material almost regains its original state which is also a requirement of photoconductive nanomaterial. The highly sensitive polymer nanocomposite has the presence of a narrow optical band gap which provides the larger surface area. Due to this reason the active sites of the material are responsible for the electron-hole pair generation through photon-phonon interaction. This phenomenon leads to enhanced photoconductive properties of the material.

1.9 Need for Gas Sensor

Gas sensors are very important for factories and manufacturing industries to detect the leakage of gases. The gas sensors are generally applicable to detect the toxic

or explosive gases concentration. Various uses of gas sensors vary across a wide range from industrial to domestic applications; for example monitoring air pollution, chemical processes, and exhaust from combustion engines [44]. Over the past 20 years, a great deal of research effort has been directed towards the development of small dimensional gas sensing devices for practical applications ranging from toxic gas detection to manufacturing process monitoring [49]. The increasing demand is for better gas sensors with higher sensitivity and greater selectivity. Intense efforts are being made to find more suitable materials with the required surface and bulk properties for use as gas sensors [50]. Metal oxides semiconductors exhibit unique electrical and optical properties which are responsible for gas sensing performance. The high surface-to-volume ratio, dangling bonds, high adsorption/desorption capacity, and porosity of the materials enhance the sensing behaviour. Generally, metal oxides and nanocomposites combination of transition and post-transition metal oxides (ZnO, CdO, WO₃, Fe₂O₃, ZnO/TiO₂, BN QDs–ZnO etc.) have been used for gas sensing.

1.9.1 Gas sensing mechanism:

The sensing mechanism is devoted to the surface adsorption and desorption of the LPG, which involves the migration of adsorbed oxygen species. The sensing principle depends on the change in electrical resistance corresponding with input owing to the electronic exchange of charges. When the gas interacts with the surface of the sensing element it leads to the electron transfer between LPG and the surface. Initially, the surface of the sensor is free from the adsorbed LPG molecules, the atmospheric oxygen molecules get attracted to the sensing element and form the chemisorbed on the surface. The oxygen species then interact with the conduction band electrons. During this process, the transfer of an electron from the conduction band to the chemisorbed oxygen occurs which is shown in Fig.1.15. The electrons concentration of the materials at the surface decreases which indicates a drastic increase in the resistance of the sensing film (sensing curve). After that, an equilibrium state is reached between the sensing surface adsorbed oxygen and atmospheric oxygen molecules through the above chemisorption process.

1.10 Synthesis of nanometallopolymers

For the synthesis of nanometallopolymers, materials scientists have used a variety of tools such as the Frontal polymerization technique. In this process, firstly the

front of monomer is ignited and this front actions towards the bottom. The second method is chain-growth condensation polymerization. In this polymerization an active centre is generated and monomers can be polymerized in a very short span of time to form large molecular weight with some by-products. The second tool includes the polycondensation, in which the molecules join together and form the condensate with some byproducts such as water and methanol. Another technique includes ring-opening polymerization, in which terminus of a polymer chain attack on the cyclic monomer and form the longer chain, the reactive centre may be free radical, cationic or anionic. Then comes the electro-polymerization, in which conducting polymer is synthesized on the conducting substrate. Another one is ionic polymerization, in which the active ionic centres are in chemical equilibrium with an exchange rate, which is far faster than the propagation rate. Further, the radical polymerization should be discussed, in which polymerization occurs by the successive addition of the active species. Some post-synthesis methods are also reported for metallopolymers such as polymer modified by combining metal centres or ions. In the processing of the metallopolymers, there are various reactions taking place such as Suzuki, Sonogashira and Heck coupling reaction.

1.10.1 Frontal Polymerization

In Frontal polymerization, the acrylamide monomer is converted into polymer in a localized reaction zone and this is short time and solvent free method. Frontal polymerization happens in a definite arrangement with suitable thermo-physical properties, which are extremely exothermic and has low heat conductivity factor. The heat changed during the polymerization of one monomer layer was consumed in the activation of the next layer. Thermal wave proceeds in a narrow temperature range close to the adiabatic heating of the reaction medium. The possible reaction mechanism for the Frontal polymerization is shown in Fig. 1.16. The Frontal polymerization is three types:

1.10.2 Thermal Frontal Polymerization:

Here, an external source is used to initiate the front for polymerization. In this technique, the contained reaction is determined by an external UV source.

1.10.3 Isothermal Frontal Polymerization:

Here, the gel effect happens when the monomer and initiator diffuse into a polymer unit. Thermal frontal polymerization starts when the heat source associates with the solution of monomer and thermal initiator.

1.10.4 UV exposure Frontal Polymerization:

This is the technique in which the UV exposure has been used for the external source. It has a faster polymerization rate, and the source of energy is in exothermic form of polymerization, raising the temperature and increasing the rate of reaction at this zone.

1.11 One-pot method:

The first time kinetic growth method was introduced by LaMer and Dinegar, who defined how the formation of mono-disperse colloids quantum dots is dependent on nucleation. In this method, the rapid growth of colloidal quantum dots has been explained. By this method, Alivisatos and Bawendi explained the one-pot or hot injection method of synthesizing quantum dots. Presently, the one-pot or hot-injection method is one of the most common routes for the synthesis of nanomaterial. This method involves the formation of consistent nuclei by the quick injection of organometallic substances into a warm solvent. During the reaction process, it also contains some surfactants and ligands to avoid quantum dots from agglomeration. The ligands are alkylphosphine oxides or trioctylphosphine, long-chain carboxylic acids or oleic acids, and long-chain amines groups (oleylamine). Once nucleation process has happened, a consistent diffusion-controlled progress is perceived through the solution. During this, the larger quantum dots produce very slowly than the smaller quantum dots, subsequent in a size effect. As the progress of the quantum dots improves, the bigger QDs continue to produce while the lesser QDs liquefy due to their greater chemical potential. The average particle size of the quantum dots increases and the concentration of the particle decreases till the point of saturation. The hot-injection or one-pot method is predominantly effective because in this method the high level of control of particles permitting rapid nucleation separated from the growth stage. Using this method, increasing the temperature, surfactants concentration, and reaction time decides the various sizes of quantum dots.

1.12 Literature survey

The international and national developments in the field of humidity sensors have been summarised year-wise through a literature survey in Table 1.3. Many research papers have been reported about polymer composite sensors. Researchers have investigated polymer nanocomposites and quantum dots as sensors. The drawbacks of the reported sensors are high cost, low sensitivity, high response, and recovery times. So it's necessary to develop efficient nanomaterials which can remove these drawbacks.

1.13 Motivation

In recent years, the size-dependent properties as physical and chemical of semiconductor nanomaterials have more attention in the Nanotechnology field. It is valuable to recognize a suitable and effective route for the fabrication of nanoparticles that reveal the novel physical and chemical properties. In this concern, the size-controlled nanoparticles are to be developed through a low toxic, eco-friendly, and easy route.

The polymer gels play an important role as humidity and gas sensors due to their hydrophilic nature, reactive bonds, and high porosity nature. Many more sensing materials have been reported based on polymers and polymer composites. Metal-based polymer nanocomposites are of great interest due to their electrical properties. Some drawbacks have been observed during the literature survey. Those are the high response and recovery times of the sensing device. To overcome this problem, nanometallopolymers (transition metal contains acrylamide polymers) are introduced in the present research work for humidity sensors. Acrylamide gels are highly hydrophilic and are good adsorbent material for humidity. Nano- metals have shown an important role in providing the stability of the material. As observed from the literature, the size is reduced and sensing performance increases. Quantum confinement is one of the main phenomena, which shows the unique electrical and optical properties of nanomaterials. Due to confinement, the surface-to-volume ratio increases as the size decreases. In the case of quantum dots, the particles are confined in three dimensions.

Presently, researchers are focused on the quantum dot as humidity and gas sensors and developed many sensors. The functional groups and high surface-to-volume ratio have promising properties towards sensing performance. This is the new class of nanomaterials for application in sensing devices. Additionally, the response, recovery times, and selectivity of any sensors are very important phenomena. Quantum dots-

based humidity and gas sensors received popularity because of their improved sensing parameters with their size.

1.14 Objective of present work

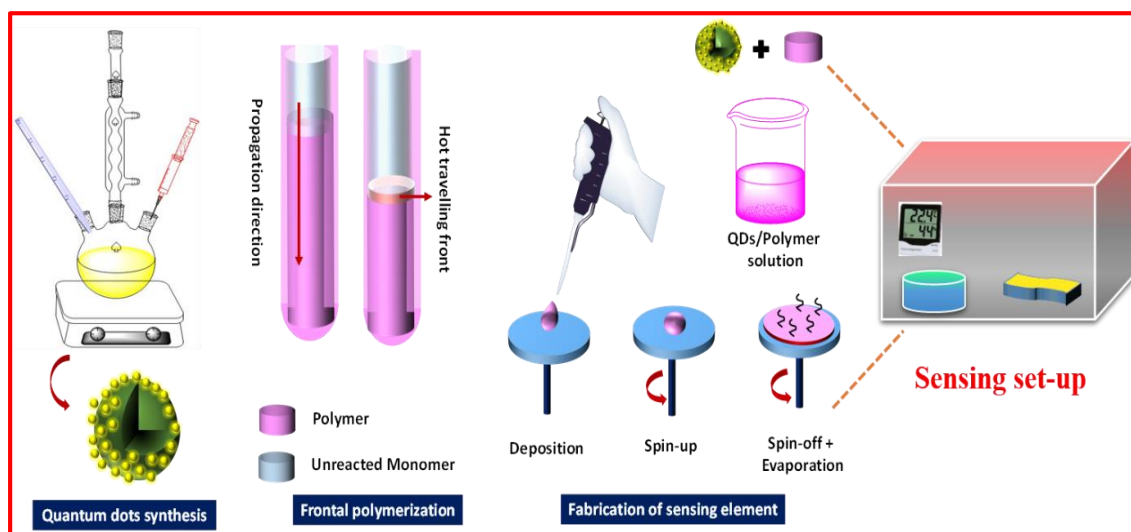
Few limitations of organic metallopolymer about their sensitivity, lifetime stability, and high sensitivity with stable structures of Quantum dots nanocrystals motivated us to make their monohybrids in the future for further novel sensing application. Nanometallopolymer and quantum dots are easy processable, cost-effective materials with excellent sensing capabilities.

The objective of this thesis is to develop highly sensitive humidity and gas sensors based on nanometallopolymer and quantum dots. The developed sensors witnessed a significant improvement in sensors parameters such as sensitivity, recovery times, repeatability, and long-term stability of sensors. These materials have excellent adsorption and desorption capacity, which enhanced the sensing response and recovery times. Also the nanometallopolymer including polymer acylamide have shown excellent properties with high sensing response.

Additionally, we have tried to develop a flexible humidity sensor using PET substrate. These flexible sensors may be used for the detection of the moisture level in baby diapers.

The objectives of the thesis are:

- ❖ To synthesize nanometallopolymer and quantum dots by using chemical method.
- ❖ To fabricate thin and thick films of synthesized nanometallopolymer and QD as a sensing element on alumina and glass substrates.
- ❖ Physical characterization of synthesized films using SEM, TEM, XRD, PL, etc., and their applications in humidity and gas sensors.



1.13 Outline of the Thesis

This thesis contains seven chapters and a brief outline of the thesis is as follows:

Chapter 1 reports a comprehensive study of the recent accomplishments in the field of sensors. Presently, the enthusiastic technological advancement of modern appliances raises a serious concern of environmental deterioration and release of toxic gases bad for human health. There is a great need to develop miniaturized & highly sensitive gas and humidity sensors for the precise monitoring of toxic gases and humidity in the atmosphere. Recently, a variety of such sensors are available for the industry as well as domestic applications. This chapter presents the fundamentals introduction, hierarchical development, and significance of the sensors.

Chapter 2 presents the nanostructured $\text{Ni}(\text{NO}_3)_2(\text{AAm})_4 \cdot 2\text{H}_2\text{O}$ thin film as an electrical humidity sensor. For this purpose, films were prepared by spin-coating method to investigate the adsorption/desorption of humidity at room ambient. The sensing element was investigated through X-ray Diffraction (XRD), Scanning Electron Microscope (SEM), Transmission Electron Microscope (TEM), and UV–Vis absorption techniques. XRD exhibited the crystalline nature of the nanomaterial thin film and evaluated the average crystallite size as 30 nm. SEM showed highly porous nanostructures of different sizes distributed throughout the film. The energy band-gap of the film was estimated as 4.034 eV. TEM image revealed the nanoparticles having sizes in the range of 4-21 nm and SAED confirmed the crystalline nature of the material. The film was further

employed for humidity sensing i.e., impedance-based electrical humidity measurement which gave a maximum average sensitivity of 37.79 M Ω /%RH at room temperature.

Chapter 3 reports the development of CdS/ polyacrylamide nanocomposite as a flexible humidity sensor, which has been fabricated by the facile spin-coating technique on PET (polyethylene terephthalate) substrate. The morphological, optical and crystalline nature of CdS/polyacrylamide nanocomposite were investigated using SEM, TEM, XRD, DSC, FTIR, UV-Visible, and Particle size analyser. Characteristic surface area and pore volume were estimated using BET analysis whereas the hydrophilicity of the sample was investigated using contact angle measurement. The fabricated sensor showed an outstanding humidity sensing response with good linearity in the humidity ranging from 11 %RH to 95 %RH. The average sensitivity of nanocomposite was calculated as 125.57 nF/%RH and may be utilized for moisture detection of commonly used baby diapers with alarm. The simulated & optimized computer model of the synthesized composite (Cd-S & Polyacrylamide) using density functional theory and performed several analyses. HOMO-LUMO and correspondingly obtained other electronic parameters were studied, which revealed that band gap of the synthesized composite material tends to decrease upon increasing the level of water molecules owing to be better humidity sensing mechanism, and therefore it is applicable for humidity sensors. These results show the establishment of the crucial fact that the developed composite material is suitable for moisture absorbent behaviours.

Chapter 4 reports the preparation of Cu_{0.8}Zn_{0.2}Sb₂AAm-polymer nanocomposite synthesized via frontal polymerization technique with its humidity sensing and photoconductive behaviour. The surface texture was examined using Scanning Electron Microscopy (SEM) analysis. X-ray diffraction and Transmission Electron Microscopy (TEM) studies confirm the crystallinity of as-fabricated nanocomposite thin film-based sensing elements. The surface area, particle size, optical absorbance and thermal stability of as-fabricated thin film were successively investigated using Brunauer–Emmett–Teller (BET), Particle size analysis, Ultra-Violet absorption, Fourier Transform Infrared spectroscopy (FTIR), Thermogravimetric analysis, X-ray photoelectron spectroscopy (XPS) and Differential Scanning Calorimetric analysis (DSC) respectively. Humidity sensing characteristics were also investigated via the capacitive performance of Cu_{0.8}Zn_{0.2}Sb₂AAm film with the exposure of moisture. The

average sensitivity (S) of the as-fabricated sensor was found to be ~ 168.477 pF/%RH at an optimum frequency of 20 Hz. The sensor exhibited a rapid response and recovery time of 4.6 sec and 5.6 sec with persistent stability of 96 % after 60 days. Thus, $\text{Cu}_{0.8}\text{Zn}_{0.2}\text{Sb}_2\text{AAM}$ polymer-based capacitive humidity sensor ensures its potential towards reliable and safer use in the detection of humidity levels as well as a photoconductor.

Chapter 5 describes the sustainable, cost-effective and rapid synthesis of gram derived carbon quantum dots (GCQD) employed as capacitive humidity sensors. Synthesis of GCQDs C-1 & C-2 at different carbonization temperatures has been performed by the pyrolysis method. Crystallinity of as prepared GCQDs was confirmed by XRD and TEM analysis revealing the average particle size 5.5 and 2 nm for C-1 & C-2 respectively. Optical properties of samples were further analysed by UV-visible and photoluminescence meter which gave the band-gap as 3.82 and 4.20 eV. Compositional analysis of GCQDs was confirmed by using XPS analysis. GCQDs were subjected to a sensing test at frequency 20 – 2 MHz. The C-2 gave an enhanced sensing performance with an average sensitivity of 254.861 pF/%RH. Also, the sensor showed a rapid response and recovery times of 7.3 & 4.7 sec respectively. Theoretical modelling has been performed to further look into the insight of interaction between functional group of GCQDs and water vapour molecules. Transient parameters such as charge density, HOMO-LUMO gap, electron clouds and H-bonds were calculated using B3LYP hybrid functional at 6-31g diffused and polarised basis set. This study provides insight chemistry of GCQDs with water molecule towards an efficient humidity sensor development.

Chapter 6 reports the facile, low-cost, and phosphine-free synthesis of Indium selenide (InSe) QDs (QDs via one-pot synthesis. The particle size analysis revealed the average particle size of InSe QDs as ~ 13 nm. Optical properties of as-synthesized QDs were investigated using photoluminescence and UV absorption spectrum. InSe QDs exhibited an excitation wavelength of 370 nm and two major absorption peaks at ~ 405 and 432 nm. The optical bandgap of the QD was estimated as 2.2 eV. The recombination time of the InSe QDs was also calculated as 6.41ns from the time-resolved photoluminescence (TRPL). The formation of QDs is confirmed using transmission electron microscopy (TEM) showing the presence of spherical particles within a size regime of 2-4 nm. The

XRD pattern matched well with the standard tetragonal chalcopyrite InSe QDs structure. The sensing film was made up by a spin-coating method and fabricated InSe QDs film was further employed as an LPG and humidity sensor. The ratio of R_g/R_a for the LPG was found as 4.41. For humidity, the average sensitivity of the sensing film was calculated as 8.89 $M\Omega/\%RH$. The sensing response and decay times of the InSe quantum dot were calculated as 5.3 sec & 13.2 sec. No ageing effect was observed and results were found 97.5 % reproducible.

Chapter 7 summarizes the study of synthesis, characterization, humidity and gas sensing properties of nanometallopolymer and quantum dots. Also, this chapter provides the guidelines for further research work in the field of nanodimensional material as a humidity and gas sensor.

References

- [1] D. B. Resnik, Responsibility for health: personal, social, and environmental, (2006) 444–446.
- [2] J. Adams, J. Bartram, Y. Chartier, J. Adams, J. Bartram, Y. Chartier, Essential environmental health standards in health care (2008)63-71.
- [3] M. P. Kelly, M. Barker, Why is changing health-related behaviour so difficult (2016) 6–13.
- [4] M. Hasanuzzaman, M.A. Islam, N.A. Rahim, Y. Yanping, Energy demand, 2020.
- [5] L. Chen, D.J. Magliano, P.Z. Zimmet, mellitus present and future perspectives, 8 (2012).
- [6] G. Wang, Y. Zhang, H. Yang, W. Wang, Y. Dai, L. Niu, C. Lv, H. Xia, T. Liu, Fast-response humidity sensor based on laser printing for respiration monitoring Gong, RSC Adv. 2020, 10 (2020) 8910–8916.
- [7] T. A. Blank, L.P. Eksperiandova, K.N. Belikov, Recent trends of ceramic humidity sensors development : A review, Sensors Actuators B. Chem. 228 (2016) 416–442.
- [8] H. Bi, K. Yin, X. Xie, J. Ji, S. Wan, L. Sun, M. Terrones, Ultrahigh humidity sensitivity of graphene oxide, Sci. Rep. (2013) 1–7.
- [9] A. Tripathy, S. Pramanik, J. Cho, J. Santhosh, N. Azuan, A. Osman, Role of Morphological Structure, Doping, and Coating of Different Materials in the Sensing Characteristics of Humidity Sensors, (2014) 16343–16422.
- [10] N. Miura, H. Mizuno, T. Srimongkon, M. Buerkle, A disposable flexible humidity sensor directly printed on paper for medical applications, (2017).
- [11] R.K. Ibrahim, M. Hayyan, A. Hayyan, S. Ibrahim, Environmental application of nanotechnology : air , soil , and water, Environ. Sci. Pollut. Res. (2016) 13754–13788.
- [12] J. Jeevanandam, A. Barhoum, Y.S. Chan, A. Dufresne, M.K. Danquah, Review on nanoparticles and nanostructured materials : history , sources , toxicity and

- regulations, (n.d.) 1050–1074.
- [13] Z.M. Rittersma, Humidity Sensor. *Encyclopedia of Sens.* 4(2006)481-509.
- [14] B.C. Yadav, R. Srivastava, C.D. Dwivedi, P. Pramanik, Moisture sensor based ZnO nanomaterial synthesized through oxalate route. *Sens. Actuators B: Chem.* 131 (2008) 216-222.
- [15] R. Srivastava, B.C. Yadav, Nanostructured ZnO, ZnO-TiO₂ and ZnO-Nb₂O₅ as solid state humidity sensor. *Adv. Mater. Letters* 3(3) (2012) 197-203.
- [16] Z. Chen, C. Lu, Humidity sensors: a review of materials and mechanism. *Sens. Lett.* (2005) 274–295.
- [17] S. Muto, O. Suzuki, O. Amano, M. Morisawa, A plastic optical fibre sensor for real-time humidity monitoring. *Meas. Sci. Technol.* 14 (2003) 746-740.
- [18] R. Srivastava, N. Verma, B.C. Yadav, Nanostructured zinc ferrite as electrical and optoelectronic humidity sensors. *Adv. Sci. Lett.* 20 (2014)917-922.
- [19] S. Kamekichi, T. Tatsumi, Wet and dry plate dew point Hygrometer, *Humidity and Moisture*1, Ed. by R. E. Ruskin (1965) 64-69.
- [20] M. Yoshitake, I. Shimizu, Experimental results of the psychrometer constant, humidity and moisture 1, Ed. by R. E. Ruskin (1965) 70-75.
- [21] R.J. Taylor, The response of psychrometer fluctuations in vapour pressure, *Humidity and Moisture* 1, Ed. by R. E. Ruskin (1965) 76-82.
- [22] W.W. Robert, Psychrometer Determination of relative humidities in the air with dry-bulb temperatures exceeding 212°F, *Humidity and Moisture*1, Ed. by R. E. Ruskin (1965) 105-109.
- [23] R.G. Wylie, D.K. Davies, W.A. Caw, The basic process of the dew-point hygrometer, *Humidity and Moisture* 1, Ed. by R. E. Ruskin (1965) 125-135.
- [24] A.W. Brewer, The dew-or frost-point hygrometer, *Humidity and Moisture* 1, Ed. by R. E. Ruskin (1965) 136-143.
- [25] C.Y. Lee, G.B. Lee, Micro-machine based humidity sensors with integrated temperature sensors for signal drift compensation. *J. Micromech. Microeng.*13 (2003) 620-625.

- [26] P. Pascal-Delannoy, B. Sorli, A. Boyer, Quartz Crystal Microbalance (QCM) used as a humidity sensor. *Sens. Actuators B: Chem.* 84 (2000) 285-291.
- [27] W.H. King Jr., The piezoelectric sorption hygrometer, *Humidity and Moisture* 1, Ed. by R. E. Ruskin (1965) 570-583.
- [28] M. Jose, M. Perez, C. Freyre, A poly(ethyleneterephthalate)-based humidity sensor. *Sens. Actuators B: Chem.* 42 (1977) 27-30.
- [29] I. Hayakawa, Y. Iwamoto, K. Kikuta, S. Hirano, Gas sensing properties of metal organics derived Pt dispersed-TiO₂ thin film fired in NH₃. *Sens. Actuators B: Chem.* 67 (2000) 270-274.
- [30] Y. Sakai, M. Matsuguchi, T. Hurukawa, Humidity sensor using cross-linked poly (chloromethyl styrene). *Sens. Actuators B: Chem.* 66 (2000) 135-138.
- [31] J. Das, S.M. Hossain, S. Chakraborty, U. Gangopadhyay, H. Saha, Capacitive type Humidity Sensor based on Porous Silicon. *Proceedings of the Tenth International Workshop on the Physics of Semiconductor Devices* 1 (1999) 707-710.
- [32] B.C. Yadav, A.K. Srivastava, P. Sharma, Resistance based humidity sensing properties of TiO₂. *Sens. & Trans. J.* 81(7) (2007)1348-1353.
- [33] W. Qu, W. Wlodarski, U. Jorg, Comparative study on micromorphology and humidity sensitive properties of thin-film and thick-film humidity sensors based on semiconducting MnWO₄. *Sens. Actuators B: Chem.* 64 (2000) 76-82.
- [34] B.C. Yadav, R. Srivastava, C.D. Dwivedi, Synthesis of ZnO nanorods and their application as humidity sensors. *Synthesis and Reactivity in Inorganic, Metal-Organic and Nano-Metal Chemistry* 37 (2007)1-7.
- [35] B.C. Yadav, P. Sharma, A.K. Srivastava, A.K. Yadav, Synthesis of antimony doped tin oxide and it's use as an electrical humidity sensor. *Sens. & Trans. J.* 92(5) (2008) 99-107.
- [36] B.C. Yadav, P. Sharma, P.K. Khanna, Morphological and Humidity Sensing Characteristics of SnO₂-CuO, SnO₂-Fe₂O₃ and SnO₂-SbO₂ nano co-oxides. *Bull.of Mater. Sci.* 34(1) (2011) 1-10.

-
- [37] W. Qu, M. Jorg-Uwe, A novel thick film ceramic humidity sensor, *Sens. Actuators B: Chem.* 40 (1997) 175-182.
- [38] *Water Vapor Measurement: Methods and Instrumentation*, Pieter R. Wiederhold, ISBN-13: 978-0824793197, CRC Press; Har/Dskt edition (April 11, 1997)
- [39] *CRC Handbook of Chemistry and Physics*, CRC Press, London, 76th Edition, ISBN 0-8493-04768
- [40] Kaye and Laby, *Tables of Physical and Chemical Constants*, 16th Edition, Harlow: Longman, ISBN 0-582-22629-5.
- [41] F.C.Quin, *The Most Common Problem of Moisture Measurement and Control*, Proceedings of the 1985 International Symposium on Moisture and Humidity, Washington, D.C.
- [42] General Eastern Instruments, *Humidity Handbook*, Doc, No. A 40103384, Rev B.00, May 1993.
- [43] *ASHRAE Handbook-Fundamentals*, American Society of Heating, Refrigeration and Air Conditioning Engineering, 1993.
- [44] *Method for Measurement of Moist Properties*, ANSI/ASHRAE 41.6-1994, American Society of Heating, Refrigeration and Air Conditioning Engineers, Inc., 19
- [45] *A guide to Measurement of Humidity*, ISBN0-904457-24-91, The Institute of Measurement and Control and NPL(UK), 1996.
- [46] I.R. Matias, F.J. Arregui, R.O. Claus, *Optical Fibre Sensors*. *Encyclopedia of Sensors* 7 (2006) 163-181.
- [47] K. Brain, *Fiber optics in Sensing and Measurements*. *IEEE J of Selected Topics in Quantum Elect.* 6(6) (2000) 1014-1021.
- [48] J.C. Simon, E. Spitz, *Communications a la Societe Francaise de Physique* 24 (1963) 1449.
- [49] C.K. Kao, G. Hockman, *Proceedings of IEEE* 113 (1966) 1151.
- [50] C. Menaider, C. Kissinger, H. Adkins, *Instruments and Control Systems* 40(1967) 114.

- [51] B.C. Yadav, R.C. Yadav, P.K. Dwivedi, Sol-gel processed (Mg-Zn-Ti) oxide nanocomposite film deposited on prism base as an opto-electronic humidity sensor. *Sens. Actuators B: Chem.* 148 (2010) 413-419.
- [52] B.C. Yadav, N.K. Pandey, Study of Optical Humidity Sensing Properties of TiO₂ and MgO Films. *Sens. & Trans. J.* 78 (2007) 1127-1133.
- [53] Y. Shimizu, H. Arai, T. Seiyama, Theoretical studies on the impedance-humidity characteristics of ceramic humidity sensors. *Sens. Actuators* 7 (1985) 11-22.
- [54] H.C. Verma, *Concepts of Physics, Part-2*, Bharti Bhawan Publishers and Distributors, India (1999).
- [55] G.W. Bundrett, *Criteria of Moisture Control* (London: Butterworths) (1990) 19.
- [56] T. Morimoto, M. Nagao, F. Tokuda, The relation between the amounts of chemisorbed and physisorbed water on metal oxides. *J. Phys. Chem.* 73 (1969) 243-248.
- [57] T. King, *Water, Miracle of Nature* (New York: Macmillan) (1953).
- [58] J.J. Fripiat, A. Jelli, G. Poncelet, J. Andre, Thermodynamic properties of adsorbed water molecules and electrical conduction in montmorillonites and silicas. *J. Phys. Chem.* 69 (1965) 2185-9.
- [59] J.H. Anderson, G.A. Parks, Electrical properties of silica-gel in the presence of adsorbed water, *J. Phys. Chem.* 72 (1968) 3662-8.
- [60] C.J. Brinker, G.W. Sherer, *Sol-gel Science*. Academic Press. San Diego.(1990).
- [61] C.J. Brinker, A.J. Hurd, P.R. Schunk, C.S. Ashley, R. Caircross, J. Samuel, K.S. Chen, C. Scotto, R.A. Schwartz, *Sol-gel derived Ceramic Films - Fundamentals and Applications*, in: K.Stern (Ed.), *Metallurgical and Ceramic Protective Coatings*, Chapman & Hall, London (1996) 112-151.
- [62] T. Troczynski, Q. Yang, Process for Making Chemically Bonded Sol-Gel Ceramics, U.S. Pat. 6(284) (2001) 682.
- [63] J. Xu, Y. Wang, S. Hu, Nanocomposites of graphene and graphene oxides, Synthesis , molecular functionalization and application in electrochemical sensors and biosensors . A review, *Microchim. Acta.* (2017) 1-44.

- [64] X. Chu, P. Dai, Y. Dong, W. Sun, L. Bai, The acetic acid gas sensing properties of graphene quantum dots (GQDs)– ZnO nanocomposites prepared by hydrothermal method, *J. Mater. Sci. Mater. Electron.* 28 (2017) 19164–19173. doi:10.1007/s10854-017-7873-7.
- [65] M. Enachi, O. Lupan, T. Braniste, A. Sarua, L. Chow, Y.K. Mishra, D. Gedamu, R. Adelung, I. Tiginyanu, Integration of individual TiO₂ nanotube on the chip: nanodevice for hydrogen sensing, *Phys. Status Solidi RRL* 9 (3) (2015) 171–174.
- [66] O. Lupan, V. Cretu, V. Postica, N. Ababii, O. Polonskyi, V. Kaidas, F. Schutt, Y.K. Mishra, E. Monaco, I. Tiginyanu, V. Sontea, T. Strunskus, F. Faupel, R. Adelung, Enhanced ethanol vapour sensing performances of copper oxide nanocrystals with mixed phases, *Sens. Actuators B* 224 (2016) 434–448.
- [67] O. Lupan, V. Cretu, M. Deng, D. Gedamu, I. Paulowicz, S. Kaps, Y.K. Mishra, O. Polonskyi, C. Zamponi, L. Kienle, V. Trofim, I. Tiginyanu, R. Adelung, Versatile growth of freestanding orthorhombic Molybdenum Trioxide nano- and microstructures by rapid thermal processing for gas nanosensors, *J. Phys. Chem. C* 118 (2014) 15068–15078.
- [68] A.M. Limarga, S. Shian, M. Baram, D.R. Clarke, Effect of high-temperature aging on the thermal conductivity of nanocrystalline tetragonal yttria-stabilized zirconia, *Acta Mater.* 60 (2012) 5417–5424.
- [69] Y. Liu, H. Wang, S. Yang, K. Chen, T. Yang, J. Wei, J. Tian, W. Chen, *Sensors and Actuators B : Chemical* ppb level ammonia detection of 3-D PbS quantum dots / reduced graphene oxide nanococoons at room temperature and Schottky barrier modulated behavior, *Sensors Actuators B. Chem.* 255 (2018) 2979–2987.
- [70] S.F.A.Z. Yuso, C.S. Lim, S.R. Azzuhri, H. Ahmad, R. Zakaria, Studies of Ag /TiO₂ plasmonics structures integrated in side polished optical fiber used as humidity sensor, 10 (2018) 308–316.
- [71] M. Leonowicz, M. Izydorzak, A.D. Pomogailo, G.I. Dzhardimalieva, Processing of Magnetic Beads for Biological Sensor Application by Pyrolysis of Metal Containing Polymers, (2012) 184–187.
- [72] Z. Duan, Q. Zhao, S. Wang, Q. Huang, Z. Yuan, Y. Zhang, Y. Jiang, H. Tai,

- Halloysite nanotubes: Natural , environmental-friendly and low-cost nanomaterials for high-performance humidity sensor, *Sensors Actuators B. Chem.* 317 (2020) 128204.
- [73] H.J. Nachash, O. Okay, Formation and Structure of Polyacrylamide Gels, *J. App. Polymer Sci.* 60 (1996) 971-979.
- [74] J.C. Eloi, L. Chabanne, Metallopolymers with emerging applications, *Mater. Today* 11(2008) 28–36.
- [75] O. Okay, Kinetics of gelation in free radical crosslinking copolymerization, *J. Polymer* 35 (1994) 2613-2618.
- [76] K.B. Girma, V. Lorenz, S. Blaurock, F.T. Edelmenn, Coordination chemistry of acrylamide, *Coord. Chem. Rev.* 249 (2005) 1283–1293.
- [77] J.P. Baker, L.H. Hong, H.W. Blanch, J.M. Prausnitz, Recent advances in polymers and composites, *Macromolecules* 27 (1994) 1446.
- [78] N. Weiss, T.V. Vliet, A. Silberberg, Permeability of heterogeneous gels, *J. App. Polymer Sci.* 17 (1974) 2229–2240.
- [79] S. Iwatsuki, T. Itoh, Amphoteric Behavior of Tetrakis (methoxycarbonyl) quinodimethane in Alternating Copolymerizations with Various Comonomers, *Adv. Polym. Sci.* 13 (1980) 983-989.
- [80] S. Palaniappan, D.N. Sathyanarayana, Polymeric charge-transfer complexes: a study by electronic absorption spectroscopy, *J. Polymer* 31 (1990) 1401-1405.
- [81] S. Sikarwar, A. Kumar, B.C. Yadav, G.I. Dzhardimalieva, N.D. Golubeva, Nanostructured spherical-shaped Sc(III) Polyacrylate for monitoring the moisture level, *IEEE Sensors* (2018).
- [82] S. Singh, B.C. Yadav, P. Tandon, M. Singh, A. Shukla, G.I. Dzhardimalieva, S.I. Pomogailo, N.D. Golubeva, A.D. Pomogailo, Polymer-assisted synthesis of metallopolymer nanocomposites and their applications in liquefied petroleum gas sensing at room temperature, *Sens. Actuators B: Chem.* 166 (2012) 281–291.
- [83] A.D. Pomogailo, V.S. Savost'janov, *Synthesis and Polymerization of Metal-Containing Monomers*, CRC Press, Boca Ration, (1994) 164.

- [84] S.I. Evstratova, B.M. Zuev, G.I. Dzhardimalieva, Abstracts of Papers, The 218th ACS National Meet, New Orleans, 74 (1999).
- [85] S.I. Evstratova, G.V. Shilov, G.I. Dzhardimalieva, A.D. Pomogailo, I.E. Uflyand, S.M. Aldoshin Copper (II) Nitrate Complex with Acrylamide: Synthesis and Crystal Structure, *Russ. J. Coordination Chem.* 27 (2001) 35–737.
- [86] D. Fortenberry, J.A. Pojman, Solvent-free synthesis of polyacrylamide by frontal polymerization, *J. Polymer Sci. Part A: Polymer Chem.* 38 (2000) 1129–1135.
- [87] J.A. Pojman, V.M. Ilyashenko, A.M. Khan, Free-radical frontal polymerization: self-propagating thermal reaction waves, *J. Chem. Soc. Faraday Trans.* 16 (1996) 2825–283.
- [88] J.A. Pojman, J. Willis, D. Fortenberry, V. Ilyashenko, A.M. Khan, Factors Affecting Propagating Fronts of Addition Polymerization: Velocity, Front Curvature, Temperature Profile, Conversion, and Molecular Weight Distribution, *J. Polymer Sci. Part A: Polym Chem.* 33(1995) 643–652.
- [89] K. Faaliyan, H. Abdoos, E. Borhani, S.S.S. Afghahi, Core-shell nanoparticles for medical applications: effects of surfactant concentration on the characteristics and magnetic properties of magnetite-silica nanoparticles, *Nanomed. J.* 6 (2019) 269–275.
- [90] A. Arafati, E. Borhani, S.M.S. Nourbakhsh, H. Abdoos, Synthesis and characterization of tetragonal/monoclinic mixed phases nanozirconia powders, *Ceramics Inter.* 45 (2019) 12975–12982.
- [91] G.N. Makarov, Laser applications in nanotechnology: nanofabrication using laser ablation and laser nanolithography, *Phys. Usp.* 56 (2013) 643–682.
- [92] H. Abdoos, Sintered steel composites reinforced with ceramic nanoparticles: fabrication, characteristics and wear behavior, *Mech. Adv. Comp. Struct.* 6 (2019) 191–200.
- [93] D. Gammon, Electrons in artificial atoms, *Nature* 405 (2000) 899–900. 6.
- [94] M.A. Reed, J.N. Randall, R.J. Aggarwal, R.J. Matyi, T.M. Moore, A.E. Wetsel, Observation of discrete electronic states in a zero-dimensional semiconductor nanostructure. *Phys. Rev. Lett.* 60 (1988) 535537.

- [95] A. Mukherjee, Y. Shim, J.M. Song, Quantum dot as probe for disease diagnosis and monitoring, *Biotechnol. J.* 11 (2016) 31–42.
- [96] M. Fang, C. Peng, D.W. Pang, Y. Li, Quantum dots for cancer research: Current status, remaining issues, and future perspectives, *Cancer Biol. Med.* 9 (2012) 151–163. 10
- [97] A.M. Iga, J.H.P. Robertson, M.C. Winslet, A.M. Seifalian, Clinical potential of quantum dots, *J. Biomed. Biotechnol.* 2007 (2007) 76087.
- [98] H.M. Kashani, T. Madrakian, A. Afkhami, F. Mahjoubi, M.A. Moosavi, Bottom-up and green-synthesis route of amino functionalized graphene quantum dot as a novel biocompatible and label-free fluorescence probe for in vitro cellular imaging of human ACHN cell lines, *Mater. Sci. Engin. B* 251 (2019) 114452.
- [99] B.T. Hoan, T.T. Thanh, P.D. Tam, N.N. Trung, S. Cho, V.H. Pham, A green luminescence of lemon derived carbon quantum dots and their applications for sensing of V 5+ ions, *Mater. Sci. Eng. B* 251 (2019) 114455.
- [100] H. Shen, Q. Gao, Y. Zhang, Y. Lin, Q. Lin, Z. Li, L. Chen, Z. Zeng, X. Li, Y. Jia, S. Wang, Z. Du, L.S. Li, Z. Zhang, Visible quantum dot light-emitting diodes with simultaneous high brightness and efficiency, *Nature photon.* 13 (2019) 192–197.
- [101] X. Shen, J. Jia, Y. Lin, X. Zhou, Enhanced performance of CdTe quantum dot sensitized solar cell via anion exchanges, *J. Power Sources* 277 (2015) 215–221.
- [102] L. Farzin, M. Shamsipur, L. Samandari, S. Sheibani, Recent advances in designing nanomaterial based biointerfaces for electrochemical biosensing cardiovascular biomarkers, *J. Pharm. Biomed. Anal.* 161 (2018) 344–376.
- [103] W. Zhang, R. Wang, F. Luo, P. Wang, Z. Lin, Miniaturized electrochemical sensors and their point-of-care applications, *Chin. Chem. Lett.* 31 (2020) 589–600.
- [104] H. Ehzari, M. Safari, M. Shahlaei, A signal amplification by QDs used for ferrocene-labeled sandwich aptasensor for determination of Hg₂₊ in water samples, *J. Iran. Chem. Soc.* 16 (2019) 2555–2564.

- [105] H. Ehzari, M. Safari, M. Shahlaei, A new sensing strategy based on thymine bases–Hg²⁺ – methylene blue coordination on the electrospun PES–QDs platform for detection of Hg²⁺ in fruit juice samples, *J. Iran. Chem. Soc.* 16 (2019) 2269–2279.
- [106] X. Xu, R. Ray, Y. Gu, H.J. Ploehn, L. Gearheart, K. Raker, W.A. Scrivens, Electrophoretic analysis and purification of fluorescent single-walled carbon nanotube fragments, *J. Am. Chem. Soc.* 126 (2004) 12736–12737
- [107] L.A. Ponomarenko, F. Schedin, M.I. Katsnelson, R. Yang, E.W. Hill, K.S. Novoselov, A.K. Geim, Chaotic dirac billiard in graphene quantum dots, *Science* 320 (2008) 356–358.
- [108] P. Tian, L. Tang, K.S. Teng, S.P. Lau, Graphene quantum dots from chemistry to applications, *Mater. Today Chem.* 10 (2018) 221–258.
- [109] L.T. Canham, Silicon quantum wire array fabrication by electrochemical and chemical dissolution of wafers, *Appl. Phys. Lett.* 57 (1990) 1046–1048.
- [110] V. Lehmann, U. Gosele, Porous silicon formation: a quantum wire effect, *Appl. Phys. Lett.* 58 (1991) 656–658.
- [111] S. Morozova, M. Alikina, A. Vinogradov, M. Pagliaro, Silicon quantum dots: synthesis, encapsulation, and application in light-emitting diodes, *Front. Chem.* 8 (2020) 191.
- [112] A. Karatutlu, M. Song, A.P. Wheeler, O. Ersoy, W.R. Little, Y. Zhang, P. Puech, F.S.Boi, Z. Luklinska, A.V. Sapelkin, Synthesis and structure of free-standing germanium quantum dots and their application in live cell imaging, *RSC Adv.* 5 (2015) 20566.
- [113] J. Luo, H. Bai, P. Yang, J. Cai, One-pot aqueous synthesis of germanium-doped cadmium sulfide quantum dots as fluorescent probes for cell imaging, *Mater. Sci. Semicon. Proc.* 34 (2015) 1–7.
- [114] D. Vasudevan, R.R. Gaddam, A. Trinchi, I. Cole, Core-shell quantum dots: properties and applications, *J. Alloys Compd.* 636 (2015) 395–404
- [115] A.R. AbouElhamd, K.A. Al-Sallal, A. Hassan, Review of core/shell quantum dots technology integrated into building’s glazing, *Energies* 12 (2019) 1058.

- [116] M. Safari, S. Najafi, E. Arkan, S. Amani, M. Shahlaei, Facile aqueous synthesis of Ni doped CdTe quantum dots as fluorescent probes for detecting pyrazinamide in plasma, *Microchem. J.* 146 (2019) 293–299.
- [117] C. Chen, H. Qiao, S. Lin, C. Man Luk, Y. Liu, Z. Xu, J. Song, Y. Xue, D. Li, J. Yuan, W. Yu, C. Pan, S. Ping Lau, Q. Bao, Highly responsive MoS₂ photodetectors enhanced by graphene quantum dots, *Scientific Reports*, 5 (2015) 11830.
- [118] J. Cao, Z. Wang, X. Zhan, Q. Wang, M. Safdar, Y. Wang, J. He, Vertical SnSe nanorod arrays: from controlled synthesis and growth mechanism to thermistor and photoresistor, *Nanotechnology*, 25 (2014) 105705.
- [119] A.S. Pawbake, R.G. Waykar, D.J. Late, S.R. Jadkar, Highly Transparent Wafer-Scale Synthesis of Crystalline WS₂ Nanoparticle Thin Film for Photodetector and Humidity-Sensing Applications, *ACS Applied Materials & Interfaces*, 8 (2016) 3359-3365.
- [120] M.B. Erande, M.S. Pawar, D.J. Late, Humidity Sensing and Photodetection Behavior of Electrochemically Exfoliated Atomically Thin-Layered Black Phosphorus Nanosheets, *ACS Applied Materials & Interfaces*, 8 (2016) 11548-11556.
- [121] M.S. Pawar, P.K. Bankar, M.A. More, D.J. Late, Ultra-thin V₂O₅ nanosheet based humidity sensor, photodetector and its enhanced field emission properties, *RSC Advances*, 5 (2015) 88796-88804.
- [122] R. K. Tripathi, O. S. Panwar, I. Rawal, B.P. Singh, B.C. Yadav, Study on nanocrystalline silicon thin films grown by the filtered cathodic vacuum arc technique using boron doped solid silicon for fast photo detectors, *Journal of the Taiwan Institute of Chemical Engineers*, 86 (2018) 185-191.
- [123] M. Peng, X. Zheng, Z. Ma, H. Chen, S. Liu, Y. He, M. Li, Ni-pattern guided GaN nanowire-array humidity sensor with high sensitivity enhanced by UV photoexcitation, *Sensors and Actuators B: Chemical*, 256 (2018) 367-373.
- [124] M.A. Zanjanchi, S. Sohrabnezhad, Evaluation of methylene blue incorporated in zeolite for construction of an optical humidity sensor. *Sens. Actuators B*.105 (2005) 502-507.

- [125] J. M. Corres, F.J. Arregui, I.R. Matias, Sensitivity optimization of tapered optical fiber humidity sensors by means of tuning the thickness of nanostructured sensitive coatings. *Sens. Actuators B: Chem.* 122 (2007) 442-449.
- [126] Z. Zhao, Y. Duan, A low-cost fibre optic humidity sensor based on silica sol-gel film. *Sens. Actuators B: Chem.* 160 (2011) 1340-1345.
- [127] B. C. Yadav, S. Sikarwar, A. Bhaduri, P. Kumar, Synthesis, characterization and development of opto-electronic humidity sensor using copper oxide thin film, *Int. Adv. Res. J. in Sci., Engg. and Tech.* 2(11) (2015) 105-109.
- [128] L. Xia, L. Li, W. Li, T. Kou, D. Lie, Novel optical fibre humidity sensor based on a no-core fibre structure. *Sens. Actuators A: Phy.* 190 (2013) 1-5.
- [129] P.J. Rivero, A. Urrutia, J. Goicoechea, F.J. Arregui, Optical fibre humidity sensors based on Localized Surface Plasmon Resonance (LSPR) and Lossy-mode resonance (LMR) in overlays loaded with silver nanoparticles. *Sens. Actuators B: Chem.* 173 (2012) 244-249.
- [130] J. Lee, D. Cho, Y. Jeong, A resistive-type sensor based on flexible multi-walled carbon nanotubes and polyacrylic acid composite films. *Solid-State Electron.* 87 (2013) 80–84.
- [131] P. Hu, X. Dong, K. Ni, L.H. Chen, W.C. Wong, C.C. Chan, Sensitivity-enhanced Michelson interferometric humidity sensor with waist-enlarged fibre bitaper. *Sens. Actuators B: Chem.* 194 (2014) 180-184.
- [132] B.C. Yadav, K.S. Chauhan, S. Singh, R.K. Sonker, S. Sikarwar, R. Kumar, Growth and characterization of sol-gel processed rectangular shaped nanostructured ferric oxide thin film followed by humidity and gas sensing, *J Mater Sci: Mater Electron* 28 (2017) 5270–5280.
- [133] D. Zhang, H. Chang, P. Li, R. Liu, Q. Xue, Fabrication and characterization of an ultrasensitive humidity sensor based on metal oxide/graphene hybrid nanocomposite. *Sens. Actuators B Chem.* 2016, 225, 233–240.
- [134] N. Irawati, T.N.R. Abdullah, H.A. Rahman, H. Ahmad, S.W. Harun, PMMA microfiber loop resonator for humidity sensor, *Sens. Actuators A: Phy.* 260 (2017) 112–116.

- [135] Y. Wang, C. Shen, Fiber optic humidity sensor based on the graphene oxide/PVA composite film, *Optic Commun.* 372 (2016) 229–234.
- [136] W. Xie, M. Yang, Y. Chen, D. Li, Y. Zhang, Z. Zhuang, Optical fibre relative-humidity sensor with evaporated dielectric coatings on fibre end-face. *Optic Fibre Techno.* 30 (2014).
- [137] Y. Pang, J. Jian, T. Tu, Z. Yang, J. Ling, Y. Li, X. Wang, Y. Qiao, Y.Y. Tian, T.L. Ren, Biosensors and Bioelectronics Wearable humidity sensor based on porous graphene network for respiration monitoring. *Biosens. Bioelectron.* 2018, 116, 123–129.
- [138] H. Bi, K. Yin, X. Xie, J. Ji, S. Wan, L. Sun, M. Terrones, M.S. Dresselhaus, Ultrahigh humidity sensitivity of graphene oxide, *Sci. Rep.* 3(2714), (2013) 1–4.

Tables:**Table 1.1.** Shows the confinement types with their conditions

Confinement types	Condition	Equation
Weak Confinement	$R \gg a_B$	$\Delta E = \frac{\hbar^2 \pi^2}{2MR^2}$
Medium Confinement	$R \ll a_e$, but $R \gg a_h$	-
Strong Confinement	$R \ll a_h$, but $R \ll a_e$	$\Delta E = \frac{\hbar^2 \pi^2}{2\mu R^2}$

Table 1.2. The confinement structure with their wave equation conditions

Structure	Confinement	Conditions
Bulk Material	0D	$g(E) = \frac{1}{2\pi^2} \left(\frac{2m^*}{\hbar^2} \right)^{3/2} \sqrt{E_g - E}$
Quantum Well	1D	$g(E) = \frac{m^*}{\pi\hbar^2} \sigma(E_g - E)$
Quantum Wire	2D	$g(E) = \frac{m^*}{\pi\hbar} \sqrt{\frac{m^*}{2(E_g - E)}}$
Quantum Dots	3D	$g(E) = 2\delta(E_g - E)$

Table 1.3 The international and national developments in the field of sensors summarised year-wise thorough literature survey

S.No.	Year	Author	Sensing Material	Sensitivity	Response time	Recovery time	Ref.

1.	2005	M.A. Zanjanchi et al.	Zeolite	-	2 min	4 min	[134]
2.	2007	J.M. Corres et al.	PDDA/Poly R-478	-	300 ms	-	[133]
3.	2011	Z. Zhao et al.	Silica sol-gel film	0.087 dB/%RH	45 s	70 s	[132]
4.	2012	P.J. Rivero et al.	LbL polymeric coating loaded with Ag NPs	0.943 nm/%RH	20 min	38 min	[131]
5.	2013	L. Xia et al.	HEC/PVDF	0.196 dB/%RH	58 s	89 s	[129]
6.	2013	J. Lee	MWCNTs	930 Ω	680 s	380 s	[130]
7.	2013	J.Lee. et al.	MWCNTs in a PAA matrix in a ratio 1:4	930 Ω	680 s	380 s	[135]
8.	2014	P. Hu et al.	Chitosan film	13.5 pm/%RH	43 s	97 s	[128]
9.	2015	B.C.Yadav	CuO	0.85 μ W/%RH	-	-	[127]
10.	2015	D. Zhang et al.	Tin dioxide/reduced graphene oxide (RGO)	146.53 pF	102 s	Several s	[137]
11.	2016	Y. Wang et al.	Graphene oxide/PVA	0.193 dB%RH	73 s	65 s	[126]
12.	2017	N. Irawati et al.	PMMA/ PMLR/ ZnO	0.1746 dBm/%RH	256 s	80 s	[125]
13.	2018	Y. Pang	GO modified poly (3,4 ethylenedioxythiophene)	4.97%	31 s	72 s	[124]
14.	2018	Y.Pang et al.	GO modified with poly (3,4 ethylenedioxythiophene)	4.97%	31 s	72 s	[136]
15.	2020	H. Bi et al.	Fe-GO	5.18 pF/%RH	31 s	11 s	[138]

Figure:

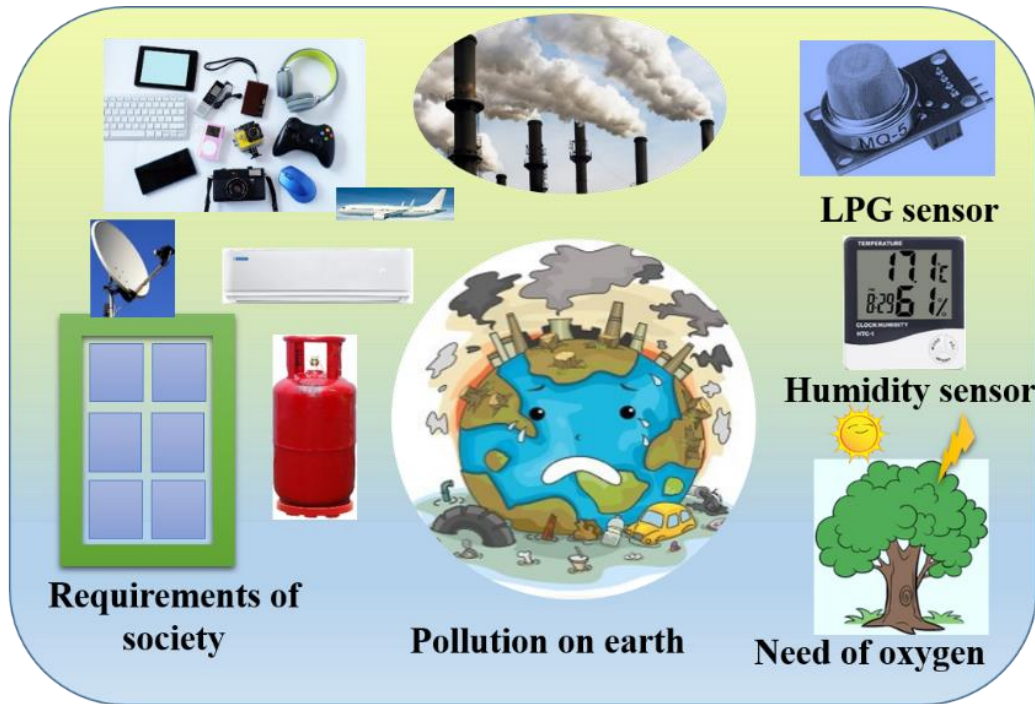


Figure 1.1: Schematic diagram of the present environmental challenges and needs of the sensor.



Figure 1.2: Representation of importance of sensors in our daily life

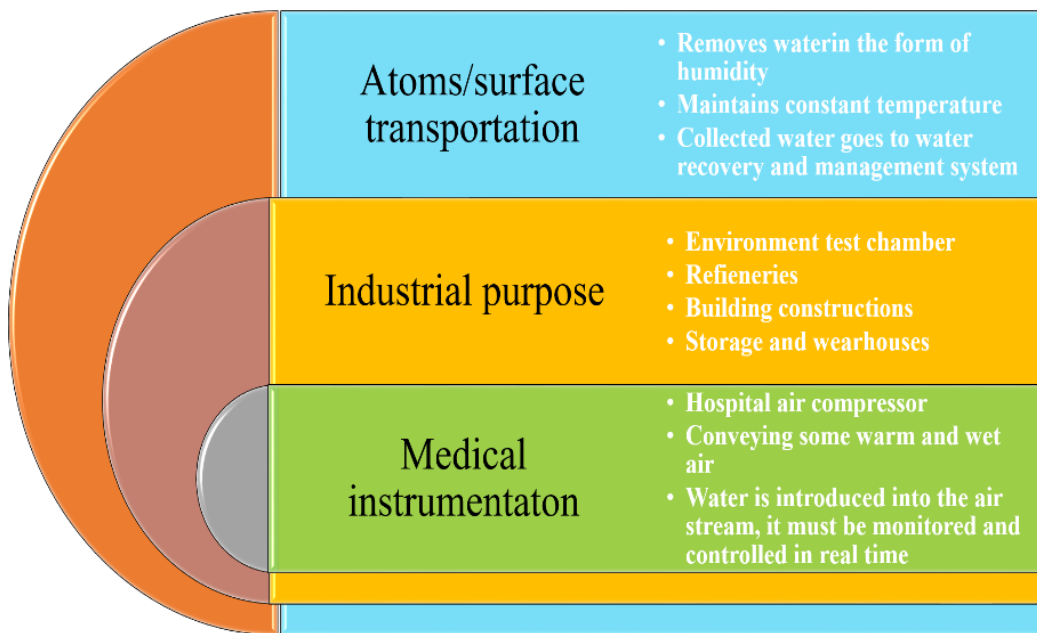


Figure 1.3: Role of humidity sensors in diverse fields

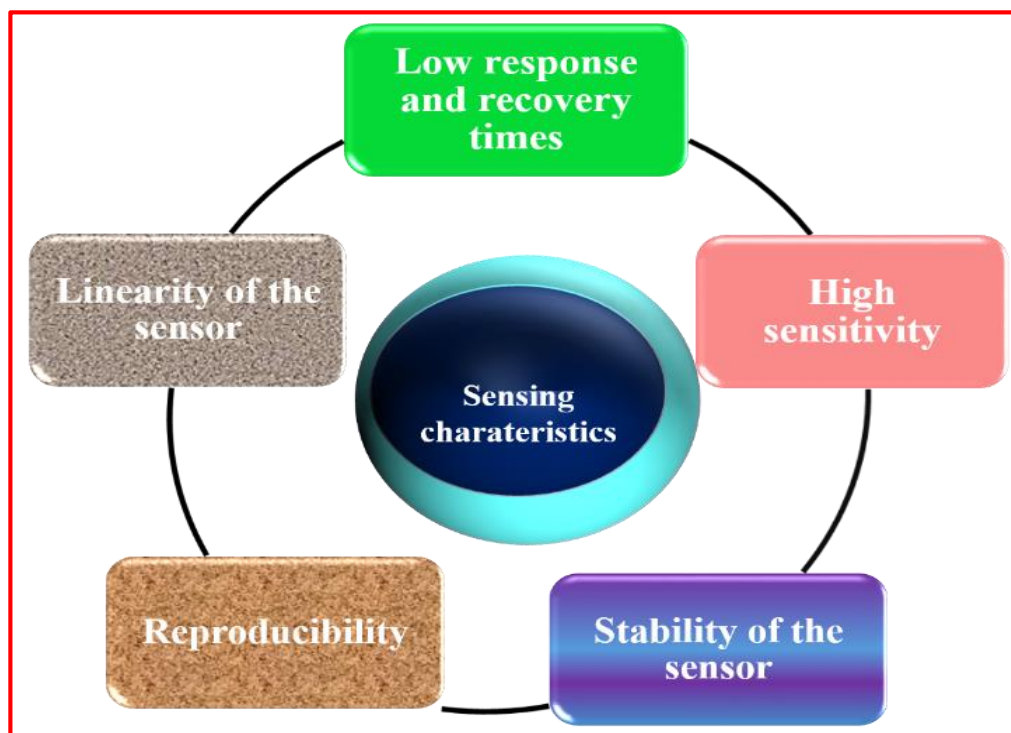


Figure 1.4: Humidity sensors affecting parameters

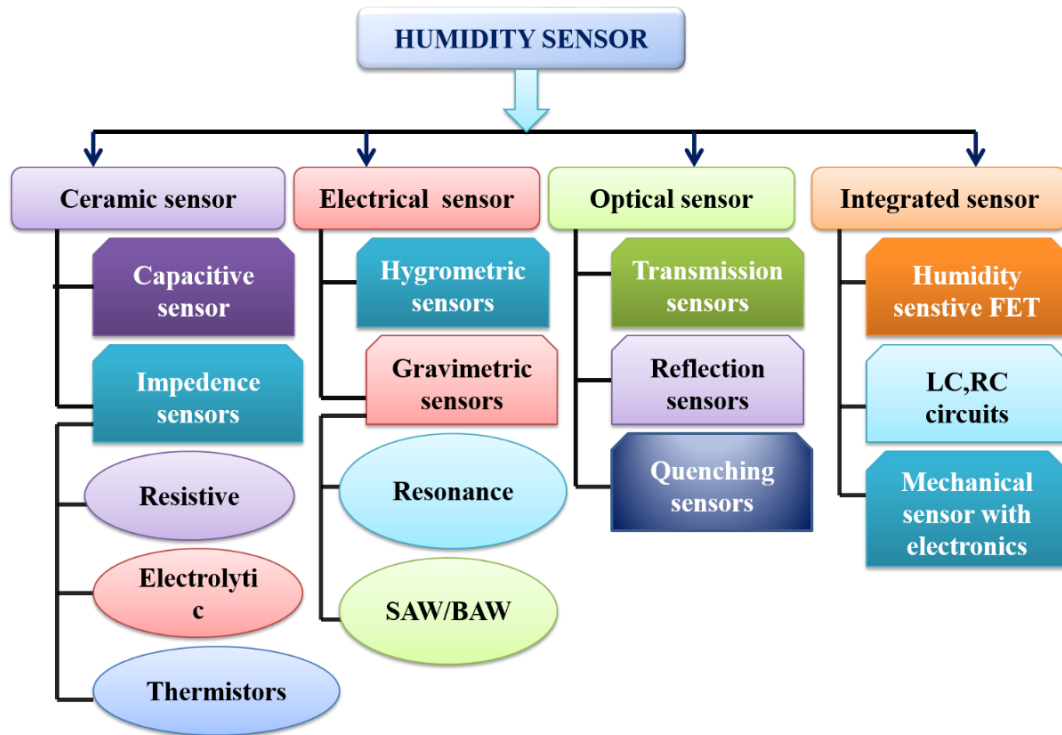


Figure 1.5: Classification of humidity sensors

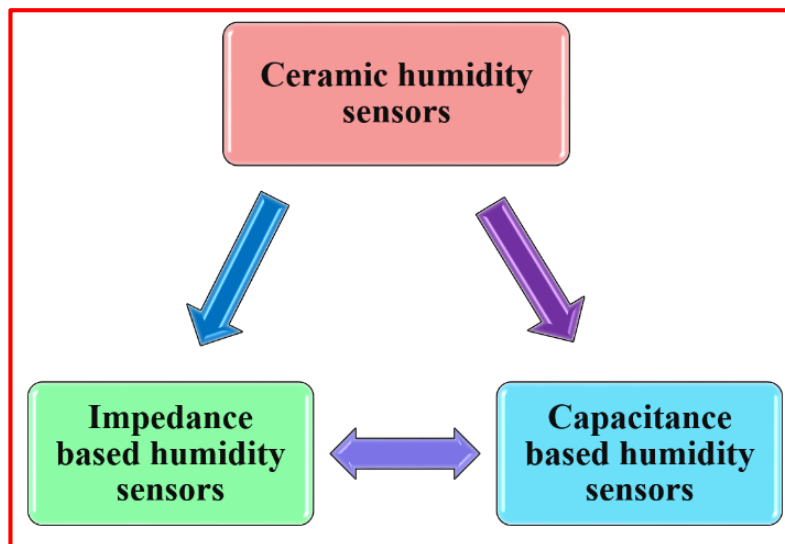


Figure 1.6: Classification of ceramic humidity sensors

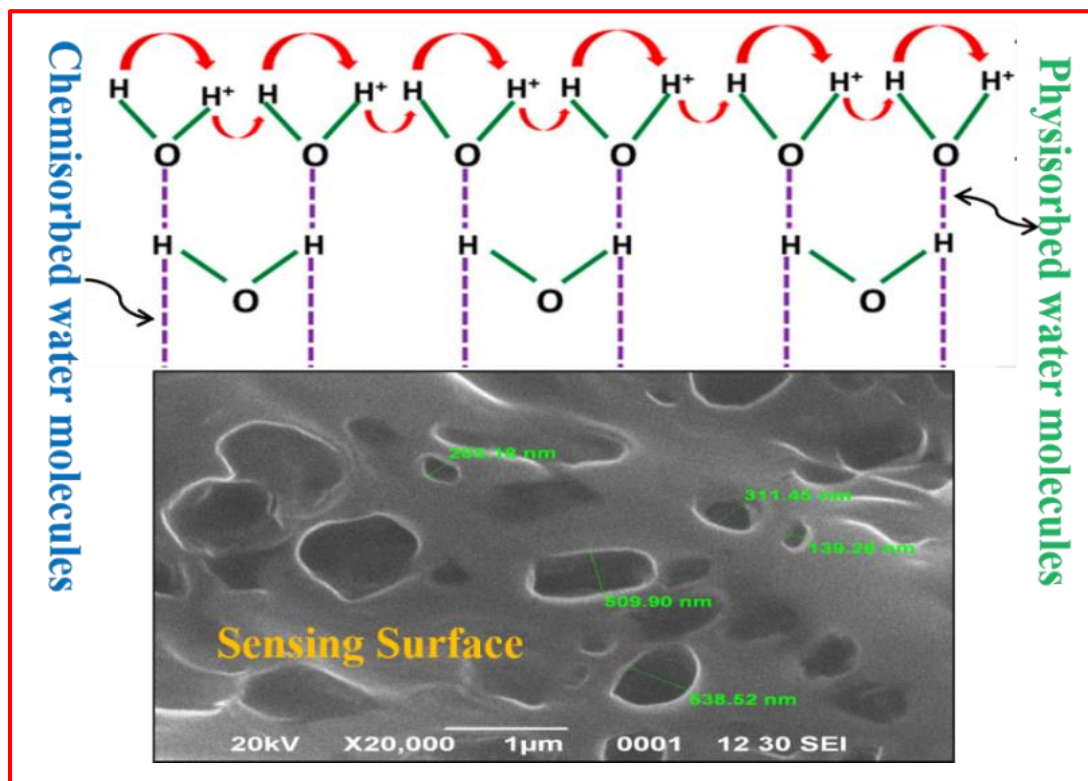


Figure. 1.7: Impedance based humidity sensing mechanism

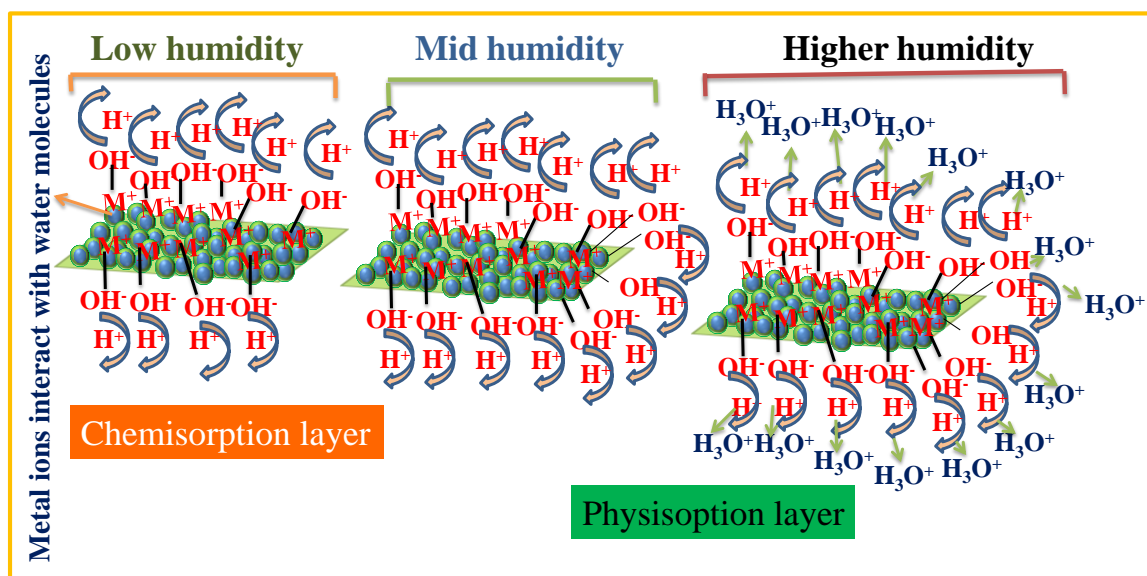


Figure 1.8: The schematic presentation of humidity sensing mechanism; three regions as low, middle, and high-level %RH

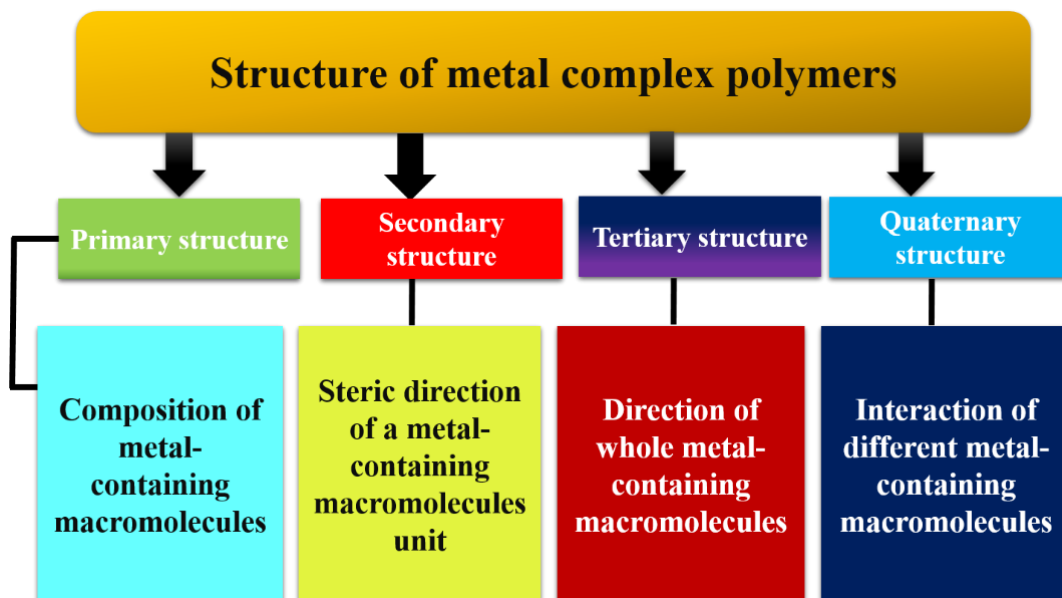


Figure 1.9: Classification of metal complex polymers.

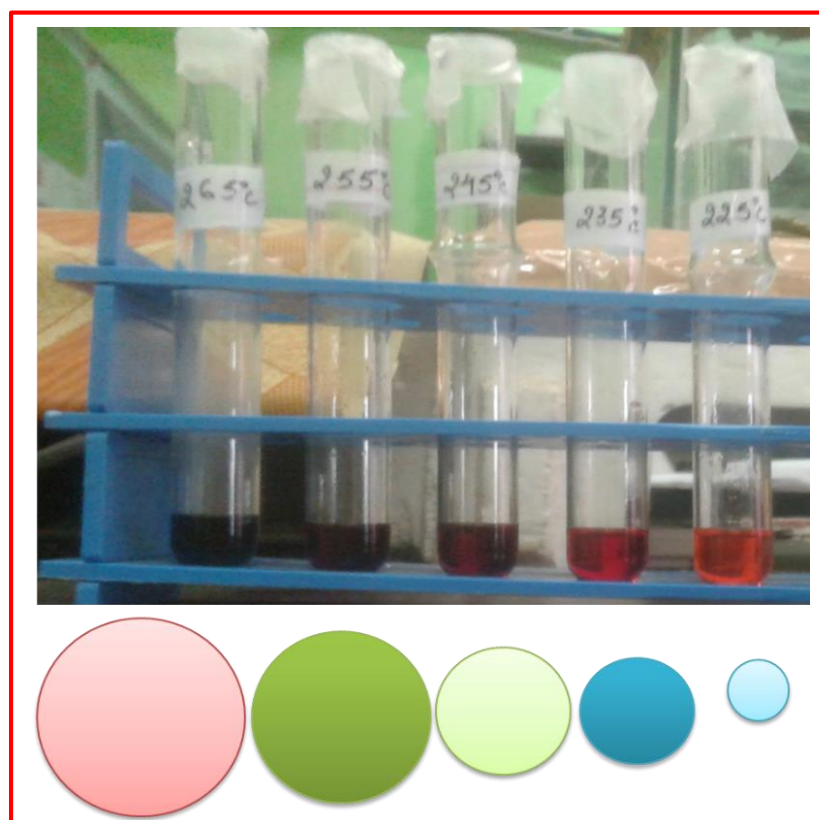


Figure 1.10: Color and size-dependent property of quantum dots.

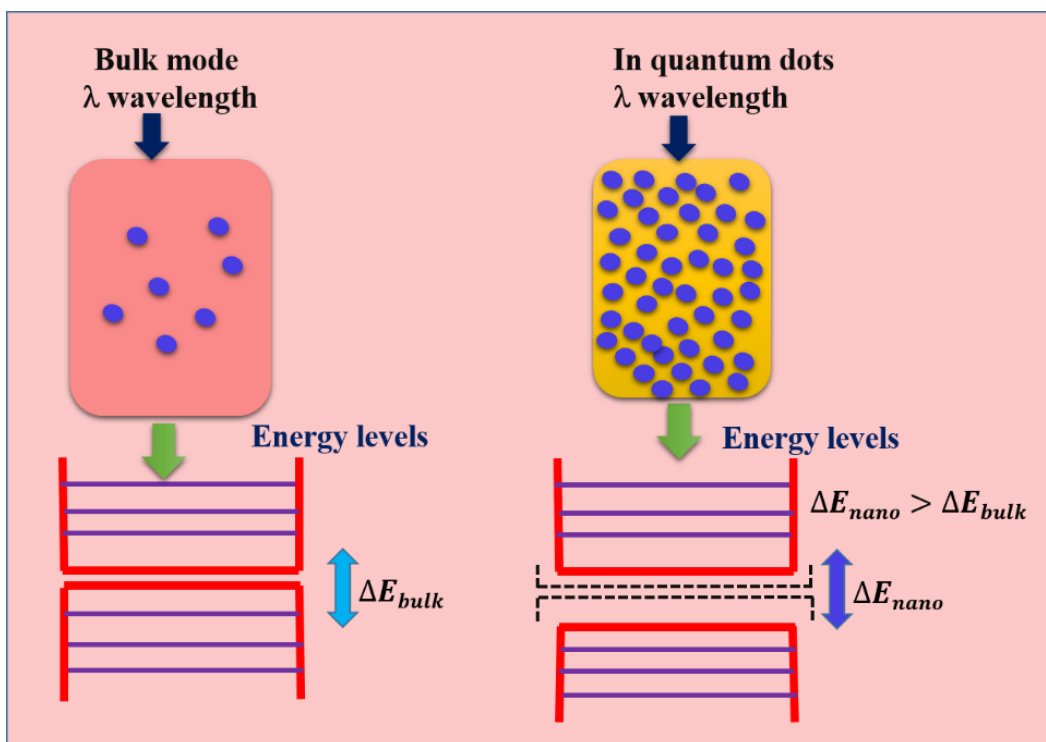


Figure 1.11: Bandgap energy levels from bulk to quantum dots.

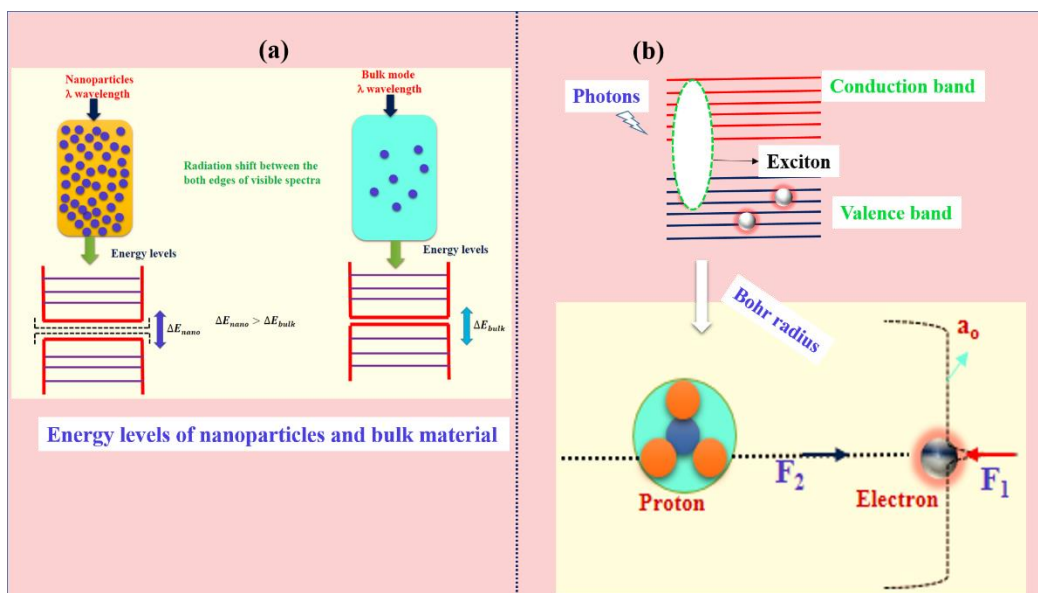


Figure 1.12: Display the comparison between energy levels of bulk and nanomaterial with Bohr radius and exciton of an atom

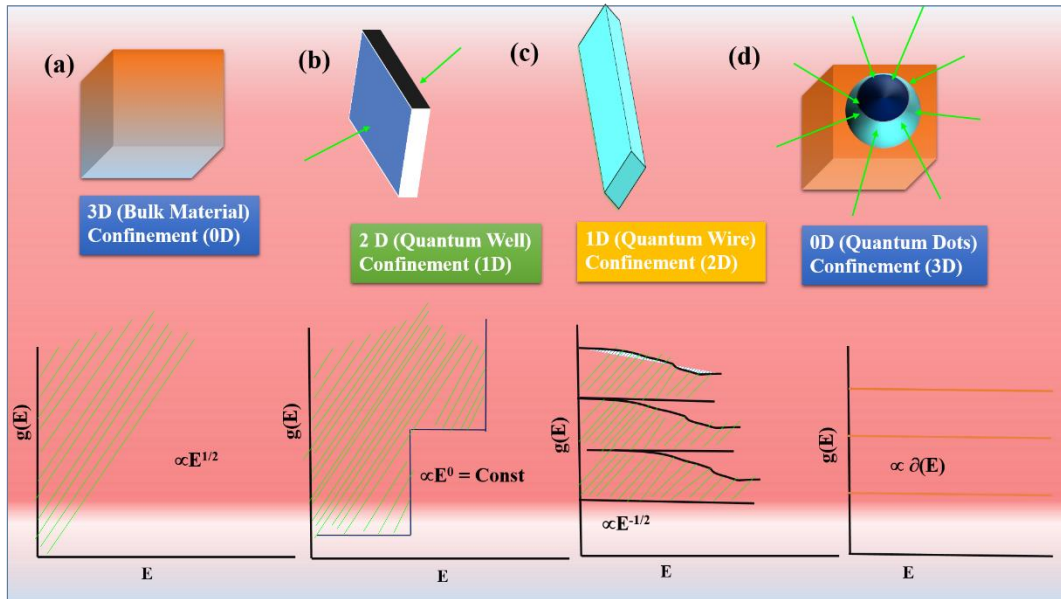


Figure 1.13: Quantum confinement of the nanomaterial with density functions.

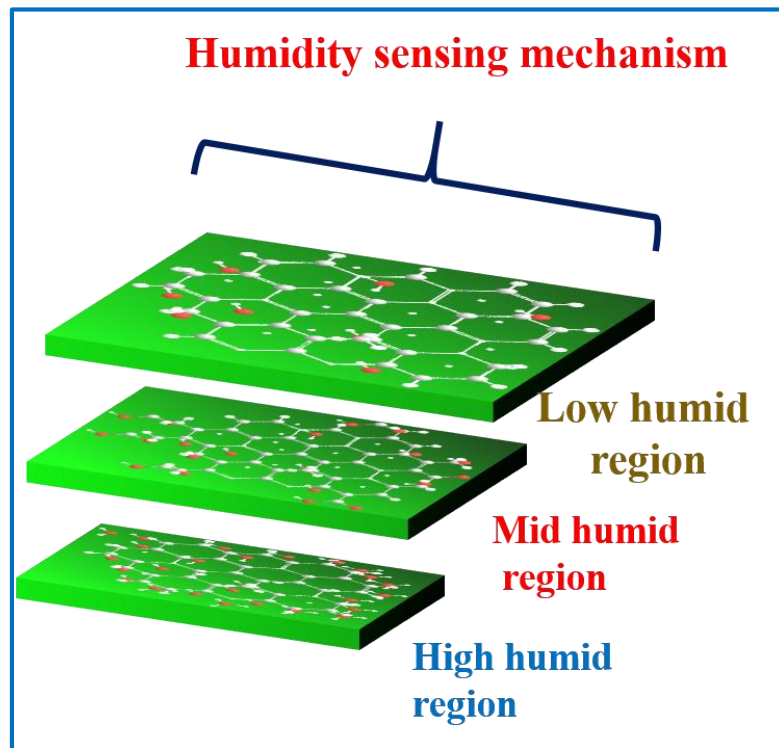


Figure 1.14: Quantum dots based humidity sensing mechanism.

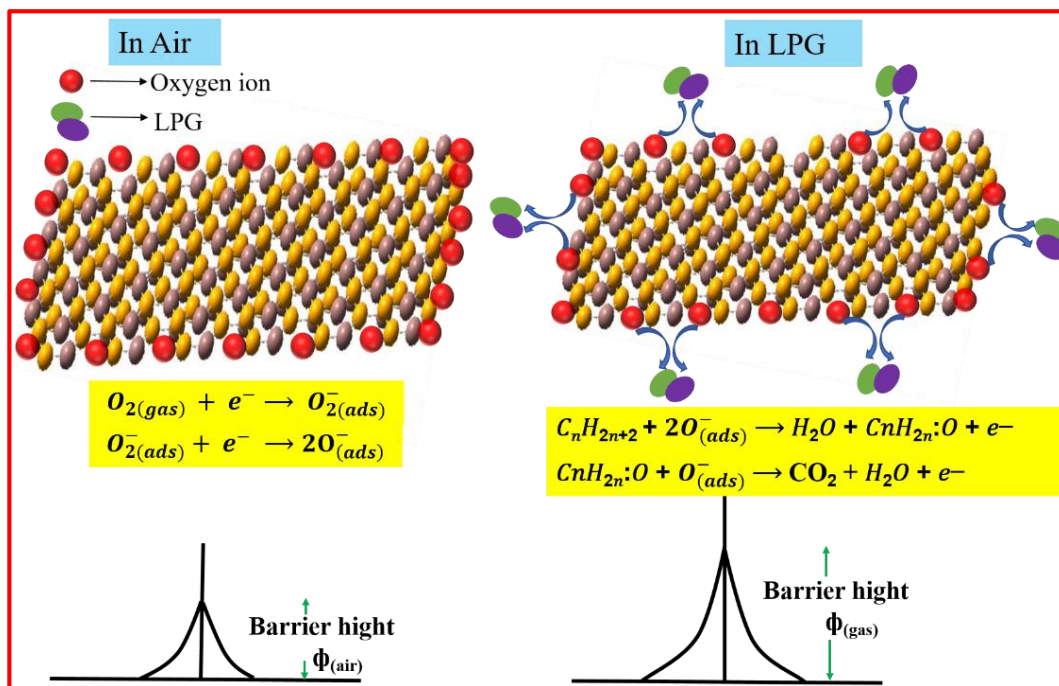


Figure 1.15: schamatic for LPG sensing mechanism.

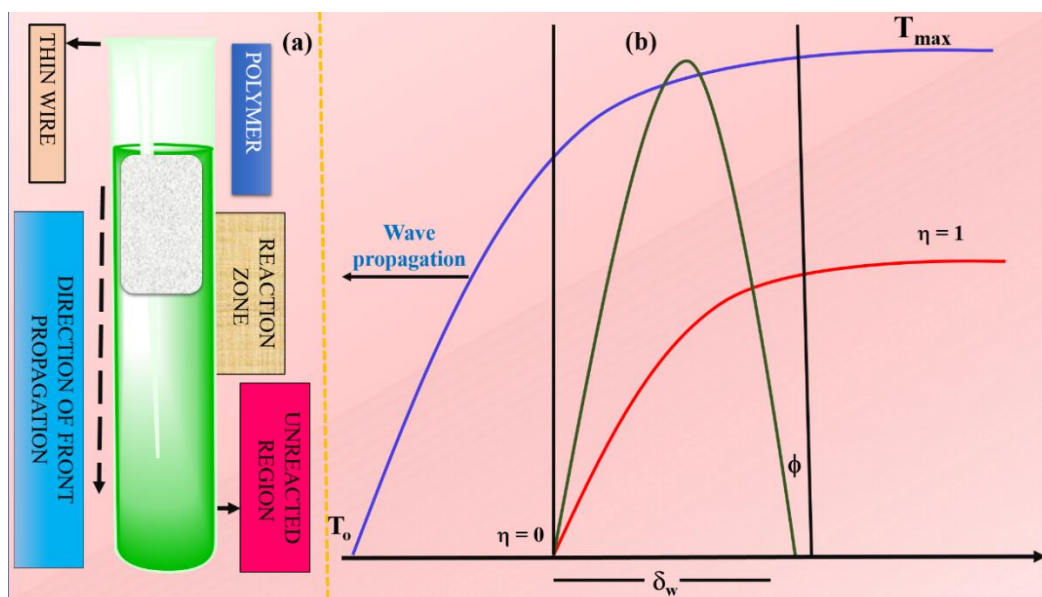


Figure 1.16: Frontal polymerization (left) and its three dimensional process.

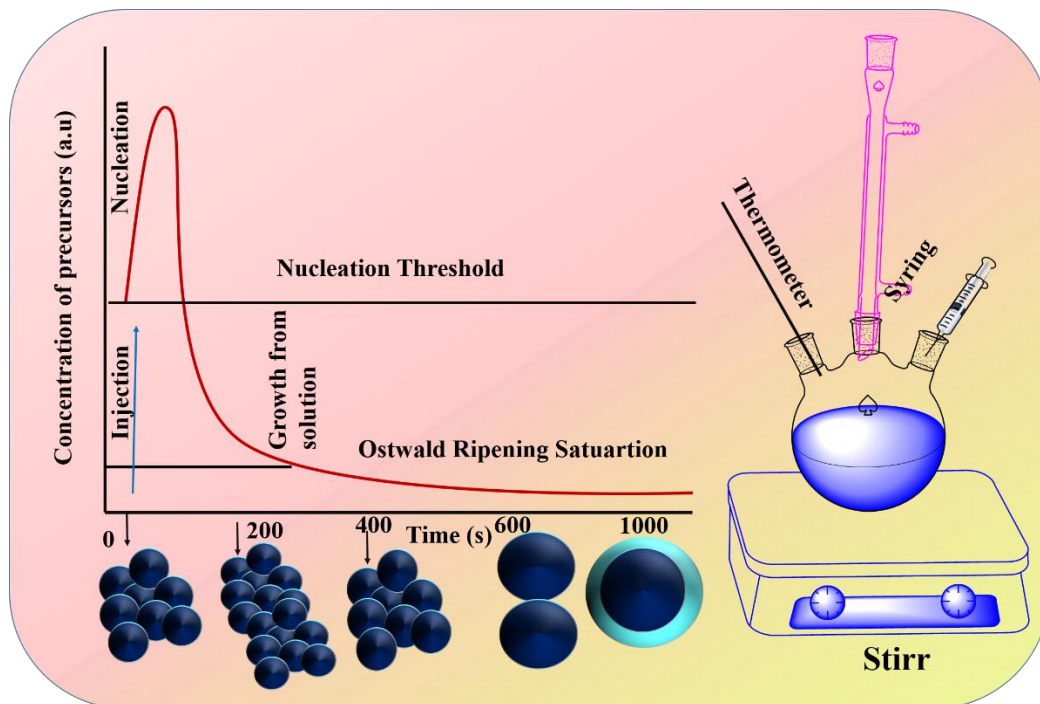


Figure 1.17: Schematic of the nucleation stage of quantum dots in the framework of the LaMer model (left), Representation of the simple synthetic apparatus preparation of quantum dots.

CHAPTER 2

Development of a reliable room temperature humidity sensor using nanostructured nickel polyacrylamide

The present chapter reports the nanostructured $\text{Ni}(\text{NO}_3)_2(\text{AAm})_4 \cdot 2\text{H}_2\text{O}$ thin film as an electrical humidity sensor. Films were created using the spin-coating method to investigate the adsorption/desorption of humidity at room temperature. The sensing element was investigated through X-ray diffraction (XRD), Scanning Electron Microscope (SEM), Transmission Electron Microscope (TEM) and UV-Vis absorption techniques. XRD exhibited the crystalline nature of the nanomaterial thin film and evaluated average crystallite size as 30 nm. SEM showed highly porous nanostructures of different sizes distributed throughout the film. The optical energy band-gap of the film was estimated as 4.03 eV. TEM image revealed the nanoparticles having sizes in the range of 4-21 nm and SAED confirmed the crystalline nature of the material. The film was further employed for electrical humidity sensing measurement, which gave a maximum average sensitivity of 37.79 $\text{M}\Omega/\%RH$ with response and recovery times of 15.15 sec & 75.25 sec at room temperature.

2.1 Introduction

Polymer gels are significant materials of fundamental and scientific concern. Currently, hydrophilic gels are referred to as "hydrogels" and they draw exceptional attention as absorbers showing their potential to perform absorption and desorption, thus ensuring their applicability in biomedical engineering [1-2]. Polyacrylamide (PAAm) gels are obtained by cross-linking copolymerization of acrylamide monomers. Since the monomers are solid during polymerization temperature [3-4], acrylamide based on hydrogels exhibits inhomogeneous cross-linking distribution. These are produced by the polymerization of acrylamide (C_3H_5NO) by the hydration of acrylonitrile. Experimentally [5-6] as well as theoretically [7-8] it has proved that PAAm has unique properties of being soluble in water and hence can be used for the treatment of industrial water. AAm is also dissolved in water. Using AAm as a ligand, new functional materials – metallopolymers composed of metal ions chemically bonded to a polymer chain – can be synthesized.

Polymer nanocomposites are cost-effective emerging materials and known for applications as gas/humidity sensors [9] working at room temperature. The acrylamide complexes of some transition metal nitrates $M(NO_3)_2 \cdot 4(CH_2=CHC(O)NH_2) \cdot 2H_2O$ were discovered and further characterized [10]. These materials undergo frontal polymerization. The structures of such compounds were studied with Co (II), Ni (II), Zn (II) and Cu (II) complexes [11]. The presence of double bond makes it possible for the complexes of acrylamide to polymerize. The solid-state chemistry of complexes $M(NO_3)_2 \cdot 4AAm \cdot 2H_2O$ ($M = Fe(III), Co(II), Ni(II), Zn(II),$ and $Cu(II)$) shows the behavior of the central atom and thus meaningfully influences the reactivity of the double bond of AAm [12]. Thus, frontal polymerization of metal nitrate complex originated, even though the reaction conditions were varied. Metal ions are well known for reserve polymerization processes [13]. These metal-containing polymers have various applications like solar cells, chips, and energy storage devices. Its applicability for sensors makes it a promising candidate for the detection of humidity.

Humidity is a sensible health parameter for human life, industrial processes and environmental balancing. Humidity has acquired such special attention because these vapours consist of highly reactive dipolar molecules which get condensed on or evaporate from the surface even with slight variations in the temperature of the

environment (this high polarity is due to the differences in electronegativity of the hydrogen and oxygen atoms) and hence controls almost all the environmental phenomenon. Therefore, humidity monitoring is quite essential for mankind.

Humidity sensors are transducers that give a signal for the amount of water (H₂O) vapour into measurable parameters in terms of %RH, absolute humidity, dew point etc. [14]. Therefore, the aim of present work is to synthesize nickel nitrate polyacrylamide using the Frontal polymerization technique and fabricate thin film for humidity detection at room temperature. An impedance-based electrical sensing set-up was used for measuring the humidity.

In the frontal polymerization technique [15], the confined zone of reaction propagates in an unstirred medium. The synthesis of polyacrylamide cross-linked with bisacrylamide provides information about the dense gels, which signifies the separation of levels. The majority of the research has concentrated on fluid monomers such as triethylene glycol dimethacrylate (TGDMA), methacrylic acid, and methyl methacrylate acid. Firstly, Pojman et al. reported in 1996 about the frontal polymerization and the transition metal-containing element nitrate polyacrylamide complexes [16] were discovered by Savostyanov et al. maintaining frontal propagation without the addition of an initiator. Fortenberry et al. considered in 1995 the effect of particle size dispersal and initial density on the front velocity and temperature [17-18]. Frontal polymerization synthesis has lots of advantages. High temperatures associated with frontal polymerization (> 200°C) can affect smaller reaction time and the capability to synthesize products that would phase-separate and retain longer reaction time. It is a well-ordered method where waste products can be reduced [19]. Frontal polymerization can be used to synthesize polyacrylamide materials cheaply, rapidly and without solvent [20-21].

2.2. Experimental details

2.2.1 Synthesis method

The solid-state polymerization of Ni(NO₃)₂·4AAm·2H₂O (acrylamide (CH₂=CH-CONH₂)) reveals that the nature of the central atom considerably influences the reactivity of the double bond of acrylamide (AAm) [10]. The thermal transformations of this metal-containing monomer yield a polymeric product.

Crystalline Ni (NO₃)₂·3H₂O was ground and mixed with acrylamide at a molar ratio of 1:5 and transferred into a test tube glowing with argon for one minute, after that the tube was sealed. After a certain time, the temperature of the reaction mixture dropped markedly and water was released. Then a thin wire or needle was used to transfer the desired water into the sealed tube containing the monomer and to release pressure. The monomer was dissolved in the tube containing water where the reaction propagated for 10 min. The process was repeated and polymerization took place. The resulting homogeneous blue paste was then obtained and dried in a desiccator over P₂O₅ for a day before being washed with benzene to remove the excess AAm. Elemental analysis data and some characteristics of the as-prepared Ni (II) nitrate acrylamide complex of transition metal nitrates are depicted in Table 2.1. The schematic for the frontal polymerization is shown in Fig. 2.1 whereas the flowchart for the synthesis is shown in Fig. 2.2.

2.2.2. Fabrication of sensing element

The films were deposited on glass substrates using a spin coating technique. For this purpose, these substrates were initially washed with laboratory detergent (Extran) followed by deionized water, isopropyl alcohol and acetone by plunging them in an ultrasonic cleaner (WUC-A02H) for around 15 min each. These cleaned glass substrates were dried in an electric oven (METREX) at a temperature of 100°C for 20 min. The obtained powder of Ni (II) nitrate PAAm was ground and dissolved in deionized water with sonication for 24 hrs to form a green gel. A small puddle of this gel was dropped on the substrate and spun at 1000 rpm using a spin coater to obtain a thin film of Ni nitrate PAAm. Finally, these films were dried on a hot plate (AMBASADOR) at 50°C for half an hour.

2.2.3. Sensing set-up

The electrical humidity sensing set-up based on impedance is shown in Fig. 2.3 which consists of a humidity-controlled glass chamber. The humidity was maintained by the static method using saturated aqueous solutions of K₂SO₄/KOH for humidification/dehumidification and %RH was measured using a standard hygrometer (HTC-1). Here the sensing element was fixed using silver electrodes which were further connected to the Impedance Analyzer (Wayne Kerr Precision Component Analyzer,

6440B) through connecting wires. The variations in %RH were measured in terms of electrical impedance and the corresponding sensing response is plotted in Fig. 2.9.

2.2.4. Characterization techniques

For the investigation of Ni (II) nitrate PAAm, various characterization techniques were employed to study its structure and morphology as a sensor. SEM (JEOL, JSEM-6490LV) analysis was carried out for the morphological investigation. TEM (FEI-G2 SPIRIT, Netherland) analysis of the dilute solution was done to reveal the structural information. Crystalline nature and phase formation were investigated using X-ray diffractometer X'Pert Pro recording system (PANalytical, Netherlands) by using CuK α radiation ($\lambda = 1.546 \text{ \AA}$). The Zeta nanosizer (Nano-ZS90) was used for obtaining the particle diameter. The UV-Vis spectrophotometer (Evolution 201) was used to obtain absorption spectrum and optical band-gap calculation. The thermal investigation was done using a Thermogravimetric analyser (PERKINELMER STA 6000).

2.3. Results and discussion

2.3.1 SEM Analysis

Morphological investigation of the film has been carried out at 5 μm and 1 μm scales using a Scanning Electron Microscope and is shown in Fig. 2.4 (a & b). It can be observed from the images that the surface exhibits highly porous morphology. The dimensions of these pores are several hundred nanometers. The porous voids on the surface act as active centers for the adsorption/desorption of water molecules, and hence are suitable for humidity detection.

2.3.2 TEM Analysis

A TEM image of Ni (II) nitrate PAAm at 200 nm scale is shown in Fig. 2.5 (a), where the inset displays the SAED pattern of the material. The magnification and voltage were $13000 \times$ and 200 kV. It can be observed from the figure that there are spherical grains. The minimum diameter of the grain is 4.5 nm. Also, the concentric rings observed by the SAED show the diffraction pattern. This regularity in diffraction pattern confirms the polycrystalline nature of the material where the minimum crystallite size as calculated from XRD is 4.8 nm, which is confirmed by TEM.

2.3.3 XRD analysis

Fig. 2.5 (b) depicts the XRD pattern of Ni (II) nitrate PAAm powder, which reveals its phase and formation. The instrument was operated using power: 45 kV, 40 mA and scanning parameters: from 20° to 60°; typical 2θ step size: 0.008°. The diffraction pattern shows good agreement with the diffraction data from JCPDS 45-0142. The diffraction peaks at 20.45°, 21.87°, 24.92°, 26.56°, 27.65°, 30.70°, 33.43°, 35.94°, 41.83°, 44.99° and 54.80° correspond to the lattice planes (201), (220), (31-1), (002), (112), (400), (42-2), (24-1), (200), (111) and (53-2) of Ni (II) nitrate PAAm crystals. The minimum crystallite size as calculated from Debye Scherrer Formula was 4.8 nm from (31-1) peak whereas the average crystallite size was found as 30 nm. Crystallite size plays a very important role in sensing as the decreasing aspect ratio provides more dangling bonds for the adsorption of water molecules.

2.3.4 Particle Size Analysis

The particle size distribution curve obtained from the Zeta nanosizer (Nano-ZS90) is shown in Fig. 2.6 (a). Here, the dilute solution of the precursor is analyzed by a dynamic light scattering system using the principle of Brownian motion of particles. The corresponding data is plotted and it can be observed that there are two ranges of particles. The minimum range of particles is between 3-23 nm and the other range of particles is between 90-250 nm.

2.3.5 UV–Vis absorption spectroscopy

The optical absorption spectrum of Ni (II) nitrate polyacrylamide film is shown in Fig. 2.6 (b). It can be observed from the figure that the material exhibits absorption in the ultra-violet range (< 350 nm). The variation of optical absorbance coefficient (α) relative to photon energy ($h\nu$) (known as Tauc plot) is shown in the inset of Fig. 2.6 (b). From this plot, the optical energy band gap of the material can be calculated using the relation given in Eqn. 2.1.

$$E_g = hc/\lambda - (\alpha h\nu)^{1/n} \quad \dots\dots\dots (2.1)$$

Where h is Planck's constant, ν is transition frequency, c is the speed of light and n , the exponent, characterizes the nature of band transition. The optical band-gap is calculated by extrapolating the straight-line part of the Tauc curve to $\alpha = 0$ and thus the estimated optical energy band-gap of the sensing element is obtained as 4.03 eV.

2.3.6 TG-DTA Analysis

According to the thermogravimetric (TG) curve, shown in Fig. 2.7 (a), the sharp changes at 304.6 °C, 317.01 °C and 462 °C devoted to the decomposition of bonds and breaking of intermolecular hydrogen bonding. The maximum portion of weight loss is between 230-650 °C where 25.22% of weight loss occurs till 400 °C and the major loss of 41.55% occurs till 650 °C. The product is formed at 650 °C. From the DTA curve as shown in Fig. 2.7 (b), the formation of polyacrylamide occurring through several peaks is confirmed. One peak at 81°C exhibits an endothermic reaction and the degradation is commenced at 120°C. The subsequent curve reveals the decomposition of the sample.

2.3.7 Electrical humidity sensing

Surface morphology is an important characteristic of the sensor. The electrical humidity sensing mechanism depends on the adsorption of water molecules on the porous surface of the sensing element and the conduction of H⁺ ions throughout the sensing surface [25]. The electrical humidity sensing response is shown in Fig. 2.8 (a-d). Fig. 2.8 (a) shows the humidity sensing characteristics at room ambient where impedance was plotted against the corresponding change in %RH from 10 to 90 %RH. Fig. 2.8 (a) shows that the %RH varies in three major regions: less humid (10-20 %RH), humid (20-75 %RH), and high humid (75-90 %RH). Initially, the chemical adsorption of water molecules takes place at the surface of the sensing element. Chemisorption occurs when Ni ions interact with water molecules to form hydroxide ions on the surface of a sensing element. In this process, two hydroxyl ions collected the water molecules, forming H₃O⁺ ions, and thus proton transfer began, i.e. water molecules collected on the sensing element's surface formed a chemisorbed layer performing proton conduction, and further propagation occurred via physisorption of water molecules forming weaker bonds. Here, the formula for the sensitivity is defined as

$$\text{Sensitivity} = \Delta I / \Delta \%RH * 100$$

where ΔI is the change in impedance and $\Delta \%RH$ is the change in %RH. Average sensitivity is calculated by taking the average of all measured sensitivities ranging from 10 to 90 %RH. Increasing the aspect ratio of the material is an important factor for a good sensor. The wide optical band-gap (4.034 eV) of material is also a very important

factor for desired sensitivity. Fig. 2.8 (a) shows that the maximum sensitivity of the sensing element is found as 37.77 M Ω /%RH in the range of 10 to 90 %RH.

The repeatability of results is also a very important factor for a good sensor. It can be determined by observing the output of sensing in the same environmental conditions frequently. Repeatability of the sensing element is shown in Fig. 2.8 (b) and it was found that the results were ~95% reproducible, which shows its relatively stable behaviour. The sensitivity observed over the entire range from 10-90 %RH, in this case, was 33.27 M Ω /%RH.

The other important parameter of the sensor is the ageing effect. It is the distribution of sensor outputs when performance is repeated under similar conditions after a long time. Here the ageing effect measurements were taken after three and four weeks and plotted in Fig. 2.8 (c). It was found experimentally that Ni(II)nitrate PAAM was moderately stable, having very less effect on ageing. Fig. 2.8 (d) shows the response and recovery times of the sensing element. The response time is defined as the time necessary to reach 10% of the final sensor output after stepwise adsorption of humidity, whereas the time taken by the sensing element to return to 10% of its initial value after a ramp-wise desorption is called as recovery time. The response and recovery times of the sensing element were calculated while measuring sensitivity and found as 15.1 and 75.2 sec respectively. The response time is fast as the film is most sensitive in the less humid range where recovery time is relatively slow as the film is less sensitive in the highly humid range. All the measurements were taken at room ambient (temperature ~300 K and atmospheric pressure 1 bar).

The electrical humidity sensing monitors the change in electrical impedance with respect to the change in humidity level. This phenomenon is well described via Grotthuss chain reaction and shown in Fig. 2.9. This chain reaction plays a vital role in the physisorption of water molecules on the surface of thin films. When this film is exposed to the humid environment, adsorption of the water molecules on its surface is initiated. The electrostatic interaction is so intense that it breaks one of the O-H bonds of the H₂O molecule and, consequently, metal ion M⁺ and OH⁻ are bonded chemically. Thus, the initial layer is chemisorbed. The hydronium ion, H₃O⁺ is formed during the decomposition of water molecule which acts as a charge carrier. In the higher humidity range, H₃O⁺ ions will further hydrate into H⁺ ions and H₂O molecules. This H₂O

molecule is weakly bonded with one of the hydroxyl groups. Therefore, at room temperature and in a humid atmosphere, protons are the dominant charge carriers. The number of physisorbed water layers and hence the concentration of H^+ ion increases with the increase of water vapor. With the increase in humidity, the charge carriers in the form of hydronium ions also increase consequently. In high humid regions, water condensation occurs inside pores and a high decrease in impedance is observed.

2.4 Conclusion

We successfully investigated the humidity sensing ability of Ni (II) nitrate PAAM complex and used it in electrical humidity sensing based on impedance variation. The crystalline nature of the material was confirmed by XRD analysis. The minimum crystallite size as calculated from the Debye Scherrer formula was 9 nm and the average size was 13 nm. This polycrystallinity was revealed using TEM (SAED) and crystallite size was evaluated using a Particle Size Analyzer. A wide optical band-gap of 4.03 eV was found by the UV-vis Spectrophotometer. The average sensitivity of the film was found as 33.27 $M\Omega/\%RH$ for impedance-based humidity sensing. The response and recovery time for the electrical mode calculated as 15.11 sec and 75.25 sec. Also, the ageing trial confirmed that the material was quite stable after a long time.

References

- [1] H.J. Nachash, O. Okay, Formation and Structure of Polyacrylamide Gels, *J. App. Polymer Sci.* 60 (1996) 971-979.
- [2] J.C. Eloi, L. Chabanne, Metallopolymers with emerging applications, *Mater. Today* 11(2008) 28–36.
- [3] O. Okay, Kinetics of gelation in free radical crosslinking copolymerization, *J. Polymer* 35 (1994) 2613-2618.
- [4] K.B. Girma, V. Lorenz, S. Blaurock, F.T. Edelmenn, Coordination chemistry of acrylamide, *Coord. Chem. Rev.* 249 (2005) 1283–1293.
- [5] J.P. Baker, L.H. Hong, H.W. Blanch, J.M. Prausnitz, Recent advances in polymers and composites, *Macromolecules* 27 (1994) 1446.
- [6] N. Weiss, T.V. Vliet, A. Silberberg, Permeability of heterogeneous gels, *J. App. Polymer Sci.* 17 (1974) 2229–2240.
- [7] S. Iwatsuki, T. Itoh, Amphoteric Behavior of Tetrakis (methoxycarbonyl) quinodimethane in Alternating Copolymerizations with Various Comonomers, *Adv. Polym. Sci.* 13 (1980) 983-989.
- [8] S. Palaniappan, D.N. Sathyanarayana, Polymeric charge-transfer complexes: a study by electronic absorption spectroscopy, *J. Polymer* 31 (1990) 1401-1405.
- [9] S. Sikarwar, A. Kumar, B.C. Yadav, G.I. Dzhardimalieva, N.D. Golubeva, Nanostructured spherical-shaped Sc(III) Polyacrylate for monitoring the moisture level, *IEEE Sensors* (2018).
- [10] S. Singh, B.C. Yadav, P. Tandon, M. Singh, A. Shukla, G.I. Dzhardimalieva, S.I. Pomogailo, N.D. Golubeva, A.D. Pomogailo, Polymer-assisted synthesis of metallopolymer nanocomposites and their applications in liquefied petroleum gas sensing at room temperature, *Sens. Actuators B: Chem.* 166 (2012) 281–291.
- [11] A.D. Pomogailo, V.S. Savost'janov, *Synthesis and Polymerization of Metal-Containing Monomers*, CRC Press, Boca Ration, (1994) 164.

- [12] S.I. Evstratova, B.M. Zuev, G.I. Dzhardimalieva, Abstracts of Papers, The 218th ACS National Meet, New Orleans, 74 (1999).
- [13] S.I. Evstratova, G.V. Shilov, G.I. Dzhardimalieva, A.D. Pomogailo, I.E. Uflyand, S.M. Aldoshin Copper (II) Nitrate Complex with Acrylamide: Synthesis and Crystal Structure, *Russ. J. Coordination Chem.* 27 (2001) 35–737.
- [14] S. Sikarwar, B.C. Yadav, Opto-electronic humidity sensor: a review, *Sens. Actuators A: Phy.* 233 (2015) 54-70.
- [15] D. Fortenberry, J.A. Pojman, Solvent-free synthesis of polyacrylamide by frontal polymerization, *J. Polymer Sci. Part A: Polymer Chem.* 38 (2000) 1129-1135.
- [16] J.A. Pojman, V.M. Ilyashenko, A.M. Khan, Free-radical frontal polymerization: self-propagating thermal reaction waves, *J. Chem. Soc. Faraday Trans.* 16 (1996) 2825-283.
- [17] J.A. Pojman, J. Willis, D. Fortenberry, V. Ilyashenko, A.M. Khan, Factors Affecting Propagating Fronts of Addition Polymerization: Velocity, Front Curvature, Temperature Profile, Conversion, and Molecular Weight Distribution, *J. Polymer Sci. Part A: Polym Chem.* 33(1995) 643–652.
- [18] I.P. Nagy, L. Sike, J.A. Pojman, Thermochromic composites and propagating polymerization fronts, *Advanced Materials* 7 (1995) 1038–1040
- [19] D.I. Fortenberry, A. Khan, V.M. Ilyashenko, J.A. Pojman, In *Synthesis and Characterization of Advanced Materials*, ACS Symposium 681, M.A. Serio, D.M. Gruen, R. Malhotra, Eds. American Chemical Society: Washington, DC (1998) 220–235.
- [20] J.A. Pojman, D.I Fortenberry, V. Ilyashenko, "Frontal Polymerization as an Analog of SHS, *Int. J. Self-Propag. High-Temp. Synth.* 63(1997) 55-376
- [21] D.I. Fortenberry, J.A. Pojman, Solvent-Free Synthesis of Polyacrylamide by Frontal Polymerization, *Polymer Sci.: Polymer Chem.* 38 (2000) 1129–1135.
- [22] H.R. Li, Solution polymerization of acrylamide using potassium persulfate as an initiator: kinetic studies, temperature and pH dependence, *Euro. Polymer J.* 37 (2001) 1507-1510.

- [23] S. Sikarwar, B.C. Yadav, S. Singh, G.I. Dzhardimalieva, S.I. Pomogailo, N.D. Golubeva, A.D. Pomogailo, Fabrication of nanostructured yttria stabilized zirconia multilayered films and their optical humidity sensing capabilities based on transmission, *Sens. Actuators B: Chem.* 232 (2016) 283–291.
- [24] P. Chaudhary, S. Sikarwar, B.C. Yadav, G.I. Dzhardimalieva, N.D. Golubeva, I.E. Uflyand, Synthesis and characterization of copper (II) nitrate polyacrylamide & its application as opto-electronic humidity sensor, *Sens. Actuators A: Phy.* 263 (2017) 415–422.
- [25] S. Kozhukharov, Z. Nenova, T. Nenov, N. Nedev, M. Machkova, Humidity sensing elements based on cerium doped titania-silica thin films prepared via a sol–gel method, *Sens. Actuators B: Chem.* 210 (2015) 676–684.

Tables:

Table 2.1 Elemental analysis data of Ni(II) nitrate AAm complex

Complex	Color	T_m , K	Elemental analysis, wt % (found/calcd)			
			C	H	N	Mt
Ni(NO ₃) ₂ ·(AAm) 4. 2H ₂ O	Light green	351–352	28.6 /29. 7	4.8/5. 2	16.7/15. 2	11.7/11. 1

Figures:

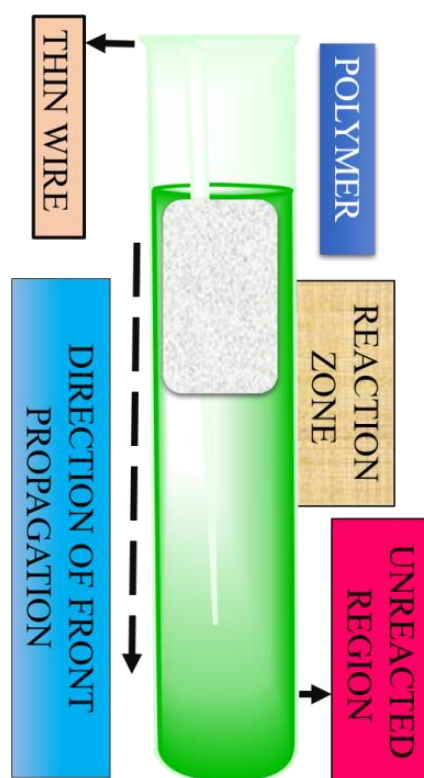


Figure 2.1 Schematic for frontal polymerization reaction technique.

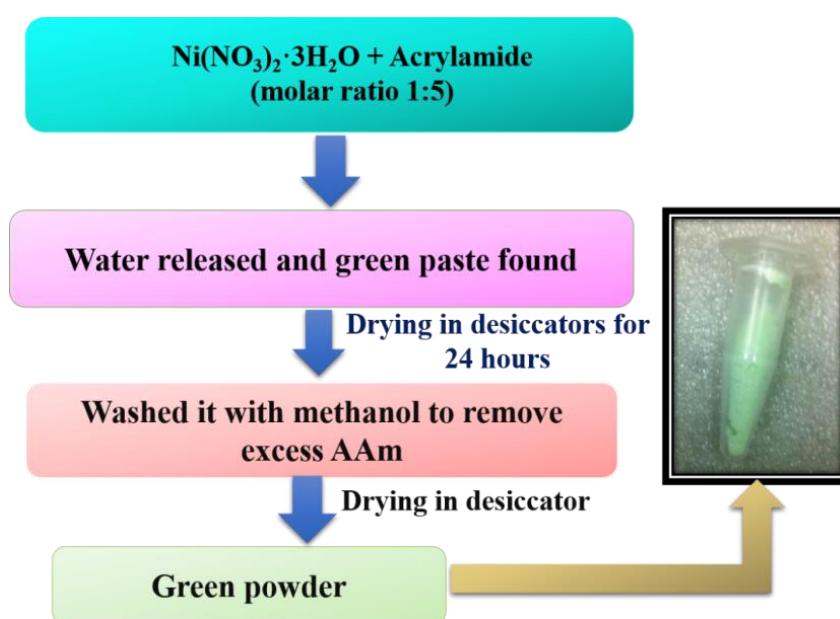


Figure 2.2 Block diagram for synthesis of Ni(II) nitrate polyacrylamide (PAAm)

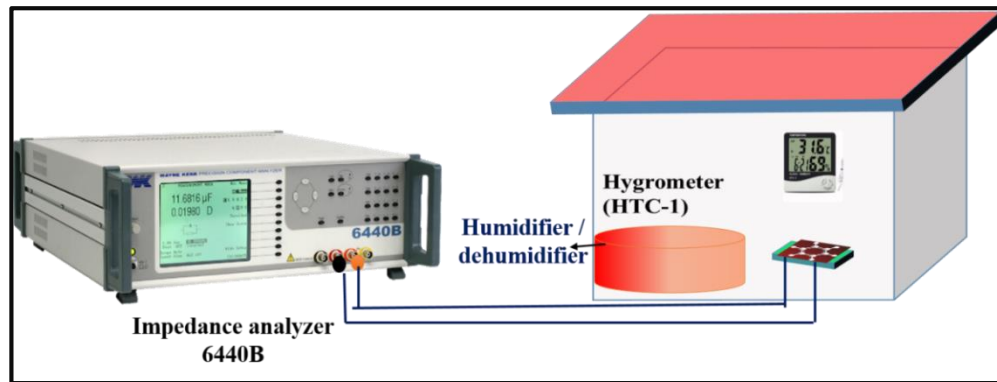


Figure 2.3 Schematic of the experimental set-up for the electrical humidity sensor.

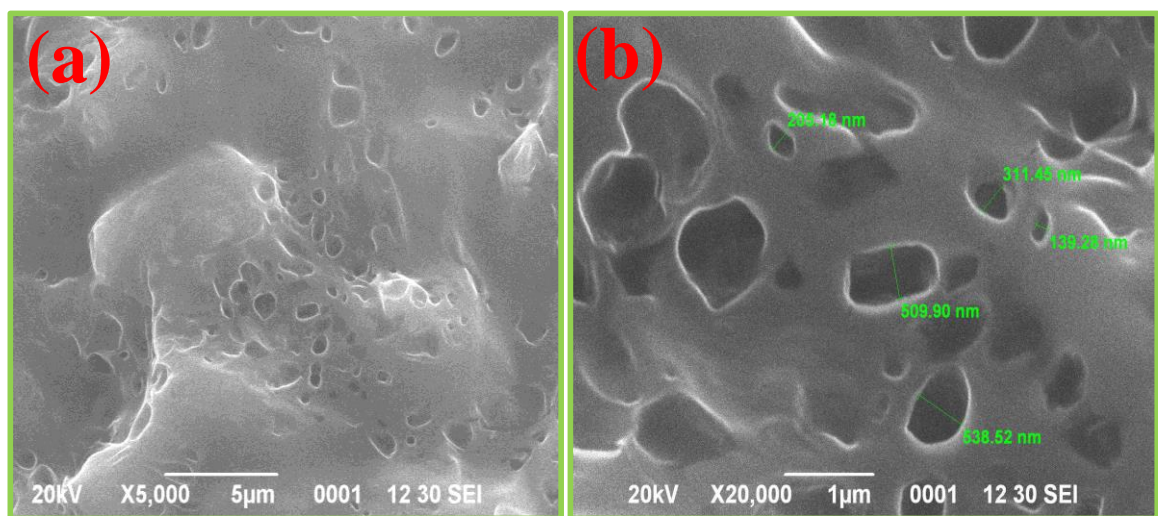


Figure 2.4 SEM image showing surface morphology of nickel nitrate polyacrylamide at (a) 5 μm and (b) 1 μm scales presenting porous nature.

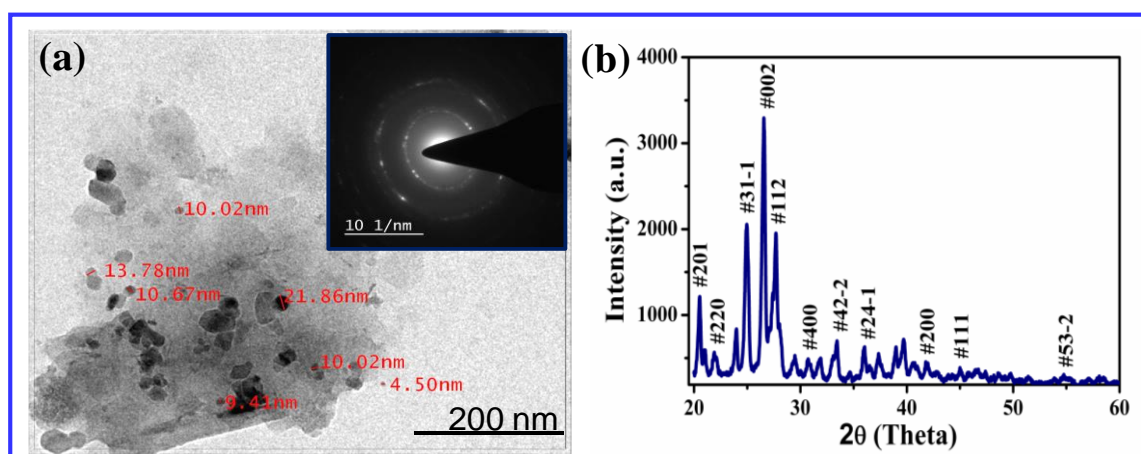


Figure 2.5 (a) TEM image of Ni(II)nitrate PAAM where the inset shows the diffraction pattern of atoms obtained by SAED (b) Powder XRD pattern of Ni(II)nitrate PAAM

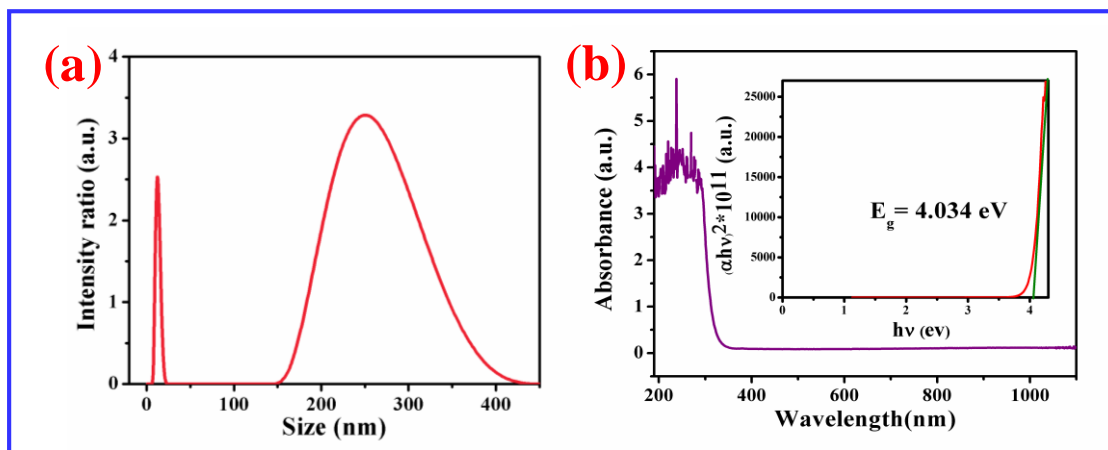


Figure 2.6 (a) Particle size distribution curve obtained from Nano-ZS90 showing the minimum range of particles between 3-23 nm (b) The absorption spectrum along with Tauc plot of the Ni(II)nitrate PAAm film where the estimated optical energy band-gap is 4.03 eV.

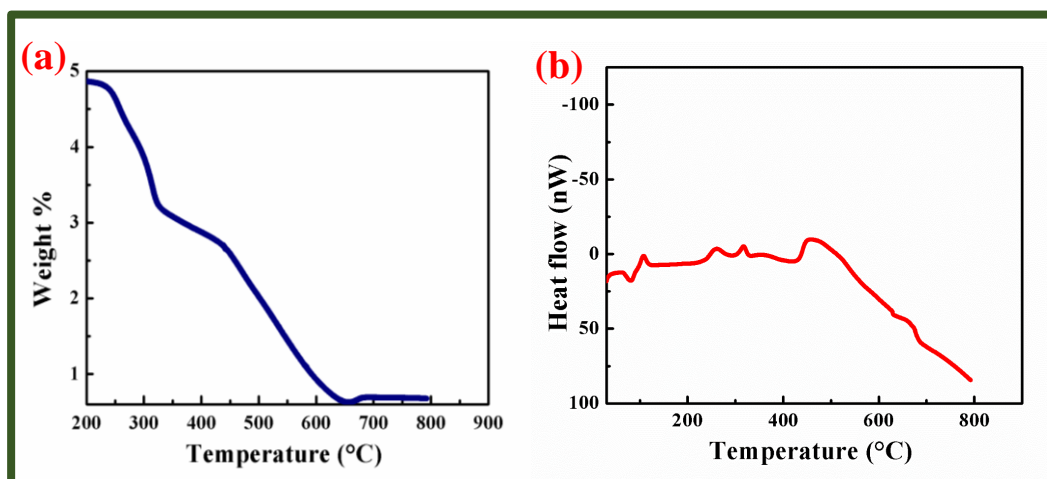


Figure 2.7 The graph between temperature (°C) and (a) weight% showing the TGA; (b) heat flow (nW) showing the DTA of the material

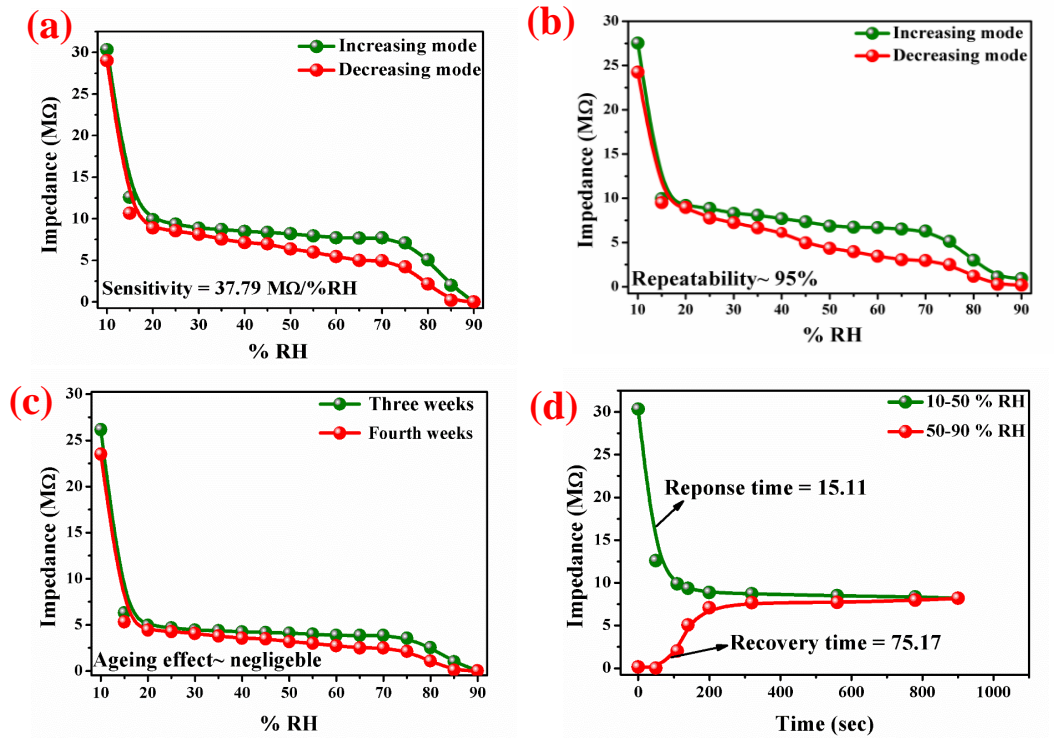


Figure 2.8 Variation of impedance in accordance with %RH to show (a) sensing response (sensitivity of 37.79 MΩ/%RH), (b) repeatability test (c) Ageing effect after 3 and 4 weeks, and (d) response time (15.1 s) and recovery time (75.2 s).

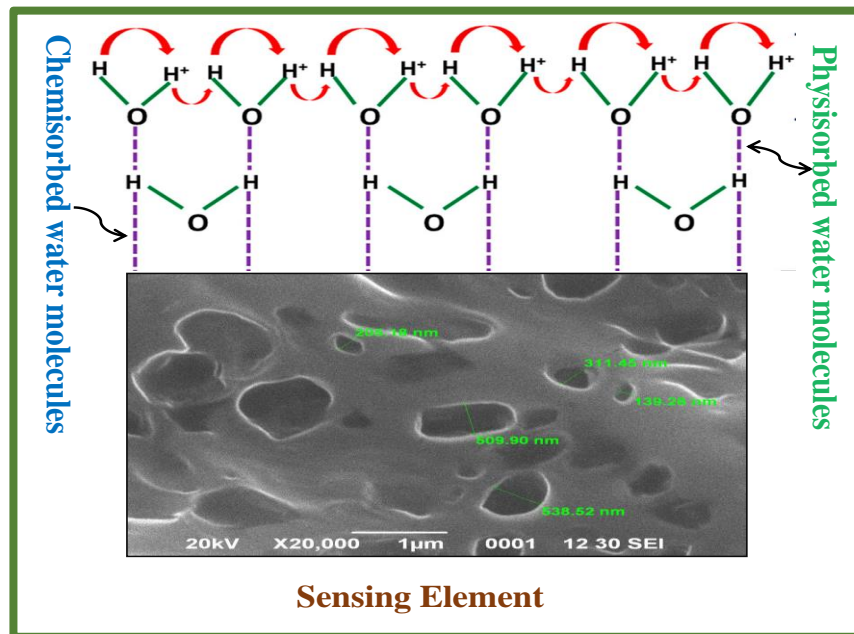


Figure 2.9 Schematic of Grotthuss chain reaction showing the interaction of surface morphology with humidity

CHAPTER 3

Polyacrylamide decorated CdS nanoparticles based flexible humidity sensor for baby diaper alarm: Experimental and theoretical study

Solvent-free synthesis of nanocomposite for humidity sensor is gaining immense interest to fulfill the criteria for its practical application. Herein, present chapter reports the development of CdS/ polyacrylamide nanocomposite as a flexible humidity sensor, which has been fabricated by the facile spin-coating technique on PET (polyethylene terephthalate) substrate. Morphological, optical and crystalline nature of CdS/polyacrylamide nanocomposite were investigated using SEM, TEM, XRD, DSC, FTIR, UV-Visible and Particle size analysis. Characteristic surface area and pore volume were estimated using BET analysis whereas the hydrophilicity of the sample was investigated using contact angle measurement. As fabricated sensor showed an outstanding humidity sensing response with good linearity in the humidity ranging from 11 %RH to 95 %RH. The average sensitivity of nanocomposite was calculated as 125.57 nF/%RH and may be utilized for moisture detection in commonly used baby diaper with alarm. The simulated & optimized computer model of the synthesized composite (CdS & Polyacrylamide) using density functional theory was performed and analyzed. HOMO-LUMO and correspondingly obtained other electronic parameters were studied, which revealed that band gap of the synthesized composite material tends to decrease upon increasing the level of water molecules owing to better humidity sensing mechanism, and therefore it is applicable for commercial humidity sensor.

3.1 Introduction

Humidity sensing plays a crucial role in monitoring all physical and biological processes in human life. Balancing the concentration of water vapour present in the environment as well as inside the human body is crucial for its functioning [1]. Presently, several kinds of humidity sensors are trending for their multifunctional applications such as switch-based sensing devices, breath analyzers and skin touched humidity sensors. Proper surveillance on the diaper wetting process is important to assess the humidity level inside baby diapers [2]. Such application requires a sensor with high sensitivity, long-term stability, low response and rapid recovery times with ease in the synthesis methods [3].

Multifunctional application of humidity sensor particularly for baby diaper should inherit the characteristics: (i) disposable and recyclable (ii) flexible (iii) nontoxic (iv) humidity monitoring at low detection limit (v) environment friendly and cost-effective [4]. Hence, our priority is to choose the sensing material which is a good absorber for water molecules [5]. For this purpose during the previous few years, the preparation of polymers like polystyrene, polyacrylamide, sodium alginate, and chitosan for instance the matrix to maintain mineral nanoparticles were involved with wide consideration [6,7].

From the recent reports, it can be stated that existing humidity sensors have two primary concerns; first, less sensitive with high response & recovery time and secondly, high working temperature [8,9]. Presently reported humidity sensors are suffering from the incapability of sensing at higher temperatures [10]. At room temperature, humidity sensors are not highly sensitive for the full range (10-95 %RH). Acrylamide polymer gel is a three-dimensional network with a high length structure. The high hydrophilicity and water adsorbing capacity of polyacrylamide play an important role in humidity detection [11]. The polymer matrix may be bulk, microstructure or nanoparticles. The hydrogels are composed of water-soluble hydrophilic polymer chains with 3D network structures linked to each other from side to side with covalent bonds or electrostatic, van der Waal and hydrogen bonding, etc [12,13]. The hydrogels are hydrophilic due to the presence of functional groups as –COOH, –SO₃H, –NH₂, –OH, and –CONH₂ which increase the adsorption capacity of the macromolecules and these functional groups are intensely bind with metal ions

[14]. Owing to these structures, the hydrogels are made available for a unique property, water adsorbed material from the environment [15]. The metal nanomaterials are responsible for stability and enhance the surface morphology of the macromolecules. Instead of these, hydrogels also have good biocompatibility and environmental friendliness properties, consequently, they showed potential in many applications such as in biomedical fields, sensors, photocatalytic activity, and purification processes [16,17].

Here, the synthesis of a condensed phase of the metallopolymers by frontal polymerization has been reported in detail [18,19]. The frontal polymerization technique is mainly employed for the conversion of monomers to polymer in a confined reaction region under the multi-level system, which proceeds above the whole volume. The interaction of acrylamide (AAm) with metal nitrate complexes during Frontal polymerization are $Mt(NO_3)_x \cdot 4AAm$, where $Mt = Fe(III), Bi(III), Y(III), x = 3; Cu(II), x = 2; Mt(NO_3)_2 \cdot 4AAm \cdot 2H_2O$, where $Mt = Co(II), Ni(II), Zn(II), Cd(II), Mn(II), Ba(II), Pb(II); Pd(NO_3)_2 \cdot 2AAm$. This method is widely used to prepare a solvent-free and rapid synthesis of metal-monomer [20]. This synthesis method uses the exothermicity of polymerization technique whereas metal nitrate as starting material. In this direction, the first stage might include the combination of the dislocation of the chemical conversion front along with the combination of reagents in conjugate reactions by the known reactions of organic and inorganic formation routes. During this process, the metal-monomers can assist as a front reactor zone [21].

Flexible humidity sensor devices are gaining immense interest in modern sensing applications [22]. Flexible electronic substrates like polyethylene terephthalate (PET), have attracted special attention due to their special advantage as wearable, light weight, good mechanical stability, and unambiguous structural properties. ITO coated PETs are also showing excellent electronic properties [23]. PET substrates are highly flexible and cheaper, mainly derived from plastic carbon-based. Previous researches on flexible substrates were established [22] with various fabrication methods (Inkjet-printing, lithography, spin coating).

In this chapter, we present CdS polyacrylamide nanocomposite as a humidity sensor (baby diaper water level detection and wetting process). The metal nanoparticles by the simple chemical route and then polymerization of

macromolecules via frontal polymerization techniques are incorporated for controlling the chain of acrylamide during the polymerization. The ITO-coated PET substrate was used, which is more efficient for flexible humidity sensors based on capacitive structure. The synthesized composite (CdS & Polyacrylamide) was simulated & optimized by using the computer model of density functional theory. HOMO-LUMO and correspondingly obtained other electronic parameters were studied, which revealed that the bandgap of the synthesized composite material tends to decrease upon increasing the level of water molecules owing to better humidity sensing mechanism, and therefore it is apt for electrical humidity sensing.

3.2 Synthesis method

CdS-polyacrylamide nanocomposite is synthesized by solvent-free Frontal polymerization technique. Initially, cadmium nitrate ($\text{Cd}(\text{NO}_3)_2$) and host monomer acrylamide $(\text{CH}_2\text{CHCONH}_2)_4(\text{H}_2\text{O})_2$ were mixed with thiourea (sulphur source), as prepared mixture was transferred in a glass tube to perform frontal polymerization. Ammonium persulfate ($(\text{NH}_4)_2\text{S}_2\text{O}_8$) was used as an initiator for the polymerization which upon addition turn the white appearance to a yellowish form. The collected powder was washed with ethanol and ether several times in order to remove excess acrylamide. Thus, obtained powder was kept drying in an inert atmosphere giving a CdS-polyacrylamide nanocomposite fine yellowish powder.

The chemical reaction involved during the synthesis is shown in Fig. 3.1:

3.2.1 Experimental Set-up

The set-up for assessing the humidity sensing capability of sensing material is well displayed in Fig. 3.2, which consists of an impedance analyzer (Wayne Kerr Precision Component Analyzer, 6440B), Keithley (6517 B) based graphical user interface for plotting humidity sensing characteristics at different humidity levels. The water vapour content inside the chamber was retained by the static process using saturated aqueous solutions of K_2SO_4 / KOH [20]. Precise measurement of relative humidity (%RH) was done using a hygrometer (HTC-1). Silver paste based interdigitated electrodes were imprinted on the sensing film, connected through the wires with an impedance analyzer. The whole sensing experiment was performed at an ambient temperature.

3.2.2 Fabrication of sensing element and physical characterization:

Fig. 3.3 shows the procedure for fabrication of the PET-based flexible humidity sensor. The deposition of sensing material over PET substrate was carried out by using the spin coating method. The sensing film was further dried at 30°C for 20 min before its use for humidity sensing. The two-point contacts (electrodes) were made using silver paste on the PET substrate with an intermediate distance of 1 mm. As fabricated sensing film on PET substrate exhibited a better adhesion compared to the glass and FTO based substrate which confirmed better compatibility towards flexible device applications [24].

The surface texture of sensing material has been carried out by using FESEM (FEI Nova NanoSEM 450), analysis. Average particle size distribution was estimated from particle size analysis (Nano-ZS90 Malvern Instruments, UK). The porosity and surface area were investigated by BET analysis (BELSORP-Mini II, Japan). The crystallinity of the CdS and CdS-Polyacrylamide nanocomposite were investigated using High-resolution Transmission Electron Microscopy (HRTEM) (JEOL-2100 F and FEIG2 SPIRIT, Netherland) and X-ray Diffractometer, X'Pert Pro recording system (PANalytical, Netherlands). The thermal analysis of nanocomposite was performed using a Thermogravimetric analyzer (PERKINELMER STA 6000).

3.3 Results and Discussion

3.3.1 Morphological analysis (Field emission scanning electron microscopy)

FESEM images of CdS-Polyacrylamide nanocomposite with different magnifications are shown in Fig. 3.4 (a-d). The presence of cubical structure in the branch like arrangement can be easily seen from Fig.3.4 (a). A magnified image of the sample confirms the formation of ideal cubical shaped nanostructures in Fig. 3.4 (b). The possible reason for the uniaxial growth in the form of a cube can be accounted on the basis of nucleation of the material in an upward direction due to low- pressure zone. Thus, cubical nanostructure provides a high surface area in the form of active adsorption sites responsible for the high sensitivity of the sensing film. The presence of unsaturated moieties on the surface of CdS-Polyacrylamide nanocomposite facilitates fast adsorption and desorption of water molecules over the sensing film.

3.3.2 Particle Size analysis:

The variation in particle size is plotted using Zeta nanosizer and is well shown in Fig. 3.5 (a). The aqueous solution of CdS-Polyacrylamide was ultrasonicated for 30 min and further subjected to the DLS (dynamic light scattering) analysis. The distribution of the size of nanoparticles is plotted with an appearance of three major peaks. The consecutive peak range of nanoparticles was found at 3.4 nm, 11.2 nm and 69.4 nm.

3.3.3 BET (Brunauer–Emmett–Teller) analysis:

The surface area and characteristic pore volume of synthesized CdS nanocomposite were measured using the Brunauer–Emmett–Teller analysis. Fig. 3.5 (b) shows the nitrogen adsorption and desorption isotherm with the characteristic distribution of pore volume (inset Fig.3.5 (b)). From BET analysis, the specific surface area (S), pore volume (V_p), and pore diameter (D_p) were estimated as $58.33 \text{ m}^2\text{g}^{-1}$, $16.878 \text{ m}^2\text{g}^{-1}$, and $0.1974 \text{ cm}^3\text{g}^{-1}$ respectively. This surface area of nanocomposite is essentially enthusiastic to the branch associated with cubes structured morphology.

3.3.4 FTIR Analysis:

FTIR spectra of as developed polymer nanocomposite is exhibited in Fig. 3.5 (c). The presence of surface groups and the absorption bands are observed in form of stretching vibrations of the hydroxyl group ($-\text{OH}$) at 3449 cm^{-1} and amine groups (NH_2) at $3210\text{--}3352 \text{ cm}^{-1}$. Peaks at 2927 cm^{-1} and 2409 cm^{-1} are the signatures of $-\text{CHO}$ and CH_2 functional groups at the surface. Availability of other functional groups such as ketone ($\text{C}=\text{O}$), amine (N-H), C-O , C-C , and $-\text{C-N}$ (nitrile) were also confirmed from FTIR peaks. These groups were solely responsible for enhancing the surface activity of the sensing material and improving the sensing capability of CdS-Polyacrylamide nanocomposite.

3.3.5 TEM and HRTEM analysis:

Fig. 3.5 (d) and (e) depicts the TEM and HRTEM images of the CdS-Polyacrylamide solution at 100 nm scale comprising bulk particles with a size of about $\sim 20\text{--}60 \text{ nm}$. At a 20 nm scale, it can be observed that the metal is decorated over the host polymers which confirms the polycrystallinity of the sample.

3.3.6 XRD analysis:

The XRD patterns of CdS-Polyacrylamide is shown in Fig. 3.5 (f). From the diffraction pattern, it's obvious that polyacrylamide has a major diffraction peak at $2\theta = 26.4^\circ$ which corresponds to the plane (111) as confirmed from the standard diffraction pattern (JCPDS No. 10-454). The diffraction peaks at 27.1° , 42.6° and 52.4° belong to the (111), (220) and (311) planes respectively [25]. The appearance of noise depicts the amorphous and polycrystalline nature of the CdS-Polyacrylamide nanocomposite.

3.3.7 X-ray photoelectron spectroscopy (XPS) Analysis:

The chemical composition of CdS-Polyacrylamide nanocomposite is confirmed by analyzing XPS spectra. XPS spectra of CdS-polyacrylamide and recorded data are shown in Fig. 3.6 (a-i). The binding energies of the Cd, S, C, N and O elements with their equivalent atomic weight % are displayed in Fig. 3.6 [26]. The full scan of XPS spectra is displayed in Fig. 3.6 (a). The characteristic peaks of cadmium and sulphide are displayed in Fig. 3.6 (b & c) which correspond to binding energies 405, 412, 162 and 168 eV. Cadmium and sulphur are having two states of energy levels i.e., oxidation states of $Cd_{d5/2}$, $Cd_{d3/2}$, $S_{2P3/2}$ and $S_{2P1/2}$. XPS spectra reveal the presence of C, O and N in CdS-Polyacrylamide. The C-O peak exhibits binding energy of corresponding energies of 532 eV whereas the (C-C, C-O) and (O-C-O) corresponds to the binding energy value of 285 eV shown in Fig. 3.6 (d-e). The presence of nitrogen is also shown in Fig. 3.6 (f) and the binding energies are found to be 400 eV and 402 eV [27]. Fig. 3.6 (g and i) corresponds to the histogram plot of atomic weight %, binding energies and peak respectively.

3.3.8 Electrical Humidity-Sensing Performance

The humidity sensing characteristics of CdS-Polyacrylamide based sensor is measured at an ambient temperature. Saturated salt solution of K_2SO_4 and KOH solutions were used to maintain the humidity level inside the glass chamber [28]. K_2SO_4 solution was used to increase the %RH concentration of the flexible sensing element and KOH was used to decrease the %RH concentration of the sensing element [29]. Fig. 3.7 (a) shows the variation of sensing film resistance with time at different humidity concentrations. It is evident from the plot that the resistance offers

by the sensing film is increasing with increasing the humidity level (10 % to 95 % RH) over a span of time.

The corresponding capacitance and impedance values at each humidity level were recorded using an impedance analyzer. Variation of capacitance corresponding to %RH is also plotted when subjected from lower to higher frequencies (20 Hz, 100 Hz, 3000 Hz, 8000 Hz, and 10000 Hz) and are well displayed in Fig. 3.7 (b). It is clear from the curve that the capacitance increases with humidity but decreases with the increasing frequencies [30]. The respective variation of capacitance with %RH were recorded for both increasing and decreasing processes. From Fig 3.7 (c), it can be observed that the relative (%RH) drastically varies from 32 %RH to 95 %RH, capacitance rate rises monotonically in the same manner. Inside the humidity chamber, the relative humidity rises with the capacitance of the CdS-Polyacrylamide based sensor and extended a higher capacitance value [31].

The accountable reason for this sensing characteristic is the adsorbed water molecules present on the surface, which allows the polarization resulting in an enhanced dielectric constant of the sensing material. This phenomenon affects the nature of capacitance [29]. It can be seen from curve given in Fig. 3.7 (b) that in all frequencies, the best linearity was found in 45 %RH to 95 %RH for sensing characteristics, at the lowest frequency of 20 Hz. The value of capacitance varies with relative humidity in all frequency regime, but in the higher frequency regime, the drastic change in the value of capacitance is negligible and because self-governing of humidity [32]. The humidity level can be seen infecting at lower frequencies beyond 10000 kHz. As reported in previous work, the ideal capacitive sensor should inherit the characteristics i.e. capacitance is independent of applied frequency. In low humidity levels, the adsorption of water molecules is very less, which acts as ideal conditions for a capacitive humidity sensor. The reason behind this is the deviation of the direction of the electric field slowly at low frequencies with the presence of space-charge polarization in adsorbed water molecules. The direction of the electric field flips abruptly at a higher frequency so that the polarization of the adsorbed molecules cannot interact with it, later the dielectric resistance is small and independent of humidity (%RH). From the data, the value of capacitance changes from 91 nF to 14531 nF, which provides the average sensitivity

of the sensing material $S \sim 125.57 \text{ nF/\%RH}$, the detailed sensitivity for each humidity regime is shown in Table 3.1. At lower frequency 10000 Hz, a very small change from 73.96 nF to 5160 nF in capacitance as compared to other frequencies, and the sensitivity was found as $S \sim 45.49 \text{ nF/\%RH}$ from the entire range of 10 to 95%RH. Impedance based characteristics in increasing and decreasing mode at the same frequencies are also shown in Fig. 3.7 (d) and (e). Impedance based sensing curve shows the gradual decline in impedance with the humidity with increasing frequency (20 Hz, 100 Hz, 3000 Hz, 8000 Hz, and 10000 Hz). Fig. 3.7 (f) displayed the hysteresis curve in adsorption and desorption mode at 20 Hz frequency.

The hysteresis is a disadvantage for any sensor [29] including the capacitive humidity sensor, because of the alteration of the sensing material, which adversely influences the performance of the sensor. The hysteresis curve reveals that the sensing characteristic is influenced by the consecutive change between relative humidity and capacitance [2]. From Fig. 3.7 (f), hysteresis was calculated as 3 %RH for CdS-Polyacrylamide nanocomposite by Eqn. 3.1:

$$\text{Hysteresis} = \frac{\text{Capacitance}_{\text{desorption}} - \text{Capacitance}_{\text{adsorption}}}{\text{Sensitivity}} (\% \text{ RH}) \dots\dots\dots (3.1)$$

Fig. 3.8 (a-f) displays other very essential parameters of the capacitive humidity sensor response at logarithmic scale, sensitivity curve by a linear fitted, logarithmic scale with time, stability and response, and recovery time. Fig. 3.8 (a) shows better linearity of the logarithmic coordinate curve (blue line) with the logarithmic coordinates (red line) and a linear curve in the whole range 10 to 95%RH. Fig. 3.8 (b) exhibits the sensitivity calculation by linear fitting data in increasing mode at 20 Hz and the average sensitivities of the CdS-Polyacrylamide nanocomposite are 125.57 nF/%RH, 65.36 nF/%RH, 55.68 nF/%RH, 51.42 nF/%RH, and 45.49 nF/%RH respectively. Table 3.1 shows the calculated sensitivities in three regions 10-30 %RH, 30-50 %RH and 50-95 %RH. Fig. 3.8 (c) displays the humidity sensor response at a logarithmic scale with time exhibiting a non-linear curve from 10-95 % RH. The stability of the capacitive humidity sensor stability curve at 20 Hz frequency is shown in Fig. 3.8 (d). We have examined the parameter of flexible humidity sensing elements at 20 Hz under different relative humidity as 15%, 35%, 55%, 75%, and 95% for 60 days. From Fig. 3.8 (d), the humidity sensing remained frequent every 5 days. The

response and recovery times are very important parameters and are shown in Fig. 3.8 (e). The response and recovery times were calculated as different frequencies with %RH and average sensitivity inset in the figure. The response and recovery times were calculated as 33 sec and 12 sec. Fig. 3.8 (f) shows the sensitivity response histogram in three regimes at different frequencies with %RH and average sensitivity in the inset of the figure. The I-V measurement of the sensor at different %RH levels is shown in Fig. 3.9 (a). The slope of graph between current and voltage increases at each relative humidity (RH) level. The linear I-V characteristics show the ohmic contact of the sensing device and electrodes. Fig. 3.9 (b) shows the application of humidity sensors for the detection of water molecules inside the chamber. The hydrophilicity of a sensing material can be tested through the contact angle measurement among the water droplets on the sensor surface. From Fig. 3.9 (b), it can be observed that the contact angle between surface and water droplet is lesser than 90° confirming the hydrophilic nature of the sensor. The sensing device with electron transfer during the humidity condition is displayed in Fig. 3.9 (d).

3.3.9 Application of as-developed humidity sensor of moisture/ wetness in the Baby diaper with an alarm system

Extensive wetting of diapers is a serious issue observed in widely used diapers for babies. They feel happy to pull around the humid consignment for long periods, but after a long time's damaged wet diapers can be a reason for painful red rashes, harmful and unhappy babies with their parents. Nowadays, researchers have been dedicated to developing a smart baby diaper fixed with a moisture detection sensor with an alarm system. These diapers can detect the moisture levels at different levels and send the output signals from inducting device. Hence signals were collected or notified to smartphones. In baby diapers, the superabsorbent polymer hydrogel (sodium polyacrylate) is already used, which soaked the moisture level inside the diaper. This super-absorbent polymer is originated in a disposable way, which is eco-friendly. The polyacrylate shows excellent absorbent properties, when the hydrogel is wet, the material increases and develops slightly conductive.

As per the literature review, we have synthesized the hydrophilic CdS/polyacrylamide nanocomposite-based sensor with superior humidity sensing performance. A new approach has been proposed for the alarm system inside the

diaper, the alarm level investigated at different mL such as 20 mL, 15 mL, 10 mL, 5 mL, and 2 mL. Fig. 3.10 (a-i) shows that the CdS / polyacrylamide is a good humidity sensor for monitoring the performance of baby diaper soaking. Fig.3.10 (a) displays the humidity adsorption and desorption curves, and corresponding response and recovery times are also shown in Fig. 3.10 (f-j). At 2 mL the sensing material also responding with less response and recovery times. This is the indication of sensing material that can be used as a sensing alarm inside the diaper.

3.4 Photoconduction properties:

Fig. 3.11 (a-d), represents the photodetection properties of CdS/polyacrylamide, which provides the way of research in the field of light systems inside the diaper. This is a new approach to develop the LDR incorporated in a baby diaper. Photodetection studies are carried out in the presence of a light source with λ_{max} of 365 nm. The photodetection is done under ambient atmospheric conditions and illumination intensity is controlled by using the Newport optical power meter [33]. The important parameters of the photodetector device are the responsivity (R), detectivity (D), linear dynamic range (LDR) and the noise equivalent power (NEP) whose relations are given in Eqn. 3.2-3.5 respectively.

$$R = \frac{I_{ph} - I_d}{A P_{inc}} \text{ A/W} \dots\dots\dots (3.2)$$

$$D = \sqrt{\frac{A}{2eI_d}} R \text{ Jones} \dots\dots\dots (3.3)$$

$$LDR = 20 \log \left(\frac{I_{ph}}{I_d} \right) \dots\dots\dots (3.4)$$

$$NEP = \frac{I_d}{R} \dots\dots\dots (3.5)$$

The responsivity of the device is generally defined as the ratio of the photocurrent to the optical power per unit area of the device surface. On analyzing our sample, responsivity of the photodetector device was found to be 43.939 mA/W, 15.904 mA/W, 8.115 mA/W and 1.435 mA/W for the optical light intensity of the 40 $\mu\text{W}/\text{cm}^2$, 150 $\mu\text{W}/\text{cm}^2$, 375 $\mu\text{W}/\text{cm}^2$ and 2.3 mW/cm^2 . The next important parameter of the photodetector device is the detectivity, which is defined as the responsiveness of the photodetector towards the low-intensity light signals. Detectivity of the photodetector device was best found to be 2.940×10^{11} Jones at the illumination

intensity of $40 \mu\text{W}/\text{cm}^2$. Linear dynamic range of the photodetector device is a significant property of the photodetector device, which tells us about the linear property of the photodetector device. The maximum LDR of the device is found at $2.3 \text{ mW}/\text{cm}^2$ with a value of 43.331 dB. Noise equivalent power of the device is the required power, which can generate the photocurrent to the level of the dark current[34]. Best NEP is found at $40 \mu\text{W}/\text{cm}^2$ with the value of $9.529 \times 10^{-8} \text{ W}$, which is the minimum among the other intensities of the illumination. By these parameters, we can fix the LDR (light dependent resistor) system inside the baby diapers and this will be very helpful. For this purpose, the data has been shown in Fig. 3.11 and detailed parameters are discussed in Table 3.2.

3.4.1 Sensing Mechanism:

From the characterization techniques, it can be observed that the CdS-Polyacrylamide nanocomposite is highly hydrophilic due to the presence of a hydroxyl group. The humidity sensing mechanism explained by the Grotthuss chain reaction is shown in Fig. 3.12 (a). In a low humid region, the adsorption capacity is very high and water molecules are separated into two parts as OH^- and H^+ . The OH^- ions interact with the metal ions on sensing elements and chemically bonded with each other through chemisorption. During this process, the protons are released, but not active in this stage. When the humidity increased in the next level, the second layer of water molecules layer formed due to physically adsorbed protons. From Fig.3.12 we can observe that the first layer of water molecules is less systematic than the second layer because of the presence of one hydrogen bond nearby [35]. At higher humid regions, the among water molecules released and made hydronium ions (H_3O^+) layers which are called as the second physisorption of layers. The arrangement of the water molecules during the adsorption might slowly vanish and protons freely move inside through compressed water by the Grotthuss mechanism [35–37]. At a low humid region, a minimal number of water molecules resides on the surface of the sensing element and resulting in the low humidity response observed in Table 3.1. As a high humid region, the humidity increases, and the hopping of protons become easier [38]. Due to the conduction of protons the response of humidity increases, which can be observed in Table 3.1.

3.5 Theoretical studies

3.5.1 DFT Studies

The results obtained from the DFT based simulation studies of the interaction between water molecules and the composite material are summarized in Table 3.2 (for electronic properties), Table 3.3 (for thermochemical properties) and Table 3.4 (for interaction distances).

We have first performed the orbital analysis by analyzing the HOMO-LUMO orbitals to demonstrate the atoms and corresponding orbitals involved in the electronic transitions during the interaction studies. Gaussian 09 software was used to carry out the calculations at b3lyp/lanl2dz basis set [39]. Fig. 3.13 represents the HOMO & LUMO orbitals and the corresponding HOMO-LUMO gap is also mentioned whereas the donor & acceptor regions are represented in Fig. 3.13. We have used the discovery studio software to visualize the donor-acceptor regions [40].

From Fig. 3.14 we can observe that as the concentration of the water molecules around the composite is increasing the bandgap tends to decrease and hence we can say that our material has very high sensitivity towards humidity as the gap tends to get minimized as demonstrated in Fig. 3.15. This trend was obtained using Microsoft Excel [41]. Further, we calculated various other parameters such as Band Gap (ΔE), Electron Affinity (EA), Ionization Potential (IP), Electronegativity (μ), Chemical Potential (χ), Chemical Hardness (η), Chemical Softness (σ) and Nucleophilicity Index (ω) for thorough investigation upon the electronic properties of the synthesized composite as well as upon its interaction with water molecules [42,43]. Eqn. 3.6 – 3.13 were used in the calculation of different electronic parameters:

$$\Delta E = E_{LUMO} - E_{HOMO} \quad \dots (3.6)$$

$$EA = -E_{LUMO} \quad \dots (3.7)$$

$$IP = -E_{HOMO} \quad \dots (3.8)$$

$$\mu = -\left(\frac{E_{HOMO} + E_{LUMO}}{2}\right) \quad \dots (3.9)$$

$$\chi = \left(\frac{E_{HOMO} + E_{LUMO}}{2}\right) \quad \dots (3.10)$$

$$\eta = \left(\frac{E_{LUMO} - E_{HOMO}}{2}\right) \quad \dots (3.11)$$

$$\sigma = \frac{1}{\eta} \quad \dots (3.12)$$

$$\omega = \frac{\mu^2}{2\eta} \quad \dots (3.13)$$

From Table 3.5, it can be seen that there is a gradual increment in all the thermochemical parameters and thus they represent that the computational study of the synthesized composite is consistent with the obtained experimental findings. Eqn. 3.14 and 3.15 were utilized in extracting various thermochemical parameters:

$$H = E + \text{Zero Point Correction Energy} + \text{Enthalpy Correction Energy} \quad \dots (3.14)$$

$$G = H - TS \quad \dots (3.15)$$

We also calculated the interaction distances of each O-atom from each water molecule from both the core elements (Cd & S) of our composite to understand the nature of interactions occurring upon stabilization of the system during the interaction studies. Table 3.5 and Fig. 3.16 represents the same. This representation was obtained using UCSF-Chimera software [41].

3.6 Conclusion

CdS/Polyacrylamide nanocomposite was prepared via frontal polymerization techniques for humidity sensing application. The flexibility of the as-developed humidity sensor was utilized for the moisture detection in a commonly used baby diaper with alarm. The simulated & optimized computer model for the synthesized composite (Cd-S & Polyacrylamide) using density functional theory were performed. HOMO-LUMO and correspondingly obtained other electronic parameters were studied, which revealed that bandgap of the synthesized composite material tends to decrease upon increasing the level of water molecules owing to be better humidity sensing mechanism, and therefore it is apt for electrical humidity applications. We also calculated several electronic parameters in order to understand their variations with an increasing number (concentration) of water molecules. Further, the thermochemical data reveals that the composite system is stable and humidity (H₂O) is absorbed well onto its surface as the thermodynamic values keep on increasing as the concentration of water molecules is increased. Since we have synthesized a metal (Cd) based absorbent composite, Cd plays a crucial role in the absorbing phenomena. In order to validate this, we calculated the distances of all the water molecules from Cd

atom and found that it lies within the interaction ranges and hence the theoretical studies also are in support of our findings. These results lay the establishment of the crucial fact that the developed composite material is suitable for absorbent behaviours and can be employed for further applications.

References

- [1] J. Zhang, X. Wang, B. Zhang, S. Ramakrishna, M. Yu, J. Ma, Y. Long, Functional Nanostructured Materials (including low-D carbon) in situ assembly of well-dispersed Ag nanoparticles throughout electrospun alginate nanofibers for monitoring human breathsmart fabrics, *ACS Appl. Mater. Interfaces* 10 (2018) 19863–19870.
- [2] U.H. Sensing, D. Zhang, Y. Sun, P. Li, Y. Zhang, Facile Fabrication of MoS₂-Modified SnO₂ Hybrid Nanocomposite for Facile Fabrication of MoS₂ -Modified SnO₂ Hybrid Nanocomposite for Ultrasensitive Humidity Sensing, *ACS Appl. Mater. Interfaces* 8 (2016) 14142–14149.
- [3] Z. Duan, M. Xu, T. Li, Y. Zhang, H. Zou, Super-fast response humidity sensor based on La_{0.7}Sr_{0.3}MnO₃ nanocrystals prepared by PVP-assisted sol-gel method Nanocrystals prepared by PVP-assisted sol-gel method, *Sensors Actuators B. Chem.* 258 (2018) 527–534.
- [4] Y. Cheng, J. Wang, Z. Qiu, X. Zheng, N.L.C. Leung, J.W.Y. Lam, B.Z. Tang, Multiscale Humidity Visualization by Environmentally Sensitive Fluorescent Molecular Rotors, *Adv. Fuctional Mater.* 1703900 (2017) 1–7.
- [5] L. Alwis, T. Sun, K.T. V Grattan, Fibre optic long period grating-based humidity sensor probe using a Michelson interferometric arrangement, *Sensors Actuators B. Chem.* 178 (2013) 694–699. doi:10.1016/j.
- [6] N. Li, X. Chen, X. Chen, X. Ding, X. Zhao, Ultra-high Sensitivity Humidity Sensor Based on MoS₂/Ag Composite Films, *IEEE Sens. J.* 3106 (2017) 2–5.
- [7] Z. Li, H. Zhang, W. Zheng, W. Wang, H. Huang, C. Wang, A.G. Macdiarmid, Y. Wei, D.U. V, V. Pennsylv, Highly Sensitive and Stable Humidity Nanosensors Based on LiCl Doped TiO₂ Electrospun Nanofibers, *JACS.* 15 (2008) 5036–5037.
- [8] F.W. Hailong Yan, Shuyue Guo, Y.L. Ping Yu, Huibiao Liu, Carbon Atom Hybridization Matters: Ultrafast Humidity Response of Graphdiyne Oxides, *Angew. Chemie* 57 (2018) 3922-3926.
- [9] H. Yu, C. Wang, F. Meng, J. Liang, H. Syed, K.K. Adhikari, L. Wang, E. Kim,

- N. Kim, Design and analysis of ultrafast and high-sensitivity microwave transduction humidity sensor based on belt-shaped MoO₃ nanomaterial, *Sensors Actuators B. Chem.* 12 (2019) 127-139.
- [10] N.H. Stefano Borini, Richard White, Di Wei, Michael Astley, Samiul Haque, Elisabetta Spigone, and T.R. Jani Kivioja, Ultrafast Graphene Oxide Humidity Sensors, *ACS Nano.* 5 (2013) 11166–11173.
- [11] J. Kim, H. Jung, Highly Enhanced Gas Adsorption Properties in Vertically Aligned MoS₂ Layers, *ACS Nano.* 7 (2015) 201-209.
- [12] S. Cwik, D. Mitoraj, O.M. Reyes, D. Rogalla, D. Peeters, J. Kim, H.M. Schütz, C. Bock, R. Beranek, A. Devi, Direct Growth of MoS₂ and WS₂ Layers by Metal Organic Chemical Vapor Deposition, *ACS Appl. Mater. Interfaces.* 18 (2018) 1–11.
- [13] Y.H. Kim, S.J. Kim, Y. Kim, Y. Shim, S.Y. Kim, B.H. Hong, Self-Activated Transparent Al-Graphene Gas Sensor with Endurance to Humidity and Mechanical Bending, *ACS Nano.* 13 (2015)1236-1243.
- [14] Z. Tian, D. Zhao, H. Liu, H. Zhu, L. Chen, Q. Sun, Optimization of Defects in Large-Area Synthetic MoS₂ Thin Films by Treatment for Switching and Sensing Devices, *Appl. Nano Mater.* 10 (2019) 1-7.
- [15] X. Wang, L. Dong, H. Zhang, R. Yu, C. Pan, Z.L. Wang, Recent Progress in Electronic Skin, *Advanced Sci.* (2015) 1–21.
- [16] S. Lee, B. J. Chul, S. Woo, Y. Kim, S. Kwon, J. Yoo, Y. Seo, Adsorption / desorption hysteresis of thin-film humidity sensors based on graphene oxide and its derivative, *Sensors Actuators B. Chem.* 237 (2016) 575–580.
- [17] P. Yasaei, A. Behranginia, T. Foroozan, M. Asadi, K. Kim, Stable and Selective Humidity Sensing Using Stacked Black Phosphorus Flakes, *Nanoscale.* (2015).
- [18] Z. Duan, Q. Zhao, S. Wang, Z. Yuan, Y. Zhang, X. Li, Y. Wu, Y. Jiang, H. Tai, Novel application of attapulgite on high performance and low-cost humidity sensors, *Sensors Actuators B. Chem.* 305 (2020) 127534-127542.
- [19] B.L. and H. Zaihua Duan, Yadong Jiang, Qiuni Zhao, Si Wang, Zhen Yuan, Yajie Zhang, Tai, Facile and low-cost fabrication of humidity sensor using

- naturally available sepiolite nanofibers, *Nanotechno.* 8 (2020)1-10.
- [20] P. Chaudhary, D.K. Maurya, R.K. Tripathi, B.C. Yadav, N.D. Golubeva, E.I. Knerelman, I.E. Uflyand, G.I. Dzhardimalieva, The synthesis of a $\text{Cu}_{0.8}\text{Zn}_{0.2}\text{Sb}_2$ polyacrylamide nanocomposite by frontal polymerization for moisture and photodetection performance, *Mater. Advances.* 1 (2020) 2804-2817.
- [21] P. Chaudhary, D. Kumar, S. Sikarwar, B.C. Yadav, G.I. Dzhardimalieva, R. Prakash, Development of nanostructured nickel reinforced polyacrylamide via frontal polymerization for a reliable room temperature humidity sensor, *Eur. Polym. J.* 112 (2019) 161–169.
- [22] J. Dennis, A. Ahmed, M. Khir, Chapter Fabrication and Characterization of a CMOS- MEMS Humidity Sensor, *Sensors* 15 (2015)16674-16687.
- [23] Z. Duan, Q. Zhao, S. Wang, Q. Huang, Z. Yuan, Y. Zhang, Y. Jiang, H. Tai, Halloysite nanotubes: Natural, environmental-friendly, and low-cost nanomaterials for the high-performance humidity sensor, *Sensors Actuators B. Chem.* 317 (2020) 128204.
- [24] V.P.J. Chung, M. Yip, W. Fang, Resorcinol – formaldehyde aerogels for CMOS-MEMS capacitive humidity sensor, *Sensors Actuators B. Chem.* 214 (2015) 181–188.
- [25] Q. Zhao, W. Chen, Q. Zhu, Synthesis of various size CdS nanocrystals in pore of polyacrylamide gels at room temperature, *Mater. Lett.* 57 (2003) 1756–1758.
- [26] W. Li, S. Xie, T. Zhai, S. Cruz, Improving the photoelectrochemical and photocatalytic performance of CdO, *CrysEngCom.* 15 (2015).
- [27] M. Electro-oxidation, Nitrogen Doped Ordered Mesoporous Carbon as Support of PtRu Nanoparticles for, *Energies.* 11 (2018) 2–16.
- [28] R.S. Priya, P. Chaudhary, E.R. Kumar, A. Balamurugan, C. Srinivas, G. Prasad, B.C. Yadav, D.L. Sastry, Evaluation of structural , dielectric and electrical humidity sensor behaviour of MgFe_2O_4 ferrite nanoparticles, *Ceram. Int.* 47 (2021) 15995-16008.
- [29] P. Chaudhary, D.K. Maurya, S. Yadav, A. Pandey, R.K. Tripathi, B.C. Yadav, Ultrafast response humidity sensor based on roasted gram derived carbon

- quantum dots: Experimental and theoretical study, *Sensors Actuators B. Chem.* 329 (2020) 1–14.
- [30] T. Capacitive, H. Sensor, U. Budget, *The Capacitive Humidity Sensor – How it Works & Attributes of the Uncertainty Budget* (2010) 1–3.
- [31] Z. Duan, Q. Zhao, S. Wang, Q. Huang, Z. Yuan, Y. Zhang, Y. Jiang, H. Tai, Halloysite nanotubes Natural environmental-friendly and low-cost nanomaterials for high-performance humidity sensor, *Sensors Actuators B. Chem.* 317 (2020) 128204-128209.
- [32] S. Mishra, P. Lohia, P. Chaudhary, B.C. Yadav, D.K. Dwivedi, Development of an Impedance-Based Electrical Humidity Sensor Using Sb-Doped Ge-Se-Te Chalcogenide Glasses, *J. Electron. Mater.* 49 (2020) 6492–6500.
- [33] A. Verma, P. Chaudhary, The functionalization of polyacrylamide with MoS₂ nanoflakes for use in transient photodetectors, *Sustain. Energy Fuels*.5 (2021) 1394-1405.
- [34] A. Verma, P. Chaudhary, R.K. Tripathi, B. C. Yadav, *Sensors and Actuators A : Physical Transient photodetection studies on 2D ZnO nanostructures prepared by simple organic-solvent assisted route*, *Sensors Actuators A. Phys.* 321(2021) 112600-112606.
- [35] N. Yadav, P. Chaudhary, K.K. Dey, S. Yadav, B. C. Yadav and R. R. Yadav Non-functionalized Au nanoparticles can act as high- performing humidity sensor, *JMSE.* 7 (2020) 17843–17854.
- [36] V. Kumar, V. Chauhan, J. Ram, R. Gupta, S. Kumar, P. Chaudhary, B. C. Yadav, S. Ojha, I. Sulania, R Kumar Study of humidity sensing properties and ion beam induced modifications in SnO₂ -TiO₂ nanocomposite thin films, *Surf. Coat. Technol.* 392 (2020) 125768.
- [37] L.G. Bach, R. Islam, S. Hong, K.T. Lim, A Simple Preparation of a Stable CdS-Polyacrylamide Nanocomposite : Structure, Thermal and Optical Properties, *Mater. Lett.* 13 (2013) 7707.
- [38] D.K. Maurya, S. Sikarwar, P. Chaudhary, S. Angaiah, B. C. Yadav, Synthesis and Characterization of Nanostructured Copper Zinc Tin Sulphide (CZTS) for

Humidity Sensing Applications, IEEE Sens. Jour. 19 (2019) 2837–2846.

Tables:

Table 3.1. Average sensitivities of CdS-Polyacrylamide at different frequencies in three regions

Frequency	Low humidity region (10-30 %RH)	Mid humidity region (30-50 %RH)	High humidity region (50-95 %RH)	Avg. sensitivity (nF/%RH)
20 Hz	10.28	59.97	306.47	125.57 nF/%RH
100 Hz	5.25	41.35	149.49	65.36 nF/%RH
3000 Hz	2.96	17.69	146.40	55.68 nF/%RH
8000 Hz	0.69	16.74	136.84	51.42 nF/%RH
10000 Hz	0.14	0.93	135.4	45.49 nF/%RH

Table 3.2. Represents the photoconduction parameters at different power

Power (W)	Ip	Id	on off ratio (Ip/Id)	Responsivity (A/W)	LDR (dB)	Detectivity (Jones)	NEP(W)
4.00E-05	1.0964E-07	4.1874E-09	26.1841	43.93964	28.3608	2.9403E+11	9.5298E-08
1.50E-04	1.4550E-07	2.3611E-09	61.6240	15.90438	35.7950	1.4173E+11	1.4846E-07
3.75E-04	1.8541E-07	2.8141E-09	65.8887	8.11555	36.3762	6.6245E+10	3.4675E-07

2.30E-			146.742		43.331	1.6860	9.4688E-
03	1.99E-07	1.36E-09	5	1.43558	1	E+10	07

Table 3.3. Table representing the electronic properties of the composite without and with interaction from water molecules

S. No.	Electronic Parameters		Composition			
			Only Composite	Composite + 1 H ₂ O	Composite + 2 H ₂ O	Composite + 3 H ₂ O
1	E _{HOMO} (eV)		-6.25	-6.33	-5.89	-5.75
2	E _{LUMO} (eV)		-5.47	-5.59	-5.19	-5.16
3	Band Gap(ΔE) (eV)		0.78	0.74	0.70	0.59
4	Electron Affinity (EA) (eV)		5.47	5.59	5.19	5.16
5	Ionization Potential (IP) (eV)		6.25	6.33	5.89	5.75
6	Electronegativity (μ) (eV)		-5.86	-5.96	-5.54	-5.45
7	Chemical Potential (χ) (eV)		5.86	5.96	5.54	5.45
8	Chemical Hardness (η) (eV)		0.39	0.37	0.35	0.29
9	Chemical Softness (σ) (eV)		2.56	2.70	2.85	3.44
10	Nucleophilicity Index		44.03	48.00	43.84	51.21

	(ω) (eV)					
12	Dipole Moment (Debye)	7.806	4.990	4.869	2.616	

Table 3.4. Table representing the thermochemical properties of the composite without and with interaction from water molecules

S. No.	Thermo-chemical Properties	Composition			
		Only Composite	Composite + 1 H ₂ O	Composite + 2 H ₂ O	Composite + 3 H ₂ O
1	Total Internal Energy(E) (Hartree)	-553.882	-630.329	-706.761	-783.158
2	Enthalpy (H) (Hartree)	-553.683	-630.125	-706.554	-782.954
3	Gibbs Free Energy(G) (Hartree)	-553.751	-630.209	-706.636	-783.040
4	Heat Capacity (C _v) (cal/mol-K)	56.247	66.72	66.918	67.272

Table 3.5. Interactions distances with water molecules

S. No.	System	Interaction Distances
1	Composite	-

2	Composite + 1 H ₂ O	Cd: 3.205 Å S: 4.753 Å
3	Composite + 2 H ₂ O	Cd: 3.783 Å, 4.917 Å S: 3.249 Å, 6.390 Å
4	Composite + 3 H ₂ O	Cd: 5.477 Å, 7.245 Å, 8.813 Å S: 3.172 Å, 5.928 Å, 6.811 Å

Figures:

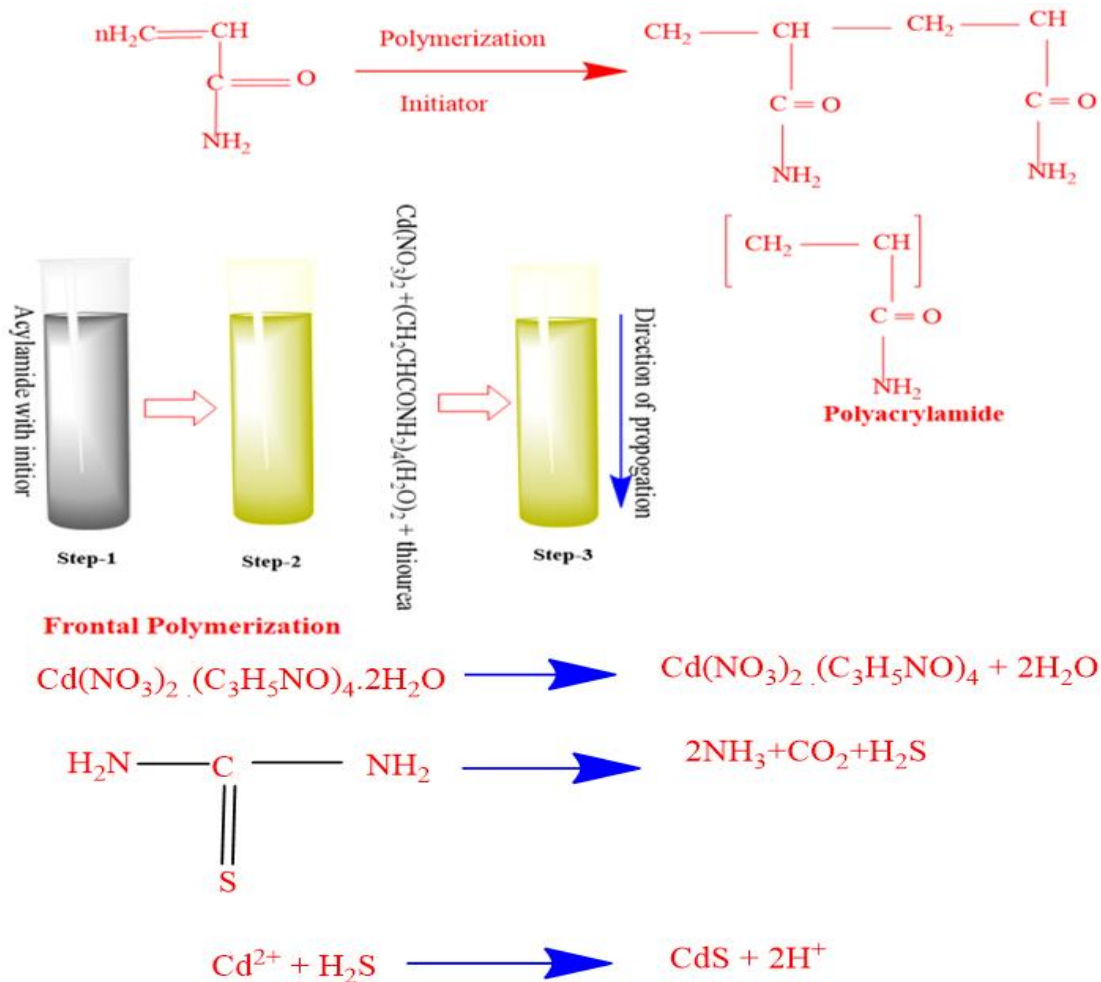


Figure 3.1: Flow chart illustration of Chemical reactions involved during the synthesis of CdS/Polyacrylamide.

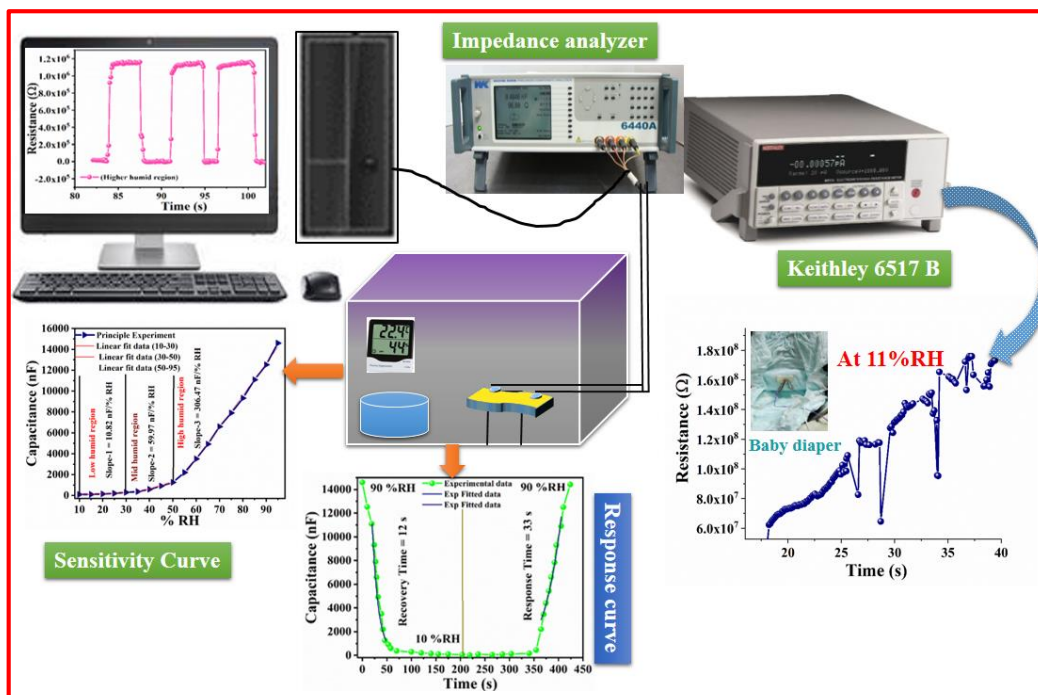


Figure 3.2: Schematic of humidity sensing set-up.

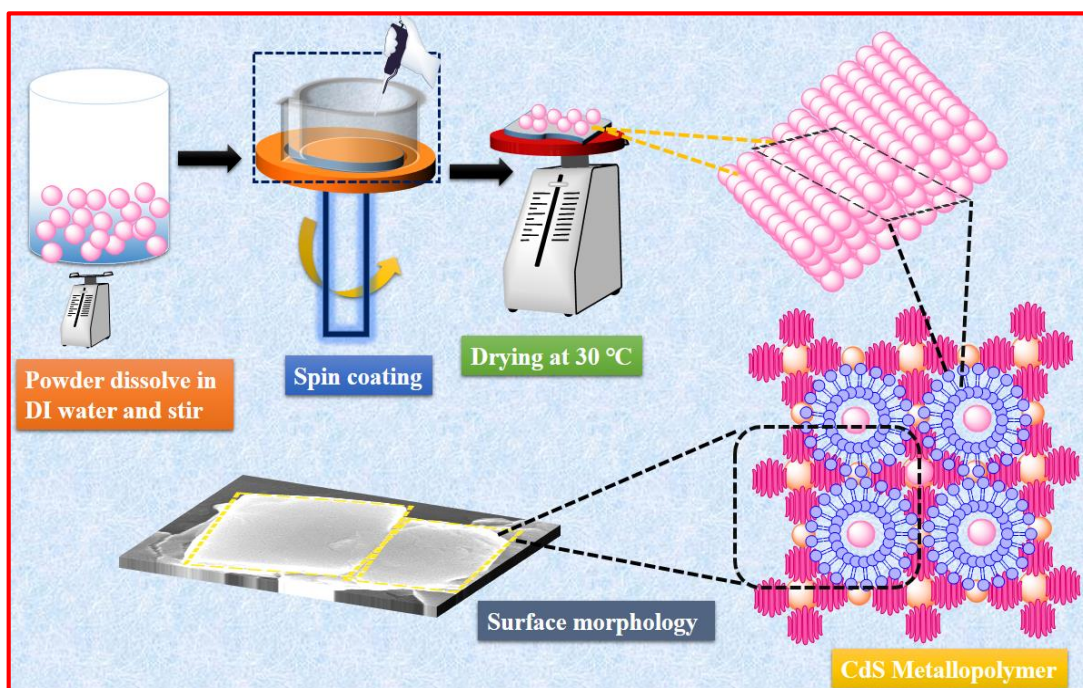


Figure 3.3: Schematic for the fabrication of sensing element.

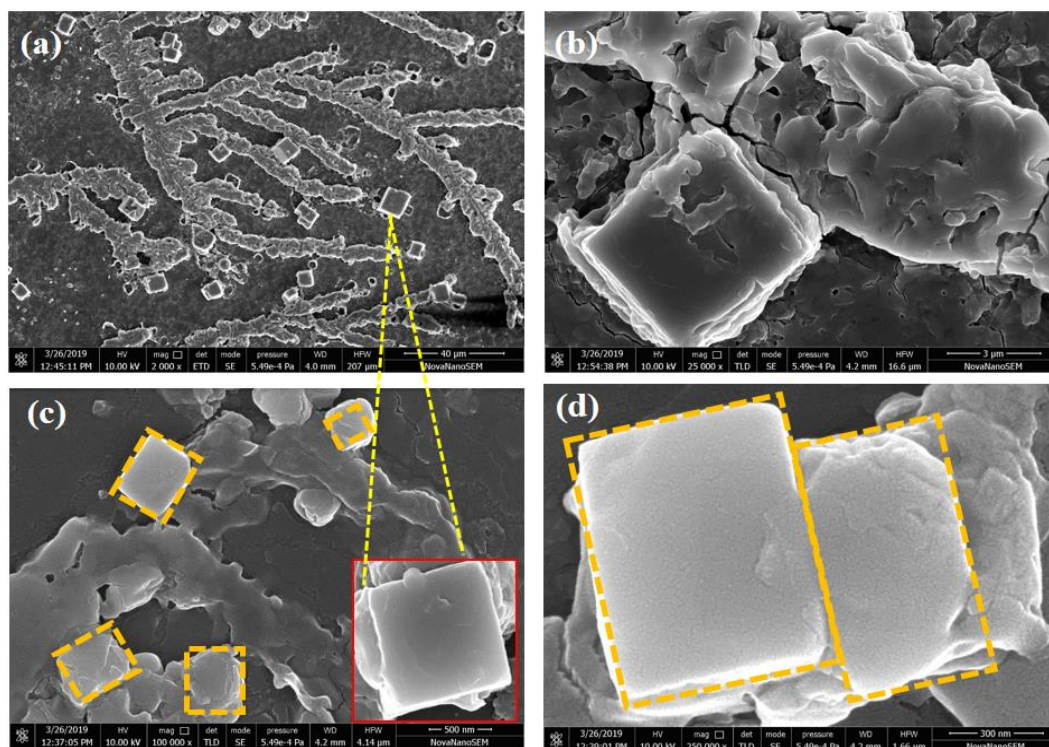


Figure 3.4: (a-d) FESEM images of CdS-Polyacrylamide nanocomposite at different magnifications.

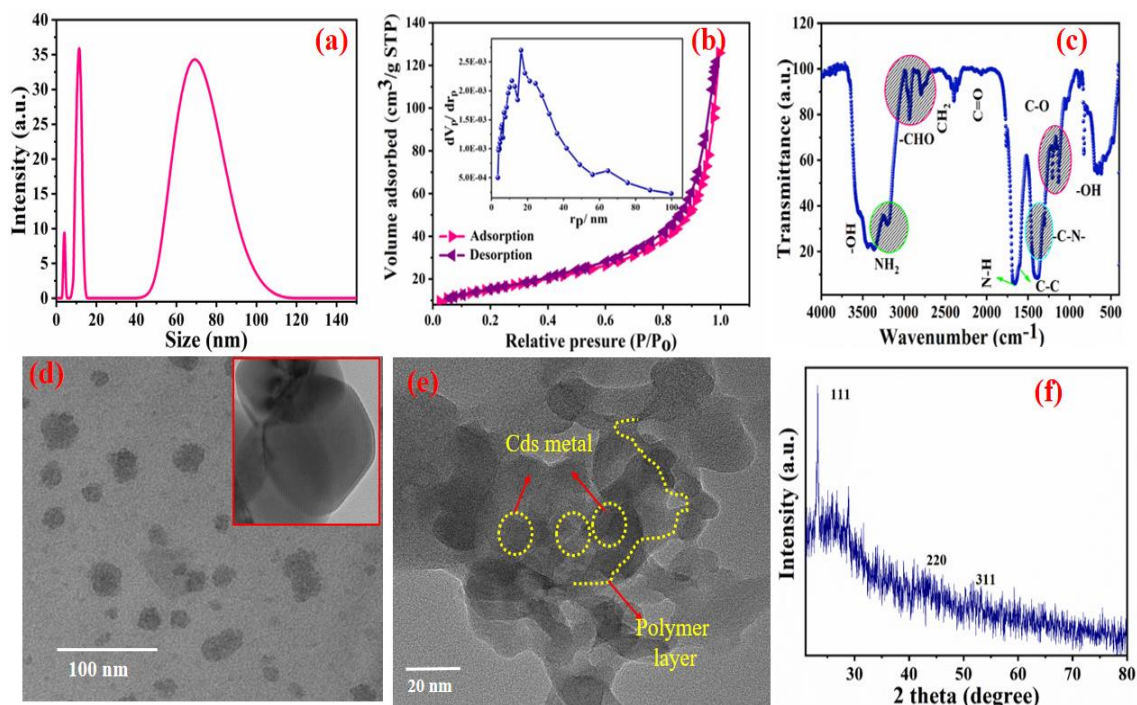


Figure 3.5: (a) DLS spectra of CdS-Polyacrylamide nanocomposite (b) BET analysis of CdS-Polyacrylamide nanocomposite (c) FTIR analysis of CdS-Polyacrylamide nanocomposite (d & e) TEM analysis at 100 nm scale HRTEM inset inside, the

polymer layer shows at 20 nm (f) XRD diffraction pattern of CdS-Polyacrylamide nanocomposite.

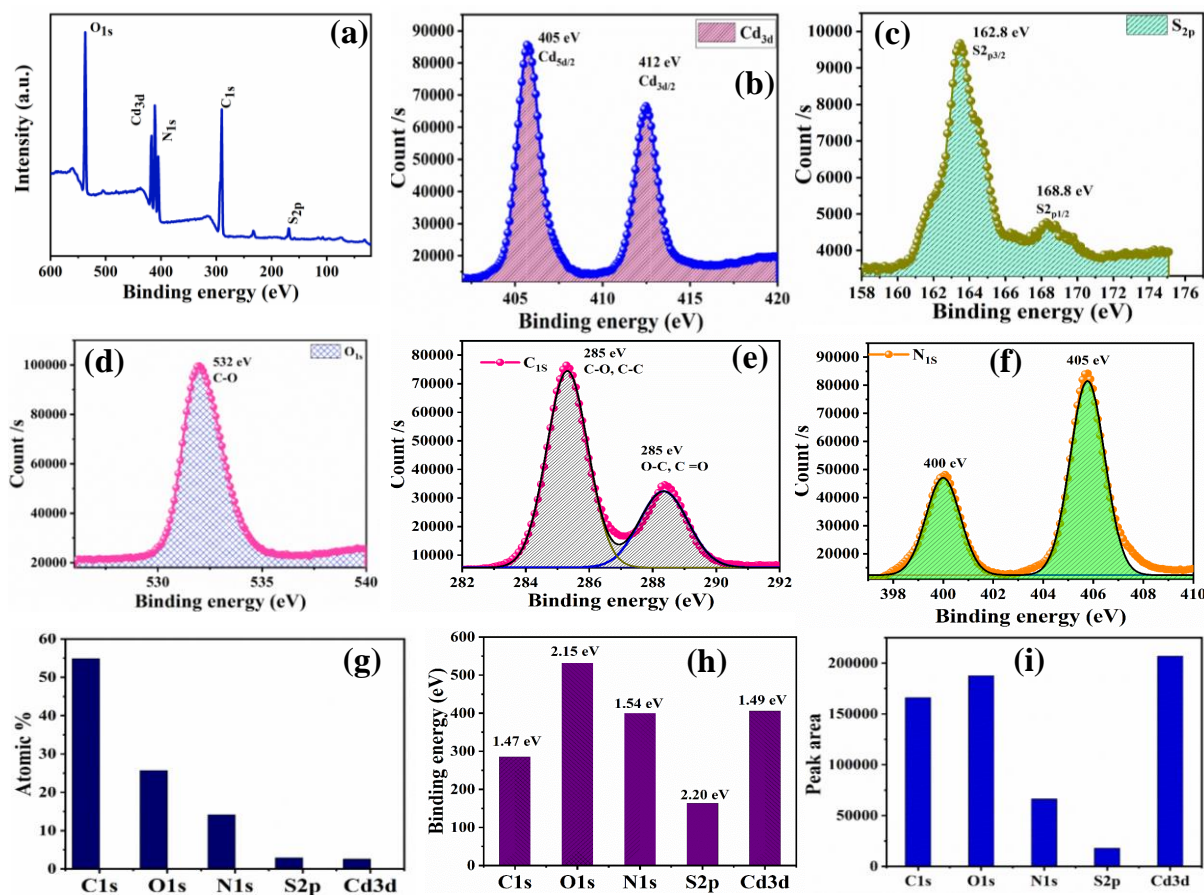


Figure 3.6: (a) XPS analysis of the CdS/polyacrylamide nanocomposite: (a) full scan data; (b) Cadmium (3d) element, (c) sulphur (S2p) element, (d) Oxygen (O1s) element, (e) carbon (C 1s) element, (f) nitrogen (N1s) element, (g) atomic weight% ratio of elements, (h) histogram showing the binding energies and (i) Peak area of elements

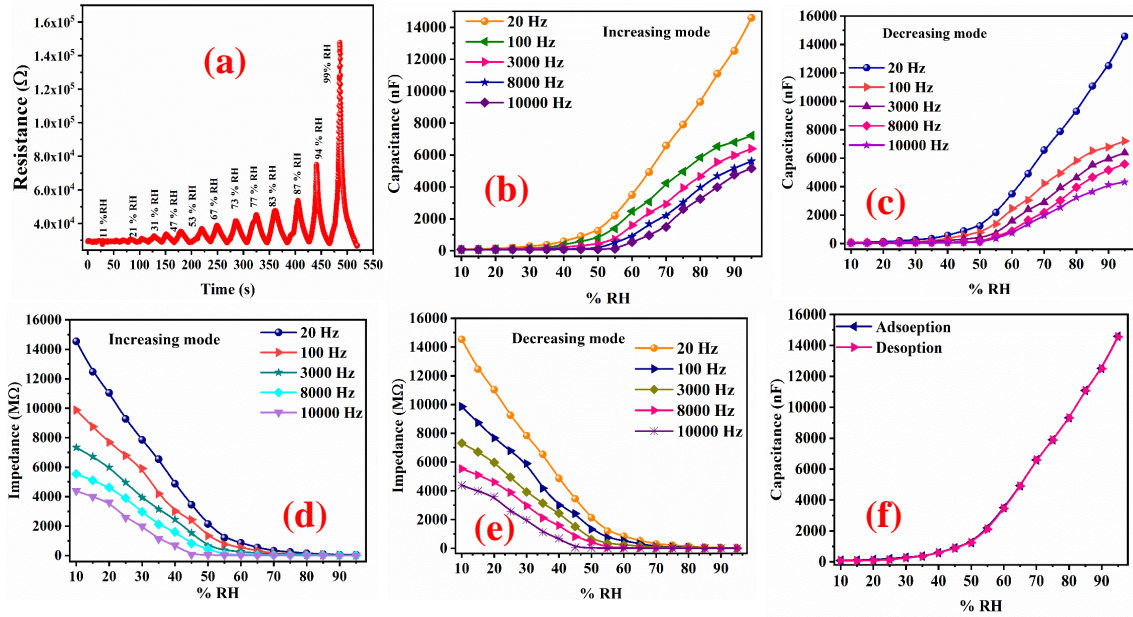


Figure 3.7: (a) The sensing response at different %RH (b) Variation of capacitance corresponding to the %RH at different frequencies in increasing mode (c) Variation of capacitance corresponding to various %RHs at different frequencies in decreasing mode (d) Impedance variation with %RH in increasing mode at different frequencies (e) Impedance variation with %RH in decreasing mode at different frequencies (f) Hysteresis curve

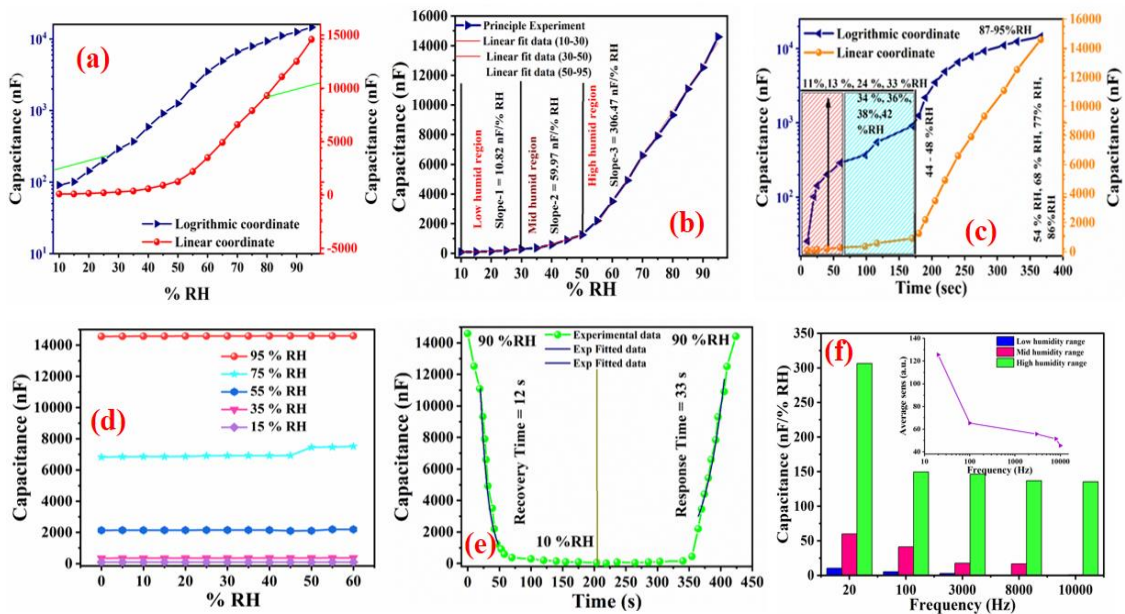


Figure 3.8: (a) The capacitive humidity sensor response at logarithmic scale with respect to relative humidity (b) linearly fitted sensitivity curve in three

regimes at 20 Hz (c) sensor response at logarithmic scale concerning time (d) capacitive stability curve at 20 Hz frequency (e) capacitance sensing response and recovery times (f) The sensitivity response histogram in three regimes at different frequencies with %RH and average sensitivity inset in the figure.

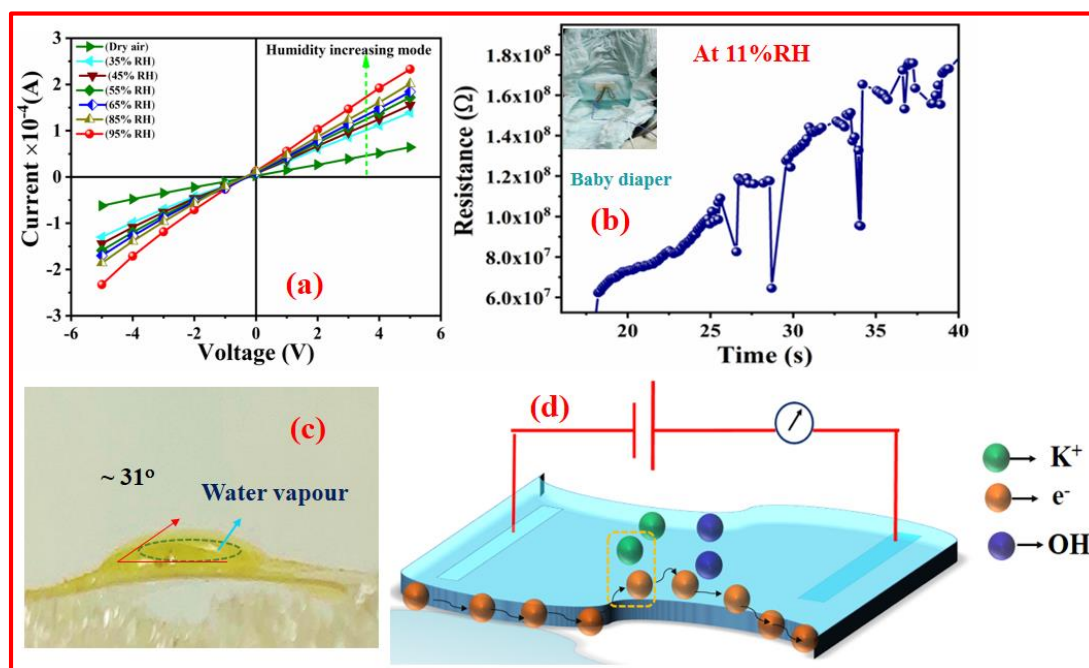


Figure 3.9: (a) I-V characteristics at different relative humidity (b) Humidity performance in a baby diaper (c) hydrophilic nature of the sensing material (d) device structure and during humidity interaction through the electron transfer process

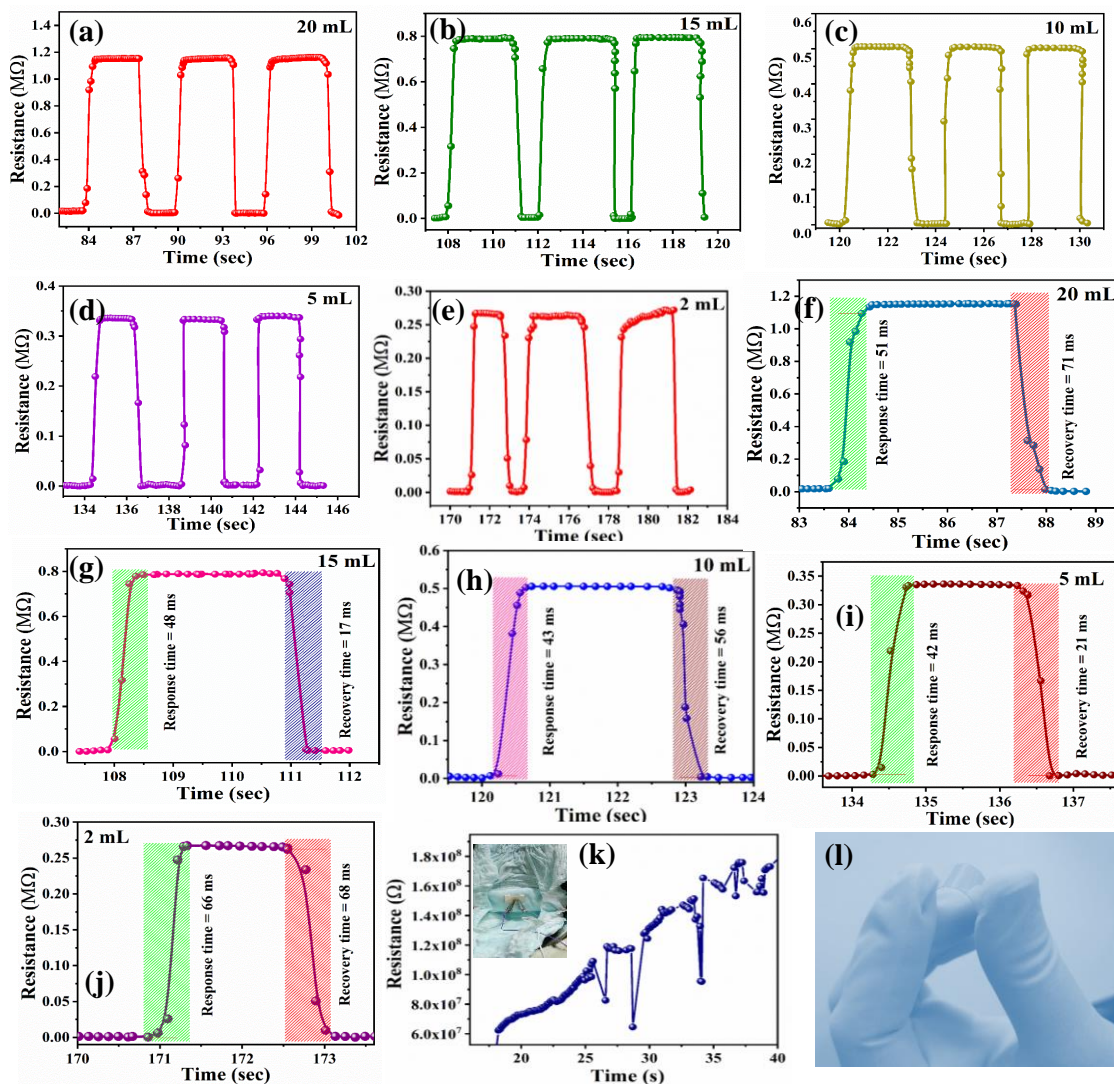


Figure 3.10: (a-e) shows the curves between resistance corresponding with time at different mL, (e-j) exhibit the response and recovery time equivalent with ml (k-l) variation in resistance inside the humidity chamber in baby diaper and flexibility of the substrate.

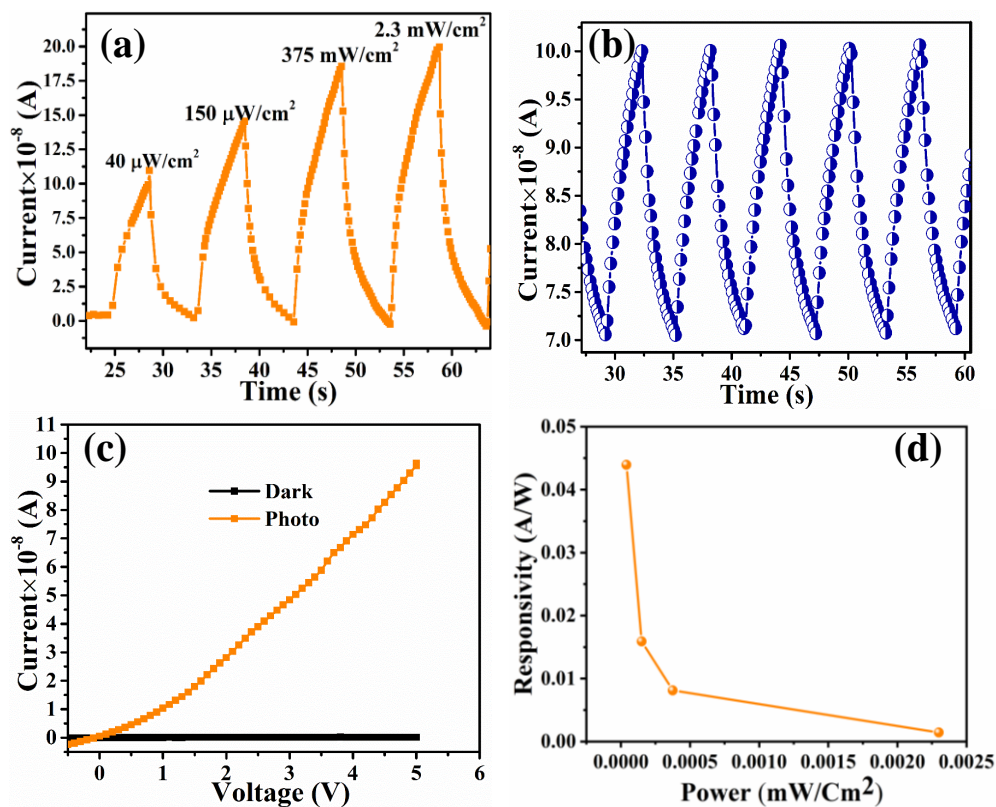


Figure 3.11: (a-d) Photoconduction studies of CdS/polyacrylamide at different power, the change in current in dark and light-medium, responsivity at different power.

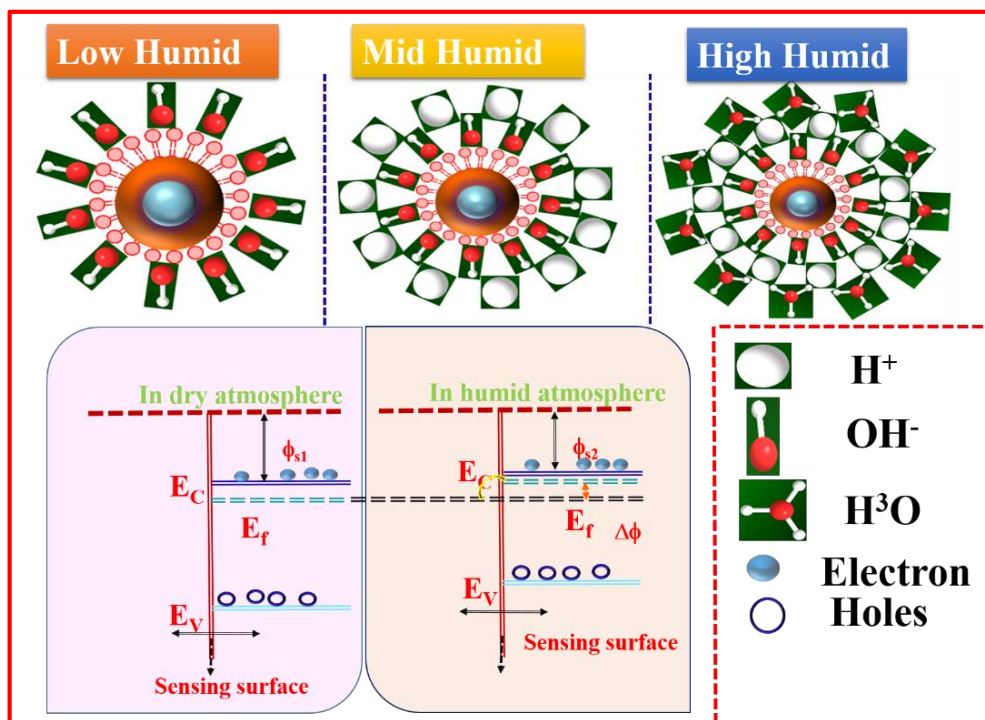


Figure 3.12: Humidity sensing mechanism at different regions

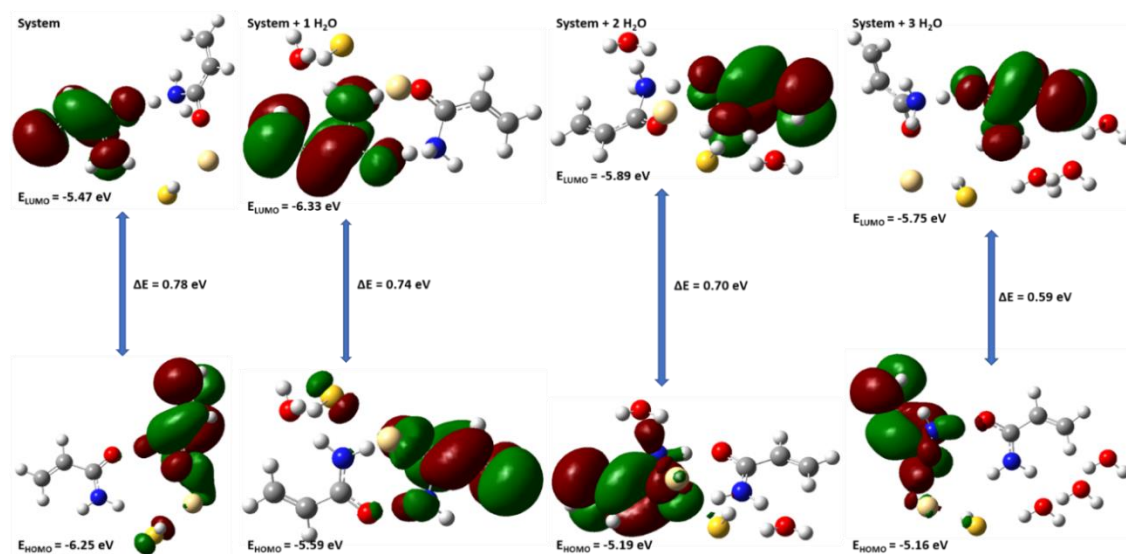


Figure 3.13: HOMO-LUMO Orbitals.

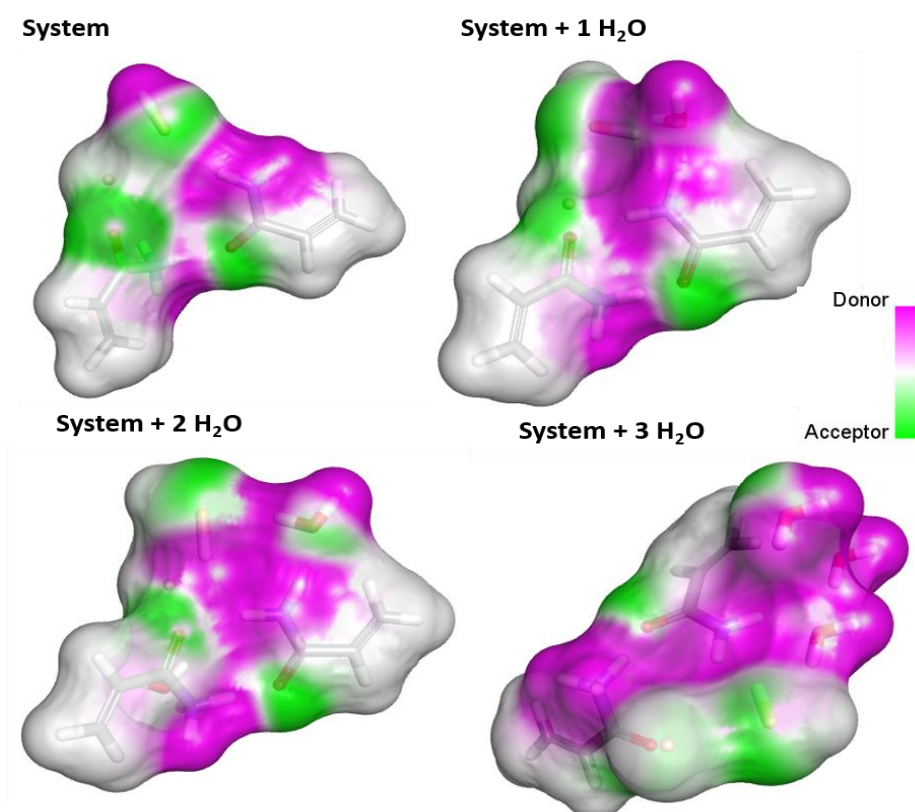


Figure 3.14: Electron donor & acceptor regions

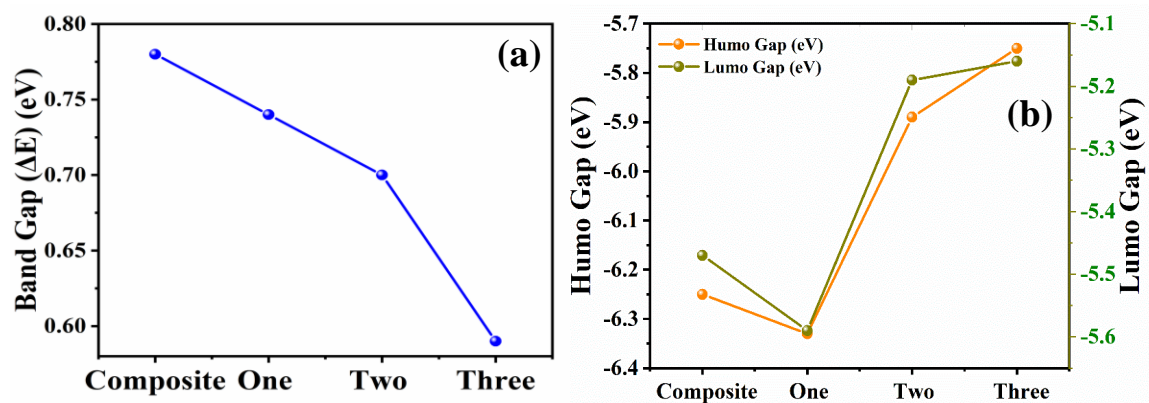


Figure 3.15: Band gap vs number of water molecules (b) HUMO –LUMO of the water molecules.

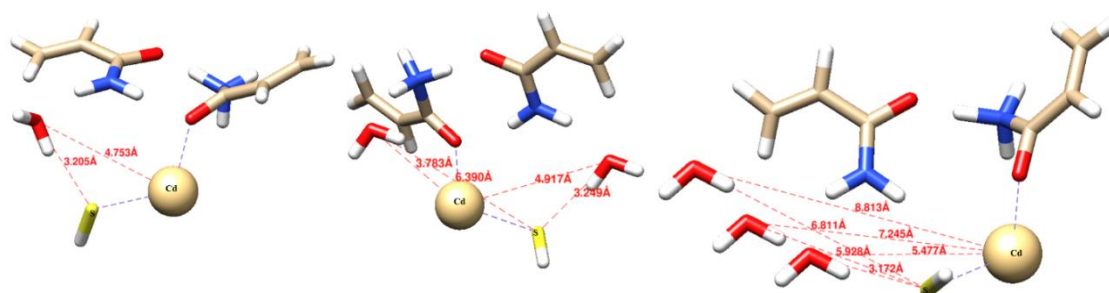


Figure 3.16: Interactions distances with water molecules

CHAPTER 4

Fabrication of $\text{Cu}_{0.8}\text{Zn}_{0.2}\text{Sb}_2$ -polyacrylamide nanocomposite via frontal polymerization and its relevance in moisture sensing and photodetection

In present chapter, we have reported the preparation of $\text{Cu}_{0.8}\text{Zn}_{0.2}\text{Sb}_2\text{AAM}$ -polymer nanocomposite synthesized via frontal polymerization technique with its humidity sensing and photoconductive behaviour. The surface texture was examined using Scanning Electron Microscopy (SEM) analysis. X-ray diffraction and Transmission Electron Microscopy (TEM) studies confirm the crystallinity of as-fabricated nanocomposite thin film-based sensing element. The surface area, particle size, optical absorbance and thermal stability of as-fabricated thin film were successively investigated using Brunauer–Emmett–Teller (BET), Particle size analysis, Ultra-Violet absorption, Fourier Transform Infrared spectroscopy (FTIR), Thermogravimetric analysis, X-ray photoelectron spectroscopy (XPS) and Differential Scanning Calorimetric analysis (DSC) respectively. Humidity sensing characteristics were also investigated via the capacitive performance of $\text{Cu}_{0.8}\text{Zn}_{0.2}\text{Sb}_2\text{AAM}$ film with the exposure of moisture. The average sensitivity (S) of as-fabricated sensor was found to be ~ 168.477 pF/%RH at an optimum frequency of 20 Hz. The sensor exhibited a rapid response and recovery time of 4.6 sec and 5.6 sec with persistent stability of 96 % after 60 days. Thus, $\text{Cu}_{0.8}\text{Zn}_{0.2}\text{Sb}_2\text{AAM}$ polymer-based capacitive humidity sensor ensures its potential towards reliable and safer use in the detection of humidity levels as well as a photoconductor.

4.1 Introduction

Polyacrylamide polymer structure is just like a polyethylene chain with an amide group attached at an end. PAam is synthesized by polymerization of acrylamide (C₃H₅NO), a compound obtained by the hydration of acrylonitrile. The dissolved monomers (acrylamide) are induced to polymerize through the action of free-radical initiators. The highly reactive amide (NH₂) group and the polymer can be chemically modified to produce a positively charged cationic polymer or a negatively charged anionic polymer[1-3]. Ionic polymers are especially useful in separating metals from residues in various mineral-processing and metallurgical operations. Due to its flocculating nature, PAam is a globally used synthetic polymer in different applications such as removal of toxic ions during water treatment, paper making industry, petroleum sector, soil conditioning, etc[4-7].

The vitality of these PAam's becomes more prominent with the development of metal-polymer complex. The rapid development of metal incorporated polymer complexes revived the modern polymer industry with more advanced materials. The complexation of metal ions with polymeric ligands affects the properties of parent polymer drastically[8]. From the technological aspect, the thermal stability of polymers matters a lot for their high-temperature application. Insertion of metal ions in the polymer matrix generates many charge carrier ions thus increasing the rigidity of polymer chains raising the glass transition temperature of the material. Metal-doped polyacrylamide extensively harvested in water-soluble polymers synthesis. The different metal-polymer complex has been successfully synthesized by doping transition metal ions with divalent nature such as Fe²⁺, Co²⁺, Cu²⁺, Mn²⁺, Ni²⁺, Zn²⁺, and Cd²⁺ possessed a better chemical and thermal stability[9-12]. These metallopolymers have the functionality of polymers as well as metals enabling their feasibility in various industries such as memory devices, humidity sensors, gas sensors, solar appliances, and light-emitting devices. Based on the precursors, different methods of production of metallopolymers (metal-containing polymers) have been reported yet. The preparation method proceeds in three steps;

- The interaction of the metal with compound (MX_n) with functionalized polymers means carboxyl-containing polymers and the analogous

transformation is defined as when the main polymer chain remains untouched with the metal compound.

- In the second step polycondensation of appropriate precursors; when metal ions are combined into and removed from the main chain of polymers annihilation.
- In the last step recently, a new method was developed for polymerization and copolymerization of metallopolymer monomers (metal-containing). Metallopolymers are based on transition metals, and it's obtained through the above methods.

Recently, a single metal-based polymer complex has been harvested for humidity sensing via electrical mode as well as optoelectronic mode[13]. Several charge carriers are a crucial factor in determining the sensing characteristic of a material[11, 13]. Allocating in the metal sites with isovalent dopant ions will certainly strengthen the synergistic effect between metal ions and host polymer. Zinc–antimony binary system is one of the best thermoelectric materials due to its low lattice thermal conductivity stable at intermediate temperatures[14, 15]. This alloy contains a higher degree of atomic disorders with whole concentration. Doping of Cu in the Zn–Sb alloys enhances the whole concentration, leads to a higher carrier concentration. Besides, an atomic radius of Cu is compatible with the Zn-Sb polymorph could be easily accommodated in interstitial gaps in the Zn–Sb lattice, this facilitated disruption in the lattice stability and reduction in the lattice thermal conductivity[14, 16, 17]. Cu-Zn-Sb-based ternary system fulfils the goals of technological as well as humidity sensing needs. This ternary system incorporation in the polymer matrix will improve thermal properties as well as better sensing capability as a humidity sensor.

For the detection and control of humidity wide numbers of materials are reported. These materials also played an important role in environmental monitoring for the atmosphere, seed storage, agriculture, chemical field, biomedical, electronics processing, and food industry, as well as used in daily life, such as air conditioners and hospitals, etc.[18-20]. A large number of sensing materials has been exploited towards humidity sensing mainly include organic polymers, metal oxides, polymer/inorganic nanohybrids, and polymer electrolytes (polyelectrolytes), every material has its inheriting property responsible for humidity adsorption and desorption[21-25]. Nowadays the photodetection properties are also thoroughly investigated along with

humidity sensing behaviour [26-29]. Some of the nanomaterials show extraordinary behaviour of responding to both humidities as well as a photo. In recent years to minimize the wastage of energy and improve energy-saving practices, photoconduction has been studied for different nanomaterials [26, 28, 30]. The literature survey based on other metal oxides humidity sensors has been depicted in Table 4.1 [31-38].

Here in the present chapter, we have used ternary metal-doped acrylamide composite for the photoconduction behaviour and humidity sensor for the measurement of moisture. Since previous investigations were focused only on single metal-doped complexes but here a stable ternary system for humidity sensing has been reported for the first time. This will provide an insight into the implementation of the ternary system in sensing applications.

4.2 EXPERIMENTAL DETAILS

4.2.1 Synthesis Method

The synthesis was performed in two phases; initially, the metal complex with polyacrylamide was prepared via frontal polymerization, and then the sensing film of Cu_{0.8}Zn_{0.2}Sb₂AAM was fabricated using the spin coating technique.

4.2.2 Preparation of Cu_{0.8}Zn_{0.2}Sb₂AAM via Frontal polymerization

The preparation of monomer of Cu_{0.8}Zn_{0.2}Sb₂ nitrate acrylamide complex was carried out by the modified procedure (Fig. 4.1). Initially, the transition metal nitrates embedded in acrylamide complexes were prepared. For this Cu(NO₃)₂·3H₂O (0.77 g, 2.26·10⁻³ mol), Zn(NO₃)₂·6H₂O (0.136 g, 0.56·10⁻³ mol), Sb(NO₃)₃ (1.74 g, 5.66·10⁻³ mol) and acrylamide (AAM) (2.0 g, 4.23·10⁻³ mol) were taken and mixed uniformly to maintain a metal into acrylamide polymer mole ratio 1:5 in an inert atmosphere. After the washing of the homogenous mixture, a green paste was obtained and it was dried in a desiccator for one day over P₂O₅. Further, rewashed the paste with methanol and ether to remove the excess AAM(acrylamide). Dried again in a desiccator for 24 hrs to a constant weight and found the fine paste of Cu_{0.8}Zn_{0.2}Sb₂AAM. After the preparation of the monomer now Cu_{0.8}Zn_{0.2}Sb₂AAM sample was used for the frontal polymerization technique, the acrylamide complex was pressed as a pellet with the fixed dimensions; the diameter *d* of the pellet was 0.5-0.8 cm, height *h* = 1.2-1.5 cm, and density $\rho = 1.45 \pm 0.02 \text{ g cm}^{-3}$. Further, this pellet was placed in a glass test tube. To initiate the

polymerization, the bottom region of the test tube with the sample was immersed by 0.2 cm into the bath with wood alloy as the heat carrier for 10-15 sec at 130 °C. The reaction rate was monitored from the movement of the front of the coloured zone in time. After that, the powder was washed several times with methanol and ether until the removal of excess AAm and then dried in a vacuum at room temperature for 24 hrs. Thus, Cu_{0.8}Zn_{0.2}Sb₂AAm powder was obtained for further characterization and application of humidity sensors.

4.2.3 Experimental set-up for photoconduction measurement

The room temperature photoconduction properties of the prepared samples have also been recorded through Keithley's 6517B source measuring unit (SMU) in the resistance mode at an illumination intensity of ~ 100 mW/cm². Fig. 4.2 shows the schematic diagram of a photoconductive device based on Cu_{0.8}Zn_{0.2}Sb₂AAm nanomaterial.

4.2.4 Fabrication of thin film

A thin film-based sensing element was fabricated by spin coating technique which is well depicted in Fig. 4.3. The uniformity in the deposition of the film is influenced by key parameters such as rotation of the spinner, temperature, and viscosity of the solution. Initially, borosilicate substrates having dimensions uniform 1.5×1.5 cm² were treated in an ultrasonic cleaner (WUC-AO2H) by using de-ionized water, isopropyl alcohol, and acetone as a cleansing agent. The solution was coated on the glass substrate using the spin coater (METREX RC100, India) with the angular rotation of 2000 rpm and further dried for 30 min at 60 °C for drying. The fabricated film was further annealed at 200 °C for 2 hrs in a tubular electric furnace for the complete removal of organic components. Probe contacts were developed on both the ends of thin film using a silver paste with a copper wire connecting with them acts as electrodes. Thus, this film was employed as a sensing element for the detection and measurement of humidity.

4.3 RESULTS AND DISCUSSION

4.3.1 Morphological Investigation (SEM analysis)

The porous surface morphology of a thin film is a key feature for humidity sensing applications. Surface morphology of as-fabricated Cu_{0.8}Zn_{0.2}Sb₂AAM thin film was investigated using SEM (JEOL, JSEM-6490LV) at different magnifications shown in Fig. 4.3 (a-d). It was confirmed from images that the surface morphology of the Cu_{0.8}Zn_{0.2}Sb₂AAM thin-film possesses a highly porous structure with intermediate voids on the surface particularly responsible for characteristic adsorption and desorption of humidity. The high surface to volume ratio decides its applicability for humidity sensing since a higher ratio facilitates the increase in active sites of the material which regulates the desorption /adsorption of humidity [13, 40, 41]. Accordingly, the mesoporous nature of the Cu_{0.8}Zn_{0.2}Sb₂AAM thin film exhibits a higher surface area solely responsible for the high sensitivity of the sensor at ambient temperature. The presence of active sites on the surface comprised of dangling bonds encourages high sensitivity in a short period. This solely favours the strong adhesion of water vapours that comes in contact with the surface[12, 42].

4.3.2 BET (Brunauer–Emmett–Teller) Analysis

The porosity and surface area are the critical parameters that affect the sensitivity of a material implicitly. So the responsible surface area of Cu_{0.8}Zn_{0.2}Sb₂AAM thin film and corresponding pore size distribution was estimated from N₂ adsorption/desorption isotherm by BET method at 77 K (AUTOSORB-1 instrument (Quantachrome, USA)). For Cu_{0.8}Zn_{0.2}Sb₂AAM thin film, the specific surface area was found to be 2.0 S_{ep}/m²g⁻¹; whereas the pore volume and pore radius were estimated at 0.0084 V/cm³ g⁻¹ and 82.4 Å respectively, which is shown in Fig. 4.5 (a-b).

4.3.3 Transmission electron microscopy (TEM) analysis

Fig. 4.6 shows the TEM image of Cu_{0.8}Zn_{0.2}Sb₂AAM thin film at 20 nm scale with an inset SAED image showing the circular fringes. These circular fringes reveal the periodic distribution among the crystal giving a well-defined diffraction pattern. TEM image confirms the well-defined crystalline nature of metallopolymer with oval-shaped voids on the surface Cu_{0.8}Zn_{0.2}Sb₂AAM.

4.3.4 Particle size analysis

The particle size of an aqueous solution of Poly-CuZnSbAAM complex was analyzed through Zeta nanosizer (Nano-ZS90) and the resultant data is plotted as shown in Fig. 4.7(a). The particle size analysis is attributed to the dynamic scattering of light phenomena. From Fig. 4.7(a) the particle size distribution curve shows that the peaks are divided into two major intensities, first one is the peak of the particles at ~ 21 nm range with the neighbouring peak at 50 nm.

4.3.5 UV-visible absorption analysis

UV- visible absorption analysis was carried out using a Spectrophotometer (Evolution 201). The absorption spectrum was recorded in the wavelength range from 190 to 1100 nm. S. Singh et al. reported that the principal band of pure acrylamide appears at 197 nm [43, 44], while in our case the characteristic band of CuZnSb acrylamide complex has been found at 320 nm due to the complexation between the metal ion and polyacrylamide polymer. Here in Fig. 4.7(b), the variation of absorbance with the wavelength has been shown with an in situ plot between the optical absorption coefficient (α) and photon energy ($h\nu$) known as the Tauc plot. The optical band-gap E_g of Cu_{0.8}Zn_{0.2}Sb₂AAM thin film was calculated using the formula

$$\alpha h\nu = A(h\nu - E_g)^n$$

Where ν is defined as the transition frequency, A is constant and n is the value of allowed transitions characteristic to the nature of the material. The direct allowed band transition ($n = 1/2$ and $3/2$) corresponds to the indirect allowed the forbidden transition respectively whereas $n = 2$ and 3 relate respectively. Here for this material, the transition is the direct allowed type, therefore, $n = 1/2$ is taken in the above formula for the calculation of the optical bandgap. The optical band gap E_g was estimated by extrapolating the straight line where $\alpha = 0$ on the $(\alpha h\nu)^2$ vs. $h\nu$ (Tauc plot) curve and it was found to be 3.91 eV.

4.3.6 XRD analysis

The influence of incorporating metal ions in the polymer matrix reflects the crystalline nature of the host polymer [45, 46]. This influence was investigated through the XRD diffraction pattern of Cu_{0.8}Zn_{0.2}Sb₂AAM thin film exhibited in Fig. 4.7(c). It can be easily observed from the diffraction pattern that the crystallinity of the host polyacrylamide decreases with the addition of Cu, Zn, and Sb metal ions [47, 48]. Here,

also the high-intensity peaks corresponding to the Cu Zn and Sb were observed at 2θ values of 24.01° , 28.94° , 40.42° and 51.25° respectively. Thus obtained diffraction pattern confirms the polycrystalline nature of the Cu_{0.8}Zn_{0.2}Sb₂AAM thin film. The minimum crystallite was calculated to be 19 nm using Debye-Scherrer's formula.

4.3.7 IR Spectroscopic Study

The IR spectroscopic analysis is well exhibited in Fig. 4.7(d). Several peaks in IR spectra indicate that the metal atom is coordinated to the oxygen atoms of the carbonyl group of the AAm ligand. The partial shift of $\nu(\text{CO})$ vibration bands (1676 cm^{-1}) towards the longer wavelength region, is in trend with previous transition metal complex analysis. The spectra of the complexes contain footprints of vibration bands of nitrate anion at 1384 cm^{-1} ($\nu(\text{NO}_3)$) along with stretching and deformation vibration bands NH-groups ($\nu_s\text{NH}$ and $\nu_{as}\text{NH}$ at 3184 cm^{-1} and 3352 cm^{-1} , respectively and δNH at 1612 cm^{-1}). The vibrations of vinyl bond: 812 cm^{-1} , 980 cm^{-1} d (out-of-plane deformation mode of $=\text{CH}_2$), 1052 cm^{-1} (stretching mode of $=\text{CH}-\text{C}$), are observed in the field $810-1000\text{ cm}^{-1}$. Due to an overlap of the strong νCO absorption band with the $>\text{C}=\text{C}<$ band, the latter was not observed in the complex.

4.3.8 Thermogravimetric Analysis

Fig. 4.8(a) reveals the thermogravimetric degradation results of Cu_{0.8}Zn_{0.2}Sb₂AAM, measured from 35°C to 400°C in a nitrogen atmosphere. From the figure, successive decomposition can be observed with an increase in temperature. There are mainly two regions as observed in the curve. Initial weight loss was observed at $35^\circ\text{C} - 200^\circ\text{C}$ due to absorption of heat and later on successive evaporation of water vapour above 100°C . Here in this region, the weight loss was observed 44.44% of the initial weight. The second major loss was observed during the range of temperature $200-400^\circ\text{C}$ due to thermal decomposition for the gases and removal of functional groups like CO, OH, and NH₂ of the polymer with a degradation observed about 33 % and the final thermal decomposition of Cu_{0.8}Zn_{0.2}Sb₂AAM occurred beyond 400°C , caused by the thermal deformation of the polymer[46]. This analysis showed that CuZnSb acrylamide is more stable than acrylamide with an increased decomposition temperature of 400°C .

4.3.9 Differential Scanning Calorimetry (DSC)

Calorimetry is particularly useful in the study of crystallization as it provides a direct measurement of thermodynamic properties, heat of fusion, melting temperatures, etc. Insertion of metal ions within the polymer matrix drastically influences the thermal characteristics of the parent polymer. To investigate the thermal behaviour of Cu_{0.8}Zn_{0.2}Sb₂AAM. The bonded metal ions embedded in polymer matrices produce a higher number of charge carrier ions causing rigidity enhancement in the polymer chain up to optimum metal salt concentration. Consequently, the glass transition temperature reaches a higher value termed T_g which is shown in Fig. 4.8 (a). DSC analysis was performed in the temperature range from 35-400 °C in the presence of N₂. The DSC curve for Cu_{0.8}Zn_{0.2}Sb₂AAM is shown in Fig. 4.8 (b). It is noteworthy from the curve that the presence of one sharp endothermic with two wider exothermic peaks was confirmed at temperatures 81.5 °C, 195 °C, and 238.7 °C respectively.

4.3.10 XPS (X-ray Photoelectron Spectroscopy) Analysis

The chemical composition of the Cu_{0.8}Zn_{0.2}Sb₂ polyacrylamide nanocomposite was confirmed by XPS analysis exhibited in Fig. 4.9(a-f). XPS results show the binding energies of the Cu, Zn, Sb, C, N, and O elements with their corresponding atomic weight %. Characteristic peaks of the Cu are shown in Fig. 4.9(b) having the binding energy of 933 eV and 953.3 eV, which corresponds to two states Cu 2p_{3/2} and Cu 2p_{1/2} respectively [48]. The presence of Zinc (Zn 2p) is also confirmed from Fig. 4.9 (c) which shows the binding energies 1022.7 eV and 1045 eV corresponding to energy states Zn 2p_{3/2} and Zn 2p_{1/2} respectively [47]. Antimony element may also observe in Fig. 4.9(d). The electronic states of this element are Sb₂O₃ and Sb₃d_{3/2}, which matches well with the binding energies of 532.14 eV and 540 eV [49]. The remaining elements O, C, and N have two broad peaks of carbon as shown in Fig. 4.9 (e). The binding energies of 285 eV and 288 eV confirm the presence of the (C-C, C-O) and O-C=O respectively. Fig. 4.9 (f, g) shows the presence of Oxygen and Nitrogen elements with binding energies of 532 eV and 400 eV which confirmed the energy states O 1s(C-O) and N1s [49]. The histogram plot of atomic weight% and binding energies are observed from Figure 4.9 (g, h).

4.4 Photoconduction Analysis

The photoconduction behaviour of Cu_{0.8}Zn_{0.2}Sb₂ polyacrylamide nanocomposite was investigated under the exposure of white light aiming to its applicability in energy-saving elements, light-dependent resistors, etc. and the characteristic curve is shown in

Fig. 4.10 (a, b). Fig. 4.10 (a) shows the variation of change in electrical resistance concerning the time at 100 mW/cm² power intensity and Fig. 4.10 (b) exhibits the photodegradation and saturation in polymer nanocomposite after few cycles of response and recovery. This maximum response accompanied by a saturated response may be due to the polymeric nature of the metallopolymer nanomaterial. Successive change in electrical resistance of the thin film under the illumination of white light was measured. On the exposure of light, reduction in resistance exhibits the generation of the excess carrier in the Cu_{0.8}Zn_{0.2}Sb₂AAm nanomaterial.

The resistance measurement was executed in two conditions; initially in dark conditions and then in light conditions at ambient temperature under the exposure of a light beam having power intensity ~ 100 mW/cm². Hence we can say that the nanomaterial performs as a photoconductive material. The photoresponse was evaluated by using the following equation:

$$\% \text{ Response} = \frac{R_d - R_l}{R_d} \times 100 \dots \dots \dots (4.1)$$

where R_d and R_e are the electrical resistance in dark conditions and light conditions, respectively. The excess carriers in photoconductive nanomaterials are generated simultaneously, they start recombining with nearby counterparts. This change in the electrical resistance of the sample can be accounted to the conduction of unrecombined photoexcited charge carriers. For a better understanding of the conduction of charge carriers, the following equation can be given as

$$\Delta R = \frac{l}{q\mu dt\Delta n} \dots \dots \dots (4.2)$$

where l, d, and t are the length, width, and thickness of the sample. q and μ are the electronic charge and mobility. Δn is the change in charge carrier concentration in the presence of light.

When the light beam incident on the surface of a material, photons of the ray interacted with the material causing the generation of the electron-hole pairs. The generated electron-hole pairs at different junctions in the sample can easily be separated from each other. Due to sufficient excitation energy, the electrons transition from the valence band to the conduction band. After the first few cycles of change in resistance, the photoresponse of the nanomaterial gets stabilized at ~ 17.1%. This may also be

possible due to the combined effect of slight photodegradation and an increase in the concentration of electron-hole pairs. The representative curve exhibits that sawtooth wave characteristic which implies that the response changed subsequently with time and repeatable. In the light region, material follows a dramatic drop in resistance value. However, when light is turned off, the material almost regains its original state which is also a requirement of photoconductive nanomaterial. The highly sensitive polymer nanocomposite Cu_{0.8}Zn_{0.2}Sb₂AAM has the presence of a narrow optical band gap which provides a larger surface area, due to this reason the active sites of the material are responsible for the electron-hole pair generation through photon-phonon interaction. This phenomenon leads to enhanced photoconductive properties of the material. The resistance of material with the presence of light and dark regions can be given by the following equation:

$$R_l = R_0 \exp \frac{-t}{\tau_{res}} \dots \dots \dots (4.3)$$

$$R_d = R_0 \{1 - \exp(\frac{-t}{\tau_{rec}})\} \dots \dots \dots (4.4)$$

where R₀ is the electrical resistance in the dark region, τ_{res} and τ_{rec} are the response and recovery time respectively. The response time is defined as the time taken to obtain 90% of the maximum resistance. Response and recovery time are very important properties of any photoconductive device, therefore, we have evaluated the response and recovery time of Cu_{0.8}Zn_{0.2}Sb₂AAM nanomaterial and found it to be 6.6 sec and 10.24 sec. Response and recovery times have been evaluated in the present work which is quite good and highly comparable with other reported results. These data have been tabulated in Table 4.2.

4.5 Humidity Sensing Measurement

The hydrophilic nature of the Cu_{0.8}Zn_{0.2}Sb₂ acrylamide favours humidity sensing properties. Morphological features of the as-synthesized thin-film strongly encourage the adsorption/desorption on the surface. The presence of mesoporous voids avails more chemical affinity towards water molecules [14, 55]. These physical and chemical properties of Cu_{0.8}Zn_{0.2}Sb₂ acrylamide, in turn, improve the sensitivity of the film.

To examine the deterministic features of the Cu_{0.8}Zn_{0.2}Sb₂ acrylamide thin-film sensor, we have tested the sensing characteristics under the frequency range of 20 Hz -

2 MHz at ambient temperature. Later on, the humidity-sensing performance of the Cu_{0.8}Zn_{0.2}Sb₂ acrylamide thin-film sensor was investigated under various levels of humidity (%RH) depicted in Fig. 4.11 (a, b). Since the sensitivity curve, response time and recovery time, and stability are the key parameters that authenticate the reliability of this material as a humidity sensor hence these parameters were plotted and discussed in the manuscript.

It has been observed that as the value of operating frequencies raises, there is a gradual decrease in the capacitance of the film [56, 57]. The maximum capacitance value at 95 %RH was found as 10000 pF at a frequency of 20 Hz while the lowest capacitance value was found at 20 MHz. The same trend has been observed for both the adsorption and desorption processes. It has been observed that as humidity (%RH) increases from 33 % to 95 %, the value of capacitance increases monotonically in the same trend. Since the relative humidity level increases, the output capacitance of the sensor ultimately reached a higher value. The responsible cause for this behaviour is the adsorbed water molecules which empower the polarization process and due to this polarization, the dielectric constant of the sensing element increases. This, in turn, affects the capacitance [58, 59]. Among the various test frequencies, 20 Hz exhibits the best linearity for humidity sensing characteristics so this frequency was selected for determining the other sensing characteristics. The Cu_{0.8}Zn_{0.2}Sb₂AAM polymer nanocomposite sensing film shows the liner curve from the 70-95 %RH in increasing mode and 95-75 %RH in decreasing mode at 20 Hz frequency which are shown as an inset in Fig. 4.11 (a & b). In Fig. 4.11 (c & d), the normalized sensor response with the exponential data fitting curves as a function of %RH for nanocomposite at 20 Hz frequency has also been provided.

The dependency of capacitance and frequency were thoroughly enquired under the influence of different %RH values well depicted in Fig. 4.11 (a). The variation of capacitance with operating frequency excellently exhibits a characteristic trend [58-60]. It is obvious from the curve that the capacitance (C) changes with increase in frequency. Interestingly, the level of decrease in capacitance value is faster at a higher %RH level compared to the lower %RH values. The capacitance value increases with (%RH) in the range of lower frequency regime (below 2 kHz) and in the higher frequency range, the change in capacitance is almost negligible and becomes independent of humidity

conditions[61]. Humidity seems to be ineffective at a frequency beyond 2 kHz. Ideal capacitive sensor inherits this property i.e. the value of capacitances is independent of applied frequency. In low humidity conditions sensing material absorbs a small quantity of water, thus serving as a favourable circumstance for an ideal capacitive sensor [61, 62]. This is because the electric field direction changes gradually at low frequencies with the appearance of space-charge polarization in adsorbed water when the frequency is high, the electrical field direction changes so fast that the polarization of the adsorbed water cannot be connected with it, and hence the dielectric constant is small and independent of relative humidity.

From Fig. 4.12 (b), it can be observed that the value of capacitance is influenced by the frequency (20 Hz - 2 MHz). The relative humidity (10 to 95 %RH) affects the sensitivity of material which varies following the frequency variation. It can be easily seen that at 20 Hz frequency, the capacitance increases rapidly with the relative humidity and the value of capacitance changes from 3.5 pF to 9486 pF which gives the average sensitivity $S \sim 168.477\%$. On the other hand, at 2 MHz frequency, a minute change from 3.6 pF to 4.59 pF in capacitance was found which corresponds to the sensitivity $S \sim 0.004\%$ across the RH range of 10%–95%. Thus the major difference in the sensitivity was observed at 20 Hz as the optimum frequency for this sensor and is well shown in Fig. 4.12 (b). The sensitivity of the humidity-dependent capacitive Cu_{0.8}Zn_{0.2}Sb₂ acrylamide thin-film is defined as [57]:

$$\text{Sensitivity} = \frac{C_{\text{final}} - C_{\text{initial}}}{RH_{\text{final}} - RH_{\text{initial}}} \dots\dots\dots(4.5)$$

Where C_{final} and C_{initial} are the capacitive values at final and initial %RH levels respectively. Fig. 4.12(b) shows that the frequency affects the sensitivity of the material. Fig. 4.12 (c) shows the humidity sensor response curve between capacitance and time. The linear coordinate curve is shown as a blue line while logarithmic coordinates are shown as a pink line. There is a non-linear curve in the whole range (10–95 %RH). Fig. 4.12 (d) displays the sensitivity calculation by linear fitting data of the adsorption curve at 20 Hz, as we know the sensor response curve shows the exponential change between capacitance and humidity [21, 63]. The humidity is linearly fitted into three regions 10-45 %RH, 45-75 %RH, and 75-95 %RH, and the values of the slope obtained are shown in Table 4.3.

4.5.2 Response and recovery

Response and recovery times are the essential demands which significantly define the performance of a humidity sensor. Sensors with short response and recovery time are the best for application and commercialization. Time taken by a sensor to accomplish ~90% of the total capacitance change is defined as the response time in case of adsorption or termed as the recovery time in case of desorption of the water vapours [10, 56, 64]. Both response and recovery times were plotted in Fig. 4.13 (a). Accordingly, the sensor response time (humidification from 10 %RH to 95 %RH) and the recovery time (desiccation from 95 %RH to 10 %RH) were calculated as 4.6 sec and 5.6 sec respectively. In comparison to the conventional polymer-based humidity sensors, the Cu_{0.8}Zn_{0.2}Sb₂ acrylamide thin-film sensor has proven better [55-62, 64]. These exceptional characteristics are contributed because of repeating units of the monomer CH₂CH(CONH₂). The nitrogen forms hydrogen bonds with water molecules resulting in a strong hydrophilic nature and can form aqueous solutions of very high concentration. Polymers are generally gel forms and due to their gel-like properties, these polymers are widely employed as flocculants in the removal of suspended particles from sewage and industrial effluents.

4.5.3 Stability

Stability is a very important parameter for any sensor. The reliability of any sensor for a long-term operation corresponds to its stability over a certain duration of time. We have monitored stability characteristics of sensing elements operating at a frequency of 20 Hz under different %RH values e.g. 15%, 35%, 55%, 75%, and 95% for 60 days. The humidity sensing parameters were repeated every 10 days and data have been plotted Fig. 4.13 (b). The stability curve shows a 4% variation in the capacitance at this operating frequency. This exhibits the consistent sensing capability of polyacrylamide film suitable for the purpose for which it was fabricated.

4.5.4 Sensing Mechanism

The mechanism devoted to the electrical response of the sensing element upon exposure to humidity is the chemical and physical adsorption of water molecules on the surface of the sensing element. Particularly concern to capacitive based humidity sensor

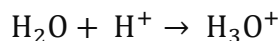
the relationship between the capacitance and the %RH can be expressed by the following equation;

$$C = (\epsilon_r - i \frac{\gamma}{\omega \epsilon_0}) C_0 \dots \dots \dots (4.6)$$

Where c indicates the conductance and v represents applied frequency. From the above expression, it is clear that the capacitance of the sensing element is proportional to C_0 whereas C is inversely proportional to operating frequency [56, 58-61, 64]. C_0 is related to the physisorption of water molecules on sensing film such that different adsorption processes yield different conduction values. From the formula, it's obvious that the capacitance increases with rising RH, depending on the frequency.

Fig. 4.14 shows the humidity sensing mechanism, despite the minimal surface area of thin-film, the presence of metals provides more surface-active sites in the form of M^+ ions to bond with the OH^- causing the formation of initial chemisorption on the sensor surface. Initially, at lower %RH, water molecules are chemisorbed onto the available unsaturated nitrogen bonds (hydrophilic group) of the sensing film through double hydrogen bonding, considered as the first-layer chemisorption of water. In this regime, it's hard for the water molecules to travel independently because of strong attraction due to double hydrogen bonding. Successively proton hopping initiates between adjacent hydroxyl groups in the first- chemisorbed layer of water influence more amount of energy thus exhibiting a strong electrical resistance. Later on a few protons available on the surface of the polymer film are confined by irregular mobile layers. These protons still contribute to the leak conduction c , which ultimately increases the capacitance at a low humidity regime. As the %RH increases, the multilayer physisorbed water molecules arise [36,50], forming the physisorbed layer, having water molecules attached through single hydrogen bonding on the hydroxyl groups. Consequently, the water molecules become transportable, likely to appear as in the bulk liquid. The formation of subsequent multilayer physical adsorption and the decomposition of physisorbed water causing ionization under an electrostatic field to produce a large number of hydronium ions (H_3O^+) in the form of charge carriers. Thus charge transport on the film took place via the conductivity of the material generated by a Grotthuss chain reaction. The charge transport expression is given as below;





Finally, at high %RH, the physisorbed water molecules will penetrate the interlayer of the sensing film. A large number of prevailing amide groups in polymer facilitate proton migration. This leads to a sudden increase of capacitance of the material, causing a quite high sensitivity at high %RH, which is very fruitful for the dielectric constant of the material.

4.6 Conclusion

Cu_{0.8}Zn_{0.2}Sb₂AAM based capacitive humidity sensor was successfully fabricated using a spin coating technique and the photoconduction behaviour of the material was also investigated. The presence of mesoporous morphology of the fabricated thin-film energized the sensing capability of film. The wide bandgap of 3.91 eV facilitates better conduction accompanied by a synergistic interaction between metal Cu-Zn-Sb ternary phase and PAAm boost the sensitivity as well as photoconductivity of the thin film based sensing element. Cu_{0.8}Zn_{0.2}Sb₂AAM-polymer interfaces exhibited the photoconduction behaviour revealing response and recovery time of 6.6 sec and 10.24 sec. Humidity sensing characteristics on film surface were evaluated by the capacitive performance of Cu_{0.8}Zn_{0.2}Sb₂AAM based thin film humidity sensor. The Average sensitivity (S) was found to be ~168.477 pF/%RH at an optimum frequency of 20 Hz. The thin-film-based sensor exhibits a rapid response and recovery time of 4.6 sec and 5.6 sec respectively, with a 96% sensitivity retention after 60 days. Thus, Cu_{0.8}Zn_{0.2}Sb₂AAM polymer-based capacitive humidity sensor provides an insight measure for a stabilized ternary system based on polymer nanocomposite for humidity sensing and photoconduction application.

References

- [1] W. Sun, G. Zhang, L. Pan, H. Li, A. Shi, Synthesis, Characterization, and Flocculation Properties of Branched Cationic Polyacrylamide, *International Journal of Polymer Science*, 2013 (2013) 397027.
- [2] M. Friedman, Chemistry, Biochemistry, and Safety of Acrylamide. A Review, *Journal of Agricultural and Food Chemistry*, 51 (2003) 4504-4526.
- [3] A.M. Schiller, T.J. Suen, Ionic Derivatives of Polyacrylamide, *Industrial & Engineering Chemistry*, 48 (1956) 2132-2137.
- [4] J. Xiang, C.-L. Ho, W.-Y. Wong, Metallopolymers for energy production, storage and conservation, *Polymer Chemistry*, 6 (2015) 6905-6930.
- [5] R. Ramay, P. Sankar, S. Anbalagan, P.N. Sudha, Adsorption of Cu(II) and Ni(II) ions from metal solution using crosslinked chitosan-g-acrylonitrile copolymer, *Int. J. Environ. Sci.*, 1 (2011) 1323-1338.
- [6] D.K. Maurya, S. Sikarwar, P. Chaudhary, S. Angaiah, B.C. Yadav, Synthesis and Characterization of Nanostructured Copper Zinc Tin Sulphide (CZTS) for Humidity Sensing Applications, *IEEE Sensors Journal*, 19 (2019) 2837-2846.
- [7] M. K.Trivedi, S. Patil, R. Mishra, S. Jain, characterization of Thermal and Physical Properties of Biofield Treated Acrylamide and 2-Chloroacetamide, *Organic Chemistry: Current Research*, 04 (2015).
- [8] G.I. Dzhardimalieva, S.A. Semenov, E.I. Knerelman, G.I. Davydova, K.A. Kydralieva, Preparation and Reactivity of Metal-Containing Monomers. 78. Scandium-Containing Monomers And Polymers: Synthesis, Structure and Properties, *Journal of Inorganic and Organometallic Polymers and Materials*, 26 (2016) 1441-1451.
- [9] P. Chaudhary, S. Sikarwar, B.C. Yadav, G.I. Dzhardimalieva, N.D. Golubeva, I.E. Uflyand, Synthesis and characterization of copper (II) nitrate polyacrylamide & its application as opto-electronic humidity sensor, *Sensors and Actuators A: Physical*, 263 (2017) 415-422.

- [10] X. He, W. Geng, B. Zhang, L. Jia, L. Duan, Q. Zhang, Ultrahigh humidity sensitivity of NaCl-added 3D mesoporous silica KIT-6 and its sensing mechanism, *RSC Advances*, 6 (2016) 38391-38398.
- [11] K.K. Jaiswal, D. Manikandan, R. Murugan, A.P. Ramaswamy, Microwave-assisted rapid synthesis of Fe₃O₄/poly(styrene-divinylbenzene-acrylic acid) polymeric magnetic composites and investigation of their structural and magnetic properties, *European Polymer Journal*, 98 (2018) 177-190.
- [12] B.C.Yadav, S. Sikarwar, R. Yadav, P. Chaudhary, G.I. Dzhardimalieva, N.D. Golubeva, Preparation of zinc (II) nitrate poly acrylamide (PAAm) and its optoelectronic application for humidity sensing, *Journal of Materials Science: Materials in Electronics*, 29 (2018) 7770-7777.
- [13] P. Chaudhary, D.K. Maurya, S. Sikarwar, B. C. Yadav, G.I. Dzhardimalieva, R. Prakash, Development of nanostructured nickel reinforced polyacrylamide via frontal polymerization for a reliable room temperature humidity sensor, *European Polymer Journal*, 112 (2019) 161-169.
- [14] S. Schlecht, C. Erk, M. Yosef, Nanoscale Zinc Antimonides: Synthesis and Phase Stability, *Inorganic Chemistry*, 45 (2006) 1693-1697.
- [15] D. Suksongkarm, S. Rojananan, S. Rojananan, Microstructure and Hardness of Cu-Zn-Si-Al-Sn Brasses with Antimony Addition, *Advanced Materials Research*, 802 (2013) 179-183.
- [16] H.-J. Gau, J.-L. Yu, C.-C. Wu, Y.-K. Kuo, C.-H. Ho, Thermoelectric properties of Zn-Sb alloys doped with In, *Journal of Alloys and Compounds*, 480 (2009) 73-75.
- [17] A. Klopotov, Y. Ivanov, V. Vlasov, N. Dedov, O. Loskutov, Phase transformations in the system Cu-Zn-Al under conditions far from equilibrium, *AIP Conference Proceedings*, 1698 (2016) 030004.
- [18] S. Praiphruk, G. Lothongkum, E. Nisaratanaporn, B. Lohwongwatana, Effects of Copper (Cu), Indium (In), Tin (Sn), Antimony (Sb) and Zinc (Zn) in Sterling Silver Alloys on Mechanical Properties Improvement, *Materialprufung*, 55 (2013) 819-823.

- [19] H.M. Rawson, J.E. Begg, R.G. Woodward, The effect of atmospheric humidity on photosynthesis, transpiration and water use efficiency of leaves of several plant species, *Planta*, 134 (1977) 5-10.
- [20] R.B. Stringfield, Effect of Humidity in Rubber Testing, *Industrial & Engineering Chemistry*, 17 (1925) 833-835.
- [21] Z. Duan, Y. Jiang, M. Yan, S. Wang, Z. Yuan, Q. Zhao, P. Sun, G. Xie, X. Du, H. Tai, Facile, Flexible, Cost-Saving, and Environment-Friendly Paper-Based Humidity Sensor for Multifunctional Applications, *ACS Applied Materials & Interfaces*, 11 (2019) 21840-21849.
- [22] Z. Duan, Q. Zhao, S. Wang, Z. Yuan, Y. Zhang, X. Li, Y. Wu, Y. Jiang, H. Tai, Novel application of attapulgite on high performance and low-cost humidity sensors, *Sensors and Actuators B: Chemical*, 305 (2020) 127534.
- [23] Z. Duan, Q. Zhao, S. Wang, Q. Huang, Z. Yuan, Y. Zhang, Y. Jiang, H. Tai, Halloysite nanotubes: Natural, environmental-friendly and low-cost nanomaterials for high-performance humidity sensor, *Sensors and Actuators B: Chemical*, 317 (2020) 128204.
- [24] H. Tai, S. Wang, Z. Duan, Y. Jiang, Evolution of breath analysis based on humidity and gas sensors: Potential and challenges, *Sensors and Actuators B: Chemical*, 318 (2020) 128104.
- [25] Z. Duan, Y. Jiang, Q. Zhao, S. Wang, Z. Yuan, Y. Zhang, B. Liu, H. Tai, Facile and low-cost fabrication of a humidity sensor using naturally available sepiolite nanofibers, *Nanotechnology*, 31 (2020) 355501.
- [26] S. Kiruthika, S. Singh, G.U. Kulkarni, Large area transparent ZnO photodetectors with Au wire network electrodes, *RSC Advances*, 6 (2016) 44668-44672.
- [27] B. Ouyang, K. Zhang, Y. Yang, Photocurrent Polarity Controlled by Light Wavelength in Self-Powered ZnO Nanowires/SnS Photodetector System, *iScience*, 1 (2018) 16-23.
- [28] R.K. Tripathi, O.S. Panwar, A.K. Kesarwani, I. Rawal, B.P. Singh, M.K. Dalai, S. Chockalingam, Investigations on phosphorous doped hydrogenated amorphous

- silicon carbide thin films deposited by a filtered cathodic vacuum arc technique for photo detecting applications, *RSC Advances*, 4 (2014) 54388-54397.
- [29] R.K. Tripathi, O.S. Panwar, I. Rawal, B.P. Singh, B.C. Yadav, Study on nanocrystalline silicon thin films grown by the filtered cathodic vacuum arc technique using boron doped solid silicon for fast photodetectors, *Journal of the Taiwan Institute of Chemical Engineers*, 86 (2018) 185-191.
- [30] M. Peng, X. Zheng, Z. Ma, H. Chen, S. Liu, Y. He, M. Li, Ni-pattern guided GaN nanowire-array humidity sensor with high sensitivity enhanced by UV photoexcitation, *Sensors and Actuators B: Chemical*, 256 (2018) 367-373.
- [31] S.W. James, R.P. Tatam, Optical fibre long-period grating sensors: characteristics and application, *Measurement Science and Technology*, 14 (2003) R49-R61.
- [32] W. Li, J. Liu, C. Ding, G. Bai, J. Xu, Q. Ren, J. Li, Fabrication of Ordered SnO₂ Nanostructures with Enhanced Humidity Sensing Performance, *Sensors*, 17 (2017).
- [33] A. Lopez Aldaba, D. Lopez-Torres, C. Elosua, J.L. Auguste, R. Jamier, P. Roy, F.J. Arregui, M. Lopez-Amo, SnO₂-MOF-Fabry-Perot optical sensor for relative humidity measurements, *Sensors and Actuators B: Chemical*, 257 (2018) 189-199.
- [34] M. Parthibavarman, V. Hariharan, C. Sekar, High-sensitivity humidity sensor based on SnO₂ nanoparticles synthesized by microwave irradiation method, *Materials Science and Engineering: C*, 31 (2011) 840-844.
- [35] L. Xia, L. Li, W. Li, T. Kou, D. Liu, Novel optical fiber humidity sensor based on a no-core fiber structure, *Sensors and Actuators A: Physical*, 190 (2013) 1-5.
- [36] W. Xie, M. Yang, Y. Cheng, D. Li, Y. Zhang, Z. Zhuang, Optical fiber relative-humidity sensor with evaporated dielectric coatings on fiber end-face, *Optical Fiber Technology*, 20 (2014) 314-319.
- [37] S.F.A.Z. Yusoff, C.S. Lim, S.R. Azzuhri, H. Ahmad, R. Zakaria, Studies of Ag/TiO₂ plasmonics structures integrated in side polished optical fiber used as humidity sensor, *Results in Physics*, 10 (2018) 308-316.

- [38] D. Zhang, Y.e. Sun, P. Li, Y. Zhang, Facile Fabrication of MoS₂-Modified SnO₂ Hybrid Nanocomposite for Ultrasensitive Humidity Sensing, *ACS Applied Materials & Interfaces*, 8 (2016) 14142-14149.
- [39] L. Alwis, T. Sun, K.T.V. Grattan, Fibre optic long period grating-based humidity sensor probe using a Michelson interferometric arrangement, *Sensors and Actuators B: Chemical*, 178 (2013) 694-699.
- [40] J.N. Mbithi, V.S. Springthorpe, S.A. Sattar, Effect of relative humidity and air temperature on survival of hepatitis A virus on environmental surfaces, *Appl Environ Microbiol*, 57 (1991) 1394-1399.
- [41] S. Sikarwar, B.C. Yadav, S. Singh, G.I. Dzhardimalieva, S.I. Pomogailo, N.D. Golubeva, A.D. Pomogailo, Fabrication of nanostructured yttria stabilized zirconia multilayered films and their optical humidity sensing capabilities based on transmission, *Sensors and Actuators B: Chemical*, 232 (2016) 283-291.
- [42] B.C. Yadav, R.C. Yadav, S. Singh, P.K. Dwivedi, H. Ryu, S. Kang, Nanostructured cobalt oxide and cobalt titanate thin films as optical humidity sensor: A new approach, *Optics & Laser Technology*, 49 (2013) 68-74.
- [43] H.J. Naghash, O. Okay, Formation and structure of polyacrylamide gels, *Journal of Applied Polymer Science*, 60 (1996) 971-979.
- [44] A.K. Solarajan, V. Murugadoss, S. Angaiah, Dimensional stability and electrochemical behaviour of ZrO₂ incorporated electrospun PVdF-HFP based nanocomposite polymer membrane electrolyte for Li-ion capacitors, *Scientific Reports*, 7 (2017) 45390.
- [45] K.B. Girma, V. Lorenz, S. Blaurock, F.T. Edelmann, Coordination Chemistry of Acrylamide 4. Crystal Structures and IR Spectroscopic Properties of Acrylamide Complexes with CoII, NiII, and Zn II nitrates, *Chemie*, 631 (2005) 1843-1848.
- [46] P. Zhang, T. Song, T. Wang, H. Zeng, In-situ synthesis of Cu nanoparticles hybridized with carbon quantum dots as a broad spectrum photocatalyst for improvement of photocatalytic H₂ evolution, *Applied Catalysis B: Environmental*, 206 (2017) 328-335.

- [47] N. Li, S. Liao, Y. Sun, H.W. Song, C.X. Wang, Uniformly dispersed self-assembled growth of Sb₂O₃/Sb@graphene nanocomposites on a 3D carbon sheet network for high Na-storage capacity and excellent stability, *Journal of Materials Chemistry A*, 3 (2015) 5820-5828.
- [48] G. Vijayaprasath, R. Murugan, Y. Hayakawa, G. Ravi, Optical and magnetic studies on Gd doped ZnO nanoparticles synthesized by co-precipitation method, *Journal of Luminescence*, 178 (2016) 375-383.
- [49] S. Yadav, P. Chaudhary, K. Uttam, A. Varma, M. Vashistha, B. Yadav, Facile synthesis of molybdenum disulfide (MoS₂) quantum dots and its application in humidity sensing, *Nanotechnology*, 30 (2019) 295501.
- [50] C. Chen, H. Qiao, S. Lin, C. Man Luk, Y. Liu, Z. Xu, J. Song, Y. Xue, D. Li, J. Yuan, W. Yu, C. Pan, S. Ping Lau, Q. Bao, Highly responsive MoS₂ photodetectors enhanced by graphene quantum dots, *Scientific Reports*, 5 (2015) 11830.
- [51] J. Cao, Z. Wang, X. Zhan, Q. Wang, M. Safdar, Y. Wang, J. He, Vertical SnSe nanorod arrays: from controlled synthesis and growth mechanism to thermistor and photoresistor, *Nanotechnology*, 25 (2014) 105705.
- [52] A.S. Pawbake, R.G. Waykar, D.J. Late, S.R. Jadkar, Highly Transparent Wafer-Scale Synthesis of Crystalline WS₂ Nanoparticle Thin Film for Photodetector and Humidity-Sensing Applications, *ACS Applied Materials & Interfaces*, 8 (2016) 3359-3365.
- [53] M.B. Erande, M.S. Pawar, D.J. Late, Humidity Sensing and Photodetection Behavior of Electrochemically Exfoliated Atomically Thin-Layered Black Phosphorus Nanosheets, *ACS Applied Materials & Interfaces*, 8 (2016) 11548-11556.
- [54] M.S. Pawar, P.K. Bankar, M.A. More, D.J. Late, Ultra-thin V₂O₅ nanosheet based humidity sensor, photodetector and its enhanced field emission properties, *RSC Advances*, 5 (2015) 88796-88804.
- [55] H. Bi, K. Yin, X. Xie, J. Ji, S. Wan, L. Sun, M. Terrones, M.S. Dresselhaus, Ultrahigh humidity sensitivity of graphene oxide, *Scientific Reports*, 3 (2013) 2714.

- [56] A. Tripathy, S. Pramanik, J. Cho, J. Santhosh, A.N. Osman, Role of Morphological Structure, Doping, and Coating of Different Materials in the Sensing Characteristics of Humidity Sensors, *Sensors*, 14 (2014).
- [57] A. Tripathy, S. Pramanik, A. Manna, S. Bhuyan, N. Shah, Z. Radzi, N. Osman, Design and Development for Capacitive Humidity Sensor Applications of Lead-Free Ca,Mg,Fe,Ti-Oxides-Based Electro-Ceramics with Improved Sensing Properties via Physisorption, *Sensors*, 16 (2016) 1135.
- [58] H.M.J. Al-Ta, Y.M. Amin, V. Periasamy, Humidity influenced capacitance and resistance of an Al/DNA/Al Schottky diode irradiated by alpha particles, *Scientific Reports*, 6 (2016) 25519.
- [59] J. Boudaden, M. Steinmaßl, H.-E. Endres, A. Drost, I. Eisele, C. Kutter, P. Müller-Buschbaum, Polyimide-Based Capacitive Humidity Sensor, *Sensors (Basel)*, 18 (2018) 1516.
- [60] C.-Y. Lee, G.-B. Lee, Humidity Sensors: A Review, *Sensor Letters*, 3 (2005) 1-15.
- [61] P.-G. Su, W.-Y. Tsai, Humidity sensing and electrical properties of a composite material of nano-sized SiO₂ and poly(2-acrylamido-2-methylpropane sulfonate), *Sensors and Actuators B: Chemical*, 100 (2004) 417–422.
- [62] J. Wang, Q. Lin, R. Zhou, B. Xu, Humidity sensors based on composite material of nano-BaTiO₃ and polymer RMX, *Sensors and Actuators B: Chemical*, 81 (2002) 248-253.
- [63] Z. Duan, M. Xu, T. Li, Y. Zhang, H. Zou, Super-fast response humidity sensor based on La_{0.7}Sr_{0.3}MnO₃ nanocrystals prepared by PVP-assisted sol-gel method, *Sensors and Actuators B: Chemical*, 258 (2018) 527-534.
- [64] S. Dinc Zor, H. Cankurtaran, Impedimetric Humidity Sensor Based on Nanohybrid Composite of Conducting Poly(diphenylamine sulfonic acid), *Journal of Sensors*, 2016 (2016) 5479092.

Tables:

Table 4.1. A detailed literature survey of other humidity sensing materials with %RH.

S.No.	Materials	Sensitivity	Range (%RH)	Ref.
1.	SnO ₂ Nanostructures	0.01 pF/%RH	11-96	[32]
2.	Fe-GO	5.18 pF/%RH	10-95	[33]
3.	Au/PVA	11.38 pF/% RH	11.3-97	[34]
4.	Polyimide	24.5pF/% RH	16-90	[35]
5.	Graphene oxide	46.253pF/% RH	15-95	[31]
6.	Modified MWCNT (Dispersed in NMP)	6.41 pF/%RH	10-90	[39]
7.	Tin dioxide/reduced graphene oxide (RGO)	146.53 pF/%RH	25-95	[37]
8.	MoS ₂ modified SnO ₂	156.97 pF/%RH	11-95	[38]
9.	Cu _{0.8} Zn _{0.2} Sb ₂ AAM nanocomposite	150.75 pF/%RH	10-95	Present work

Table 4.2 Comparative study of response and recovery times

Material name	Synthesis Method	Response time	Recovery time	Reference
MoS ₂	Chemical vapour deposition	20 sec	10.97 sec	[50]

SnSe	Chemical vapour deposition	8.2 sec	5.3 sec	[51]
WS ₂	Chemical vapor deposition	51 sec	88 sec	[52]
Phosphorus	Electrochemical exfoliation	15 sec	30 sec	[53]
V ₂ O ₅	Hydrothermal method	65 sec	75 sec	[54]
Cu _{0.8} Zn _{0.2} Sb ₂ AA m nanomaterial	Frontal polymerization	6.6 sec	10.24 sec	This work

Table 4.3. Sensitivity at different frequencies of Cu_{0.8}Zn_{0.2}Sb₂AAm polymer nanocomposite

Frequency	Low humidity region (10-45 %RH)	Mid humidity region (45-75 %RH)	High humidity region (75-95 %RH)	Avg. sensitivity (pF/%RH)
2*10 ¹ Hz	3.890	45.466	456.076	168.477 pF/%RH
2*10 ² Hz	2.801	3.562	66.980	24.447 pF/%RH
2*10 ³ Hz	1.890	2.145	4.961	2.998 pF/%RH
2*10 ⁴ Hz	0.161	0.552	5.990	2.234 pF/%RH
2*10 ⁵ Hz	0.002	0.006	0.041	0.016 pF/%RH
2*10 ⁶ Hz	0.001	0.004	0.009	0.004 pF/%RH

Figures:

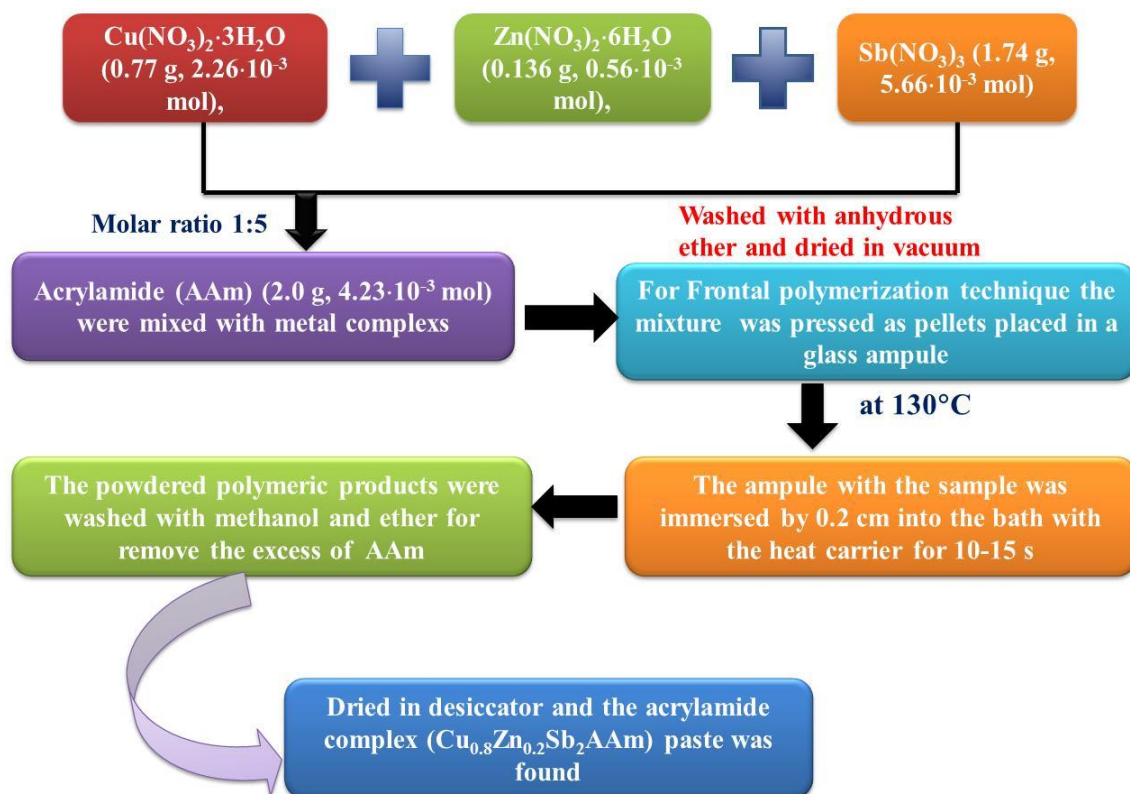


Figure 4.1 Flow chart for the synthesis of polymer nanocomposite ($Cu_{0.8}Zn_{0.2}Sb_2AAM$).

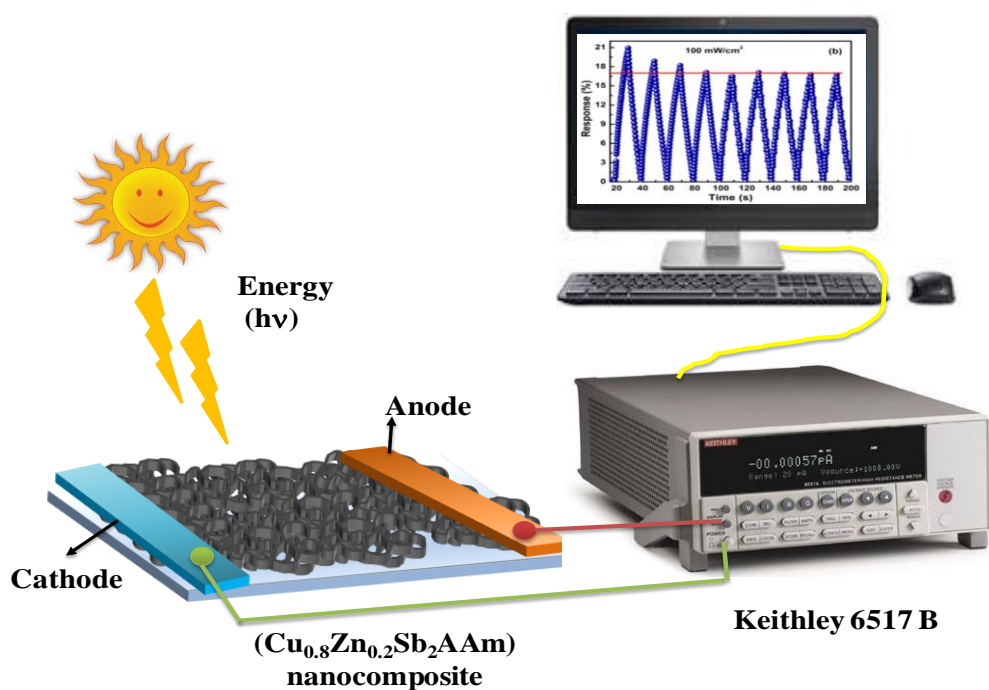


Figure 4.2 Schematic diagram of Photoconduction set-up.

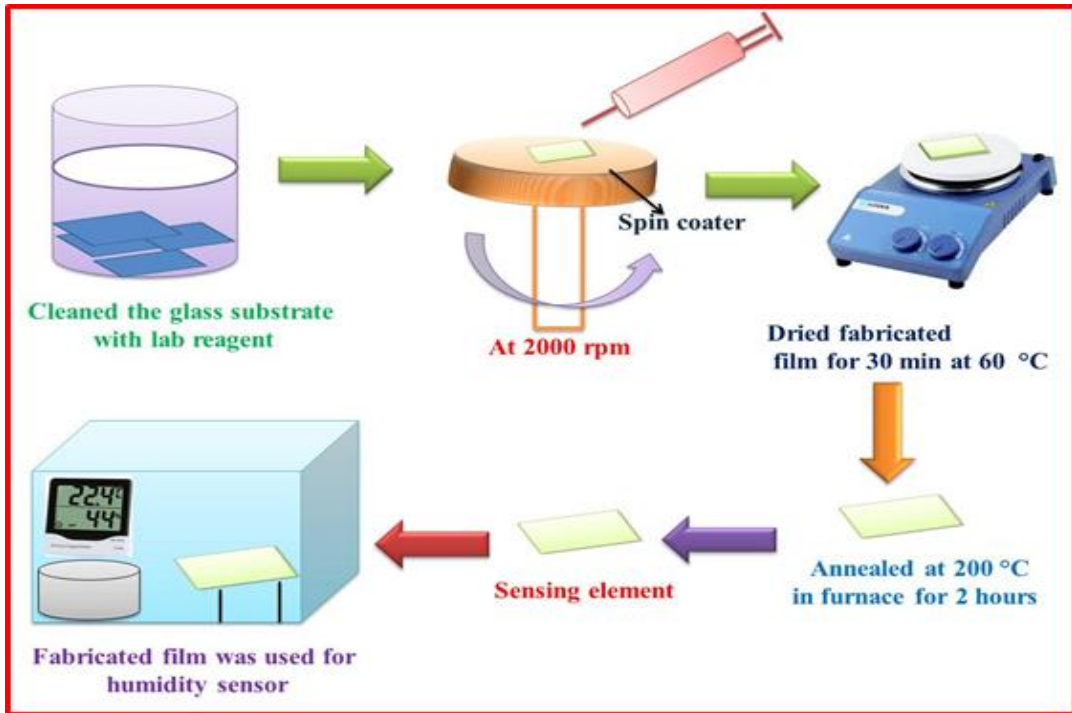


Figure 4.3 Schematic presentation of the preparation of $\text{Cu}_{0.8}\text{Zn}_{0.2}\text{Sb}_2\text{AAm}$ film by the spin coating method.

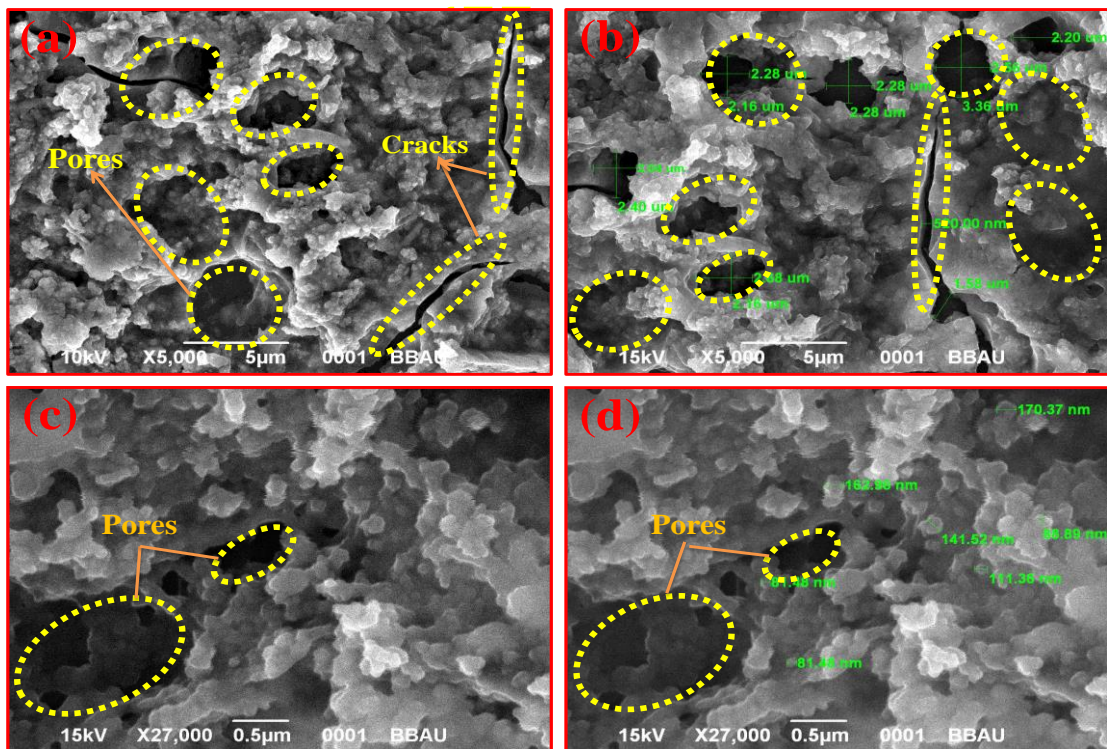


Figure 4.4 SEM images showing the morphology of $\text{Cu}_{0.8}\text{Zn}_{0.2}\text{Sb}_2\text{AAm}$ thin-film possess a highly porous rigid structure with few cracks and pores on the surface with a different scale.

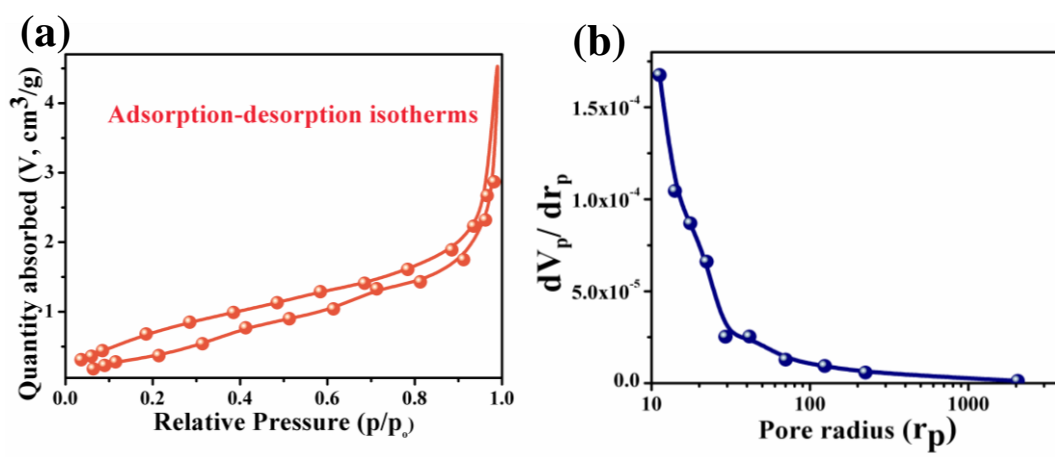


Figure 4.5 (a) adsorption-desorption isotherms of $(\text{Cu}_{0.8}\text{Zn}_{0.2}\text{Sb}_2\text{AAm})$ (b) Pore radius distribution curves relative to variation in the pore volume.

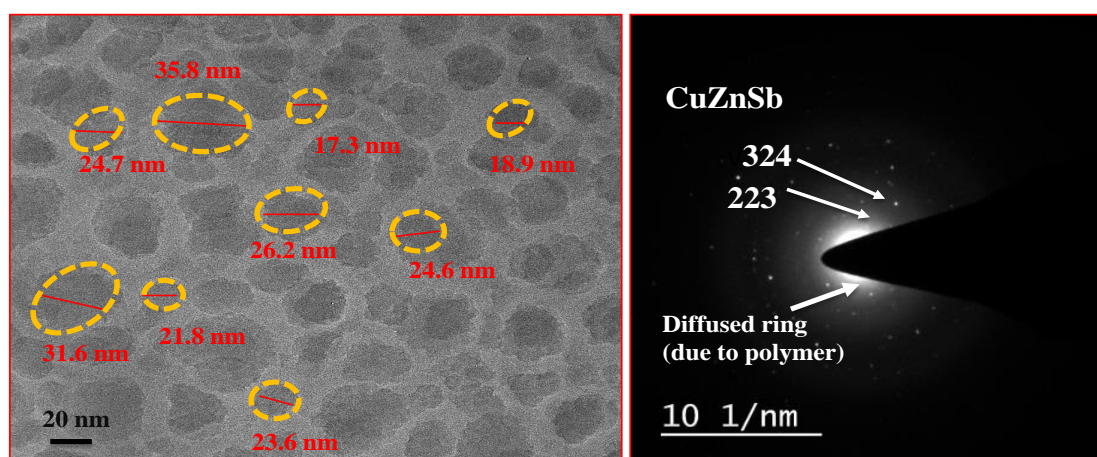


Figure 4.6 (a) The TEM image of $\text{Cu}_{0.8}\text{Zn}_{0.2}\text{Sb}_2\text{AAm}$ thin film (b) SAED pattern of $\text{Cu}_{0.8}\text{Zn}_{0.2}\text{Sb}_2\text{AAm}$.

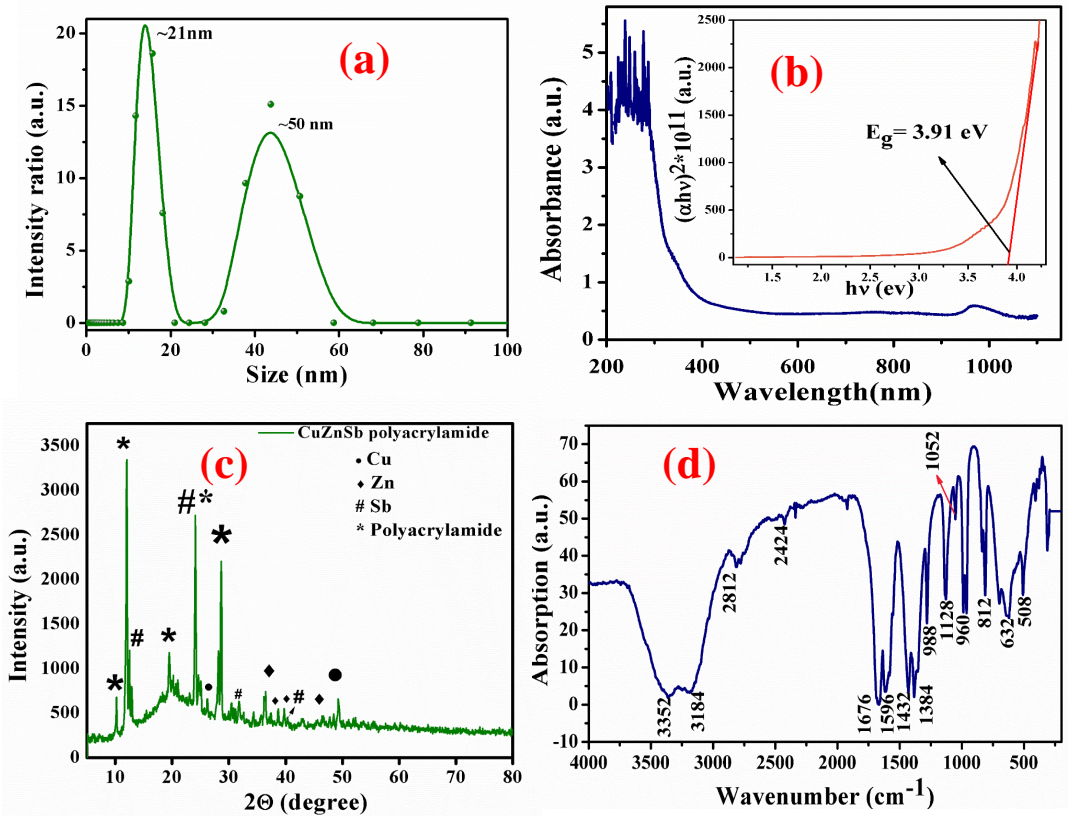


Figure 4.7 (a) The particle size distribution curve shows that the peaks are divided into two major intensities. (b) The optical absorbance spectra of the fabricated film in the wavelength range of 190-1100 nm where inset shows the Tauc plot (c) XRD pattern of $\text{Cu}_{0.8}\text{Zn}_{0.2}\text{Sb}_2\text{AAm}$, confirms the crystalline nature and the presence of Cu, Zn and Sb with their characteristic peaks. (d) IR spectra of $\text{Cu}_{0.8}\text{Zn}_{0.2}\text{Sb}_2\text{AAm}$ thin film.

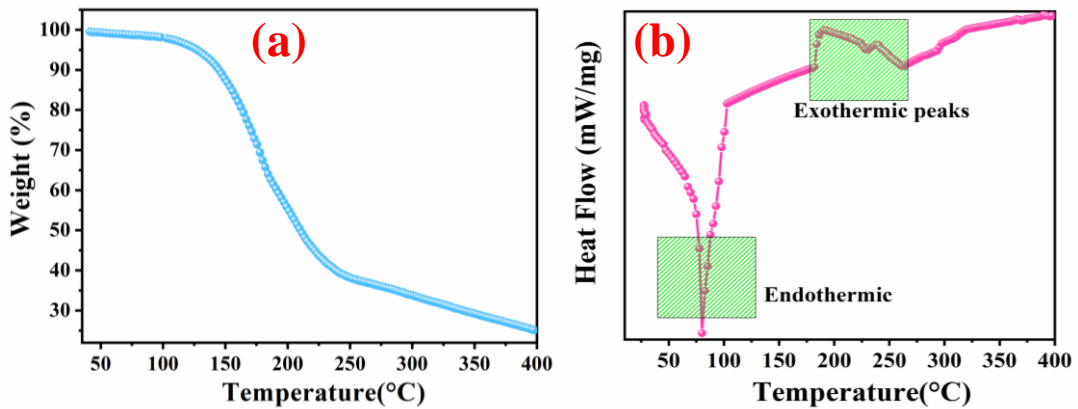


Figure 4.8 (a) TGA (b) DSC curves of $\text{Cu}_{0.8}\text{Zn}_{0.2}\text{Sb}_2$ polyacrylamide in an argon atmosphere with the heating rate of $10\text{ }^\circ\text{C}$ per minute.

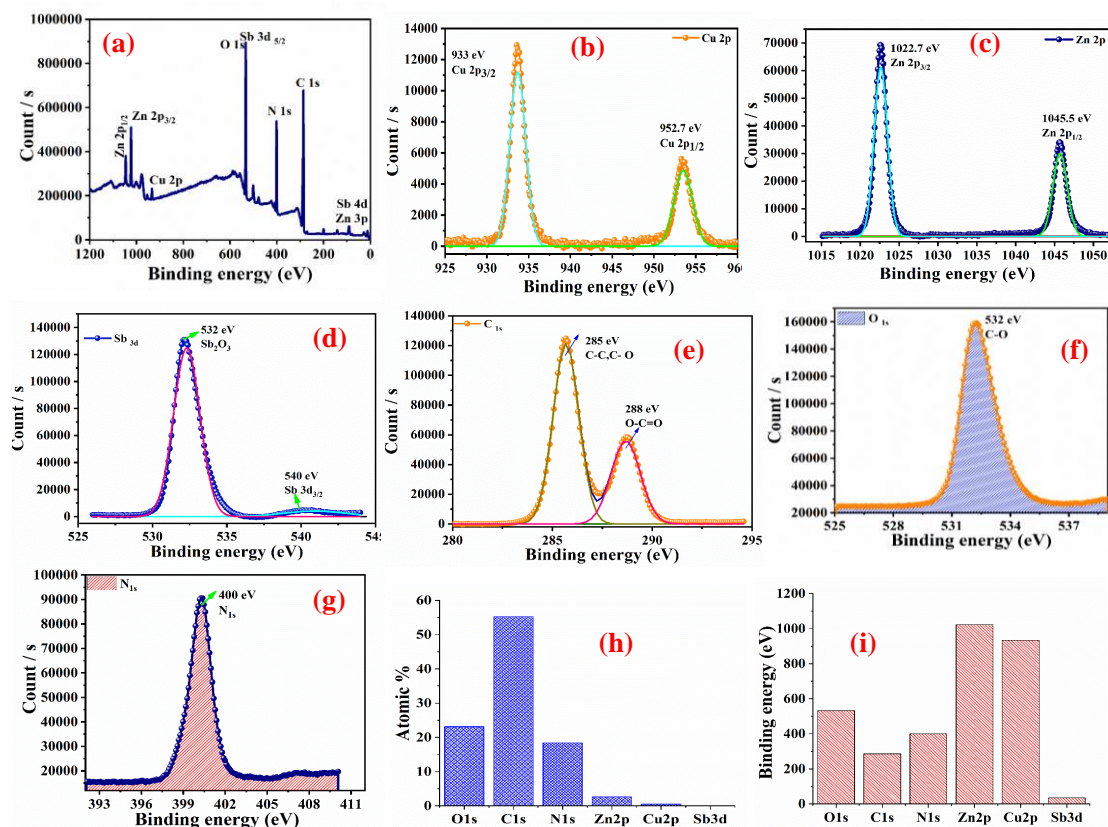


Figure 4.9 (a) XPS analysis of $\text{Cu}_{0.8}\text{Zn}_{0.2}\text{Sb}_2$ polyacrylamide nanocomposite (b) Copper (Cu 2p) element (c) zinc (Zn 2p) element (d) Antimony (sb 3d) element (e) Carbon (C 1s) element (f) Oxygen (O 1s) element (g) Nitrogen (N 1s) element (h) Atomic weight % of elements (i) Histogram for binding energy of the nanocomposites.

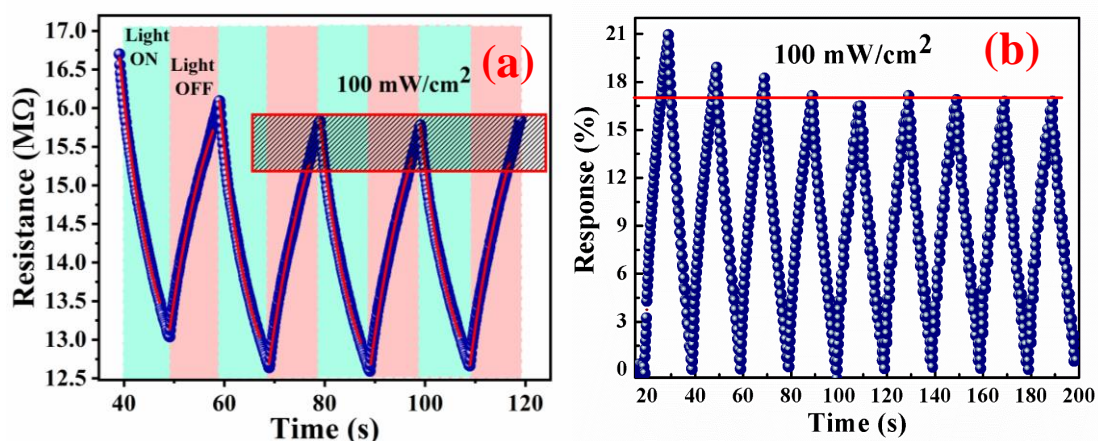


Figure 4.10 (a-b) Photoconduction behaviour of $\text{Cu}_{0.8}\text{Zn}_{0.2}\text{Sb}_2\text{AAM}$ nanomaterial.

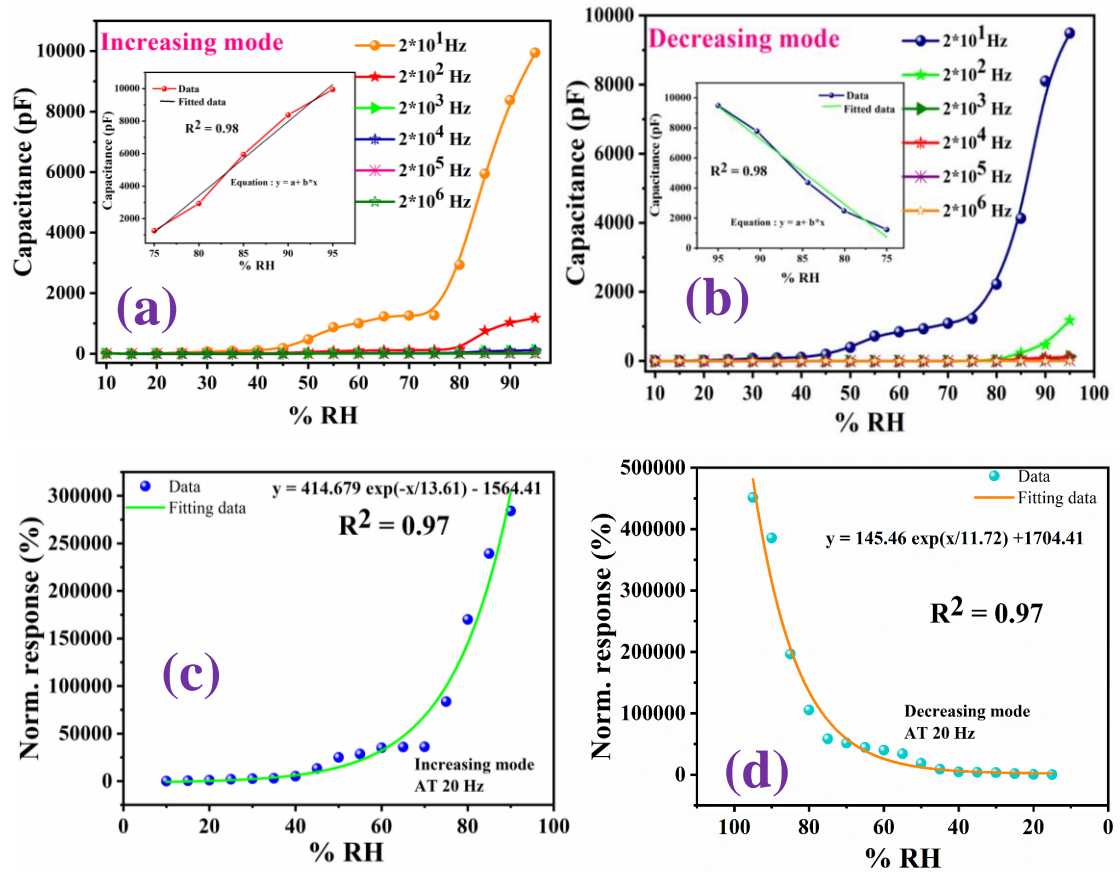


Figure 4.11 Humidity sensor response curves at room temperature (a) Variation of capacitance corresponding to the variation of %RH in increasing mode at different frequencies (20 Hz to 2 MHz). (b) Capacitive humidity sensor curve at different frequencies in decreasing mode (c & d) Normalized response with exponentially fitting data function for increasing mode and decreasing mode

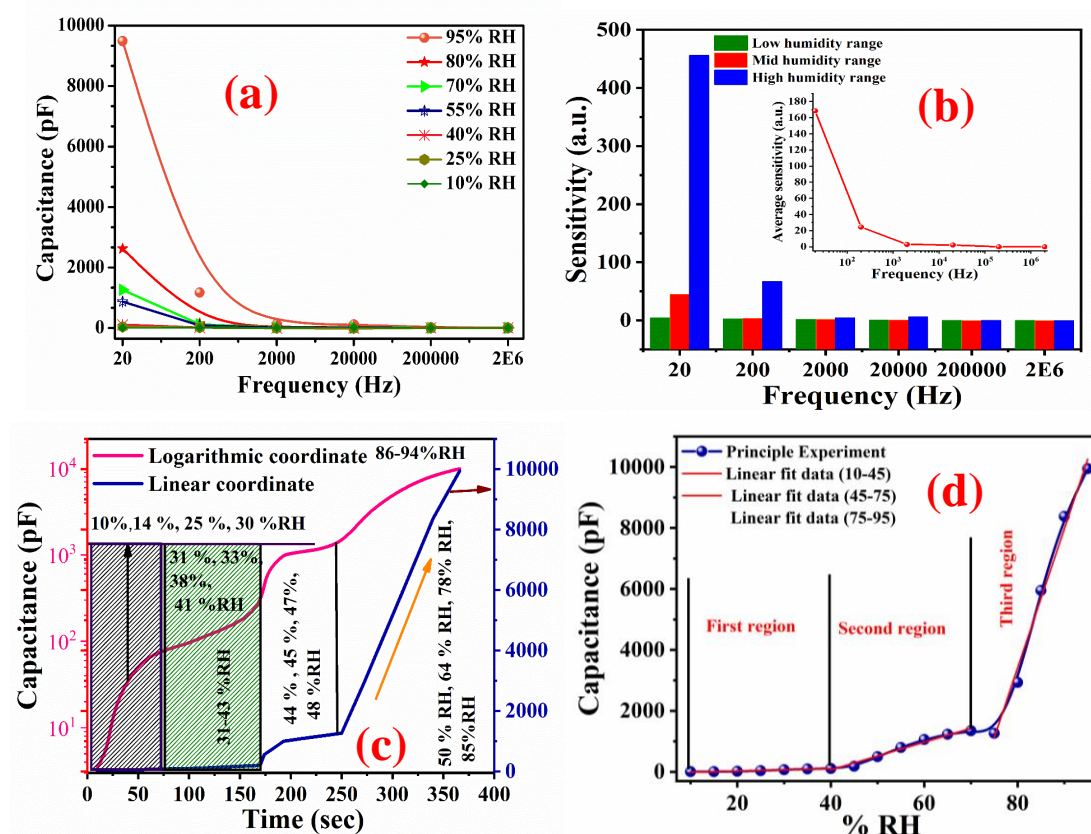


Figure 4.12 (a) Variations of capacitance curve with frequency at different %RH (10 to 95 %RH) for Cu-Zn-Sb PAam thin-film based humidity sensor at room temperature. (b) The sensitivity response at different test frequencies at 25 °C with %RH (c) Humidity sensor response at logarithmic scale (d) Linearly fitted curve for the sensitivity calculation

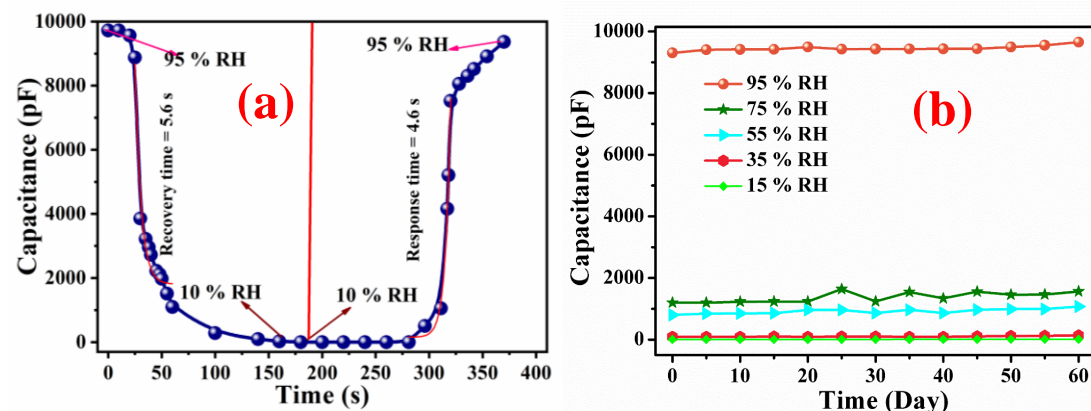


Figure 4.13 (a) Response curve showing response time 4.6 s and recovery curve showing recovery time (b) Stability curve of sensing element at different %RH

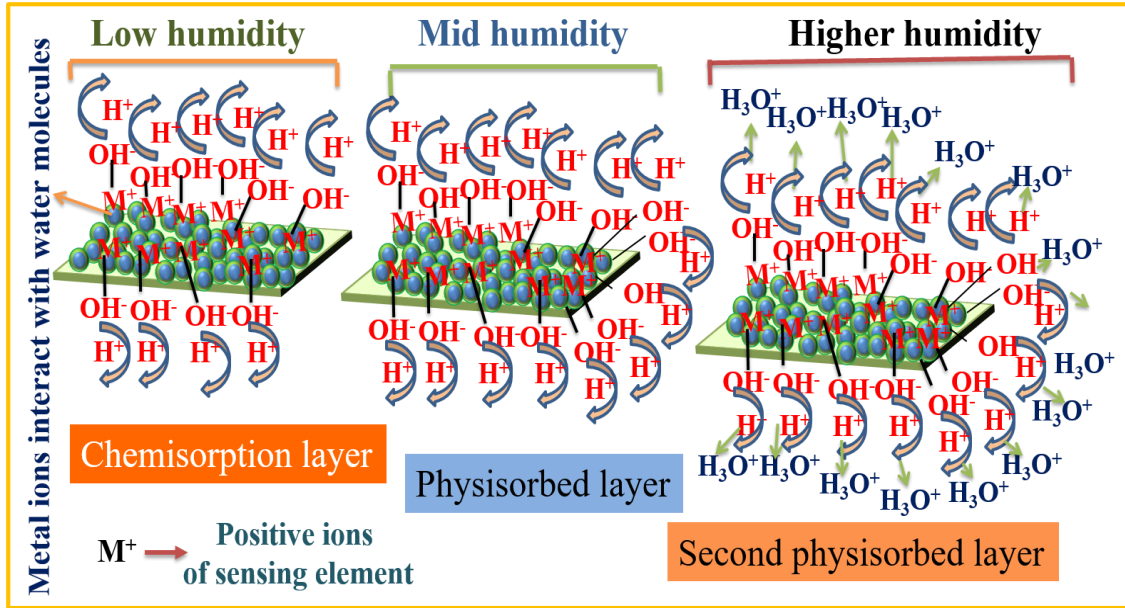


Figure 4.14 The schematic presentation of humidity sensing mechanism on the surface of film; three regions as low, mid and high level of %RH

CHAPTER 5

Improved humidity sensing response of roasted gram derived carbon quantum dots

Herein, we have reported the sustainable, cost-effective and rapid synthesis of gram derived carbon quantum dots (GCQD) employed as capacitive humidity sensor. Synthesis of GCQDs C-1 & C-2 at different carbonization temperature has been performed by pyrolysis method. Crystallinity of as prepared GCQDs were confirmed by XRD and TEM analysis revealing the average particle size 5.5 and 2 nm for C-1 & C-2 respectively. Optical properties of samples were further analysed by UV-visible and photoluminescence meter which gave the band gap as 3.82 and 4.20 eV. Compositional analysis of GCQDs were confirmed by using XPS analysis. GCQDs were subjected to sensing test at frequency 20 – 2 MHz. The C-2 gave an enhanced sensing performance with an average sensitivity of 254.861 pF/%RH. Also, sensor showed rapid response and recovery times of 7.3 & 4.7 sec respectively. Theoretical modelling has been performed to further look into the insight of interaction between functional group of GCQDs and water vapour molecules. Transient parameters such as charge density, HOMO-LUMO gap, electron clouds and H-bonds were calculated using B3LYP hybrid functional at 6-31g diffused and polarised basis set. This study provides an insight chemistry of GCQDs with water toward an efficient humidity sensor development.

5.1 Introduction

Carbon quantum dots (CQDs) are quasi-spherical shaped structures in the size less than 10 nm. CQDs are mainly self-possessed of sp^2 carbon containing nitrogen, oxygen and newly doped heteroatoms. It emerges as a versatile carbonaceous nanomaterial due to its unique chemical, physical and biological features [1,2]. Carbon quantum dot (CDs) was accidentally discovered by Xu et al. in 2004 [3]. They observed the exceptional fluorescence properties while developing the single-walled carbon nanotube (SWCNTs). Later on, further studies were conducted on the synthesis of carbon quantum dots with improved photoluminescence (PL) characteristics. CQDs due to their high aqueous solubility and strong luminescent characteristics are used in nano lights [3]. Photoluminescence of CQDs is highly efficient for application in bioimaging/drug delivery and biosensors development [4]. CQDs acts as electron acceptors and donors as a result of their excellent electronic properties[5,6].

CQDs are generally synthesized by two approaches: Bottom-up and top-down; in the bottom-up method, organic molecules like folic acid, gelation and citric acid has been used as preliminary material to comprehensive carbon quantum dots [6-7]. In the top-down approach, the petroleum coke prepared by oxidation process with H_2SO_4 and $KMnO_4$ has been used to synthesize CQDs [8]. Both techniques are quite hazardous for humans as well as the environment due to the involvement of toxic solvents [9]. To overcome the above-said drawbacks of the previously reported synthesis techniques of CQDs, researchers have put a significant effort towards the preparation of CQDs without using any organic compounds, particularly termed as green synthesis [10-14]. Lu W. et al. have reported the formation of carbon quantum dots via the green synthesis method for Hg^{2+} detection [15]. This group also investigated in the field of sensitive detection of metal oxides by using the microwave-assisted green synthesis route and developed the fluorescent carbon quantum dots from wheat flour [16]. Zhou J et al. reported the green synthesis of CQDs from watermelon peel for their application in cell imaging probes [17]. In 2013 Ramanan V et al. used green synthesis for the preparation of fluorescent carbon quantum dots [18]. One-step synthesis method and hydrothermal method using orange juice [19] were used for the synthesis of CQDs. Liu W et al. in 2017 prepared carbon dots derived from rose-heart radish via green synthesis for Fe^{3+} detection and cell imaging, Pandey S et al. in 2013 synthesised CQDs at room

temperature [20-22]. In arrears to the promising properties, CQDs have been widely used in applications as, optical and electrical [23], solar cell [24], photocatalyst [25], bioimaging [26] and humidity sensors [27]. Carbon-based materials are of immense interest in humidity sensing due to their exceptional physical, chemical and electrical properties. Humidity plays a vital role in health monitoring, manufacturing, food packaging, and testing processes [28]. A lot of research work has been reported for carbonaceous material towards humidity sensing application [29-30]. Recently, it has been reported that ~ 80% of the humidity sensors market is dominated by capacitive type humidity sensors. Such types of humidity sensors accompany many advantages like low power intake and high output signals as compared to other humidity sensors [31]. These sensors are capable of measuring the humidity level via induced charge in the dielectric constant of hygroscopic layers. Capacitive based humidity sensors are the combination of two interdigitated electrodes (IDE) enclosed by a dielectric layer, which is responsible for humidity changes. The humidity sensor is very important for human comfort and the environment, due to the increasing demand in industry, agriculture and daily life [32].

From the sensor point of view, the surface morphology is very important for validating any sensing material. High sensitivity requires the availability of a surface functional group and a wide optical bandgap of the sensing material. Being motivated by these accomplishments, we have reported a green synthesis method for synthesizing highly fluorescent carbon quantum dots. It is synthesised by modified pyrolysis [33] of gram peels and further tested as a humidity sensing material. Carbon quantum dots have unique characteristics like the presence of large oxygen-contained functional group on the surface and a large surface to volume ratio responsible for high humidity sensing. Humidity sensing can be possible because of the adsorption of water molecules and the formation of hydrogen bonds in CQDs through the surface oxygen-contained groups facilitating electron movement among the water molecules and carbon quantum dots.

The novelty of this work relies on the facile, cost-effective and eco-friendly synthesis of fluorescent GCQDs derived from the waste peel of gram with its application in electrical humidity sensors in a sustainable, cost-effective and non-toxic approach. GCQDs shows a higher sensitivity compared to other metal oxides and metallopolymeric materials reported so far. Modern sensors are facing the problem of

large response and recovery times. In this regard, improved sensing characteristics was achieved from the CQDs derived from the waste peel of easily available gram. Also, we have performed a theoretical study regarding the interaction of water molecules on GCQDs surface using DFT based B3LYP hybrid functional at 6-31g diffused and polarised basis set. Theoretical results were found in close agreement with experimental data obtained from humidity sensing by GCQDs. The literature survey related to capacitive carbon-based humidity sensors has been carried out and tabulated form in Table 5.1 which founds the significance of carbon-based humidity sensors.

5.2 Experimental Methods

5. 2.1 Preparation of GCQDs

The synthesis of gram peel derived carbon quantum dots (GCQD) was performed by the modified pyrolysis method [33]. Initially, roasted grams were purchased from the local market and subsequently peeled off to get the peels. As collected gram peels were kept in a crucible and further subjected to the carbonization process at two different temperatures 200°C and 450°C for 8h in a digital furnace (METRIX). The roasted gram peels were pyrolysed at 200°C and 450°C, coded as C-1 and C-2 respectively. The brownish coloured gram peel turned dark black after the carbonization process. The dark black shells were finely grounded with mortar pestle to obtain a fine black powder. Thus 0.001g of the fine powder of each sample C-1 and C-2 were dissolved in 15 ml DI water and stirred for 15 hr to get a homogeneous and transparent solution. This solution was filtered through 0.22 µm pore filter paper and the filtrate was collected with an appearance of the light brown colour solution. The formation of CQDs was physically confirmed by illuminating both samples under UV radiation. C-1 showed the dark sky blue colour, whereas C-2 exhibited the light blue colour. The schematic for the synthesis of CQDs is depicted in Fig.5.1.

5.3 Physical Characterization

The structure and average size distribution of GCQDs were analysed by Transmission electron microscope (TEM) (JEOL-2100F). The optical properties of GCQDs were characterized using photoluminescence spectroscopy (Spectrofluorimeter-Fluorolog-FL3-11). UV absorption studies were performed using UV-Vis spectrophotometer (Evolution 201) in the wavelength range from 190 to

1100 nm. XPS has been carried out by the instrument (PHI 5000 Versa Probe II, FEI Inc. spectrometer), which reveals the chemical composition of as-synthesized GCQDs. The Raman analysis was carried out by the instrument (UniRAM confocal micro Raman mapping system).

5.3.1 Theoretical Studies

During the theoretical study, the distance between water molecules and GCQD structures were kept as close as 3Å and then the whole system was put under geometry optimization using B3LYP hybrid functional at 6-31g diffused and polarised basis set of Gaussian 09 software package.

5.4 Results and Discussion

5.4.2 Fourier Transmission Infrared Spectra Analysis (FTIR)

The FTIR spectra of GCQDs (C-1 & C-2) is shown in Fig. 5.2 (a). The broad peak of the hydroxyl group is found at a range from 3300 cm⁻¹ - 3400 cm⁻¹ [41], revealing the presence of vibrational stretching and hydrogen bonding. It can be observed that the intensity of the hydroxyl bond of C-1 is lesser intensity than C-2, resulting in the larger number of OH⁻ groups present on the surface of GCQDs (C-2). Some other groups such as N-H stretching signifying the conjugation of amine groups, sp³ hybridization, C-H bonds were also confirmed the stability of GCQDs. The additional groups C=O carboxyl bond represent the more oxygen and carbon bonding, N-H bending and Alkene group (C=C) are observed in C-2. From the results, we can conclude that the C-2 is better GCQDs as compared to C-1 and may enhance the properties of the GCQDs.

5.4.3 X-Ray Diffraction Analysis

The XRD patterns of the GCQDs (C-1 & C-2) are shown in Fig. 5.2 (b). The lattice spacing values are different in both GCQDs. The C-1 shows lattice spacing of graphene (002) [42] while C-2 shows the two peaks at (002) and (101). Both samples reveal an intense characteristic peak with a position that corresponds to the interplanar spacing of ~ 3.77 Å, particularly the distance between (002) planes of bulk graphite (3.34 Å). Therefore, GCQDs have a carbon structure [43].

5.4.4 X-ray Photoelectron Spectroscopy (XPS) Analysis

Fig. 5.2 (c & d) shows the elemental analysis of gram CQDs of sample C-2. The XPS graphs of the optimized C-2, confirms the existence of carbon and oxygen in synthesized as quantum dots. Deconvoluted peaks in XPS at the positions 285.8 eV, 285 eV and 287 eV correspond to available bonds between C-C, C-O and C=O respectively [44]. The pronounced peak at 285.8 eV reveals the sp^2 graphitic structure of as-synthesized GCQD. No traces of impurities were found in the XPS analysis which confirms the purity of as-synthesized GCQD.

5.4.5 High-Resolution Transmission Electron Microscopy (HR-TEM)

The particle size distribution of GCQDs can be seen through TEM images of C-1 and C-2 which are well shown in Fig. 5.3(a-f). TEM image of C-1 presented in Fig. 5.3 (a) exhibits the uniform size distribution of particles. Histogram plot of particle size ranges 2-10 nm and most of the particles have an average size of 5.5 nm as shown in Fig. 5.3 (c). From Fig. 5.3 (d,e,f) the TEM images of the C-2 confirmed the uniform particle size distribution of the gram quantum dots at 20 nm scale. From Fig. 5.3 (f), it is confirmed that the size of the particles lies in the range of 2-8 nm. Small particle size is a peculiar demand for sensor application owing to the reason that as the size of particles decreases, the surface to volume ratio increases. Herein, it can be concluded that both samples C-1 and C-2 are suitable for humidity sensing application.

5.4.6 UV- Absorption Spectroscopy

Fig. 5.4 (a) shows that the absorption spectra of the C-1 and Tauc plot in the inset revealing an energy band gap of 3.82 eV. Fig. 5.4 (b) shows the absorption spectra of C-2 which corresponds to the 4.2 eV bandgap. These absorption peaks also give the information that synthesized material is of direct bandgap type. The characteristic energy band gap was calculated using the formula [29]. The conclusion of UV-Vis absorption displays that two peaks exist with and optical band gaps 3.82 eV and 4.2 eV, which might be allotted to π - π^* electronic transitions.

5.4.7 Photoluminescence Spectroscopy (PL) Studies

Photoluminescence is the prominent characteristic shown by the quantum dots. It is the optical emission spectra that show the size-dependent properties and also characteristic symbols of quantum confinement. The GCQDs shows two emission spectra at 454 nm for sample C-1 and second is 428 nm for sample C-2 respectively with

an exciting wavelength (λ_{ex}) of 360 nm. The aqueous solution showing two colours in UV light chamber placed as inset image in Fig.5.4 (c,d). Therefore, on varying the excitation wavelength the gradual shift in emission is obvious. Hence we can say that the PL mechanism is dependent on the size and surface of the quantum dots. Also, transition spectra are dependent on the excitation wavelength. PL spectra exhibit blue-shift among quantum dots. This may be due to the enhanced surface area present in GCQDs [45]. Thus C-2 shows a better luminescence property as compared to C-1.

5.4.8 Raman Analysis

The Raman analysis of carbon quantum dot (C-1 and C-2) are shown in Fig. 5.5 (a & b). Raman peaks confirmed the presence of bond stretching carbon quantum dots. From Fig.5 (a) the positions of bands (D & G) for sample C-1 are 1340 cm^{-1} and 1358 cm^{-1} and for sample C-2, these D and G are 1549 cm^{-1} and 1587 cm^{-1} respectively. The concentration of the D-band is relative to the amount of disordered sp^2 carbon and for the G-band it is proportional to the amount of ordered graphitic sp^2 carbon enclosed in the evaluated samples. The determination of graphitization degree is confirmed by the intensity ratio of I_D/I_G . According to this ratio, low value means that the graphitization degree is high and the conductivity of the material is also increased [46]. The intensity ratio calculated for C-1 and C-2 GCQDs, C-1 gives the I_D/I_G which is 0.59 and for C-2 it is 0.32 respectively, which are shown in Fig. 5.5 (a & b). From the Raman analysis, it can be concluded that the C-2 shows the lowest intensity ratio with high conductivity [47].

5.5 Experimental Investigation

5.5.1 Capacitive Humidity Sensing Characteristics

The capacitive humidity sensing characteristics of Gram carbon quantum dots based fabricated film deposited on the borosilicate glass. The spin coating method was used for the fabrication of the sensing element. Humidity sensing is mainly a surface phenomenon that depends on the adsorption and desorption of water molecules. The sensing set-up of the electrical humidity sensing already mentioned in our previous chapter 4 [30] and the present work shows it in graphical abstract. Initially, the fabricated film was dried and to take the increasing mode sensing data inside the chamber, the potassium sulphate solution was put in the chamber. This process is called

humidification. The decreasing mode data was analysed by dehumidification inside the chamber by a saturated aqueous solution of potassium hydroxide. The variations in capacitance corresponding with relative humidity (%RH) of the sensing film were noted by Impedance Analyser (Wayne Kerr Precession Component Analyser, 6440B) at operating temperature 300 K.

The sensing characteristics of the fabricated humidity sensor was tested in the frequency range of (20 Hz-2 MHz) at ambient temperature. Fig. 5.6 (a & b) shows the sensing characteristics of C-1 in increasing mode i.e. 10 – 95 %RH and decreasing mode i.e. 95 – 10 %RH. Similar studies were also conducted for C-2 presented in Fig. 5.6 (c & d). It can be perceived from the sensing curves that capacitance linearly increases with relative humidity at lower frequencies for both C-1 and C-2. From the humidity sensing curve, the capacitance increases with the relative humidity in increasing mode and decreases with decreasing in relative humidity.

The sensitivity of the C-1 and C-2 was measured at different frequencies 20 Hz - 2 MHz, mentioned in Table 5.2 & Table 5.3. At a frequency of 20 Hz, the highest sensitivity was found for both samples. The primary reason for it is the slight change in the direction of the electrical pitch at a small frequency which facilitates the space charge separation with the adsorbed water molecule. When subjected to high frequency, the direction of the electrical field changes quickly, and the separation of the adsorbed water molecules could not latch up [48]. Owing to this, the dielectric persistent is minor and free with respect to relative humidity. Therefore, high sensitivity was found for both samples at low frequency.

The maximum value of capacitance remained found at 95 %RH at 20 Hz and the lowest capacitance value was found at 10 %RH at 2 MHz for C-1 and C-2 in increasing mode. The increasing and decreasing mode shows the capacitance tends to increase from 45 %RH to 95 %RH. The sensing curve grew exponential with respect to the comparative humidity. Similarly, in decreasing mode, the sensor exponentially decreases corresponding to the relative humidity. The concerning reason for the higher sensitivity of C-2 is devoted to lesser particle size (~ 4-5) nm of the GCQDs. This is due to the enhanced surface area responsible for the increases in the sensitivity of the quantum dots. Sensitivity can be calculated from the following equation:

$$\text{Sensitivity} = \frac{C_{\text{final}} - C_{\text{initial}}}{\%RH_{\text{final}} - \%RH_{\text{initial}}} \dots\dots\dots(5.1)$$

Where C_{final} and C_{initial} are the capacitive values for C-1 and C-2 samples at final and initial %RH levels, respectively.

Hysteresis is a crucial drawback for capacitive humidity sensors. It may cause distortion of the sensing material owing to water groups and hence, influences the sensor performance. The nature of hysteresis curve followed by the sensing depends on the successive variation of relative humidity and capacitance value [49]. Hysteresis was calculated for both samples (C-1 and C-2) using following equation [50]

$$\frac{C_{\text{desorption}} - C_{\text{adsorption}}}{\text{Sensitivity}} (\% RH)$$

where C is capacitance value measured at different %RH during the adsorption and desorption mode. According to the calculation, the maximum and minimum hysteresis were observed at 95 %RH respectively in both samples (C-1 and C-2). The maximum hysteresis value for C-1 is 7.851 %RH and for C-2 is 3.945 %RH.

The sensor response was calculated from the range of 15 %RH to 95 %RH for both samples C-1 and C-2 at 20 Hz frequency. From Fig. 5.7 (a-d) we can see that the normalized response Y displays an exponential fitting of the %RH X, the corresponding function also has been depicted as an inset of Fig. 5.7.

The graph between capacitance and frequency at dissimilar relative humidity values are presented in Fig. 5.8 (a-d). At higher frequencies, the capacitance is negligible and independent of the humid atmosphere. From curves, it can be concluded that the capacitance values shows maximum at a lower frequency and at high frequency, which might be negligible. The capacitance exponential change corresponding with the relative humidity. At 20 Hz the values of capacitance vary from 2.64 pF to 8751 pF for C-1 and 5.28 pF to 10502 pF for C-2. A higher sensitivity was found for C-2 rather than C-1 at 20 Hz.

5.5.2 Sensor response and recovery time

Rapid sensor response and recovery times are essential factors for any good sensor [51]. Fig. 9 (a & b) displays the response and recovery curve where humidity varies from 10 %RH to 95 %RH. The response and recovery were estimated by

exponential fitting for C-1 and C-2 respectively. For C-1 the response and recovery times were found as 13.3 s and 14.1 sec respectively. Similarly, for C-2 the response and recovery times were found 7.3 & 4.7 sec respectively.

5.5.3 Stability Analysis

The stability of the sensing element was observed at an optimum frequency of 20 Hz. The curve was tested at various humidity ranges (15, 35, 55, 75 and 95 %RH)[52] for both C-1 and C-2. The reliability of the sensor for a long term process depends on the stability of the material. A good sensor should have high sensitivity, short response, recovery time, and long-time durability. From Fig.10 (a, b) we can say that at 95 %RH there is no variation in capacitance of GCQDs based humidity sensor with time and thus results are more stable. Also, the changes in capacitance at other humidity levels are very less, so GCQDs based sensor shows good stability at the optimum frequency.

5.5.4 Sensing Mechanism

The humidity sensing mechanism of carbon-based materials (CNTs, Graphene oxide and Carbon quantum dots) depends on the existence of hydrophilic functional groups present on its surface such as hydroxyl groups. As we have already explained in the synthesis method that GCQDs were dissolved in deionized water and no other chemical reagents were used. So GCQDs do not have any type of impurity in the solution phase. As synthesized GCQDs have oxygen-contained groups such as COOH and OH groups on the surface which show a significant role in the humidity sensing mechanism [53]. The capacitive based humidity sensor performs according to the change in capacitance comparative to the change of relative humidity (%RH). For the capacitive humidity sensor, the sensing mechanism depends on the active layer of dielectric constant and also the collection of water molecules of the surface in sensing material. Since water is a polar molecule, so change in dielectric constant is an essential parameter for the assessment of the performance of sensor.

For the capacitive humidity sensor the association between the relative humidity and capacitance may be explained by the given equation;

$$C = (\epsilon_r - i \frac{\gamma}{\omega \epsilon_0}) C_0 \dots \dots \dots (5.2)$$

Where C shows the capacitance of the sensing element, and ω denotes frequency. From the above equation, it is obvious that the capacitance is directly proportional to C_0 whereas, C is inversely proportional to frequency ω [Eqn.5.2]. ϵ_0 is permittivity and the value of dielectric permittivity of the pure water molecule which is 78.54. For the humidity sensor, the hygroscopic nature of the material is essential. Also, the working of capacitance-based humidity sensor depends on the polarization effect due to the dielectric nature of the material and distance between the electrode areas.

The sensing mechanism may also be explained by the Grotthuss chain reaction. Initially, the sensing component is free from water molecules and when exposed the moisture, the surface of sensing element adsorbs water vapour in a larger amount. Consequently, there is a change in the dielectric constant value of the sensing film. The water molecule breaks into two parts H^+ ions and OH^- ions. OH^- ions interact with metal ions to form the chemisorbed layer and hence, a small change in capacitance value was observed which is well shown in Fig. 5.11 (a). In mid humidity region, the protons (H^+) increase the conductivity of the material and forms the physisorption layer. Due to the formation of layer, the value of capacitance sharply changed which can be easily observed in Fig. 5.11(b). In the high humidity region, the capacitance value rises exponentially due to multi physisorbed layer formation on the sensing element. The water molecules are singly bonded in the physisorption layer so that these can be easily polarized and due to this phenomenon the capacitance increases. Next from Fig. 5.11 (c) the protons have the freedom to move inside the layer so one more layer of a physisorbed layer formed, which is known as the second physisorbed layer.

5.6 Theoretical studies

5.6.1 Interaction of GCQD with water molecule (H_2O):

Carbon quantum dot structures were gradually aligned with one, two, three water molecules, etc. The distances between water molecules and CQD structures were kept as close as 3\AA for keen interception of their mutual interactions and then the whole system was put under geometry minimization using DFT based hybrid functional, B3LYP using 6-31g** basis set of Gaussian 09 software package [54]. Here, the first (*) corresponds to diffused functions whereas the second (*) corresponds to polarized functions. The geometry was optimised to lower the interaction energy between water molecules and carbon quantum dots. Obtained data was visualised using the Discovery

Studio software package [55]. It was also observed that the theoretical calculations performed are in sound agreement with the obtained experimental results and thus validates our model.

5.6.2 Hydrogen Bonding Interaction

Due to the presence of Carbon and Oxygen atoms in CQD, its interaction with water could be established only by the presence of hydrogen bonds. To our considerations, hydrogen bonding interactions were observed in nearly all the systems put under theoretical simulations. Table 5.3 shows the h-bond distances for their corresponding number of H₂O molecules interaction with CQD and the number of h-bonds formed, respectively. In the case of a humidity sensor, the formation of hydrogen bond is an extraordinary property that validates the existing interaction between water molecules and CQD [Fig. 5.12].

From Fig. 5. 13 (a-c), it is evident that the water molecules interact with carbon quantum dots when aligned at about 3Å and consequently form hydrogen bonds. It is also evident from the computational experiment that the interaction occurs by forming the layers and thus providing a larger surface area of CQD for better interaction and thus owing to the stability of system.

5.6.3 Electrostatic and Hydrogen Bonding Charge densities

Fig. 5.13 represents the isocontour surfaces for H-donor/acceptor clouded regions at binding sites. These acceptor and donor regions assist in finding the electron-rich and electron-deficient sites in the GCQD-Water system and thus helps in the prediction of possible hydrogen binding sites within the system. These regions represent those atoms which have the tendency to donate/accept electrons to achieve stability during their geometry optimization.

Fig. 5.13 shows the isocontour surface distribution of electrostatic charges throughout the system leading to the electron transfer between definite pair of atoms, and eventually, no distortions in the chemical structures are offered. The values of electrostatic potentials are represented using different colours in the isocontour surface of the GCQD-Water system Fig. 5.13 (c). The electrostatic potential increases in the order of the following colours: red < orange < yellow < green < blue (however, here we have only red and blue) and is shown in Fig. 5.13. The blue colour indicates the regions

of highest attraction whereas the red colour indicates the region corresponding to the highest repulsion in the electrostatic isocontour potential maps of GCQD-Water system.

5.6.4 HOMO-LUMO Gap

Fig. 5.14 displays the chemical stability of the GCQD-Water system can be estimated from the HOMO (Highest Occupied Molecular Orbital) and LUMO (Lowest Unoccupied Molecular Orbital) energy levels. The HOMO-LUMO gap, also known as bandgap (in case of continuous bands) was calculated in order to get an atomistic insight of the optoelectronic characteristics regarding the optical activity of GCQD [56, 57]. The HOMO–LUMO of the GCQD-Water system are shown in Table 5.5. These energies associated with HOMO and LUMO orbitals, reflect the electron-donating and accepting tendencies, respectively Fig. 5.15. Some of the other crucial physical and chemical parameters such as ionization potential, electron affinity, electronegativity, absolute hardness and softness can also be calculated theoretically, at the same level by using HOMO and LUMO energy differences and thus can add mode to the theoretically calculated databases [58-60].

5.7 Conclusion

The gram carbon quantum dots have been successfully synthesized via waste gram peels, which is the source of carbon. As synthesized carbon quantum dot is water-soluble and shows the green and blue luminescent property. We have prepared GCQDs at two different temperatures 315 °C (C-1) and 650 °C (C-2) and the average size of GCQDs are 7 and 5 nm, respectively. In UV light samples C-1 and C-2 exhibit green and blue emission respectively. The chemical composition of GCQDs was confirmed by Raman and XPS analysis. The simple and cost-effective GCQDs showed good sensing characteristics. We have used both the samples C-1 and C-2 for the capacitive humidity sensor at different frequencies (20 Hz - 2 MHz). Among C-1 and C-2 based sensors, C-2 displays the best result at optimized frequency. The response and recovery time for sample C-1 are 13.3 sec and 14.1 sec and for C-2 these are 7.3 sec and 4.7 sec, respectively. From the theoretical study, we can conclude that the water molecules easily interact with carbon quantum dots. The electrostatic isocontour map shows that the red regions represent the most electronegative sites, whereas the blue regions represent the most electropositive sites within the CQD-water system. These sites also reveal crucial information concerning the regions where the CQD-water system can undergo intra- and

intermolecular interactions to attain stability. Since the energy gap between HOMO and LUMO is very small and this energy gap is sufficient to give significant information about the CQD-water system that it has almost planar geometry and assists in layer-based interaction and hence tends to decrease the HOMO-LUMO gap. Thus gram carbon quantum dots easily interact with water molecules and are performed as humidity sensors. Also, the theoretical data confirmed the experimental results.

References

- [1] L. Shen, J. Liu, New development in carbon quantum dots technical applications, *Talanta*, 156 (2016) 245-256.
- [2] S. Kalytchuk, K. Poláková, Y. Wang, J. P. Froning, K. Cepe, A. L. Rogach and R. Zboril, Carbon Dot Nanothermometry: Intracellular Photoluminescence Lifetime Thermal Sensing, *ACS Nano*, 11 (2017) 1432-1444.
- [3] X. Xu, R. Ray, Y. Gu, H. J. Ploehn, L. Gearheart, K. Raker, and W. A. Scrivens, Electrophoretic Analysis and Purification of Fluorescent Single-Walled Carbon Nanotube Fragments, *J. Am. Chem. Soc.*, 126 (2004) 12736-12737.
- [4] Y. Wang and A. Hu, Carbon quantum dots: synthesis, properties and Applications, *J. Mater. Chem. C*, 2 (2014) 6921–6939.
- [5] M. Tuerhong, X. Yang, Y. Xue-Bo, Review on Carbon Dots and Their Application, *Chin J Anal Chem*, 45 (2017) 139–150.
- [6] J. Zhang and S. Yu, Carbon dots large-scale synthesis, sensing and bioimaging, *Materials Today*, 19 (2016) 382-393.
- [7] X. Zhang, H. Ming, R. Liu, X. Han, Z. Kang, Y. Liu, Y. Zhang, Highly sensitive humidity sensing properties of carbon quantum dots films, *Materials Research Bulletin*, 48 (2013) 790–794.
- [8] H. Li, X. He, Z. Kang, H. Huang, Y. Liu, J. Liu, S. Lian, C. Him, A. Tsang, X. Yang, and S. Lee, Water-Soluble Fluorescent Carbon Quantum Dots and Photocatalyst Design, *Angew. Chem. Int. Ed.* 49 (2010), 4430–4434.
- [9] X. Yan, X. Cui, B. Li, and L. Li, Large Solution-Processable Graphene Quantum Dots as Light Absorbers for Photovoltaics, *Nano Lett.* 10 (2010), 1869–1873.
- [10] J. Lu, J. Yang, J. Wang, A. Lim, S. Wang, and K. Loh, One-Pot Synthesis of Fluorescent Carbon Nanoribbons, Nanoparticles, and Graphene by the Exfoliation of Graphite in Ionic Liquids, *ACS Nano*, 3 (2009) 2367–2375.
- [11] B. Bourlinos, A. Stassinopoulos, D. Anglos, R. Zboril, V. Georgakilas, and E. P. Giannelis, Photoluminescent Carbogenic Dots, *Chem. Mater.*, 20 (2008) 4539–4541.

- [12] X. Jia, J. Lia and E. Wang, One-pot green synthesis of optically pH-sensitive carbon dots with upconversion luminescence, *Nanoscale*, 4 (2012) 5572–5575.
- [13] Y. Fang, S. Guo, D. Li, C. Zhu, W. Ren, S. Dong, and E. Wang, Easy synthesis and imaging applications of cross-linked green fluorescent hollow carbon nanoparticles, *ACS Nano* 6(2011) 400–409.
- [14] Z. Zhu, S. Wu and W. Pong Highly photoluminescent carbon dots derived from egg white: facile and green synthesis, photoluminescence properties, and multiple applications *ACS Sustainable Chem. Eng.* 3 (2015) 1412–1418.
- [15] H. Xu, X. Yang, G. Li, C. Zhao and X. Liao, Green synthesis of fluorescent carbon dots for selective detection of tartrazine in food samples, *J. Agri. Food Chem.* 63 (2015) 6707–6714.
- [16] S. Zhao, M. Lan, X. Zhu, H. Xue, T.W. Ng, X. Meng, C.S. Lee, P. Wang, W. Zhang, Green synthesis of bifunctional fluorescent carbon dots from garlic for cellular imaging and free radical scavenging, *ACS Appl. Mat. Interfaces* 7 (2015) 17054–17060.
- [17] W. Lu, Economical, green synthesis of fluorescent carbon nanoparticles and their use as probes for sensitive and selective detection of mercury (II) ions *Anal. Chem.* 84 (2012) 5351–5357.
- [18] Q. X, L. W, A. A M, Al-Youbi A O and Sun ,Microwave-assisted rapid green synthesis of photoluminescent carbon nanodots from flour and their applications for sensitive and selective detection of mercury (II) ions, *Sens. Actuators B: Chem.* 184(2013) 156–162.
- [19] J. Zhou, Z. Sheng , H. Han, M. Zou and C. Li, Facile synthesis of fluorescent carbon dots using watermelon peel as a carbon source, *Mater. Lett.* 66 (2012) 222–224.
- [20] V. Ramanan, S. K. Thiyagarajan, K. Raji, R. Suresh, R. Sekar and P. Ramamurthy, Outright green synthesis of fluorescent carbon dots from eutrophic algal blooms for in vitro imaging, *ACS Sustainable Chem. Eng.* 4 (2016) 4724–4733.

- [21] R. Das, R. Bandyopadhyay and P. Pramanik, Carbon quantum dots from natural resource: A review, *Materials Today Chemistry* 8 (2018) 96-109.
- [22] S. Sahu, B. Behera, T. K. Maiti and S. Mohapatra Simple one-step synthesis of highly luminescent carbon dots from orange juice: application as excellent bio-imaging agents *Chem. Commun.* 48 (2012) 8835–7.
- [23] W. Liu, H. Diao, H. Chang, H. Wang, T. Li and W. Wei, Green synthesis of carbon dots from rose-heart radish and application for Fe³⁺ detection and cell imaging, *Sens. Actu. B: Chem.* 241 (2017) 190–208.
- [24] S. T. Yang, L. Cao, P. G. Luo, F. Lu, X. Wang, H. Wang, M. J. Mezziani, Y. Liu, G. Qi, and Y. P. Sun, Carbon dots for optical imaging in vivo, *Journal of the American Chemical Society*, 131(2009) 11308–11309.
- [25] H. Li, X. He, Z. Kang, H. Huang, Y. Liu, J. Liu, S. Lian, C. H. A. Tsang, X. Yang and S.-T. Lee, Water-soluble fluorescent carbon quantum dots and photocatalyst design, *Angew. Chem., Int. Ed.*, 49 (2010), 4430–4434.
- [26] D. Tang, J. Liu, X. Wu, R. Liu, X. Han, Y. Han, H. Huang, Y. Liu and Z. Kang, Carbon Quantum Dot/NiFe Layered Double-Hydroxide Composite as a Highly Efficient Electrocatalyst for Water Oxidation, *ACS Appl. Mater. Interfaces*, 6(2014) 7918–7925.
- [27] H. Wang, G. Ning, X. He, X. Ma, F. Yang, Z. Xu, S. Zhao, C. Xu, Carbon quantum dots derived by direct carbonization of carbonaceous microcrystals in mesophase pitch, *Nanoscale*, 10 (2018) 21492
- [28] P. Su, W. Tsai, Humidity sensing and electrical properties of a composite material of nano-sized SiO₂ and poly (2-acrylamido-2-methylpropane sulfonate), *Sens. Actuators B: Chem.* 100 (2004) 417–422.
- [29] S. Yadav, P. Chaudhary, K.N. Uttam, A. Verma, M. Vashistha, B. C. Yadav, Facile synthesis of molybdenum disulfide (MoS₂) quantum dots and its application in humidity sensing, *Nanotech.* 30 (2019) 1-10.
- [30] S. Mishra, P. Lohia, P. Chaudhary, B.C. Yadav, and D.K. Dwivedi, Development of an Impedance-Based Electrical Humidity Sensor Using Sb-

- Doped Ge-Se-Te Chalcogenide Glasses, Journal of electronic materials
<https://doi.org/10.1007/s11664-020-08362-w> 2020.
- [31] A.S. Pawbake, R.G. Waykar, D.J. Late, S.R. Jadkar, Highly Transparent Wafer-Scale Synthesis of Crystalline WS₂ Nanoparticle Thin Film for Photodetector and Humidity-Sensing Applications, ACS Applied Mat. and Inter. 8 (2016) 3359–3365.
- [32] P. Chaudhary, D. Kumar, S. Sikarwar, B. C. Yadav, G.I. Dzhardimalieva, R. Prakash, Development of nanostructured nickel reinforced polyacrylamide via frontal polymerization for a reliable room temperature humidity sensor, Eur. Polymer Jour. 112 (2019) 161–169.
- [33] V. Kumar, V. Chauhan, J. Ram, R. Gupta, S. Kumar, P. Chaudhary, B.C. Yadav, S. Ojha, I. Sulania, and R. Kumar, Study of humidity sensing properties and ion beam induced modifications in SnO₂-TiO₂ nanocomposite thin films Surf. Coat. Technol. 392 (2020) 125768.
- [34] J. Lee, D. Cho, Y. Jeong, A resistive-type sensor based on flexible multi-walled carbon nanotubes and polyacrylic acid composite films. Solid-State Electron 87 (2013) 80–84.
- [35] Y.Pang, J. Jian, T. Tu, Z. Yang, J. Ling, Y. Li, X. Wang, Y. Qiao, Y.Y. Tian, T.L. Ren, Biosensors and Bioelectronics Wearable humidity sensor based on porous graphene network for respiration monitoring. Biosens. Bioelectron. 116 (2018) 123–129.
- [36] U. Kumar and B.C. Yadav, Development of humidity sensor using modified curved MWCNT based thin film with DFT calculations, Sensors & Actuators: B. Chemical 288 (2019) 399–407.
- [37] D. Zhang, H. Chang, P. Li, R. Liu, Q. Xue, Fabrication and characterization of an ultrasensitive humidity sensor based on metal oxide/graphene hybrid nanocomposite. Sens. Actuators B Chem. , 225 (2016) 233–240.
- [38] H. Bi, K. Yin, X. Xie, J. Ji, S. Wan, L. Sun, M. Terrones, M.S. Dresselhaus, Ultrahigh humidity sensitivity of graphene oxide, Sci. Rep. 3 (2013) 1–4.

- [39] K. Kumar, U. Kumar, M. Singh, B. C. Yadav Synthesis and characterizations of exohedral functionalized graphene oxide with iron nanoparticles for humidity detection, *Journal of Materials Science: Materials in Electronics* <https://doi.org/10.1007/s10854-019-01663-9>.
- [40] C.L. Zhao, M. Qin, W.H. Li, Q.A. Huang, in *Proceedings of the 16th International Solid-State Sensors, Actuators and Microsystems Conference (2011)* 1954–1957.
- [41] P. Das, M.O. Bose, S. Ganguly, S. Mondal, A. K. Das, S. Banerjee and N. C. Das, Green approach to photoluminescent carbon dots for imaging of gram-negative bacteria *Escherichia coli*, *Nanotechnology* 28 (2017) 195501-195513.
- [42] V. Kumar, V. Chauhan, J. Ram, R. Gupta, S. Kumar, P. Chaudhary, B.C. Yadav, S. Ojha, I. Sulania, R. Kumar, Study of humidity sensing properties and ion beam induced modifications in SnO₂-TiO₂ nanocomposite thin films, *Surface & Coatings Technology* 392 (2020) 125768.
- [43] D.K. Maurya, S. Sikarwar, P. Chaudhary, S. Angaiah, B. C. Yadav, Synthesis and Characterization of Nanostructured Copper Zinc Tin Sulphide (CZTS) for Humidity Sensing Applications, *IEEE Sens. Jour.* 19 (2019) 2837–2846
- [44] J. Mintza, Y. Zhoua, and R. M. Leblanca, Recent Development of Carbon Quantum Dots Regarding their Optical Properties, Photoluminescence Mechanism, and Core Structure Keenan, *Nanoscale*, 11 (2019) 4634-4652.
- [45] H. Zhao, T. Zhang, R. Qi, J. Dai, S. Liu, and T. Fei, Drawn on Paper: A Reproducible Humidity Sensitive Device by Handwriting, *ACS Appl. Mater. Interfaces*, 9 (2017) 28002–28009.
- [46] H. Maktuff, J. Alta, Y.M. Amin, V. Periasamy, Humidity influenced capacitance and resistance of an Al / DNA / Al Schottky diode irradiated by alpha particles, *Scientific Reports* 3 (2016) 11-3.
- [47] Bi, K. Yin, X. Xie, J. Ji, S. Wan, L. Sun, M. Terrones, Ultrahigh humidity sensitivity of graphene oxide, *Scientific Reports* (2013) 1–7.
- [48] T. Chudoba, A new method for investigating the columnar structure of dielectric thin films, *Thin Solid Film*, 131 (1985) 96 - 104.

- [49] Z. H. Duan, Q. N. Zhao, C. Z. Li, S. Wang, Y. D. Jiang, Y. J. Zhang, B. H. Liu, H. L. Tai, Enhanced positive humidity sensitive behavior of p-reduced graphene oxide decorated with n-WS₂ nanoparticles, *Rare Met.* 7 (2020).
- [50] M. Q. Liu, C. Wang and N. Y. Kim, High-Sensitivity and Low-Hysteresis Porous MIM-Type Capacitive Humidity Sensor Using Functional Polymer Mixed with TiO₂ Microparticles, *Sensors* 17, 284 (2017).
- [51] G. Hass, M. H. Francombe and J. L. Vossen, Oxygen Ion and Mixed Conductors and Their Technological Applications, *Physics of Thin Films*, 12 (1982) 46 - 48.
- [52] Nutional Semiconductor Linear Databook, National Semiconductor Corporation, Santa Clara, CA, (1982) 939 - 941.
- [53] Y. Shimizu, H. Arai and T. Seiyama, Theoretical studies on the impedancehumidity characteristics of ceramic humidity sensors, *Sensors and Actuators*, 7 (1985) 11 - 22.
- [54] Gaussian 09, Revision E.01, Frisch, M. J., Trucks, G. W., Schlegel, H. B., Scuseria, G. E., Robb, M. A., Cheeseman, J. R., Scalmani, G., Barone, V., Mennucci, B., Petersson, G. A., Nakatsuji, H., Caricato, M., Li, X., Hratchian, H. P., Izmaylov, A. F., Bloino, J., Zheng, G., Sonnenberg, J. L., Hada, M., Ehara, M., Toyota, K., Fukuda, R., Hasegawa, J., Ishida, M., Nakajima, T., Honda, Y., Kitao, O., Nakai, H., Vreven, T., Montgomery, J. A., Jr., Peralta, J. E., Ogliaro, F., Bearpark, M., Heyd, J. J., Brothers, E., Kudin, K. N., Staroverov, V. N., Kobayashi, R., Normand, J., Raghavachari, K., Rendell, A., Burant, J. C., Iyengar, S. S., Tomasi, J., Cossi, M., Rega, N., Millam, J. M., Klene, M., Knox, J. E., Cross, J. B., Bakken, V., Adamo, C., Jaramillo, J., Gomperts, R., Stratmann, R. E., Yazyev, O., Austin, A. J., Cammi, R., Pomelli, C., Ochterski, J. W., Martin, R. L., Morokuma, K., Zakrzewski, V. G., Voth, G. A., Salvador, P., Dannenberg, J. J., Dapprich, S., Daniels, A. D., Farkas, Ö., Foresman, J. B., Ortiz, J. V., Cioslowski, J., Fox, D. J. Gaussian, Inc., Wallingford CT, 2009.
- [55] Dassault Systèmes BIOVIA, Discovery Studio Modeling Environment, San Diego (2017). <https://3ds.com/products-services/biovia/products>
- [56] F. D. Proft, P. Geerlings, Conceptual and Computational DFT in the Study of Aromaticity *Chem. Rev.* 101 (2001) 1451-1464.

- [57] J. Feng, H. Dong, B. Pang, F. Shao, C. Zhang, L. Yu and L. Dong, Theoretical Study on Optical and Electronic Properties of Graphene Quantum Dots Doped with Heteroatoms, *Phys. Chem. Chem. Phys.*, 20 (2018) 15244-15252.
- [58] T. Alizadeh, S. Mirzagholidpur, A Nafion-free non-enzymatic amperometric glucose sensor based on copper oxide nanoparticles-graphene nanocomposite, *Sens. Actuators B*, 198 (2014) 438-447.
- [59] J. T. Robinson, F. K. Perkins, E. S. Snow, Z. Wei, P. E. Sheehan, Reduced graphene oxide molecular sensors, *Nano Lett.* 8 (2008) 3137-3140.
- [60] R. K. Paul, S. Badhulika, N. M. Saucedo, A. Mulchandani, Graphene nanomesh as highly sensitive chemiresistor gas sensor, *Anal. Chem.* 84 (2012) 8171-8178.
- [61] B. De and N. Karak, A green and facile approach for the synthesis of water soluble fluorescent carbon dots from banana juice, *RSC Adv.* 3 (2013) 8286-8290.
- [62] S. Kumar, A. K. Ojha, B. Ahmed, A. Kumar, J. Das, A. Materny, Tunable (violet to green) emission by high-yield graphene quantum dots and exploiting its unique properties towards sun-light-driven photocatalysis and supercapacitor electrode materials, *Materials Today Communications* 11 (2017) 76-86.

Tables:

Table 5.1. The literature survey related to the capacitive carbon-based humidity sensor

S.No.	Sensing material	Sensitivity	Response time	Recovery time	Reference
1.	MWCNTs in a PAA matrix in a ratio 1:4	930 Ω	680 s	380 s	[34]
2.	GO modified poly (3,4 ethylenedioxythiophene)	4.97%	31 s	72 s	[35]
3.	Modified MWCNT (Dispersed in NMP)	6.41 pF/%RH	36 s	32 s	[36]
4.	Tin dioxide/reduced graphene oxide (RGO)	146.53pF/%RH	102 s	Several s	[37]
5.	GO	37,800%	10.5 s	41 s	[38]
6.	Fe–GO	5.18 pF/%RH	31 s	11 s	[39]
7.	Graphene oxide	-9.5 fF/%RH	5 s	-	[40]
8.	Gram Carbon quantum dot (C-1)	178.6 pF/%RH	13.3 s	14.1 s	This work
	Gram Carbon quantum dot (C-2)	254.861 pF/%RH	7.3 s	4.7 s	

Table 5.2 Sensitivity at different frequencies of gram carbon quantum dots (C-1)

Frequency	Low humidity region (10-45%RH)	Mid humidity region (45-70%RH)	High humidity region (70-90 %RH)	Avg. sensitivity (pF/%RH)
2*10 ¹ Hz	1.92	28.43	509.16	179.83 pF/%RH

2×10^2 Hz	0.54	3.319	37.00	13.61 pF/%RH
2×10^3 Hz	0.21	1.47	24.40	8.69 pF/%RH
2×10^4 Hz	0.04	0.68	1.4	0.706 pF/%RH
2×10^5 Hz	0.014	0.02	0.88	0.304 pF/%RH
2×10^6 Hz	0.002	0.008	0.096	0.035 pF/%RH

Table 5.3 Sensitivity at different frequencies of gram carbon quantum dots (C-2)

Frequency	Low humidity region (10-45%RH)	Mid humidity region (45-70%RH)	High humidity region (70-95%RH)	Avg. sensitivity (pF/%RH)
2×10^1 Hz	3.83	56.87	703.96	254.861pF/%RH
2×10^2 Hz	0.24	6.63	73.97	26.940 pF/%RH
2×10^3 Hz	0.51	0.10	48.81	16.470 pF/%RH
2×10^4 Hz	0.12	0.15	2.85	1.020 pF/%RH
2×10^5 Hz	0.03	0.04	2.95	1.006 pF/%RH
2×10^6 Hz	0.008	0.01	0.192	0.071 pF/%RH

Table 5.4 shows the H-bond distance

S. No.	No. of H₂O molecules interacting with CQD	No. of H-bonds formed	H-bond distances (Å)
1	01	03	1.66807, 1.78109, 2.54097

2	02	04	1.68064, 1.81469, 2.15428, 2.24792
3	03	07	1.67213, 1.68632, 1.76473, 1.77330, 1.89765, 2.44036, 3.01139

Table 5.4 The HOMO-LUMO gap of the carbon quantum dots

S. No.	No of H ₂ O molecules interacting with CQD	HOMO (a.u.)	LUMO (a.u.)
1	01	-0.20318	-0.09050
2	02	-0.20422	-0.09293
3	03	-0.20265	-0.09279

Figures:

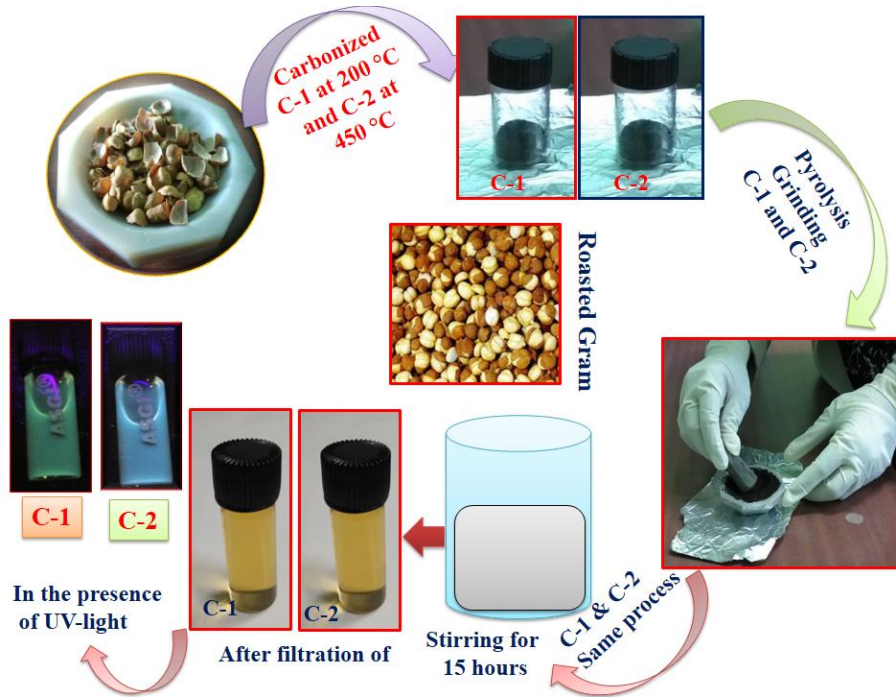


Figure 5.1 Schematic representation of the preparation of GCQDs using pyrolysis technique.

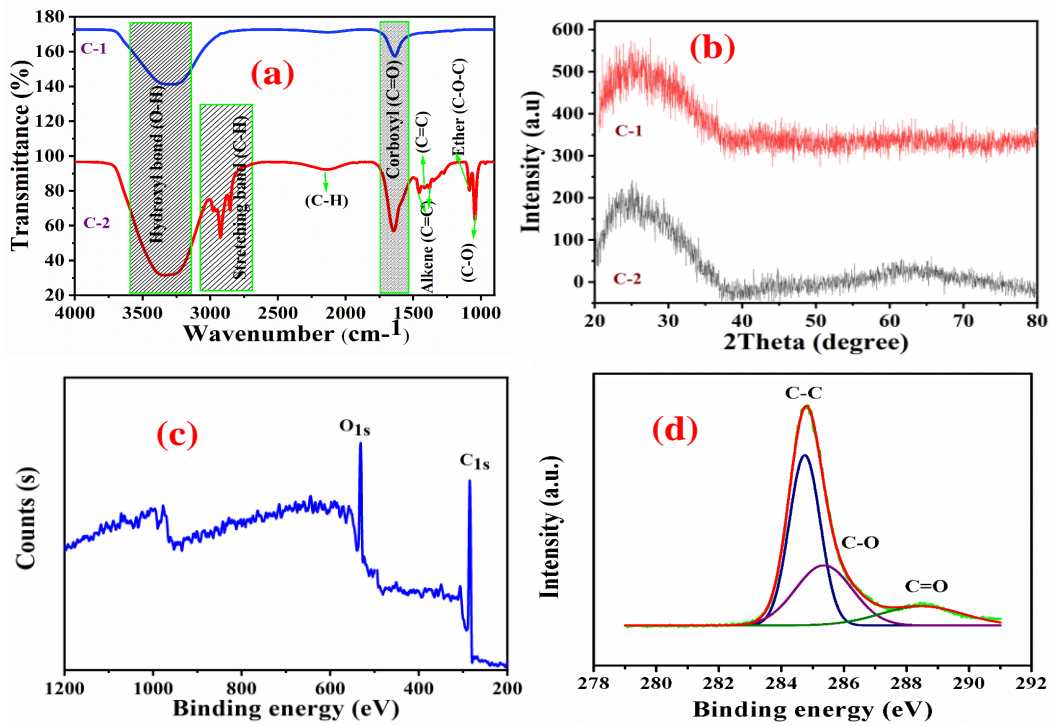


Figure 5.2 (a) FTIR spectra of GCQDs (b) XRD pattern (c) Oxidation state and (d) Binding energies curve of C-2.

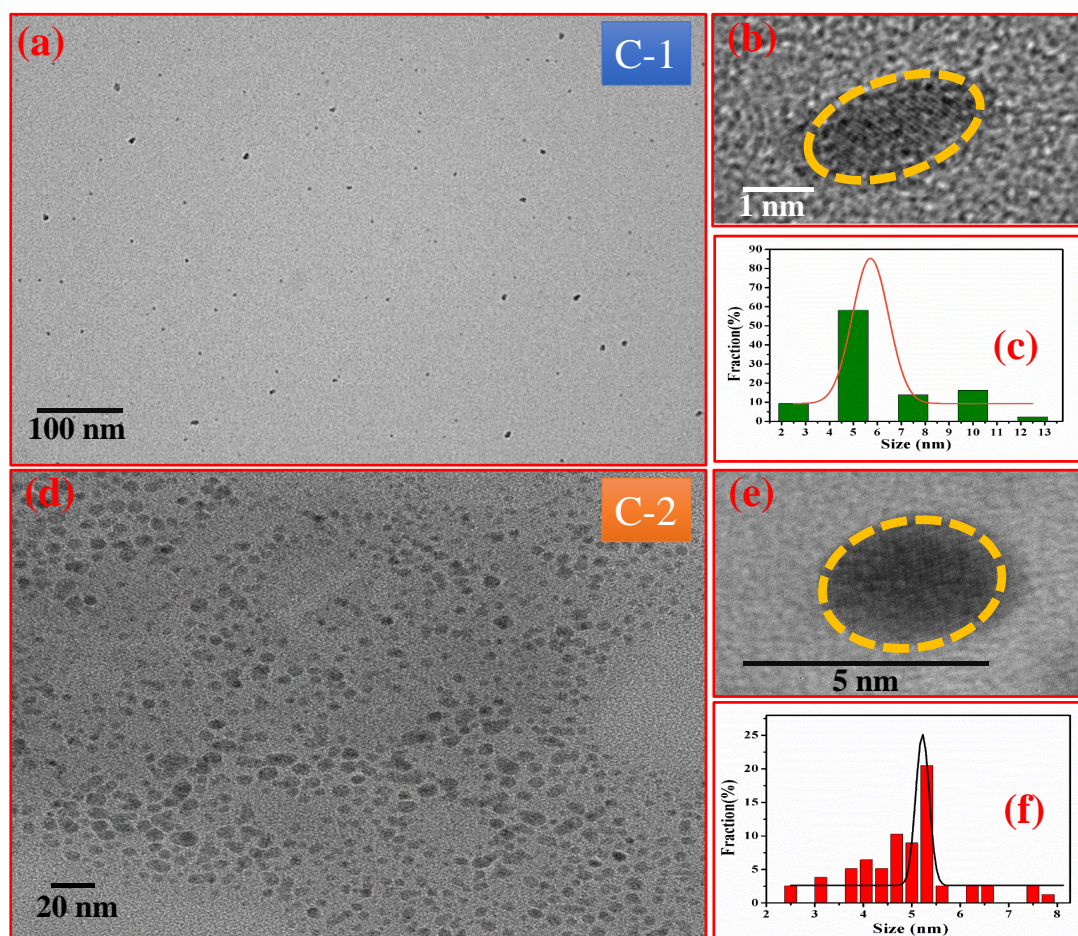


Figure 5.3 (a) TEM image of C-1 at 100 nm scale (b) HRTEM image of the GCQDs at 1 nm scale (c) Particle size distribution curve of C-1 (d) TEM image of C-2 at 20 nm (e) HRTEM image of GCQDs at 5 nm scale (f) Particle size distribution curve for the sample C-2.

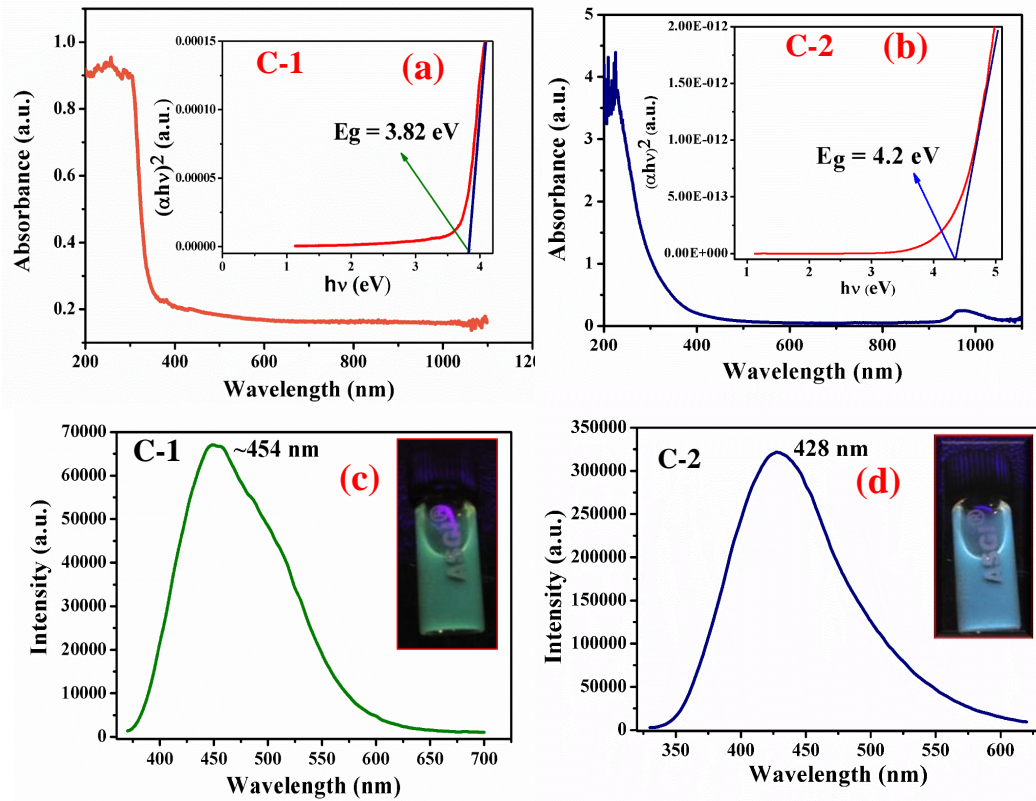


Figure 5.4 UV absorption spectra of GCQDs (a) Absorbance Vs wavelength (nm) plot for the C-1 with an energy band gap of 3.82 eV (b) Absorbance Vs wavelength (nm) for the C-2 with an energy band gap of 4.2 eV. (c) Photoluminescence of C-1 with an emission peak at 454 nm (d) an emission peak of C-2 at 428 nm.

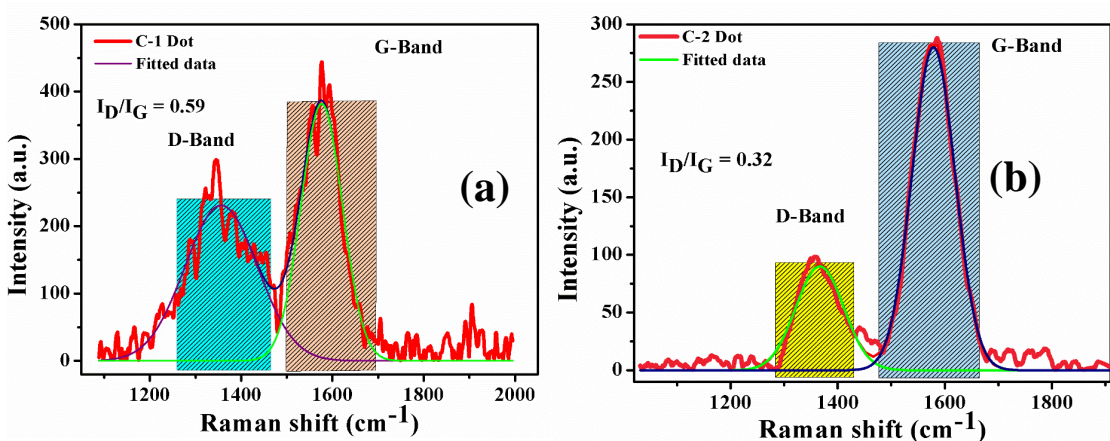


Figure 5.5 (a) Raman spectra of C-1 and (b) C-2 samples.

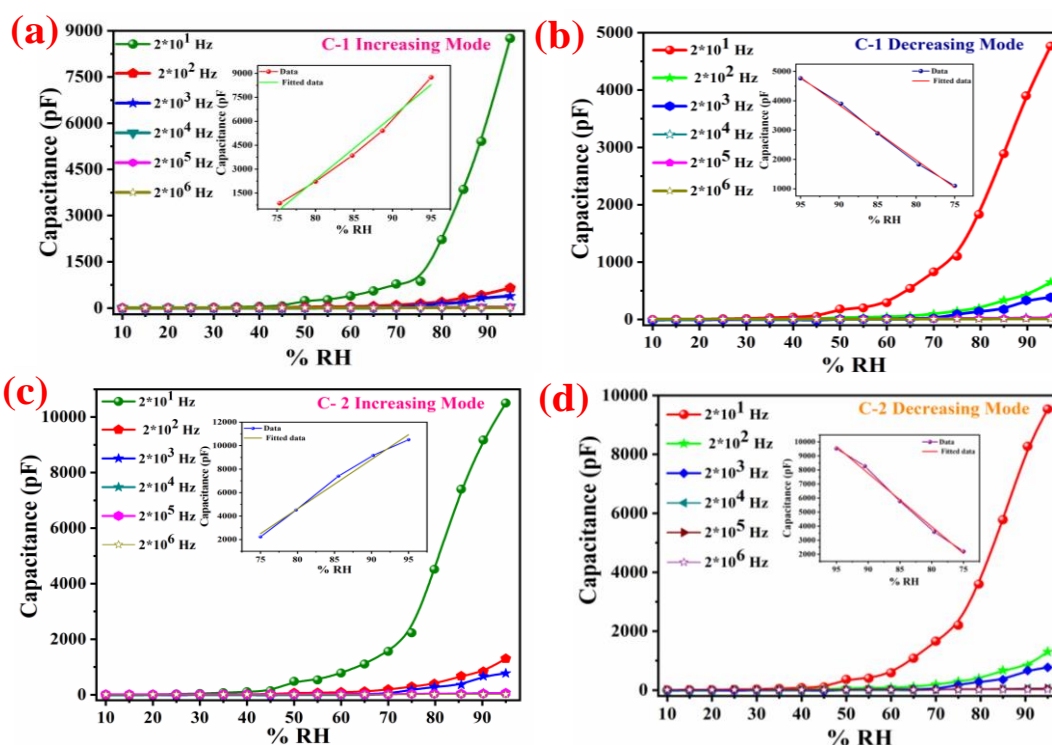


Figure 5.6 Sensing characteristics of GCQDs based sensor at different operating frequencies (20 Hz -2 MHz) (a,b) increasing and decreasing mode curve at different frequencies of C-1 (c,d) increasing and decreasing mode at different frequencies of C-

2

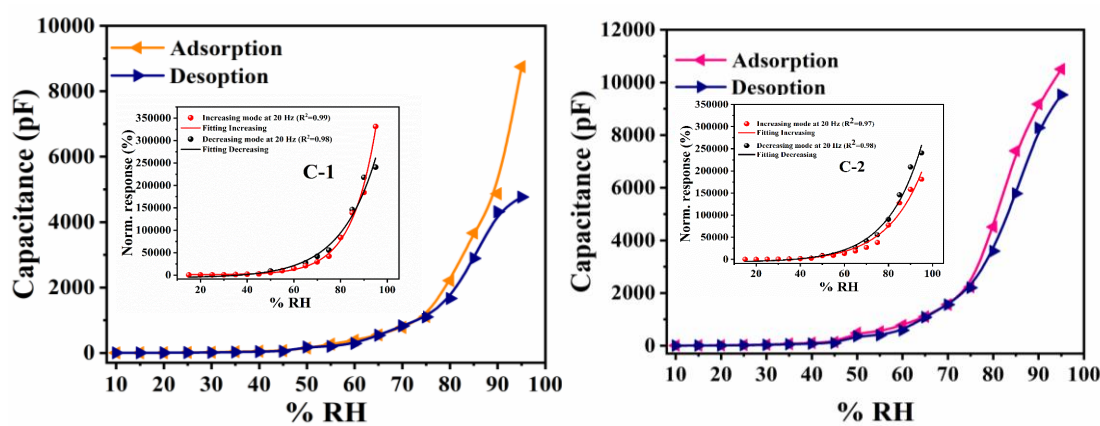


Figure 5.7 (a) Adsorption and desorption curve with hysteresis of gram carbon quantum dot (a) C-1 and (b) C-2. Inset shows corresponding normalized sensor response curve.

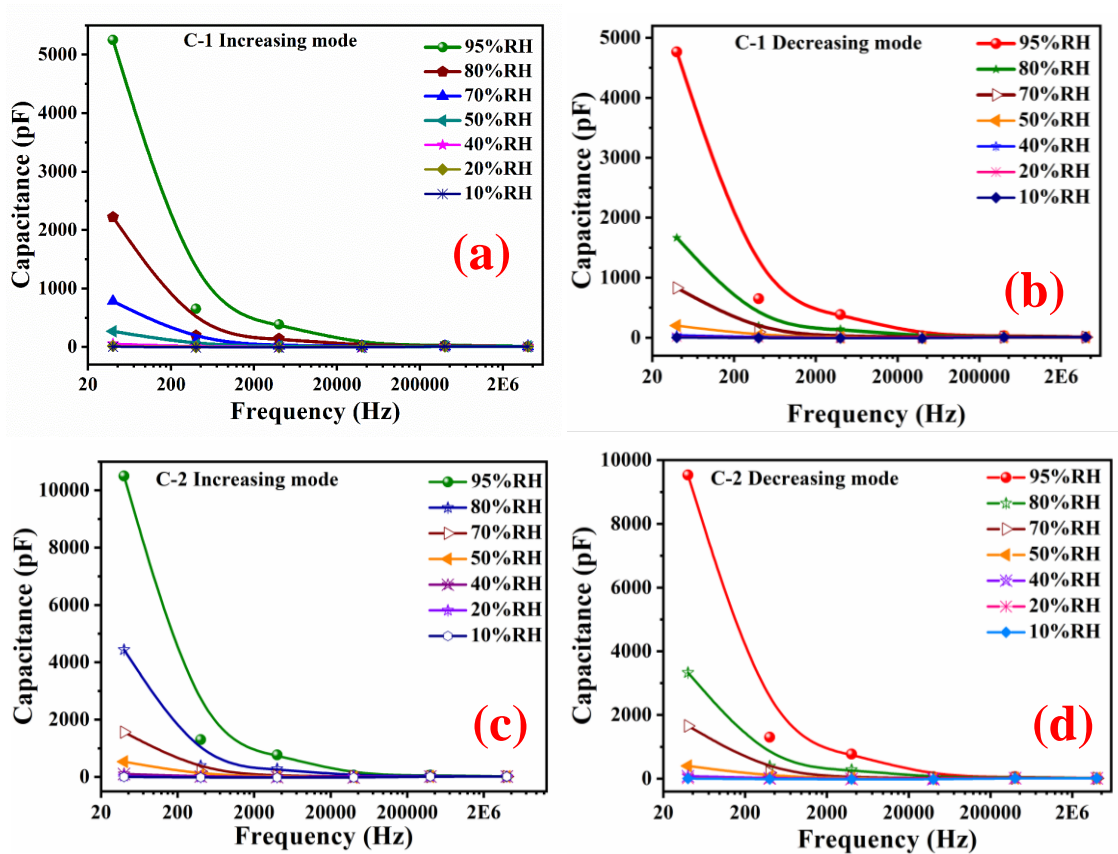


Figure 5.8 Variation of capacitance with respect to frequencies (a) increasing mode (b) decreasing mode of C-1 (c) increasing mode (d) decreasing mode curve of C-2.

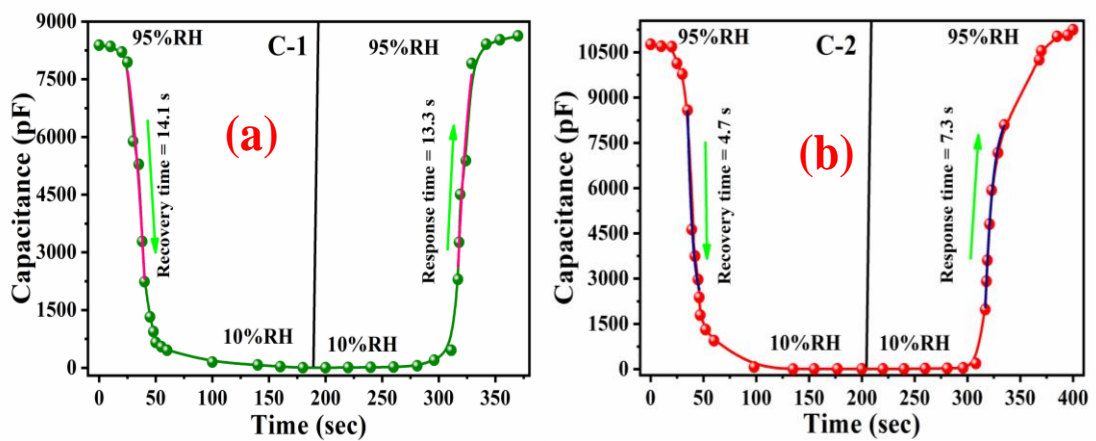


Figure 5.9 Response and recovery times curve of C-1 and C-2

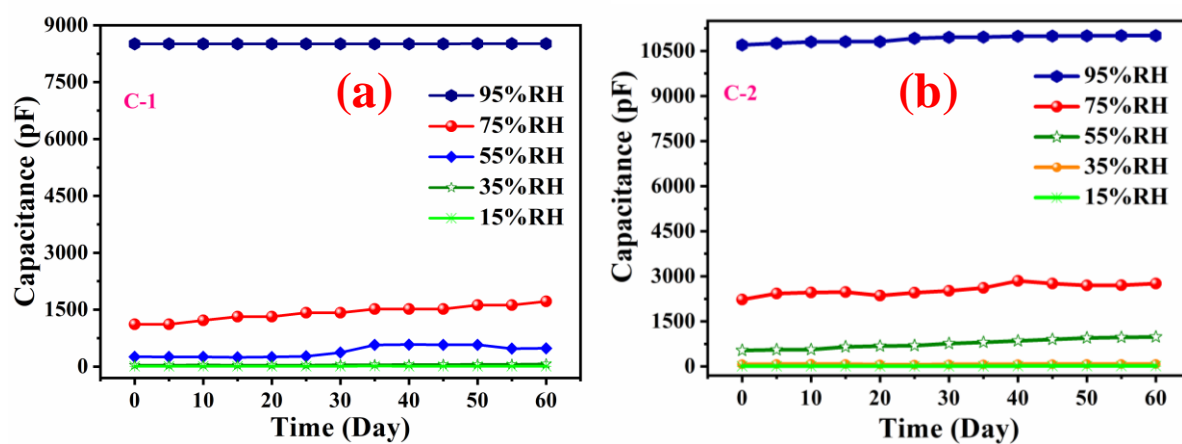


Figure 5.10 Variation of capacitance with time (a) stability curve of C-1 (b) stability curve of C-2

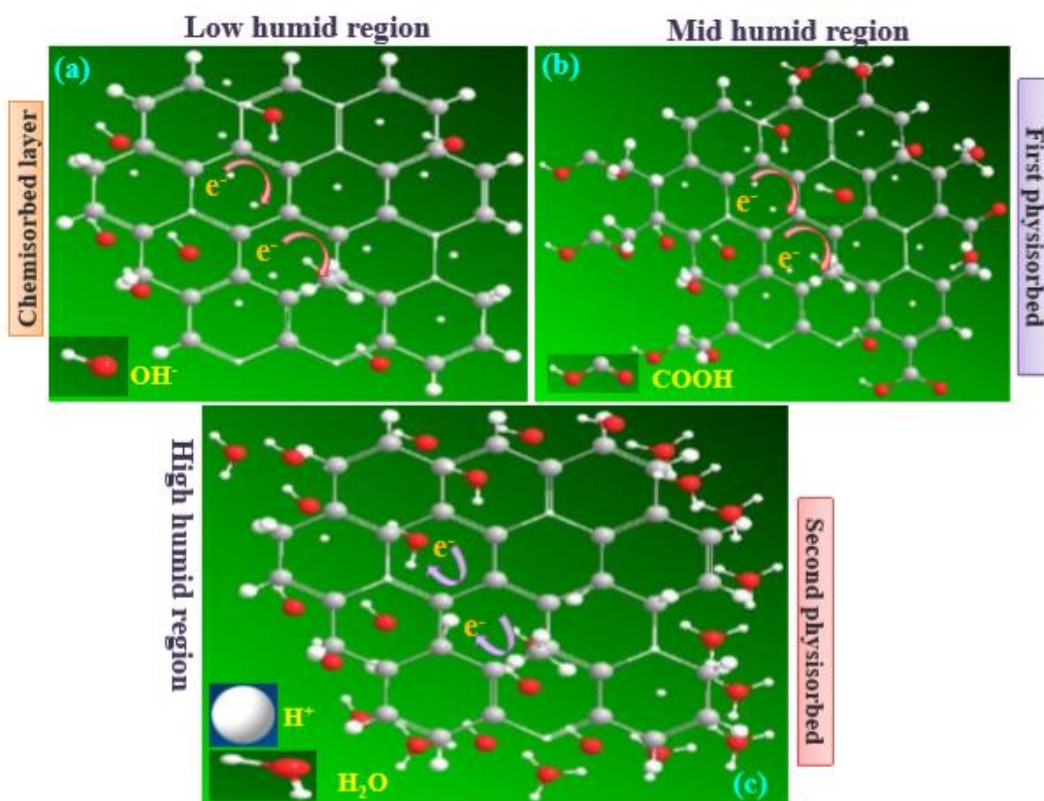


Figure 5.11 Schematic of humidity sensing mechanism of GCQDs

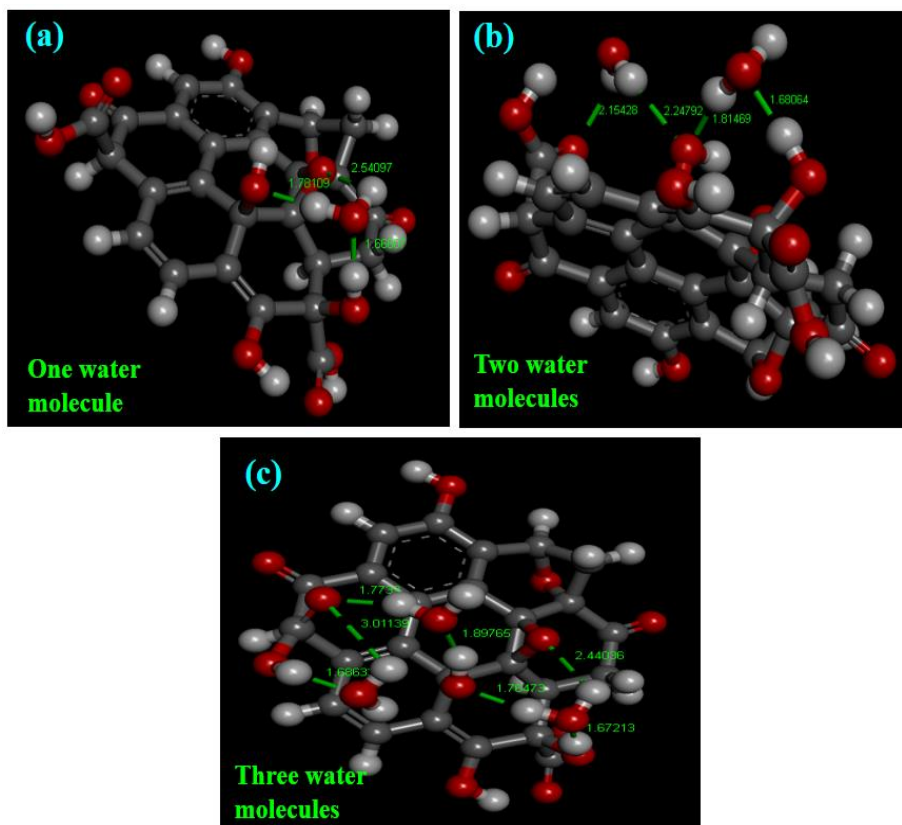


Figure 5.12 Formation of H-bond interaction for (a) one, (b) two and (c) three water molecules with GCQDs

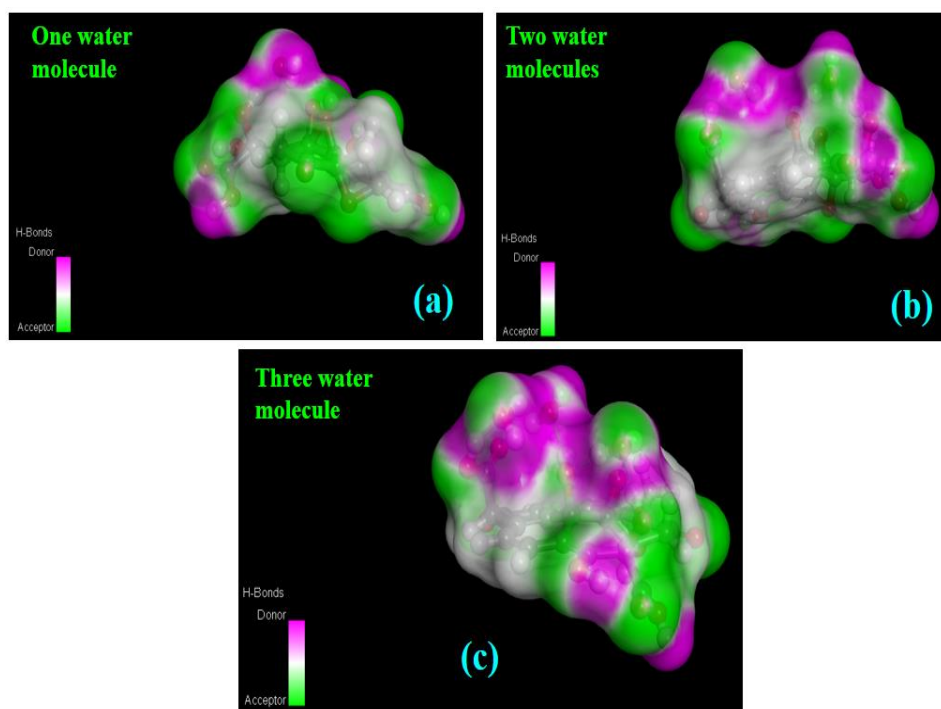


Figure 5.13 H-donor/acceptor clouded regions of (a) one, (b) two and (c) three water molecules with GCQDs

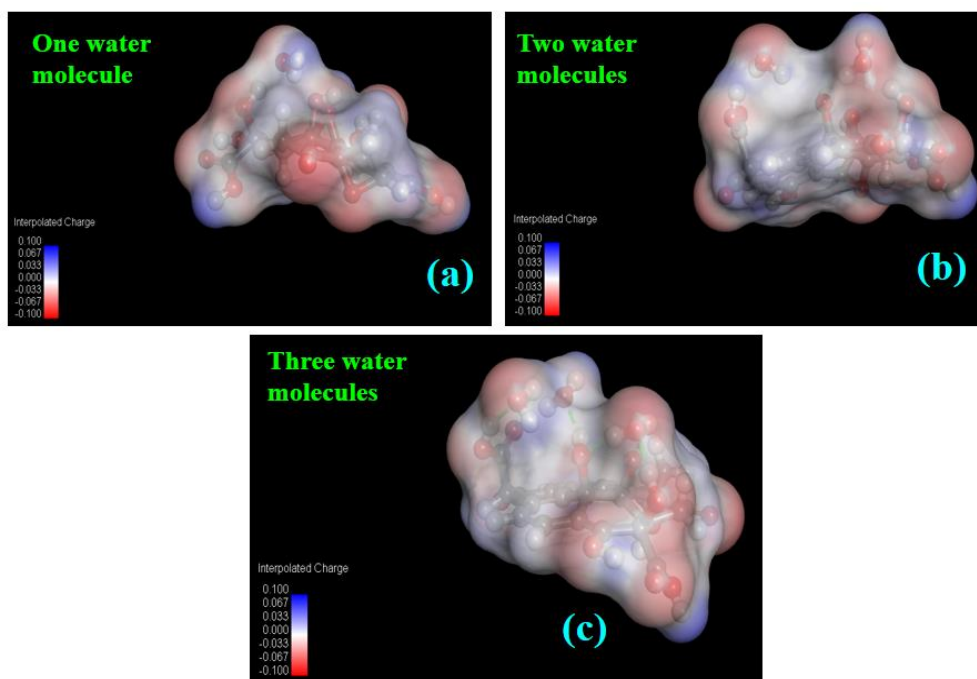


Figure 5.14 The electron cloud densities in the interaction of (a) one, (b) two and (c) three water molecules with GCQD.

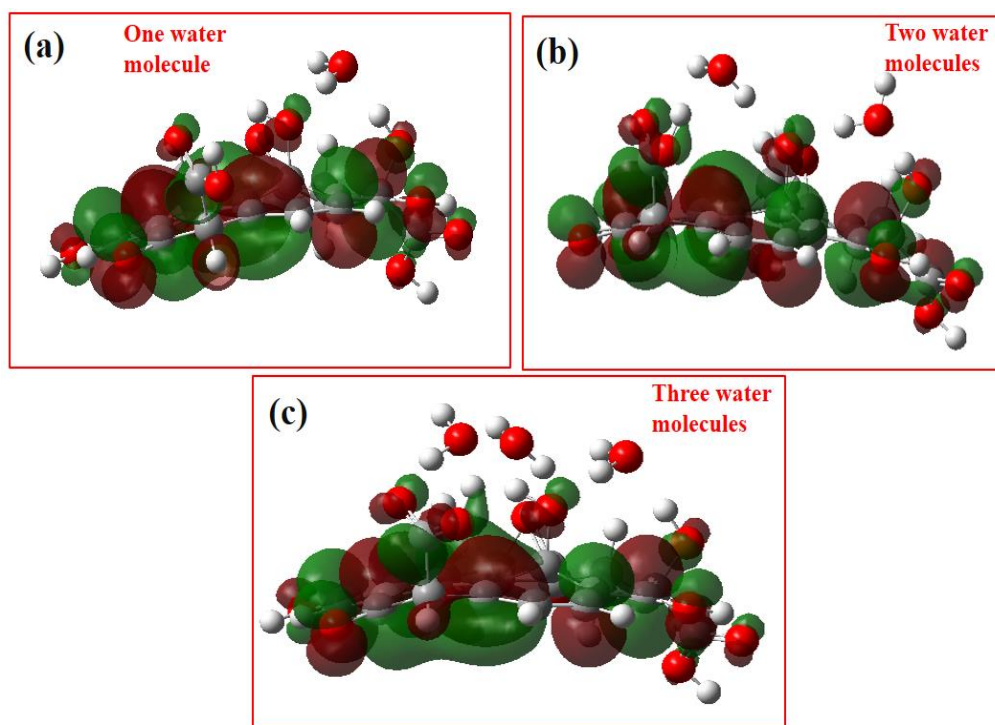


Figure 5.15 HOMO-LUMO molecular orbital structure of gram carbon quantum dots.

CHAPTER 6

One-pot synthesis of phosphine free indium selenide (InSe) QDs and their structural characterization for LPG and humidity sensing

Present chapter reports the facile, low-cost, and phosphine-free one-pot synthesis of Indium selenide (InSe) QDs. The particle size analysis revealed the average particle size of InSe QDs as ~13 nm. Optical properties of as-synthesized QDs were investigated using photoluminescence and UV absorption spectrum. InSe QDs exhibited an excitation wavelength of 370 nm and two major absorption peaks at ~405 and 432 nm. The optical bandgap of the QD was estimated as 2.2 eV. The recombination time of the InSe QDs was also calculated as 6.41ns from the time-resolved photoluminescence (TRPL). Formation of QDs is confirmed using transmission electron microscopy (TEM) showing the presence of spherical particles within a size regime of 2-4 nm. The XRD pattern matched well with the standard tetragonal chalcopyrite InSe QDs structure. The sensing film was made up by a spin-coating method and fabricated InSe QDs film was further employed as an LPG and humidity sensor. The ratio of R_g/R_a for the LPG was found as 4.41. For humidity, the average sensitivity of the sensing film was calculated as 8.89 $M\Omega/\%RH$. The sensing response and decay times of the InSe quantum dot were calculated as 5.3 sec & 13.2 sec. No ageing effect was observed and results were found 97.5 % reproducible.

6.1 Introduction:

A wide range of nanomaterials is exploited based on intertwined physics and chemistry. Quantum dots (QDs) have drawn exceptional interest in modern nanotechnology owing to the smallest particle size and high luminescent structures superior to the big clusters and bulk solids in terms of optical, chemical, and physical properties [1]. Intrinsic emission spectra of a nanomaterial could be changed with the reduction of the size of particles or the formation of shells. These intrinsic properties of a nanomaterial can be extensively functionalized by the different synthesis routes [2]. Numerous synthesis routes are proposed for the successful synthesis of QDs [3]. The capping agent plays a vital role in minimizing the size regime, sustaining stability, uniform growth, and inhibition of agglomeration of the clusters during the synthesis of QDs [4]. The presence of surface ligands controlled the undesirable growth during the nucleation process [5]. The excellent properties such as nanometer size, tunable energy band-gap, fluorescence, and high surface-to-volume ratio serve as a potential candidate for sensing applications. Additionally, the proper selection of an organic surfactant protective coating modifies the nanostructured material to shape according to the opportunity of surface manufacturing.

Synthesis of QDs generally involves the highly toxic phosphine-based organic solvent. Considerable attention has been paid towards the strategy of preparing QDs using a phosphine-free synthesis route [6]. Peng et. al employed the non-coordinating solvent for the synthesis of cadmium oxide QDs. Some solvents such as oleic acid and octadecene dissolved at room temperature [7]. The boiling point of these liquids is 320 °C and it is also capable of dissolving the sulfur content. By TOPO solvents, it is very difficult to purify the QDs. As we know that, colloidal QDs (QDs) are a kind of nanocrystals that are dispersed in their respective solutions [8]. The long-chain capping agents such as oleic acid (OA) or oleylamine (OLA) capping on the surface of the QDs [9]. This capping agent reduces the size of QDs due to its hexagonal chemical structure. Due to the excellent optical and electronic properties, QDs have a high surface area with active sites for the solid-gas interaction and crystalline nature [10]. The reported solvents play a vital role during the formation of QDs by providing tunable surface chemistry, which affects the electric and optical things of the material [11].

The sensing parameters like fast response, recovery, real-time, and high stability have a major role in monitoring harmful and explosive gas in the atmosphere [12]. There are many kinds of gas/ humidity sensors based on metal oxides, semiconductors, and nanocomposites [13]. The sensing properties are enhanced due to some parameters as the surface-to-volume ratio of material and its functional groups attached to the surface. Liquefied petroleum gas (LPG) sensor is a very essential sensing device [7], which is used for the exposure of hazardous LPG outflow in many places such as homes, stations, cars, storage tanks, and factories. LPG is a combination of flammable vapours such as propane (C_3H_8), butane (C_4H_{10}), and hydrocarbon. According to the Occupational Safety and Health Administration (OSHA) and (NIOSH) have consistent the LEL of propane with butane is 2.2 vol.% and 1.8 vol.% in appearance. LEL is defined as the lowermost fraction of the absorption of some objective gas in air, which may be able to simply produce fire in the presence of explosive material. Henceforth to escape any hazardous condition owing to LPG leakage, sensors to sense LEL of LPG are highly required.

A variety of nanostructured materials with different dimensions (nanoparticles, nanorods, nanowires) are reported as highly sensitive gas and humidity sensors [14]. QDs due to their exceptional photoluminescence, tunable band-gap, surface-to-volume ratio, and optical properties are extensively useful for humidity and gas sensing applications [15].

The present work deals with the synthesis of phosphine-free InSe QDs and their application as LPG and humidity sensors.

6.2 Experimental Details

6.2.1 Resources

Indium chloride (99%), oylamine (98%), oleic acid (capping agent), and selenium and these chemicals were purchased from Thermo fisher scientific without further purification.

6.2.2 Preparation Method

6.2.3 Selenium solution (Step-1)

The stock solution of selenium precursor was prepared by dissolving selenium powder (0.05 mmol) in 20 ml of oleylamine at a temperature of 120 °C for 1 hr. As-prepared selenium solution was turned into blackish which is shown in Fig. 6.1.

6.2.4. Preparation of Stock solution (Step-2)

Indium chloride (4 mmol) and oleic acid (1 ml) were taken into the stoichiometric amount and further dissolved in oleylamine (20 ml) with vigorous stirring at a temperature of 130 °C. The temperature of the solution was raised to 250 °C for the hot injection of the previously prepared selenium stock solution. For kinetic growth of InSe QDs, the stock solution of selenium was injected and uniformly resulted in the appearance of the solution to light yellow. InSe QDs were isolated by dissolving the solution into n-hexane and further centrifuging at 3000 rpm with n-hexane and acetone several times to get a fine powder.

6.3 Fabrication of Sensing Element

For the humidity and gas sensor, the fabrication of the sensing element was done by using the spin-coating method. The glass substrates were initially cleaned and additionally ultrasonicated for 50 min. The washed substrates were laid further in the oven for 10 min and placed on a spin coater. A homogeneous solution of InSe QDs was dropped on a glass substrate by a micro pipet with a rotation of 1000 rpm. The prepared film was dried on the hot plate for 30 min and further used for sensing.

6.4 Characterization Techniques

Estimation of the average size distribution of InSe QDs was done using a Transmission Electron Microscope (TEM) (JEOL-2100 F). The optical properties of InSe QDs were investigated by particle size analysis (Nano-zeta sizer), photoluminescence spectroscopy (Spectrofluorimeter-Fluorolog-FL3-11), time-resolved photoluminescence spectroscopy (TRPL), and UV absorption studies (UV-vis spectrophotometer Evolution 201) in the frequency regime of 190 to 1100 nm. Stretching of characteristic bonds was revealed by plotting FTIR transmission spectra. Sensing characteristics of InSe QDs were plotted by measuring the impedance and

resistance using an Impedance analyzer (Wayne Kerr Precision Component Analyzer, 6440B) and Keithley Electrometer (6517B).

6.5 Experimental Set-up

6.5.1 LPG measurement system

The gas sensing system for the experiment is presented in Fig. 6.2. The variation of current and time was recorded using Keithley Electrometer (6517B). The capacity of the gas container is 3 lt., connected with a gas inlet at the top of the gas chamber and outlet of the side of the chamber. The concentration of the gas was measured by a flow meter inside the chamber, the whole experiment was performed at room temperature.

6.5.2 Moisture detection set-up

The impedance-based humidity sensing system contains several components as a humidity-controlled glass chamber, hygrometer, humidification/ dehumidification solutions, and sensing element [16]. The sensing element was connected with two silver electrodes, impedance analyzer was used to measure the impedance of the sensing element. Saturated K_2SO_4 and KOH aqueous solutions were used for the adsorption/desorption cycles of humidity sensing in the chamber. These solutions maintain the humidity level inside the system and a hygrometer was used to measure the relative humidity. The experimental setup for humidity sensing is shown in Fig. 6.3.

6.6 Results and Discussion

6.6.1 Particle Size Analysis

The particle size analysis is a technique, which confirms the average particle size of the nano range and micro range materials. This technique is based on the Brownian motion of the particles and is called the DLS technique. For this purpose, the InSe QDs were dissolved in n-hexane and ultrasonicated for 20 min for the homogenous solution. Nanozeta sizer instrument was used for the analysis of the particle size distribution of InSe QDs[17] and corresponding data has been plotted in Fig. 6.4 (a). The curve shows the average size of the InSe QDs lies in the range of 1-13 nm.

6.6.2 UV-Visible spectroscopy Analysis

The optical absorbance spectra of the InSe quantum dot corresponding with its Tauc plot are presented in Fig. 6.4 (b). This shows an absorption spectrum in the

ultraviolet range and the change of absorption constant corresponding to change with its photon energy can be calculated. The optical energy band gap E_g of the QDs can be predictable from the relation reported in the published research paper [17]. UV absorption spectra of InSe QDs are shown in the wavelength range of the range 200-800 nm. The characteristic band-gap of the InSe QDs was plotted by extrapolating the Tauc plot and is found to be 2.2 eV.

6.6.3 Photoluminescence (PL) spectroscopy Analysis

The Photoluminescence (PL) and Time-resolved photoluminescence (TRPL) analysis were also performed to examine the optical properties of the InSe QDs. Photoluminescence is the size-dependent property and this is the confirmation of quantum confinement. The excitation wavelength at 370 nm[18], showing a strong broad emission peak ranging from 400 to 700 nm, with two max positions at ~ 405 and 432 nm. Hence, a gradual shifting was observed in the curve. From the curve, the blue colour may be seen and the inset of Fig. 6.4(c) also confirms the blue colour of the InSe QDs which is because of the luminescence.

TRPL analysis of InSe QDs has been investigated through the TRPL analyzer. From Fig. 6.4 (d) the variation of the PL intensity corresponding with its lifetime has been displayed. These deviations in a lifetime can be recognized as an extension in the density of states. The transition state will be relative to the density of states consequently, the exponential peak is observed from the curve and this shows the density of states will be revealed in the energy requirement of the emission lifetime. This exciton electron lifetime for InSe QDs was calculated and found to be 6.41 ns and this lifetime is also called the recombination time of the QDs.

6.6.4 TEM, HRTEM and XRD analysis

Crystal structure and size estimation of QDs were done via TEM analysis. Fig. 6.5(a) exhibits the morphology of the InSe QDs. TEM images reveal a sphere-shaped geometry and size distribution of QDs. From Fig. 6.5 (b) the average size was expected around 2-4 nm at 20 nm scale [19]. Fig. 6.5 (c) shows pure InSe quantum dots without UV light. The HRTEM images also confirm the presence of QDs at a 5 nm scale. Most of the particles show at a 1.0 nm scale, which indicates that the spherical particles are

distributed at 1.0 nm scale. The corresponding SAED pattern is shown as an inset of Fig. 6.5 (d).

The crystallinity of InSe QDs film was shown via the X-ray diffraction pattern analysis presented in Fig. 6.5 (e). As it can be seen from the pattern that the three main comprehensive peaks at 26.94, 46.20, and 54.93 correspondings to the Miller indices values are (112), (220), and (312) planes. The XRD pattern well matches with the previously synthesized tetragonal chalcopyrite InSe QDs structure (ICDD 36-1311) [20]. According to the pattern, the broad peak at (111) shows the minimum crystallite size of the quantum dot which is also confirmed by the TEM analysis.

6.6.5 LPG Sensor

The basic principle of the LPG sensing mechanism is the resistive type i.e. output change in resistance of sensing element was recorded upon the exposure of target gas. The mechanism of any sensor is contingent on the surface morphology and availability of the functional group of the sensing element also the capacity of the adsorption and desorption of objective gas on the surface. We have reported the LPG sensing capability of the InSe QDs. The sensing mechanism of QDs depends on the resistance of the material. The change in electrical resistance of QDs with time for different LPG gas concentrations is shown in Fig.6.6 (a-f). As we could see from the curve that the concentration of LPG increases, the respective parameters such as sensitivity, decay, and grow times of the sensor would also increase. The sensitivities of InSe QDs for different LPG concentrations are shown in Fig. 6.6 (f). It exhibits the linear response for 0.5–2.0 vol.% of LPG, and after that it becomes saturated. Also, the InSe QDs respond at a very low LPG concentration below LEL i.e. 0.5 vol.% resulting an inferior surface exposure of LPG molecules, which shows that a small amount of LPG increases the resistance maximum. From the sensitivity curve, the maximum sensitivity and response of the sensor were found higher at high concentrations & low sensitivity at lower concentrations and the data have been tabulated in Table 6.1. The lowest response and recovery times are also observed in Fig. 6.6 (b). Therefore, as the liquified petroleum gas was turned ON, the response time of the sensing film was observed, and when the outlet was opened LPG was in an off state, which indicates the recovery of the sensing film. The less response, recovery times, good sensitivity, and

high stability properties of the sensing element are responsible for the commercial purpose.

6.6.5.1 LPG Sensing Mechanism

The sensing mechanism is devoted to the surface adsorption and desorption of the LPG, it involves the movement of adsorbed oxygen species. The sensing principle depends on the change in electrical resistance corresponding with input owing to the electronic exchange of charges. When the target gas interrelates on the surface of the sensing element (InSe QDs) it leads the electron transfer between LPG and surface. Initially, the surface of the sensor is free from the absorbed LPG molecules, the atmospheric oxygen molecules get attracted to the sensing element and formed the chemisorbed on the surface. The oxygen molecule ions species were interrelating with the conduction band electrons. During this process, the transfer of an electron from the conduction band to the chemisorbed oxygen molecules is shown in Fig. 6.7. The electrons concentration of the materials at the surface decrease which causes a drastic increase in the resistance of the sensing film. After that, an equilibrium state is reached concerning the sensing object adsorbed the oxygen and atmospheric oxygen molecules over the beyond chemisorption process. During the chemisorption, the possible reaction involved is depicted in Fig. 6.7. From the reactions, when LPG gas has interacted with the surface of the material, the gas molecules reacted with the ions surrounding the surface. LPG molecules are a combination of hydrocarbons, and they are considered owing to covalent bonds between carbon and hydrogen.

6.6.6 Humidity sensing characteristics

Fig. 6.8 (a-f) shows the InSe based humidity sensing characteristics with both adsorption and desorption modes. The variations in impedance have been recorded with changes in humidity from the initial 10 %RH to the final 90 %RH [21]. The deviation in impedance corresponding to the humidity of sensing film is divided into three regions: low humid region (10–45 %RH), mid humid region (45–70 %RH), and high humid region (70–90 %RH). From the curves, impedance decreases as relative humidity increases for both adsorption and desorption cycles. The humidity range covered from 10 %RH to 95 %RH during an experiment at room temperature. As the humidity level increases, the impedance changes according to the region and sharp changes may be observed in the mid humid region. The impedance decreases slowly in higher humidity

regions i.e. 70-90 %RH. Consequently, we were able to accomplish that the sensor film is most sensitive in the mid humid (45-70 %RH) region. The decreasing mode (green curve) also follows a parallel pattern[22]. Other significant parameters of the sensor are an ageing effect, reproducibility, response, and recovery times [23,24]. The ageing effect is defined as the spreading of sensor outputs when the sensor shows repetition under the same circumstances after an extensive time. Fig. 6.8 (b) shows the characteristic ageing effect after one, two, and three weeks and it can be seen that the InSe based QDs humidity sensor is stable having the least variation in output impedance with time [25].

Fig. 6.8 (c) shows the linear coordinate curve like a green line while the logarithmic coordinate is exposed as a pink line, it can be observed that the non-linear curve is found over the range (10–90% RH). The next parameter is the reproducibility of the sensor which is very important and defined as reobserving the sensing output of the sensor in the same ecological situations. The reproducibility curve of the sensing element is shown in Fig. 6.8 (d) and the reproducibility is estimated as 97.5%. Fig. 6.8 (e) displays the most important parameter response/ recovery times and it was calculated as 5.3 sec and 13.2 sec. The sensitivity at every region was calculated from the adsorption curve and found as more sensitive in the mid humid region which can be seen in Fig. 6.8 (f).

6.6.6.1 Selectivity and Effect of Humidity on LPG Sensing

To study the selectivity of the QDs-based sensing element, the different gases as humidity, LPG, ethanol, acetone, and carbon dioxide were exposed on the surface. The corresponding histogram is plotted in Fig. 6.9 (a) which shows the sensing element is sensitive for gases but highly responsive for humidity sensors. To investigate the effect of LPG on the humidity sensing curve, the testing was achieved in presence of a humidity chamber. The corresponding data were plotted in Fig. 6.9 (b) which shows the sensing characteristics with LPG (blue) and without LPG (pink) at 0.5 vol% LPG. From the curve, it can be seen that the presence of LPG affects the humidity characteristics of the sensor.

6.7 Conclusion

In the present work, the phosphine-free InSe quantum dots have been synthesized successfully using the least toxic hot injection route and the films were fabricated via the spin coating method. The fabricated InSe QDs film was further used for LPG and humidity sensing purposes. The fluorescence was observed in the blue range by the UV-light chamber and further confirmed by the photoluminescence spectroscopy analysis. The particle size distribution curve gave the average particle size of the QDs as ~13 nm. The UV- absorption spectra were taken and calculated optical band gap as 2.2 eV. The TRPL analysis exhibited the relaxation time of QDs as 6.14 ns. The formation of quantum dots was also confirmed by TEM and HRTEM analysis which gave the particle size in the range 2 to 4 nm. XRD pattern revealed the crystalline nature of QDs. Further, the fabricated film was used for LPG and humidity sensing. The humidity sensing properties were studied in the range 10 %RH to 90 %RH and found as the most sensitive i.e. 19.50 MΩ/%RH in the mid humidity range (45-70 %RH). The average sensitivity of the sensor was found as 8.89 MΩ/%RH. Response and recovery times of the InSe quantum dot-based humidity sensor were found as 5.3 sec & 13.2 sec. The sensing element was also exposed with the LPG of various concentrations 0.5 to 2.0 vol.%. The maximum sensor response was found as 4.41 for 2.0 vol.% of LPG. This sensor exhibited the sensor response 2.29 for 0.5 vol.% of LPG which is below LEL. The minimum response and recovery times were calculated as 7.5 sec and 6.3 sec. The investigated sensing parameters favour this material for the commercial development of a humidity sensor at room ambient.

References

- [1] N. Revaprasadu, M.A. Malik, J. Carstens, P.O. Brien, S. Kensington, S. Africa, Novel single-molecule precursor routes for the direct synthesis of InS and InSe quantum dots, (1999) 2–5.
- [2] N.J. Simi, L. Kuriakose, R. Vinayakan, V. V Ison, CuInS₂–In₂Se₃ quantum dots – a novel material via a green synthesis approach, (2018) 37146–37150.
- [3] M.J. Hamer, E. Tóvári, M. Zhu, M.D. Thompson, A.S. Mayorov, J. Prance, Y. Lee, R. Haley, Z.R. Kudrynskiy, A. Patanè, D. Terry, D. Kovalyuk, K. Ensslin, A. V Kretinin, A.K. Geim, R.V. Gorbachev, Gate-Defined Quantum Confinement in InSe- based van der Waals Heterostructures, (2018).
- [4] M. Green, The nature of quantum dot capping ligands, *J.Mat.Chemistry* (2010) 5797–5809.
- [5] E.M. Boatman, G.C. Lisensky, K.J. Nordell, A Safer, Easier, Faster Synthesis for CdSe Quantum Dot Nanocrystals, *J. Chem. Educ.* 82 (2005) 1697–1699.
- [6] J. Hass, W.A. De Heer, E.H. Conrad, Graphene-based quantum dots, *J. Phys Condens. Matter* 22 (2010).
- [7] T. Kim, Y.K. Jung, J. Lee, The formation mechanism of CdSe QDs through the thermolysis of Cd (oleate)₂ and TOPSe in the presence of alkylamine, *J. Mater. Chem. C*, (2014) 5593–5600.
- [8] M. Dutta, S. Sarkar, T. Ghosh, D. Basak, ZnO/Graphene Quantum Dot Solid-State Solar Cell, *J. Phys. Chem. C*, 116(2012)20127-20131.
- [9] M. Echabaane, D. Chaudanson, M. Petit, L. Bideux, B. Gruzza, Synthesis and Study of Stable and Size-Controlled ZnO – SiO₂ Quantum Dots: Application as a Humidity Sensor, *J. Phys. Chem. C*, 120 (2016)11652-11662.
- [10] S. Chakraborty, M. Pal, Sensors and Actuators B : Chemical Improved ethanol sensing behaviour of cadmium sulphide nanoflakes: Beneficial effect of morphology, *Sensors Actua B. Chem.* 242 (2017) 1155–1164. doi:10.1016/j.snb.2016.09.129.
- [11] H. Yu, Z. Song, Q. Liu, X. Ji, J. Liu, S. Xu, H. Kan, Colloidal synthesis of tungsten oxide quantum dots for sensitive and, *Sen Actuators B.*

- Chem,10(2017)123-129.
- [12] G. Si, Y. Hu, H.O.H. Churchill, D.J. Reilly, J. Xiang, C.M. Lieber, C.M. Marcus, Double quantum dot with integrated charge sensor based on Ge/Si heterostructure nanowires, *Appl. Phys. Lett.* 117(2020) 1–5.
- [13] X. Xing, Y. Lei, W. Shang, L. Du, P. Guo, Theoretical Research on Ellipsoidal Structure Methane Gas Detection Based on Near-Infrared Light Sources of PbSe Quantum Dots, *J. nanomaterial* 20 (2017) 1–7.
- [14] H. Liu, M. Li, O. Voznyy, L. Hu, Q. Fu, D. Zhou, Z. Xia, E.H. Sargent, J. Tang, Physically Flexible, Rapid-Response Gas Sensor Based on Colloidal Quantum Dot Solids, *Adv Mater*(2014) 2718–2724.
- [15] O.S. Wolfbeis, Materials for fluorescence-based optical chemical sensors, *J. Mater. Chem.* (2005) 2657–2669.
- [16] D.K. Maurya, S. Sikarwar, P. Chaudhary, S. Angaiah, B. C. Yadav, Synthesis and Characterization of Nanostructured Copper Zinc Tin Sulphide (CZTS) for Humidity Sensing Applications, *IEEE Sens. Jour.* 19 (2019) 2837–2846.
- [17] P. Chaudhary, D.K. Maurya, R.K. Tripathi, B.C. Yadav, N.D. Golubeva, E.I. Knerelman, I.E. Uflyand, G.I. Dzhardimalieva, The synthesis of a Cu_{0.8}Zn_{0.2}Sb₂–polyacrylamide nanocomposite by frontal polymerization for moisture and photodetection performance, *Mater. Advances.* (2020).
- [18] P. Chaudhary, D. K. Maurya, S. Yadav, A. Pandey, R. Kant, B.C. Yadav, Ultrafast responsive humidity sensor based on roasted gram derived carbon quantum dots : Experimental and theoretical study, *Sens. actuators B. Chemical* 329 (2021).
- [19] S. Yadav, P. Chaudhary, K.N. Uttam, A. Varma, M. Vashista, B.C. Yadav, Facile synthesis of molybdenum disulfide (MoS₂) quantum dots and its application in humidity sensing, *Nanotechnology*, 30 (2019).
- [20] N. Yadav, P. Chaudhary, K.K. Dey, Non-functionalized Au nanoparticles can act as high- performing humidity sensor, *JMSE.* (2020) 17843–17854.
- [21] R.K. Tripathi, O.S. Panwar, I. Rawal, C.K. Dixit, A. Verma, Study of variable range hopping conduction mechanism in nanocrystalline carbon thin films deposited by modified anodic jet carbon arc technique : application to light-

- dependent resistors, JMSE 32 (2021) 2535–2546.
- [22] V. Kumar, V. Chauhan, J. Ram, R. Gupta, S. Kumar, Study of humidity sensing properties and ion beam induced modifications in SnO₂-TiO₂ nanocomposite thin films, Surf. Coat. Technol. 392 (2020).
- [23] Z. Duan, Q. Zhao, S. Wang, Q. Huang, Z. Yuan, Y. Zhang, Y. Jiang, H. Tai, Halloysite nanotubes: Natural, environmental-friendly, and low-cost nanomaterials for the high-performance humidity sensor, Sensors Actuators B. Chem. 317 (2020) 128204.
- [24] Z. Duan, Q. Zhao, S. Wang, Z. Yuan, Y. Zhang, X. Li, Y. Wu, Y. Jiang, H. Tai, Sensors and Actuators B: Chemical Novel application of attapulgite on high performance and low-cost humidity sensors, Sensors Actuators B. Chem. 305 (2020) 127534.
- [25] M. Liu, C. Wang, N. Kim, MIM-Type Capacitive Humidity Sensor Using Functional Polymer Mixed with TiO₂ Microparticles, Sensors 2(2017) 284.

Tables:

Table 6.1 shows the LPG sensing parameters of InSe based sensor.

Target gas concentration (vol %)	R_g/R_a	Growth time (sec)	Decay time (sec)
0.5	2.96	7.5	6.3
1.0	3.40	9.5	9.0
1.5	3.76	11.0	11.5
2.0	4.41	12.6	14.0

Figures:

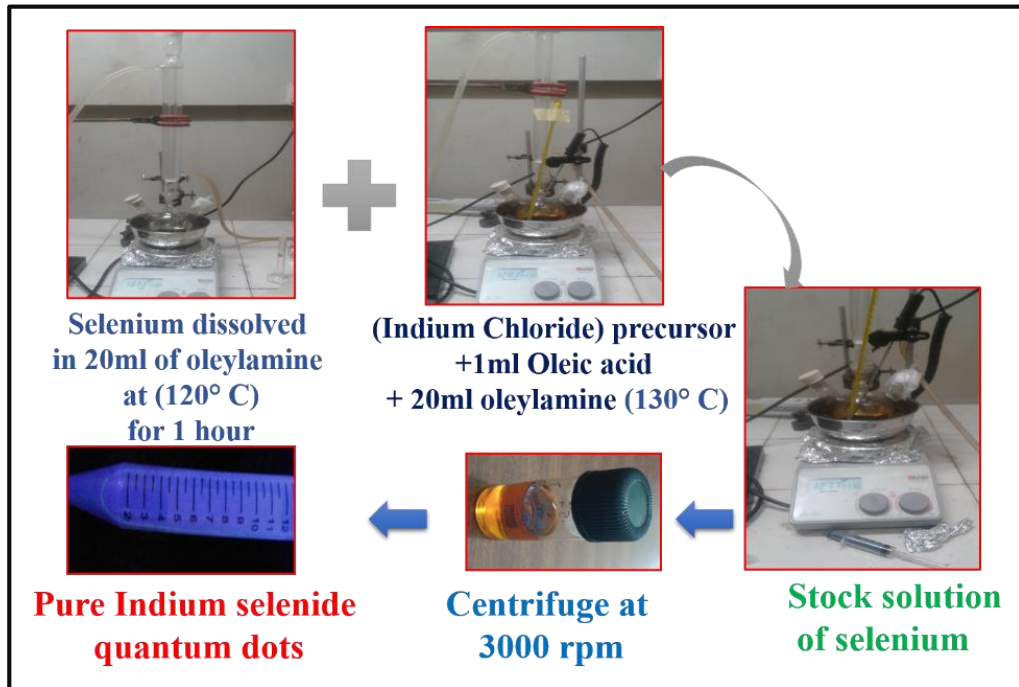


Figure 6.1: Schematic for the synthesis of InSe QDs by kinetic growth method

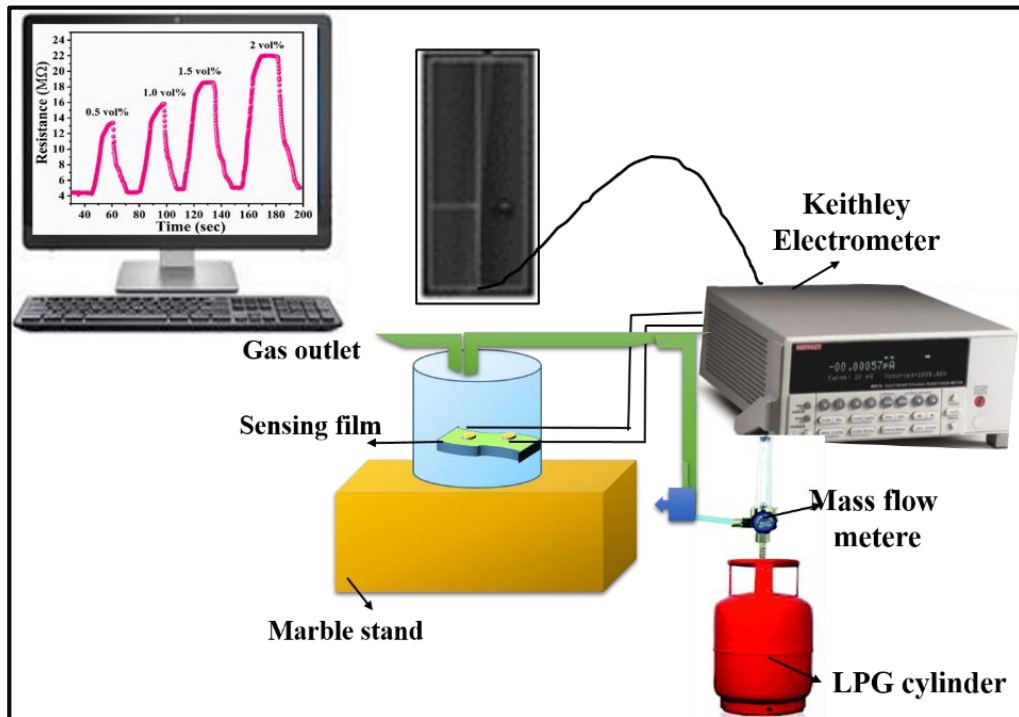


Figure 6.2: Schematic for the LPG sensing set-up

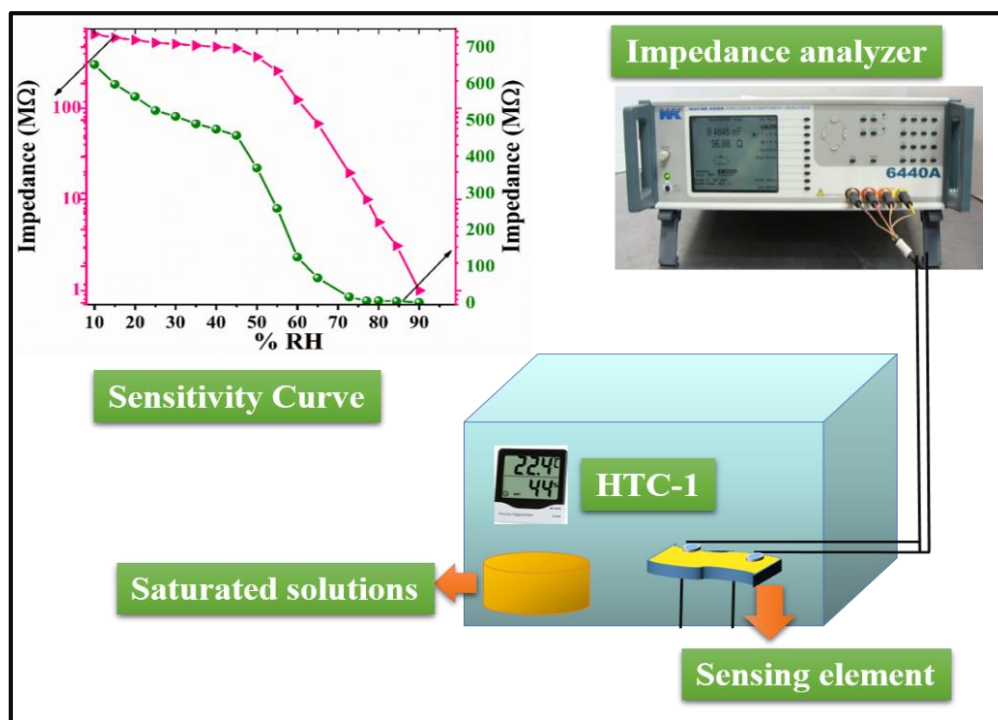


Figure 6.3: Experimental set-up for humidity sensing

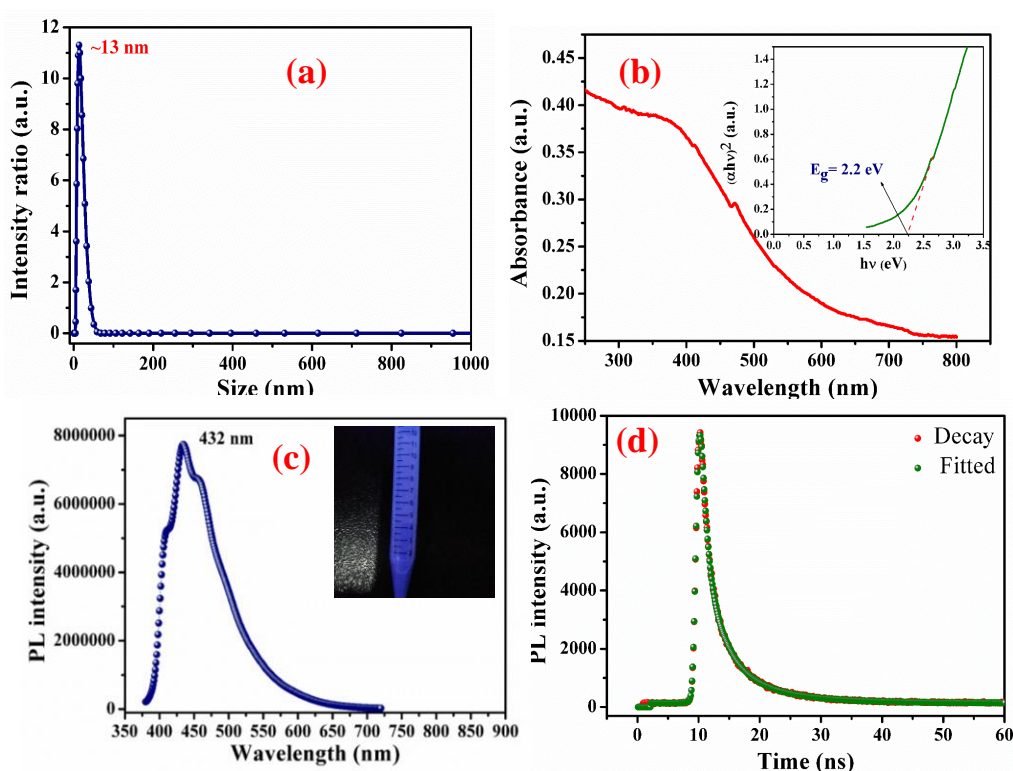


Figure 6.4: (a) Particle size analysis of QDs (b) UV-Visible absorbance spectra with Tauc plot (c) Time-resolved PL spectra of InSe QDs (d) Photoluminescence spectra of QDs.

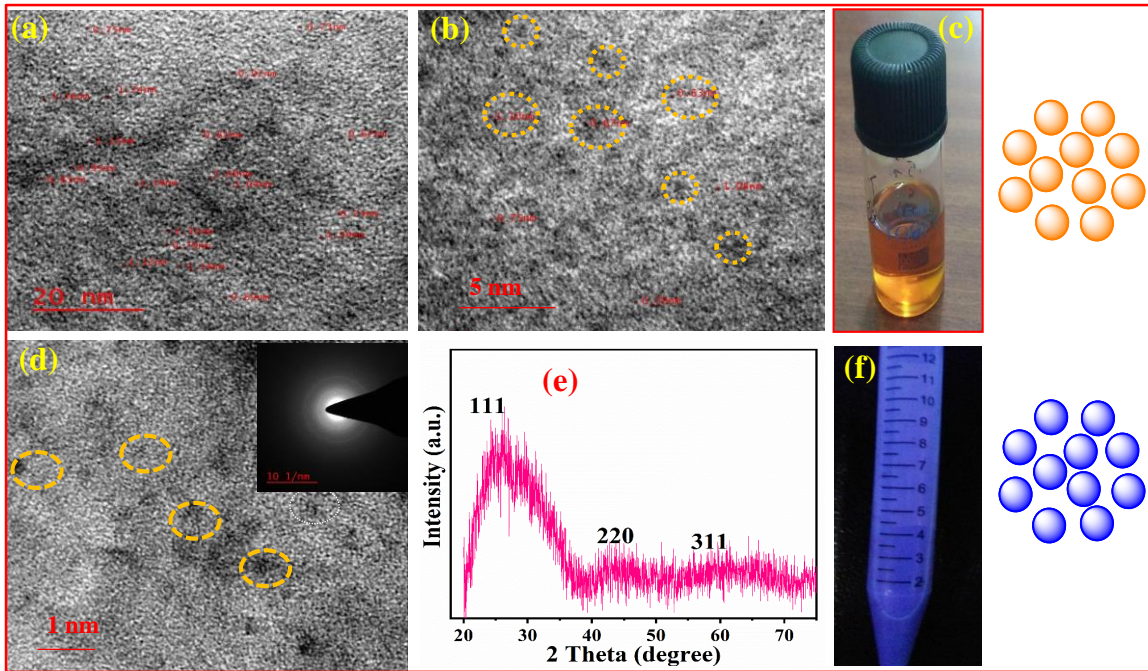


Figure 6.5: (a) Topological analysis at 20 nm scale (b,d) HRTEM analysis at 5 nm scale and 1 nm scale (c) pure InSe QDs without UV light (e) XRD analysis of quantum dot (f) fluorescence image of QDs in presence of UV light.

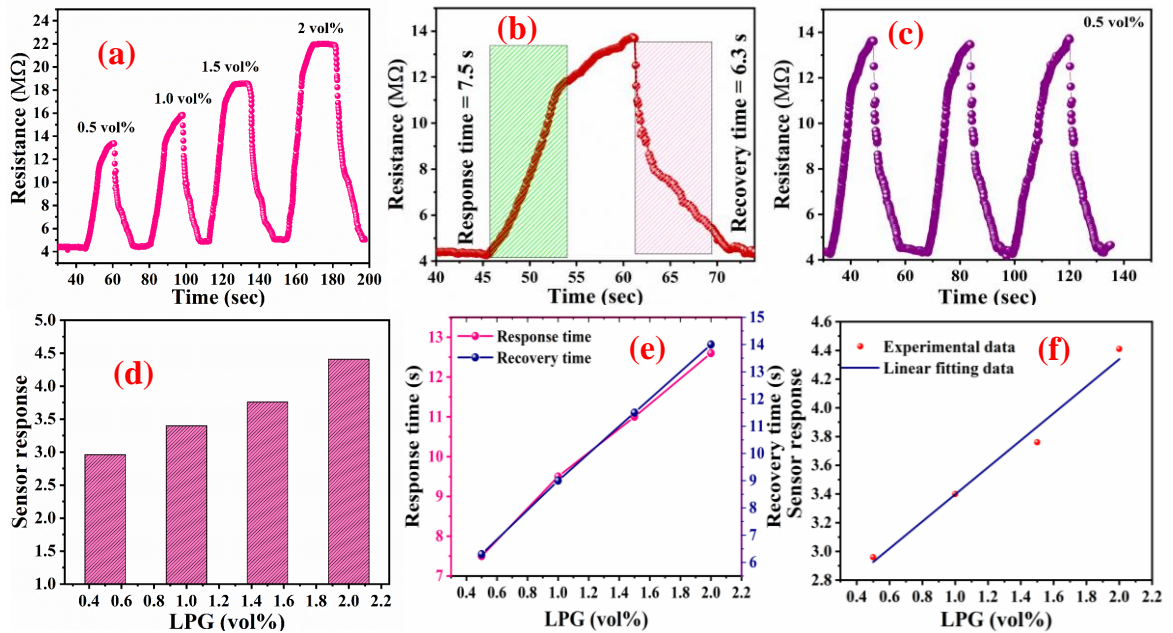


Figure 6.6: (a) LPG gas sensing response of the InSe QDs at different vol.% (b) response and recovery time curve shows the 7.5 sec and 6.3 sec respectively at 0.5 vol.% (c) repeatability test at 0.5 vol.% (d) sensor response histogram at different vol.% (e) response and recovery time at different vol.% (f) linear sensor response.

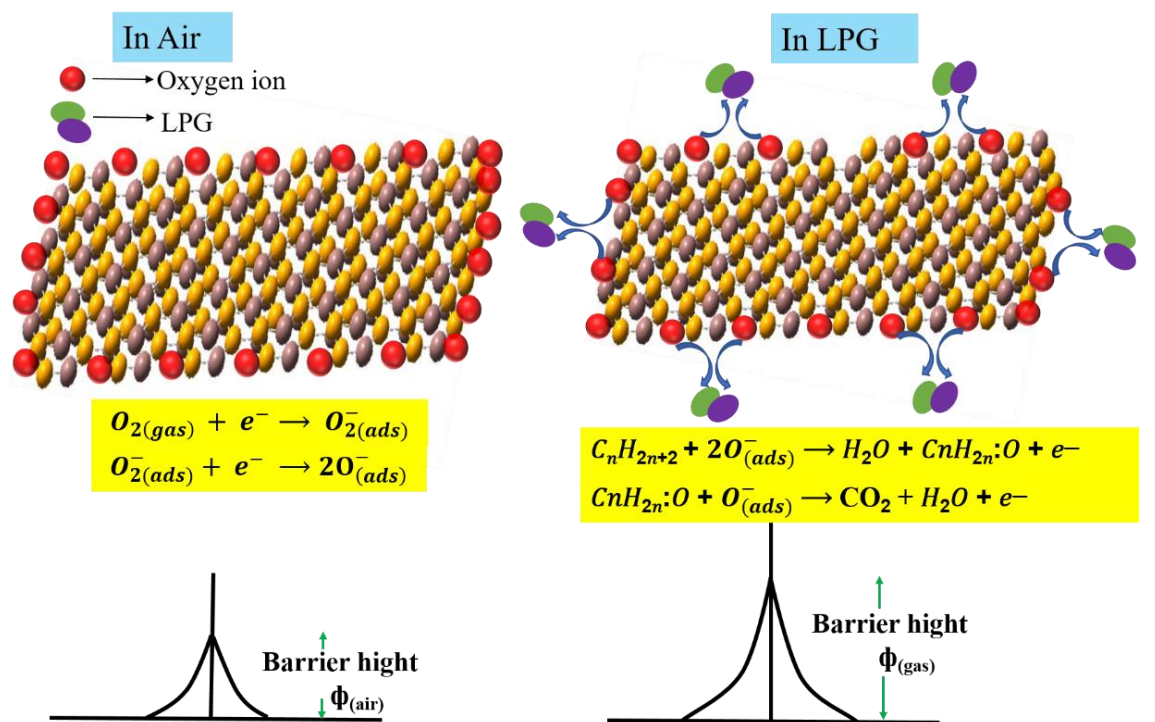


Figure 6.7: Schematic for LPG sensing mechanism.

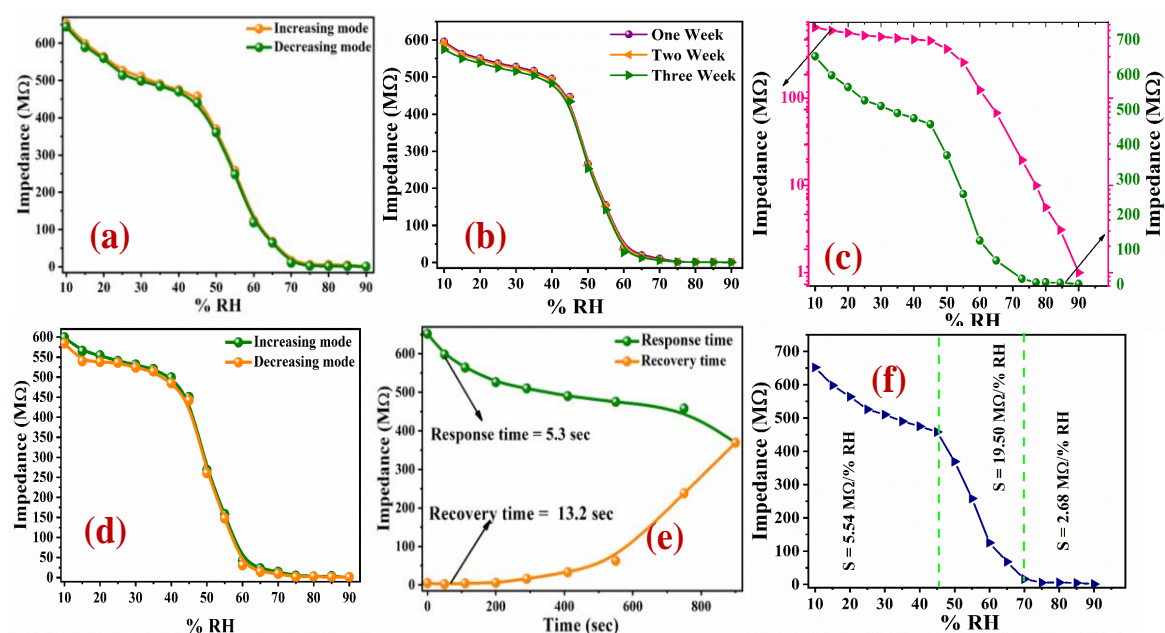


Figure 6.8: (a) Humidity sensing response of the InSe QDs (b) ageing effect after one, two, three weeks (c) repeatability test (d) response and recovery curve of the InSe QDs (e) response and recovery time (f) linear sensor response

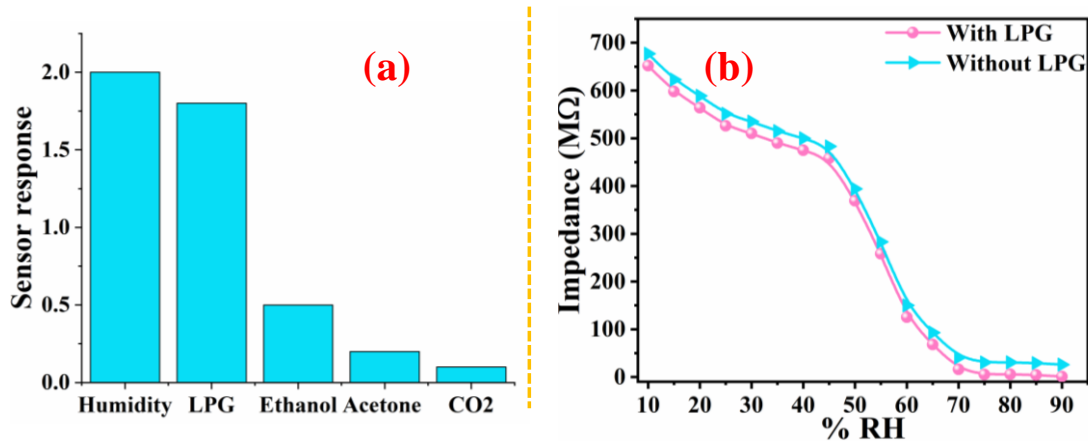


Figure 6.9: (a) Selectivity of InSe QDs with other gases (b) effect of humidity during LPG sensing.

CHAPTER 7

Concluding Remarks and Scope of Further Research

A study of synthesis, characterization, humidity and gas sensing properties of nanometallopolymer and quantum dots are summarized in the present chapter. This chapter also provides the guidelines for further research work in the field of nanodimensional material as a humidity and gas sensor.

7.1 Conclusion

The field of nanotechnology is one of the most popular areas for current research and development in basically all technical disciplines. Another field of interest is metal-organic frameworks (MOF) which mainly include metallopolymers. Nanometallopolymers are emerging polymer nanocomposites which are very cost-effective and can be used as solar cells, IC chips, and energy storage devices. Polymer gels are significant materials for both fundamental and scientific research. Also, hydrogels are quite interesting owing to their excellent property of absorption/desorption which ensures their applicability in biomedical engineering. Acrylamide-based hydrogels can be best suited for versatile applications.

During the last few years, the optical and electronic properties of semiconductor nanostructures have been of great interest theoretically and experimentally. At the nanometer scale, continuous energy levels changes in discrete energy levels due to the quantum confinement phenomena. Quantum confinement effects are present in many systems e.g. in quantum well, quantum wire and quantum dots. In quantum dots, due to the 3-D confinement, the density of states shows discrete energy levels. The energy levels can be monitored to different values by controlling the shape, size, dot material and confinement potential. The electronic transitions in the discrete energy levels can be used to tailor the optical properties of quantum dots. Quantum dots are very tiny particles, having a diameter of 2 to 10 nanometers. They have unique optical and electronic properties due to their three-dimensional quantum confinement regime. In a semiconductor bulk material, the conduction and valence band are separated by a bandgap and when light absorption takes place, the electron is excited from the valence band to the conduction band, creating a hole in the valence band. After a certain time (10^{-8} sec), when the electron returns to the valence band, fluorescence is observed. Because of the small-time lag in the process of light absorption, the electron and hole don't move independently due to the Coulomb attraction and form hydrogen-like species. When all the three dimensions of the semiconductor material are reduced to few nanometers and the particle becomes smaller than the Bohr radius, the quantum confinement effect comes into the scene and in this situation, these nanoparticles are defined as quantum dots. Quantum dots (QDs) are compounds with specific characteristics like the bandgap of QDs increases when the size of the particle decreases.

Also, the colour that QDs emits is directly proportional to its size (smaller dots appear blue). Few limitations of organic metallopolymers (sensitivity, stability etc.) have motivated us towards QDs to make their nanohybrids for humidity/gas sensing applications as the humidity/gas sensors play a vital role in various fields like medical, agriculture, industries etc.

Chapter 1 deals with the fundamental concept of sensors and their comparison with the existing sensing devices. Briefly introducing the classification of humidity, gas and photosensors, the underlying mechanism and their performance index. A detailed overview of current sensor materials (metal oxide polymer composite, metallopolymers and quantum dots), strategies of enhancing the performance with their characteristics of sensing materials. Also, the sensing mechanism and responsible parameters of sensing material have been discussed in detail. The chapter concludes with the concept of metallopolymers and quantum dots materials for humidity, gas and photosensors and the plausible solutions to overcome the present challenges. The wide literature review of the past decade has been tabulated. The multipurpose applications of impedance and capacitance-based humidity sensors have also been explained in this chapter. The orientation of work, aims and objectives of the present research work are well described at the end of the Chapter. **Chapter 2** deals with the synthesis of nanometallopolymers $\text{Ni}(\text{NO}_3)_2(\text{AAm})_4 \cdot 2\text{H}_2\text{O}$ and its fabrication by spin coating. The humidity sensing application at room temperature has also been investigated. In **Chapter 3** a purpose has been completed to synthesize the CdS/polyacrylamide using the frontal polymerization route. Further, its film was fabricated using the spin coating technique for the detection of humidity at room temperature. A new approach to the application of an as-developed humidity sensor to detect the moisture/ wetness in the Baby diaper with an alarm system was also investigated in this chapter. **Chapter 4** deals with the synthesis of ternary metal-doped polyacrylamide as a humidity sensor. **Chapter 5** describes the synthesis of carbon quantum dots from roasted grams using the pyrolysis method. These quantum dots easily interact with water molecules and were utilized as humidity sensors. Also, the DFT data confirmed the experimental results. **Chapter 6** designates the synthesis, characterization and humidity sensing properties of quantum dots such as carbon quantum dots and InSe quantum dots. In this chapter the gas sensing properties were also investigated. **Chapter 7** deals with a study of synthesis, characterization, humidity and gas sensing properties of nanometallopolymer and quantum dots which are

summarized in the present chapter. This chapter also provides the guidelines for further research work in the field of nano dimensional materials as humidity and gas sensors.

7.2 Development of a reliable room temperature humidity sensor using nanostructured nickel polyacrylamide

The humidity sensing ability of Ni(II) nitrate PAAm complex was investigated by recording the variation in impedance on exposing the humidity. The crystalline nature of the material was confirmed by XRD analysis. The minimum crystallite size as calculated from the Debye - Scherrer formula was 9 nm and the average crystallite size was 13 nm. This crystallinity was revealed through TEM image revealed the nanoparticles having sizes in the range of 4-21 nm. A wide optical band-gap of 4.034 eV was found by the UV-vis Spectrophotometer. The average sensitivity of the film was found as 33.27 M Ω /%RH for impedance-based humidity sensing. The response and recovery time for the electrical mode were calculated as 15.11 sec and 75.25 sec. Also, the ageing trial confirmed that the material was quite stable after 60 days.

7.3 Polyacrylamide decorated CdS nanoparticles based flexible humidity sensor for baby diaper alarm: Experimental and theoretical study

CdS/Polyacrylamide nanocomposite was prepared via frontal polymerization techniques for humidity sensing application. The flexibility of the as-developed humidity sensor was utilized for the moisture detection in commonly used baby diapers with alarm. The computer model was simulated & optimized for the synthesized composite (Cd-S & Polyacrylamide) using density functional theory and performed several analyses. HOMO-LUMO and correspondingly obtained other electronic parameters were studied, which revealed that the bandgap of the synthesized composite material tends to decrease upon increasing the level of water molecules owing to be better humidity sensing mechanism, and therefore it is apt for developing an electrical humidity sensor. We also calculated several electronic parameters in order to understand their variations with the increasing number (concentration) of water molecules. Further, the thermochemical data reveals that the composite system is stable and humidity (H₂O) is absorbed well onto its surface as the thermodynamic values keep on increasing as the concentration of water molecules is increased. Since we have synthesized a metal (Cd)

based absorbent composite, Cd plays a crucial role in the absorbing phenomena. In order to validate this, we calculated the distances of all the water molecules from Cd atom and found that it lies within the interaction ranges and hence the theoretical studies also are in support of our findings. These results lay the establishment of the crucial fact that the developed composite material is suitable for absorbent behaviour and can be employed for further applications.

7.4 Fabrication of $\text{Cu}_{0.8}\text{Zn}_{0.2}\text{Sb}_2$ -polyacrylamide nanocomposite via frontal polymerization and its relevance in moisture sensing and photodetection

$\text{Cu}_{0.8}\text{Zn}_{0.2}\text{Sb}_2\text{AAM}$ based capacitive humidity sensor was successfully fabricated using a spin coating technique and the photoconduction behaviour of the material was also investigated. The presence of mesoporous morphology of the fabricated thin-film energized the sensing capability of film. The wide bandgap of 3.91 eV felicitates better conduction accompanied by a synergistic interaction between metal Cu-Zn-Sb ternary phase and PAAm boost the sensitivity as well as photoconductivity of the thin film-based sensing element. $\text{Cu}_{0.8}\text{Zn}_{0.2}\text{Sb}_2\text{AAM}$ -polymer interfaces exhibited the photoconduction behaviour revealing response and recovery time of 6.6 sec and 10.24 sec. Humidity sensing characteristics on film surface were evaluated by the capacitive performance of $\text{Cu}_{0.8}\text{Zn}_{0.2}\text{Sb}_2\text{AAM}$ based thin film humidity sensor. The Average sensitivity (S) was found to be ~ 168.477 pF/%RH at an optimum frequency of 20 Hz. The thin-film-based sensor exhibits a rapid response and recovery time of 4.6 sec and 5.6 sec respectively, with a 96% sensitivity retention after 60 days. Thus, $\text{Cu}_{0.8}\text{Zn}_{0.2}\text{Sb}_2\text{AAM}$ polymer-based capacitive humidity sensor provides an insight measure for a stabilized ternary system based on polymer nanocomposite for humidity sensing and photoconduction application.

7.5 Improved humidity sensing response of roasted gram derived carbon quantum dots

The gram carbon quantum dots were synthesized via waste gram peels, which is the source of carbon. As synthesized carbon quantum dot is water-soluble and shows the green and blue luminescent property. We have prepared GCQDs at two different temperatures 315 °C (C-1) and 650 °C (C-2) and the average size of GCQDs are 7 and

5 nm, respectively. In UV light samples C-1 and C-2 exhibit green and blue emission respectively. The chemical composition of GCQDs was confirmed by Raman and XPS analysis. The simple and cost-effective GCQDs showed good sensing characteristics. We have used both the samples C-1 and C-2 for the capacitive humidity sensor at different frequencies (20 Hz - 2 MHz). Among C-1 and C-2 based sensors, C-2 displays the best result at optimized frequency. The response and recovery time for sample C-1 are 13.3 sec and 14.1 sec and for C-2 these are 7.3 sec and 4.7 sec, respectively. From the theoretical study, we concluded that the water molecules easily interact with carbon quantum dots. The electrostatic is a contour map which shows that the red regions represent the most electronegative sites, whereas the blue regions represent most electropositive sites within the CQD-water system. These sites also reveal crucial information concerning the regions where the CQD-water system can undergo intra- and intermolecular interactions to attain stability. Since the energy gap between HOMO and LUMO is very small and this energy gap is sufficient to give significant information about the CQD-water system that it has almost planar geometry and assists in layer-based interaction and hence tends to decrease the HOMO-LUMO gap. Thus gram carbon quantum dots easily interact with water molecules and were performed as a humidity sensor. Also, the theoretical data confirmed the experimental results.

7.6 One-pot synthesis of phosphine free indium selenide (InSe) QDs and their structural characterization for LPG and humidity sensing

The phosphine-free InSe quantum dots have been synthesized successfully using the least toxic hot injection route and the films were fabricated via the spin coating method. The fabricated InSe QDs film was further used for LPG and humidity sensing purposes. The fluorescence was observed in the blue range by the UV-light chamber and further confirmed by the photoluminescence spectroscopy analysis. The particle size distribution curve gave the average particle size of the QDs as ~13 nm. The UV-absorption spectra were taken and calculated optical band gap as 2.2 eV. The TRPL analysis exhibited the relaxation time of QDs as 6.14 ns. The formation of quantum dots was also confirmed by TEM and HRTEM analysis which gave the particle size in the range of 2 to 4 nm. XRD pattern revealed the crystalline nature of QDs. Further, the fabricated film was used for LPG and humidity sensing. The humidity sensing properties were studied in the range 10 %RH to 90 %RH and found as the most sensitive i.e. 19.50

MΩ/%RH in the mid humidity range (45-70 %RH). The average sensitivity of the sensor was found as 8.89 MΩ/%RH. Response and recovery times of the InSe quantum dot-based humidity sensor were found as 5.3 sec & 13.2 sec. The sensing element was also exposed with the LPG of various concentrations 0.5 to 2.0 vol.%. The maximum sensor response was found at 4.41 for 2.0 vol.% of LPG. This sensor exhibited the sensor response of 2.29 for 0.5 vol.% of LPG which is below LEL. The minimum response and recovery times were calculated as 7.5 sec and 6.3 sec. The investigated sensing parameters favour this material for the commercial development of a humidity sensor at room ambient.

A chapter-wise outline of the thesis including the sensing nanomaterials, their crystallite size, energy band-gap, sensitivity, response and recovery time are depicted in Table 7.1. The main aim of our research work carried out was to investigate and fabricate a low-cost humidity sensor with high responsiveness than previously reported sensors that would be applicable in the multifunctional field. From this table, it can be observed that InSe quantum dots is an excellent material for electrical humidity sensing application at room temperature. Application of an as-developed humidity sensor based on CdS/Polyacrylamide nanocomposite for the detection of moisture/ wetness level in the baby diaper with an alarm system has proven an innovative approach.

7.7 The scope of Further Research Work

In future, research work for creative and efficient devices, the understanding about the role of nanodimensional material at room temperature applications would be desirable. This includes a combination of the recovery aspects onto the surface of the sensing element.

- In the present work, the InSe quantum dots has been optimized to improve the sensing parameters, due to the high surface to volume ratio while there is scope for integration of modifiers like of similar radius or some other less toxic quantum dots for reducing the response and recovery times of humidity and gas sensor.
- An effort may also be made for the synthesis of reported materials using other methods and their versatile sensing applications.

- The dielectric behaviour of these nanometallopolymers and quantum dots may be interesting. The effects of other gases at room temperature on the thin films of synthesized nanomaterials may be investigated in future.
- Detailed analysis of the evolution of the surface reactions concerning temperature needs to be carried out so that the exact understanding of the reaction products from the surface interaction may be possible.
- The theoretical investigation may be very helpful to investigate the interaction between the surface of sensing elements and gases.

Tables:

Table 7.1: A chapter-wise outline of the Thesis

Chapter No.	Sensing Material	Size (nm)	Energy Band-gap (eV)	Sensitivity (M Ω /%RH)	Capacitive (pF/%RH)	Recovery Time (sec)	Response Time (sec)
Ch. 1	Introduction						
Ch. 2	Ni(NO ₃) ₂ (AAm) ₄ .2H ₂ O	4.0-21.0	4.03	0.37	94.63	75.25	15.15
Ch. 3	CdS/polyacrylamide	5.0-3.1	3.50	3.89	125.57	33.00	12.50
Ch. 4	Cu _{0.8} Zn _{0.2} Sb ₂ AAm	17.3-21.8	3.91	4.45	168.47	5.65	4.65
Ch. 5	Carbon quantum dots	2.0-10.0	4.20	5.12	254.86	4.75	7.35
Ch. 6	InSe quantum dots	4.0-6.0	2.20	8.89	261.63	4.32	12.21
Ch. 7	Conclusion						

APPENDIX

Experimental Methods and Characterization Techniques

The experimental techniques used through the whole work for the preparation and characterization of the nanomaterials and sensor are over-viewed in this part. The synthesis of nanometallopolymer and quantum dots were performed by frontal polymerization and one pot method. The sensing film fabrication was done by spin coating method. For the confirmation of the prepared samples were characterized by, X-ray Diffractometer, Scanning Electron Microscopy, Transmission Electron Microscopy, UV-visible spectroscopy, photoluminescence and Particle Size Analysis. Further the variation in the impedance corresponding with relative humidity was observed by impedance analyzer.

A.1 Introduction

The methodology and various experimental techniques used in the synthesis and investigation of nanometallopolymers and quantum dots thin films have been described.

X-ray diffractometer (XRD) Scanning electron microscope (SEM), Particle Size Analyzer, Photoluminescence, Transmission electron microscope (TEM) and UV-vis spectrophotometer were used to characterize these films. A large number of experimental techniques have been employed for accomplishment the overall evidence about the properties as structure, shape, size and topology etc. of the material. Some of the experimental techniques which have been used in this thesis work are described in detail in this chapter.

A.2 Methodology of Present Work

Following steps were carried out for the present investigation;

1. Synthesis of nanometallopolymers and quantum dots.
2. Fabrication of the sensing film.
3. Investigation of the material using different characterization techniques to know phase, structure, size, morphology, band gap and surface area etc. of the sensing film. The techniques used here are as follows:
 - a. **X-ray Diffraction (XRD):** XRD is used for the study of phase identification and structural properties. It is also used to find crystallite size.
 - b. **Scanning Electron Microscopy (SEM):** SEM technique is used to know the surface morphology of the nanocomposite thin film.
 - c. **Transmission Electron Microscopy (TEM):** TEM is used to obtain the topography of the sample which deals with the internal structure of the sample, and its grain distribution and grain diameter.
 - d. **Particle Size Analyzer:** It is used to find out the particle size distribution in the sample.
 - e. **Photoluminescence spectroscopy:** It is used for the luminescence property of the quantum dots.

- f. **UV-visible Spectroscopy:** This spectroscopy will provide information about the absorption spectra and the optical band gap of the sample.

A.3 Synthesis

A.3.1 Frontal Polymerization Method

➤ Synthesis of nanometallopolymers

For the synthesis of nanometallopolymers, materials scientists has been used a variety of tools such as Frontal polymerization technique, in this process first ignite front of the monomer and this front actions towards the bottom. The second method is chain-growth condensation polymerization, in this polymerization an active centre is generated and monomers can be polymerized in a very short span of time to form large molecular weight with some by-products, polycondensation, in which the molecules join together and form the condensate with some byproducts such as water and methanol, ring-opening polymerization, in this method terminus of a polymer chain attack on the cyclic monomer and form the longer chain, the reactive centre may be free radical, cationic or anionic, electro-polymerization, in this technique, conducting polymer synthesized on the conducting substrate, living ionic polymerization, in this process, the active ionic centres are in chemical equilibrium with an exchange rate, which is far faster than the propagation rate and radical polymerization, in this polymerization polymers are formed by successive addition of the active species. Some post-synthesis methods are also reported for metallopolymers as polymer modified by combining metal centres or ions. In the processing of the metallopolymers, there are various reactions taking place as Suzuki, Sonogashira and Heck coupling reaction.

A.3.2 Frontal Polymerization

In Frontal polymerization process the acrylamide monomer is converted into polymer in a localized reaction zone and this is short time and solvent free method for polymerization. Frontal polymerization happens in a definite arrangement with suitable thermo-physical properties, which are extremely exothermic and low heat conductivity factor. The heat changed during the polymerization of one monomer layer was consumed in the activation of the next layer. Thermal wave proceeds in a narrow temperature range close to the adiabatic heating of the reaction medium. The Frontal polymerization are three types:

- ❖ **Thermal Frontal polymerization:** The TFP is the technique, in which an external source used to initiate the front for polymerization. In this technique, the contained reaction is determined by an external UV source..
- ❖ **Isothermal Frontal polymerization:** The (IFP) is process in which shows the gel effect that happens when the monomer and initiator diffuse into a polymer unit. Thermal frontal polymerization starts when heat source associates with solution of monomer and thermal initiator.
- ❖ **UV exposure Frontal polymerization:** This is the technique in which the UV exposure used for the external source. It has also faster polymerization rate, and the source of energy is in exothermic form of polymerization, raising the temperature and increasing the rate of reaction at this zone. A schematic diagram of synthesis of nanometallopolymer is shown in Fig.A.1.

A.3.3 One-pot method:

The first time kinetic growth method introduced by LaMer and Dinegar, who defined how the formation of monodisperse colloids quantum dots is dependent on nucleation. In this method the rapid growth of colloidal quantum dots also explained. By this method, Alivisatos and Bawendi also explained the one pot or hot injection method of synthesizing quantum dots. Presently, the one pot or hot-injection method is one of the most common route for the synthesis of nanomaterial. This method involves the formation of consistent nuclei by the quick injection of organometallic substances into a warm solvent. During the reaction process it also contains the some surfactant and ligands to avoid quantum dots from agglomeration. The ligands that are alkylphosphine oxides or trioctylphosphine, long-chain carboxylic acids or oleic acids, and long-chain amines groups (oleylamine). Once a nucleation process has happened a consistent diffusion-controlled progress is perceived through the solution. During this the larger quantum dots produce very slowly than the smaller quantum dots, subsequent in a size effect. As the progress of the quantum dots improves, the bigger QDs continue to produce while the lesser QDs liquefy due to their greater chemical potential. The average particle size of the quantum dots increases and the concentration of the particle decreases till the point of saturation. The hot-injection or one pot method is predominantly effective because in this method the high level of control of particles permitting a rapid nucleation separated from the growth stage. Using this method, increasing the temperature,

surfactants concentration, and reaction time and possible to obtain various size of quantum dots. A schematic diagram of synthesis of nanometallopolymer is shown in Fig.A.2.

A.4 Fabrication Techniques for Thin Film

A.4.1 Spin coating method

Spin coating is a technique in which a thin layer is coated on a solid platform (substrate) using a machine called spin coater (Metrex RC100, India) which is shown in Fig. A.3. The spin coater, which is used for thin film deposition having many components but mainly a powerful motor, generally which can spin up to 6000 round per minute (rpm) and a vacuum pump for holding substrate. In spin coater spinning speed and time of spinning are responsible for the thickness of thin films, if time of spinning and rate of spinning is increased the thickness of thin film decreased. The coated thin films were dried at temperature 150-200°C to eliminate excess solvents from the resulting. The required thickness of thin film was obtained by the repeating the process of spinning and drying.

Dispense of the resin plays an important factor in the preparation of thin film. For this, the substrate must be cleaned in ultrasonic bath. Then after loading the substrate on spin coater, the main task starts. There are two ways to dispense the resin fluid on the substrate. They are as follows:

Static resin: Static dispense is the deposition of a small puddle of resin fluid on the center of the substrate. Highly viscous solution and large substrate is needed in this process with a higher spinning speed. It also requires a large amount of fluid to cover the whole substrate and due to high spinning rate much of the fluid is wasted.

Dynamic resin: In this process speed of the arm rotator is slow around 500-1000 rpm. This is more advantageous than static resins as the chances of void formation are low in this method. In this less amount of fluid is required and due to low speed, the wastage of fluid around the rotator is less.

A.6 Characterization Techniques

The nanometallopolymer and quantum dots were characterized by various characterization techniques which are described as follows:

A.6.1 X-ray Diffractometer

X-ray diffraction (XRD) is one of the most important non-destructive tools to analyze all kinds of matter ranging from fluids, to powders and crystals. From research to production and engineering, XRD is an indispensable method for materials characterization and quality control. X-ray diffraction experiment is performed by machine called X-ray diffractometer, the photograph of which is shown in Fig. A.3. Here crystalline structure causes a beam of incident X-rays to diffract into many specific directions. By measuring the angles and intensities of these diffracted beams, a crystallographer can produce a three-dimensional picture of the density of electrons within the crystal. From this electron density, the mean positions of the atoms in the crystal, chemical bonds, crystallographic disorder etc. can be determined. An X-ray striking an electron produces secondary spherical waves emanating from the electron. This phenomenon is known as elastic scattering, and the electron is known as the scatterer. A regular array of scatterers produces a regular array of spherical waves. Although these waves cancel one another out in most directions through destructive interference, they add constructively in a few specific directions, determined by Bragg's law given in Eqn. A.1:

$$2d\sin\theta = n\lambda \quad \dots (A.1)$$

Here d is the spacing between diffracting planes, θ is the incident angle, n is any integer, and λ is the wavelength of the beam. The schematic diagram for Bragg's law is shown in Fig. A.4. These specific directions appear as spots on the diffraction pattern called reflections. X-rays are used to produce the diffraction pattern because their wavelength λ is typically the same order of magnitude (1–100 Å) as the spacing d between planes in the crystal.

X-rays are generated in a cathode ray tube by heating a filament to produce electrons, accelerating the electrons toward a target by applying a voltage, and bombarding the target material with electrons. When electrons have sufficient energy to dislodge inner shell electrons of the target material, characteristic X-ray spectra are

produced. These spectra consist of several components, the most common being K_{α} and K_{β} . K_{α} consists, in part, of $K_{\alpha 1}$ and $K_{\alpha 2}$. $K_{\alpha 1}$ has a slightly shorter wavelength and twice the intensity as $K_{\alpha 2}$. The specific wavelengths are characteristic of the target material (Cu, Fe, Mo, Cr). Filtering, by foils or crystal monochrometers, is required to produce monochromatic X-rays needed for diffraction. $K_{\alpha 1}$ and $K_{\alpha 2}$ are sufficiently close in wavelength such that a weighted average of the two is used. Copper is the most common target material for single-crystal diffraction, with Cu K_{α} radiation = 1.5418Å. These X-rays are collimated and directed onto the sample. As the sample and detector are rotated, the intensity of the reflected X-rays is recorded. When the geometry of the incident X-rays impinging the sample satisfies the Bragg Equation, constructive interference occurs and a peak in intensity occurs.

The basic component of diffractometer is an X-rays coherent source (Cu K_{α} , 0.15418 nm) which provides a beam of X-ray directed towards the crystal (sample) and a detector which monitors diffracted beam intensity. Other components are several focusing optics, rotating stand sample holder and software. The X-rays diffraction software provides an intensity of diffractive X-rays as a function of d-spacing/ 2θ which contains peaks at certain positions. This XRD pattern is a signature of certain materials and these signature patterns are provided by International Centre for Diffraction Data (ICDD) and Joint Committee on Powder Diffraction Standards (JCPDS). The information obtained from this pattern includes types and nature of crystalline phases present, structural make-up of phases, degree of crystallinity, amount of amorphous content, micro strain & size and orientation of crystallites. The following formulae are used to calculate these parameters [2-4]. The crystalline size (D) of crystal was calculated by Debye-Scherrer's formula given in Eqn. A.2

$$D = \frac{K\lambda}{\beta \cos\theta} \quad \dots (A.2)$$

where, constant factor K is nanostructure constant, β is the broadening of diffraction line measured at half of its maximum intensity (FWHM) and λ is the wavelength of the X-ray used (0.15418 nm).

A.6.2 Scanning Electron Microscope

A scanning electron microscope (SEM) is a type of electron microscope that produces images of a sample by scanning the surface with a focused beam of electrons.

The electrons interact with atoms in the sample, producing various signals that contain information about the surface topography and composition of the sample. The most common SEM mode is the detection of secondary electrons emitted by atoms excited by the electron beam. By scanning the sample and collecting the secondary electrons that are emitted using a special detector, an image displaying the topography of the surface is created. The photograph of scanning electron microscope used in the reported research is shown in Fig. A.5(a).

SEM consists of an electron gun of some kind such as Tungsten or Lanthanum Hexaborate (LaB_6) which acts as the source of electron beam. The filament inside the electron gun is heated until a stream of electron is produced. This stream of electron is then condensed by first condenser lens, this lens serves two purposes at a time. One, it eliminates the high-angled electron from the beam and second, it limits the amount of current in the beam. The second condenser lens makes the beam narrower and focused. Near the bottom of SEM a set of scanning coils is present that is used to focus the beam in the back and forth direction. When this beam hits the spot on the sample surface, it removes the secondary electrons and these electrons are detected by the detectors. The detectors role is to count the electrons and amplify the current and record it to visualize the image based on the number of electrons removed from the particular spot in pixels by a computerized system. The working of the SEM is shown in Fig. A.5(b).

Specimen interaction with the beam

Specimen interaction is the process that makes electron microscopy possible. The various interactions that occur at the surface of the specimen is shown in Fig. A.6 and listed in the following sub-heads:

Secondary electron emission: The emission of secondary electron is caused when the energized electrons strikes the surface of the sample. These electrons transfer some energy to the lower energy electrons (usually the K-shell) and this causes the ionization of the atoms present at the surface of sample. This electron removed from the surface is called as “secondary electron”. This is the most common mode used in the imaging with SEM. The brightness of the signals depends upon the number of secondary electrons reaching the detector.

Backscattered electrons: Backscattered electrons are reflected or backscattered out of the specimen interaction volume. This is caused by collision of incident electron to an atom which is nearly normal to the incident path. The production of backscattered electrons varies directly with the atomic number of the specimen, that is, higher the atomic number, higher will the brightness. Backscattered electrons thus can be used to detect different chemical composition, by examining the contrast between the areas.

Cathodo luminescence: When the high energy electrons strike the surface they excite the atoms and when these atoms return to their ground state they emit light. This process is termed as Cathodo luminescence (CL). In SEM, CL detectors can be used to give image in real colour.

Auger electron: When the electron is removed from the core level of the atom, a vacancy is created which is filled by higher energy electron releasing energy which is transferred to another electron, which is then ejected as auger electron. Auger electron has a characteristic energy feature which is unique for each element. Thus these auger electrons are collected and provide useful compositional information of the sample surface.

A.6.3 Transmission Electron Microscope (TEM)

Transmission electron microscopy (TEM) is a microscopy technique in which a beam of electrons is transmitted through a specimen to form an image. The specimen is most often an ultrathin section less than 100 nm thick or a suspension on a grid. An image is formed from the interaction of the electrons with the sample as the beam is transmitted through the specimen. The image is then magnified and focused onto an imaging device, such as a fluorescent screen, a layer of photographic film, or a sensor such as a charge-coupled device. TEM provides the image in real time. The image of a TEM machine is shown in Fig. A.7 (a).

The TEM consists of an emission source, which may be a tungsten filament or needle, or a lanthanum hexaboride (LaB₆) single crystal source. The gun is connected to a high voltage source (typically ~100–300 kV) and, given sufficient current; the gun will begin to emit electrons either by thermionic or field electron emission into the vacuum. The electron source is typically mounted in a Wehnelt cylinder to provide preliminary focus of the emitted electrons into a beam. The upper lenses of the TEM then further

focus the electron beam to the desired size and location. The schematic set-up depicting different parts is shown in Fig. A.7 (b).

Description of sample holder

TEM specimen stage includes airlocks which allow the insertion of the specimen holder into the vacuum with minimal loss of vacuum in other areas of the microscope. The specimen holders hold a standard size of sample grid or self-supporting specimen. Standard TEM grid sizes are 3.05 mm diameter, with a thickness and mesh size ranging from a few to 100 μm . The sample is placed onto the meshed area having a diameter of ~ 2.5 mm. Usual grid materials are copper, molybdenum, gold or platinum. This grid is placed into the sample holder, which is paired with the specimen stage. A wide variety of designs of stages and holders exist, depending upon the type of experiment being performed. Once inserted into the TEM, the sample has to be manipulated to locate the region of interest to the beam, such as in single grain diffraction, in a specific orientation. To accommodate this, the TEM stage allows movement of the sample in the XY plane, Z height adjustment, and commonly a single tilt direction parallel to the axis of side entry holders. Sample rotation may be available on specialized diffraction holders and stages. The various steps involved in the working of TEM are:

- The electron beam produces a beam of electrons, which is then focused to a thin, coherent beam.
- This beam of electron is further restricted by the condenser lenses which knock out the high angled electron.
- This beam transmits through the specimen and is focused by the objective lenses to give an image.
- The image is then passed by the project lenses to enlarge the image, which then strikes the phosphor screen.
- The darker area represents the presence of few number of electrons transmitted through the sample (i.e. the sample must be thick there) whereas the brighter part will represent more transmitting electron area.

Detection of transmitted electrons

Following steps are involved in the detection of transmitted electrons and image formation:

Unscattered electrons: These are the incident electrons that are transmitted through the sample without any interaction. The image will appear darker if the unscattered electrons are few as they vary inversely with the thickness and the image will appear brighter for large number of unscattered electrons.

Elastically scattered electron: There are incident electrons that get deflected from their path. The scattering of the electron follows Bragg's Law ($\lambda = 2d \sin\theta$). Since all the incident electrons have same energy and atomic spacing, so they will scatter with same angle. These scattered electrons can thus be collected by magnetic lenses to give pattern of spots which in turn are very useful in determining the orientation, atomic arrangement and phases present in the given sample.

Inelastically scattered electrons: There are many electrons that interact inelastically with the specimen transferring out all their energy to the atoms in the specimen. These electrons then transmit through the rest of the specimen. These unscattered electrons can be used to provide following information:

- The inelastic loss of energy is dependent on the element and is unique to the bonding state of the element, thus gives the information about composition and bonding.
- The alternate light and dark lines (Kakuchi bands) formed due to inelastic scattering; the width of these bands is inversely proportional to the atomic spacing.

A.6.4 UV-Vis Spectrophotometer

Ultraviolet and visible (UV-vis) absorption spectroscopy is the measurement of the attenuation (weakening of strength) of a beam of light after it passes through a sample or after reflection from a sample surface. Ultraviolet and visible light are energetic enough to promote outer electrons to higher energy sublevels. The technique is usually applied to molecules or inorganic complexes in solution. Absorption measurements can be at a single wavelength or over an extended spectral range. UV-vis spectra have broad features that are of limited use for sample identification but are very useful for quantitative measurements. The concentration of an analyte in solution can be determined by measuring the absorbance at some wavelength and applying the Beer-

Lambert Law. Since the UV-vis range spans the range of human visual acuity of ~400-750 nm, UV-vis spectroscopy is useful to characterize the absorption, transmission, and reflectivity of a variety of technologically important materials, such as pigments, coatings, windows, and filters. This more qualitative application usually requires recording at least a portion of the UV-vis spectrum for characterization of the optical or electronic properties of materials. Electronic orbital of atoms and molecules have characteristic energies, giving rise to a set of discrete energy levels. An electron is able to change from an occupied orbital to another orbital, gaining or losing energy only in amounts exactly corresponding to the difference between two levels. The spectrophotometer used here for the determination of optical properties is shown in Fig. A.8(a).

The promotion of an electron from the ground state (lowest possible energy) at energy E_1 to higher energy state at E_2 is possible if the molecule absorbs electromagnetic radiation of the corresponding wavelength $\lambda = hc/(E_2 - E_1)$ (where, c = speed of light, h = Planck's constant). The electron at a higher energy is then said to be in an excited state. Excited states usually exist only for very short periods of time (femto seconds to microseconds), because the higher energy state is unstable and the extra energy is lost through relaxation processes such as emission of light. The typical energy difference between the ground and the first excited levels of many molecules corresponds to electromagnetic waves of the ultra-violet (UV) and visible regions of the electromagnetic spectrum.

The UV-visible range is only a small part of the total electromagnetic spectrum, and is generally defined from wavelengths of 190 nm at the high energy UV end to about 800 nm at the low energy red end of the spectrum. Light of other regions of the spectrum gives rise to different types of transitions and hence different types of spectroscopy. For example, IR radiation is usually not energetic enough to cause electronic transitions but can excite vibrations of molecules.

UV-visible spectrophotometers usually measure absorbance, which is the log-ratio of transmitted (sample in beam) over incident (no sample in beam) intensities. The UV-vis photo spectrum of solution is recorded with respect to water placed in the reference beam using single beam spectrophotometer. The spectrum is analyzed by plotting $(\alpha h\nu)^2$ vs $h\nu$, based on eqn A.3:

$$\alpha h\nu = A(h\nu - E_g)^n \quad \dots (A.3)$$

where, α is absorption coefficient, A is a constant and n is the exponent that depends upon the quantum selection rules for the particular material. The value of n characterizes the nature of band transition ($n = 1/2$ and $3/2$ corresponds to direct allowed and direct forbidden transitions while $n = 2$ and 3 corresponds to indirect allowed and indirect forbidden transitions, respectively). A straight line is obtained when $(\alpha h\nu)^2$ is plotted against photon energy ($h\nu$), which indicates that the absorption edge is due to direct allowed transition. The intercept of the straight line on $h\nu$ axis corresponds to the optical energy band-gap (E_g).

In a standard UV-vis spectrophotometer, a beam of light is split; one-half of the beam (the sample beam) is directed through a transparent cell containing a solution of the compound being analyzed, and one-half (the reference beam) is directed through an identical cell that does not contain the compound but contains the solvent. The instrument is designed so that it can make a comparison of the intensities of the two beams as it scans over the desired region of the wavelengths. If the compound absorbs light at a particular wavelength, the intensity of the sample beam will be less than that of the reference beam. Absorption of radiation by a sample is measured at various wavelengths and plotted by a recorder to give the spectrum which is a plot of the wavelength of the entire region versus the absorption of light at each wavelength. And the band gap of the sample can be obtained by plotting the graph between $(\alpha h\nu$ vs $h\nu$) and extrapolating it along the x-axis. Ultraviolet and visible spectrometry are almost entirely used for quantitative analysis; that is, the estimation of the amount of a compound known to be present in the sample. The sample is usually examined in solution form. The working is shown in Fig. A.8(b).

A.6.5 Particle Size Analyzer

As the name suggests, Particle Size Analyser is a technique used to measure the size of the particles present in the solution. The idea behind this size measurement is called Dynamic Light Scattering (also known as PCS-Photon Correlation Spectroscopy) which measures the Brownian motion and relates this to the particle size. It does this by illuminating the laser and analyzing the intensity fluctuations in the scattered light. The photograph of the instrument is shown in Fig. A.9(a).

If a small particle is illuminated by a light source such as a laser, the particle will scatter the light in all directions. If a screen is held close to the particle, the screen will be illuminated by the scattered light. Fig. A.9(b) shows the propagated waves from the light scattered by the particles. The bright areas of light are where the light scattered by the particles arrive at the screen with the same phase and interferes constructively to form a bright patch. The dark areas are where the phase additions are mutually destructive and cancel out each other.

Particles suspended in a liquid are never stationary. The particles are constantly moving due to Brownian motion. Brownian motion is the movement of particles due to the random collision with the molecules of the liquid that surrounds the particle. An important feature of Brownian motion for DLS is that small particles move quickly than large particles. As the particles move around, the constructive and destructive phase addition of the scattered light will cause the bright and dark areas to grow and diminish in intensity or to put it another way, the intensity appears to fluctuate.

References

- [1] S.M. Attia, J. Wang, G. Wu, J. Shen, J. Ma, Review on sol–gel derived coatings: process, techniques and optical applications, *J. Mater. Sci. Technol.* 8 (2002) 211–217.
- [2] D.W. Schubert, T. Dunkel, Spin coating from a molecular point of view: its concentration regimes, influence of molar mass and distribution; *Mater. Res. Innovations* 7 (2003) 314.
- [3] J.D. Verhoeven, *Fundamentals of Physical Metallurgy*, Wiley, New York (1975) 326.
- [4] D. Merkulovs, Cylindrical cell based refractometer and its applications methodology, Thesis: Riga Technical University (2015).
- [5] W.H. Bragg, W.L. Bragg, The reflexion of X-rays by crystals, *Proceedings of the Royal Society of London A* 88 (1913) 428–438.
- [6] A. Patterson, The Scherrer formula for X-ray particle size determination, *Physical Review* 56 (1939) 978–982.
- [7] D.J. Stokes, *Principles and Practice of Variable Pressure Environmental Scanning Electron Microscopy (VP-ESEM)*. Chichester: John Wiley & Sons. (2008) ISBN 978-0470758748.
- [8] J. Frank, *Electron tomography: methods for three-dimensional visualization of structures in the cell*, Springer (2006) ISBN 978-0-387-31234-7.
- [9] L. Sooväli, E.I. Rõõm, A. Kütt et al. Uncertainty sources in UV–Vis spectrophotometric measurement. *Accreditation and Quality Assurance* 11 (2006) 246–255.
- [10] Zetasizer Nano Series User Manual Zetasizer: Malvern

Figures

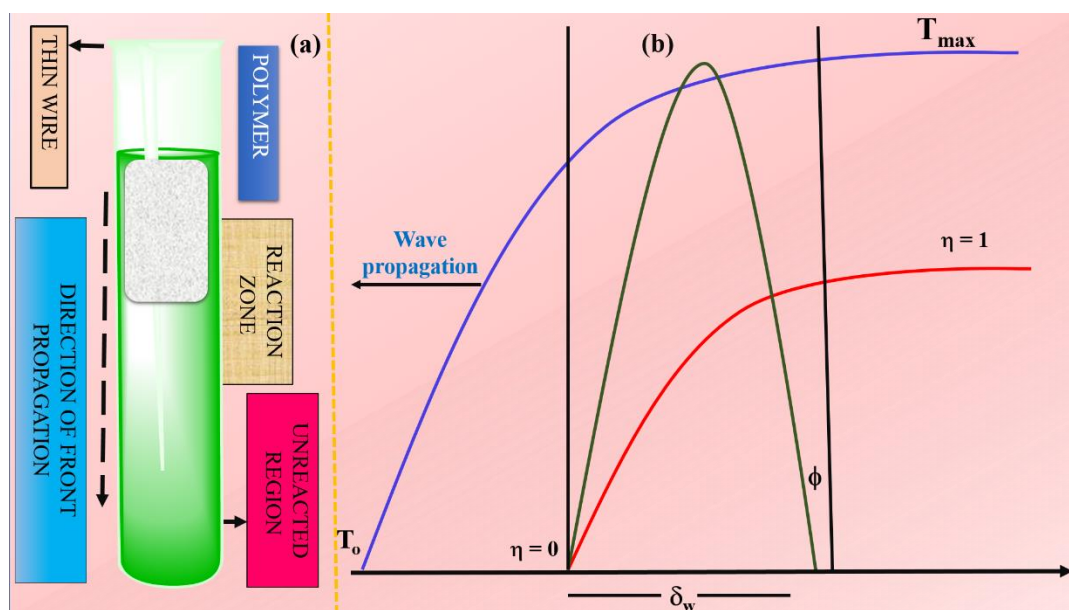


Figure. A.1: Frontal polymerization (a) and (b) its three dimensional process.

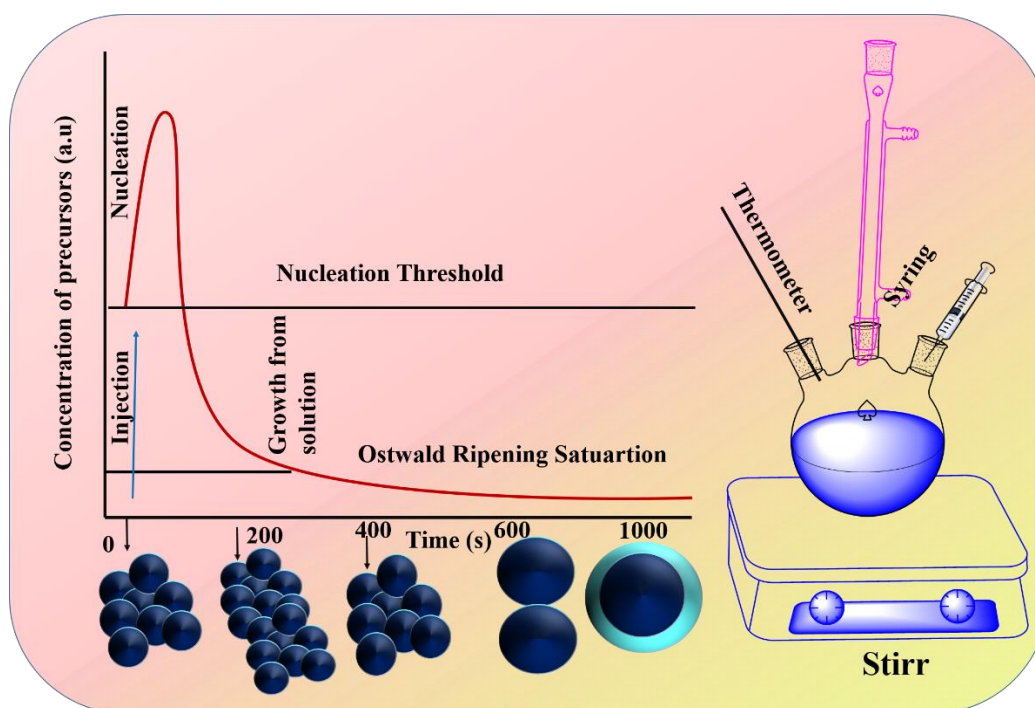


Figure. A.2: Schematic of the nucleation stage of quantum dots in the framework of the LaMer model (left), Representation of the simple synthetic apparatus preparation of quantum dots.



Fig. A.3: Photograph of spin coater (Metrex) used in the preparation of thin film.



Figure. A.4: Photograph of X-ray diffraction setup (X' Pert PRO PANalytical Ltd., Netherlands).

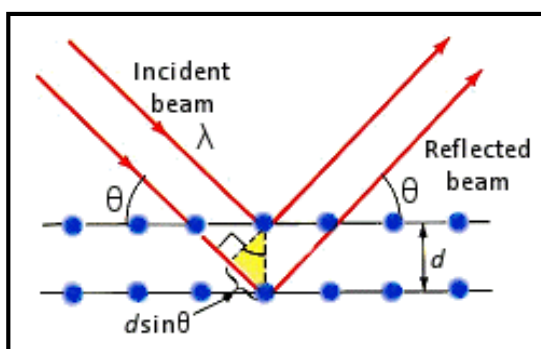


Figure. A.5: Schematic diagram showing the phenomena of Bragg's law.

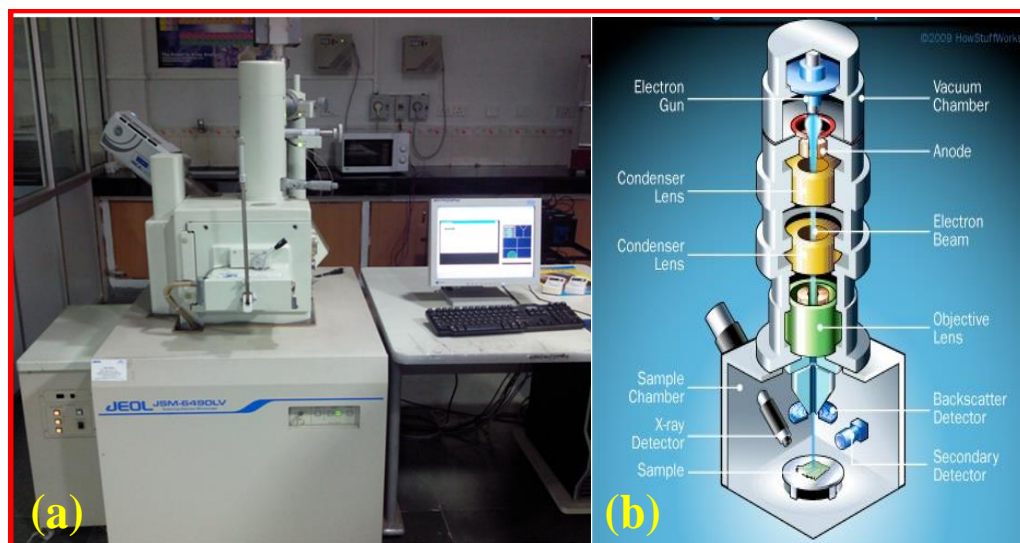


Figure. A.6 (a) Photograph of Scanning Electron Microscopes (JEOL, JSM-6490LV) and its (b) working mechanism.

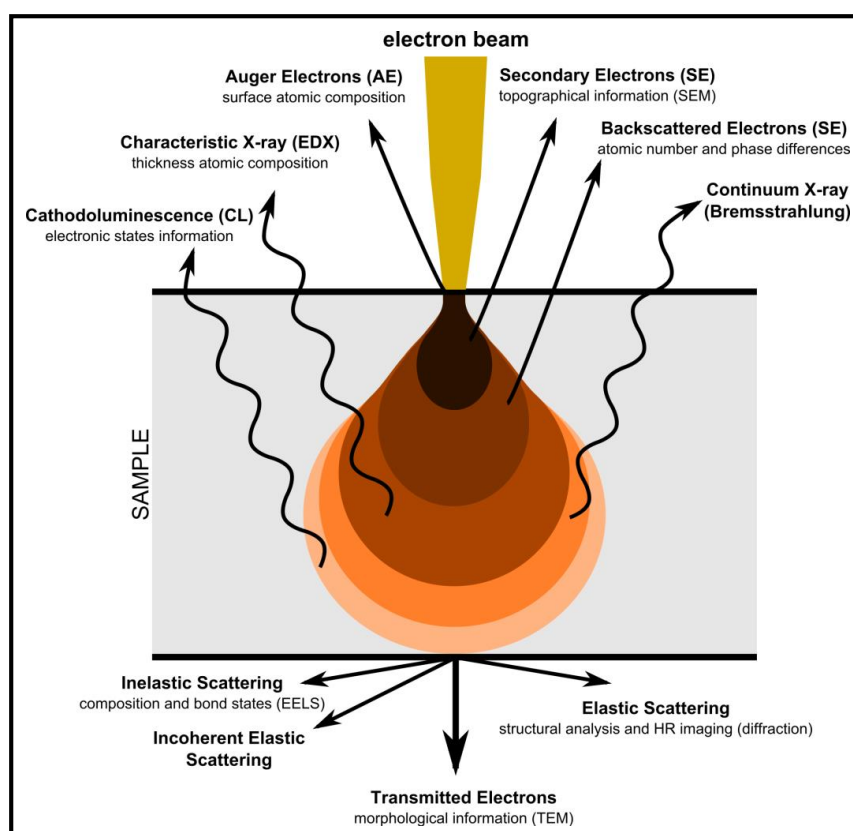


Figure. A.7: Representation of various types of interactions of electron beam with the sample surface

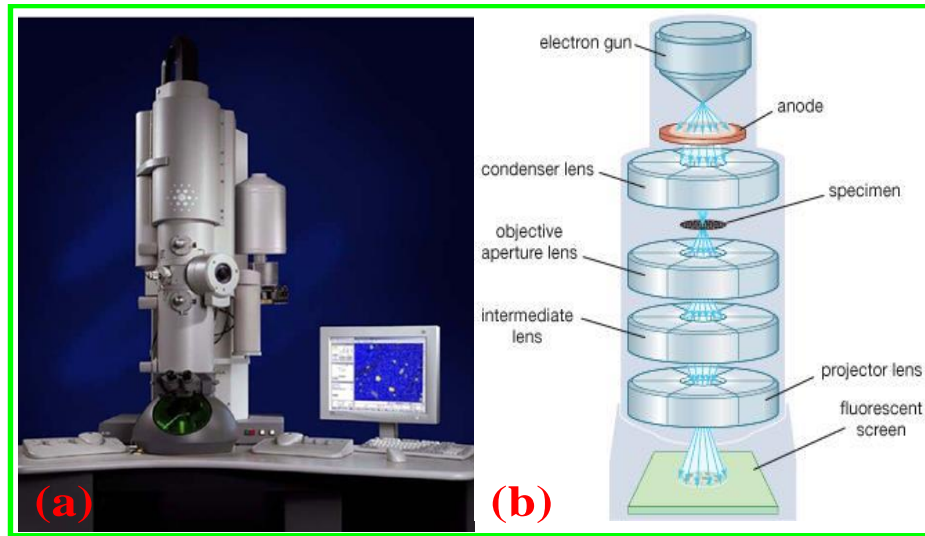


Figure. A.8: (a) Photograph of High-Resolution Transmission Electron Microscope (Philips T20ST) and its (b) working mechanism

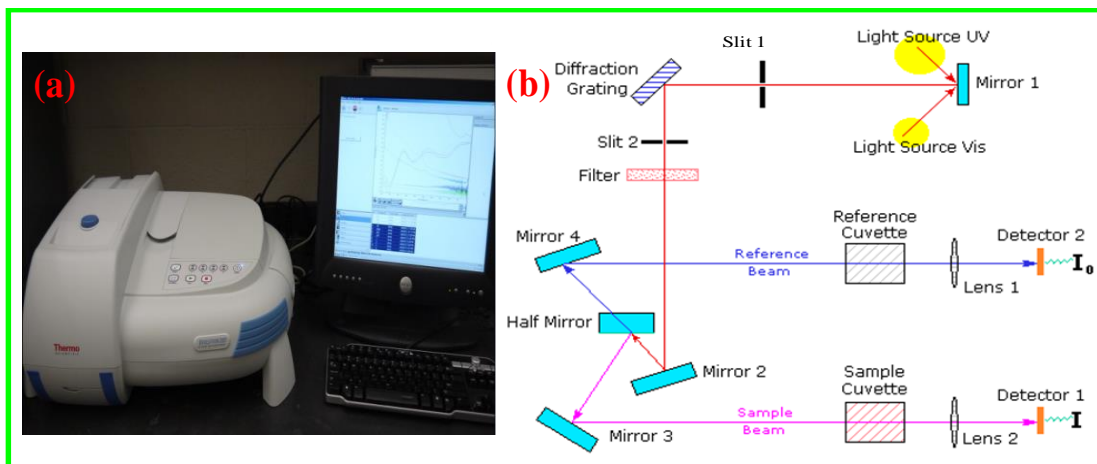


Figure. A.9: Photograph of UV-Visible spectrophotometer (Evolution 201) and its (b) working mechanism

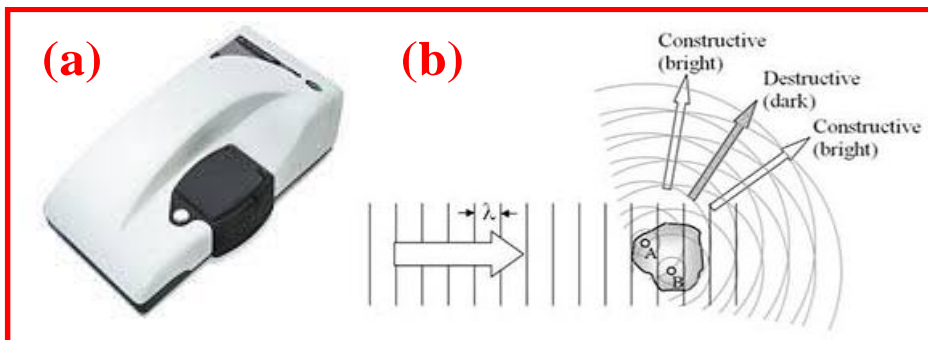


Figure. A.10: (a) Photograph of Particle Size Analyzer (Nano-ZS90) (b) Scattering of light beam through a particle.